

2018

Construction Of Supramolecular And Coordination Compounds From Pyridyl Bis-Urea Macrocycles

Bozumeh Som
University of South Carolina

Follow this and additional works at: <https://scholarcommons.sc.edu/etd>

 Part of the [Chemistry Commons](#)

Recommended Citation

Som, B.(2018). *Construction Of Supramolecular And Coordination Compounds From Pyridyl Bis-Urea Macrocycles*. (Doctoral dissertation). Retrieved from <https://scholarcommons.sc.edu/etd/4788>

This Open Access Dissertation is brought to you by Scholar Commons. It has been accepted for inclusion in Theses and Dissertations by an authorized administrator of Scholar Commons. For more information, please contact dillarda@mailbox.sc.edu.

CONSTRUCTION OF SUPRAMOLECULAR AND COORDINATION COMPOUNDS
FROM PYRIDYL *BIS*-UREA MACROCYCLES

by

Bozume Som

Bachelor of Science
University of Cape Coast, 2007

Master of Science
Norwegian University of Science & Technology, 2011

Master of Science
East Tennessee State University, 2013

Submitted in Partial Fulfillment of the Requirements

For the Degree of Doctor of Philosophy in

Chemistry

College of Arts and Sciences

University of South Carolina

2018

Accepted by:

Linda S. Shimizu, Major Professor

Dmitry V. Peryshkov, Chair, Examining Committee

Aaron K. Vannucci, Committee Member

Scott R. Crittenden, Committee Member

Cheryl L. Addy, Vice Provost and Dean of the Graduate School

© Copyright by Bozumah Som, 2018
All Rights Reserved.

DEDICATION

To my late uncle Francis D. Benia

ACKNOWLEDGEMENTS

It has been a long journey to get to this point. I say thank you LORD for guiding me through this journey. My family and friends (too many to list all of you here), I truly appreciate your support. You do your best to check up on me, even though we are thousands of miles apart.

I would especially like to thank my supervisor Dr. Linda Shimizu, for the great guidance, encouragement and advice she has provided throughout my time as her student. I have been extremely lucky to have a supervisor who cared so much about my work, and who responded to my questions and queries so promptly.

I must express my gratitude to the professors on my dissertation committee, Dr. Dmitry V. Peryshkov, Dr. Aaron K. Vannucci, and Dr. Scott R. Crittenden for their encouragement and insightful comments. Also thanks to Dr. Miao Yu and Dr. Jason R. Hatrick-Simpers who were on my committee during the plan and proposal presentations respectively. Special thank you to Dr. Mark Smith for the X-ray crystallography studies of my materials.

I would also like to thank the University of South Carolina and our funding sources (NSF; CHE-1305136, CHE-1608874) for their financial support.

Last but not the least, I am also very thankful to all the Linda Shimizu group members (past and present) and all the collaborators I have worked with for lending me their expertise and intuition to my scientific and technical problems.

ABSTRACT

The self-assembly of macrocyclic molecules in solution and in the solid state modulates and in many cases enhances their properties for applications in sensing, catalysis and optoelectronics. The self-assembled structures are typically organized by non-covalent interactions such as hydrogen bonding, π - π stacking and dipole-dipole interactions. Our group has focused on the design and synthesis of *bis*-urea macrocycles that can self-assemble into solid cylinders or tubular structures affording crystalline materials. These macrocycles consist of two urea groups and two rigid C-shaped spacers. Easy functionalization of this system enables access to *bis*-urea macrocycle structures that could serve as molecular reactors, coordinating ligands and co-crystalizing agents.

This dissertation focuses on probing the utility of pyridyl functionalized *bis*-urea macrocycles as well as expanding applications of the largest self-assembled phenylethyne *bis*-urea macrocycle. Chapters 1-3 examine the utilization of a smaller pyridyl *bis*-urea macrocycle that self-assembles into strong pillars as a co-crystal former for hydrogen/halogen bond donors. In these pillars, the individual macrocycle units are held together by two different hydrogen bonds (N-H \cdots N and N-H \cdots O) where the urea NHs interact with the urea carbonyl oxygen and the pyridine nitrogen. This affords pillars with basic lone pairs on carbonyl oxygen that can be used to absorb guest molecules in the solid-state. Guest binding occurs through non-covalent interactions, which are either hydrogen bonding or halogen bonding. Co-crystals and molecular salts were successfully synthesized from this macrocycle combined with diiodotetrafluorobenzenes or

naphthalene-1,5-disulfonic acid respectively (chapter 2-3). These demonstrated the utility of the pyridyl *bis*-urea macrocycle motif to control the organization and properties of guests by co-crystallization.

To further investigate this idea, we redesigned and successfully synthesized a constitutional isomer of the pyridyl macrocycle that incorporates the pyridyl N on the exterior of the macrocycle. Chapter 5 reports the synthesis of the key protected *bis*-urea and *tris*-urea macrocyclic intermediate as well as their crystal structures. We explore the urea protected versions of these new *bis*-urea and *tris*-urea macrocycles as ligands to synthesize copper(I) and silver(I) coordination polymers. Two coordination polymers were obtained with protected pyridyl *bis*-urea macrocyclic ligand **4**; $[\text{Cu}_2\text{I}_2(\mathbf{4})_2 \cdot (\text{CH}_3\text{CN})_{1.63(1)}]$ and $[\text{Ag}(\mathbf{4})(\text{NO}_3)(\text{H}_2\text{O})_{2.5}]$ as 2D and 3D coordination networks respectively. Initial photoluminescence studies showed that only complex $[\text{Cu}_2\text{I}_2(\mathbf{4})_2 \cdot (\text{CH}_3\text{CN})_{1.63(1)}]$ exhibit fluorescence properties in the solid state at ambient temperature. In addition, the new pyridyl *bis*-urea macrocycle was successfully deprotected and crystallized by heating 6.0 mg of it in a DMSO-acetonitrile (1:1.5 v/v) mixture (5 mL) in a pressure tube to dissolve completely at 120 °C, then slowly cooled to room temperature at a rate of 1 °C/h. This crystal structure analysis revealed that this redesigned pyridyl *bis*-urea macrocycle also self-assembles into pillars (columns) using the urea···urea bifurcated hydrogen bonds as shown in Appendix D.

Also, in this dissertation (chapter 4), we investigated the loading of a small dye, 5-(dimethylamino)-5'-nitro-2,2-bithiophene into the 1D channels of our self-assembled phenylethyne *bis*-urea macrocyclic host, which has no pyridyl functional groups. These 1D nanochannels have a round cross-section with a diameter of ~9 Å. Here, we were

interested in understanding how the guest molecules aligned inside the host channels and the properties of the host-guest complex. The complex was prepared by soaking the crystalline host in an acetonitrile solution of the dye for 24 hours to give a purple solid. This complex was then characterized by ^1H NMR, UV-visible absorption and fluorescence emission spectroscopies, and wide-angle X-ray scattering. The organization of the guest was probed using linear polarization fluorescence microscopy and time-dependent density functional theory (TDDFT) calculations at the B3LYP/TZ2P level of theory. The guest fluorescence was shown to be polarized along the fiber axis with emission polarization values up to 0.729, indicating a high degree of orientation within the 1D channels.

TABLE OF CONTENTS

Dedication	iii
Acknowledgements	iv
Abstract	v
List of Tables	xi
List of Schemes	xii
List of Figures	xiii
Chapter 1: Introduction	1
1.0 Introduction	2
1.1 Dipyridylureas in Crystals and Co-crystals	8
1.2 Dipyridylureas as Building Blocks for Metallo-assemblies	11
1.3 Pyridyl Functionalized <i>Bis</i> -urea Macrocycles	12
1.4 Conclusion	17
1.5 References	18
Chapter 2: Pillars of Assembled Pyridyl <i>Bis</i> -urea Macrocycles: A Robust Synthon to Organize Diiodotetrafluorobenzenes	26
2.0 Abstract	27
2.1 Introduction	27
2.2 Results and Discussion	30
2.3 Conclusions	43
2.4 Experimental	44

2.5 References.....	51
Chapter 3: Synthesis of Molecular Salts from a Pyridyl <i>Bis</i> -urea Macrocycle and Naphthalene-1,5-disulfonic Acid.....	58
3.0 Abstract.....	59
3.1 Introduction.....	59
3.2 Results and Discussion	62
3.3 Conclusion	70
3.4 Experimental.....	71
3.5 References.....	74
Chapter 4: Absorption of Fluorescent Dyes by a Self-assembled Phenylethynylene <i>Bis</i> -urea Macrocyclic Host	79
4.0 Abstract.....	80
4.1 Introduction.....	81
4.2 Results and Discussion	86
4.3 Future Plans	101
4.4 Conclusions.....	101
4.5 Experimental.....	102
4.6 References.....	109
Chapter 5: Multi-dimensional Copper(I) and Silver(I) Coordination Complexes of a Protected Pyridyl <i>Bis</i> -urea Macrocycle	114
5.0 Abstract.....	115
5.1 Introduction.....	115
5.2 Synthesis and Solution Structures of Macrocylic Ligands 4-5	122
5.3 X-ray diffraction Studies	128
5.4 Investigation of Complex Formation Between 4 and d ¹⁰ Transition Metal Ions	133

5.5 FT-IR Spectroscopy.....	138
5.6 Photophysical Studies of Coordination Complexes	140
5.7 Conclusion	143
5.8 Experimental.....	144
5.9 References.....	153
Appendix A: Permission to Reprint: Chapter 2	161
Appendix B: Permission to Reprint: Chapter 3	162
Appendix C: Permission to Reprint: Chapter 4	167
Appendix D: Deprotected New Pyridyl <i>Bis</i> -urea Macrocyclic (ML2)	168

LIST OF TABLES

Table 2.1 Crystallographic data and structure refinement parameters of co-crystals.....	33
Table 2.2 Comparison of hydrogen and halogen bond distances, and DFT calculated energies of the halogen bonds.....	35
Table 2.3 Comparison of C=O bond lengths, and indicative FT-IR peaks for host 1 and its co-crystals	39
Table 3.1 Crystallographic data and structure refinement parameters of salt co-crystals.	64
Table 3.2 Geometrical data for hydrogen bonding in salt co-crystals	66
Table 4.1 Molecular dimensions and polarity of guests	85
Table 4.2 Fluorescence life times of host 2 and host-guest complex 7	95
Table 4.3 Moves and associated probability of Canonical Monte Carlo simulations for guest dye 6 chemical potential calculations.....	108
Table 4.4 Moves and associated probability of Grand Canonical Monte Carlo simulations for host-guest complex 7	108
Table 5.1 Crystallographic data and structure refinement parameters of macrocyclic ligands 4-5 , and $[\text{Cu}_2\text{I}_2(4)_2 \cdot (\text{CH}_3\text{CN})_{1.63(1)}]$ and $[\text{Ag}(4)(\text{NO}_3)(\text{H}_2\text{O})_{2.5}]$	129
Table 5.2 FT-IR peak positions of key functional groups	139
Table D.1 Crystal data and structure refinement for ML2.....	173

LIST OF SCHEMES

Scheme 2.1 Synthesis of host 1	45
Scheme 4.1 An overview of phenylethynylene <i>bis</i> -urea macrocycle synthesis	103
Scheme 5.1 Synthesis of pyridyl <i>bis</i> -urea macrocycles 1-3	118
Scheme 5.2 Synthesis of new pyridyl <i>bis</i> -urea macrocycles 4-5	123
Scheme D.1 Synthesis of macrocycle ML2	168

LIST OF FIGURES

Figure 1.1 Four possible conformations of N,N'-diphenyl urea compounds	4
Figure 1.2 Common hydrogen bond motif found in self-assembled structures of urea compounds	5
Figure 1.3 Schematic of the synthetic route and self-assembly of the <i>bis</i> -urea macrocycles.....	7
Figure 1.4 Linear dipyridylurea compounds.....	9
Figure 1.5 Crystal structures of co-crystals of dipyridylureas with para-diiodotetrafluorobenzene (p-DITFB).....	10
Figure 1.6 X-ray crystal structure of co-crystals of dipyridylureas and 1,4-diiodobuta-1,3-diyne.....	11
Figure 1.7 X-ray crystal structure of co-crystal of diacetylene diacetylenic acid with dipyridylurea (L3).....	11
Figure 1.8 Two-dimensional hydrogen-bonded frameworks of coordination polymers ...	12
Figure 1.9 Pyridyl functionalized <i>bis</i> -urea macrocycles.....	13
Figure 1.10 X-ray crystal structure of bipyridine <i>bis</i> -urea macrocycle	14
Figure 1.11 Assembly of pyridyl-phenylethynylene <i>bis</i> -urea macrocycle (2)	15
Figure 1.12 Hydrogen-bonded columns of self-assembled <i>bis</i> -urea macrocycles	17
Figure 2.1 Testing pyridyl <i>bis</i> -urea macrocycle 1 as a co-crystal former for ditopic halogen bond donors	29
Figure 2.2 The utility of the assembled macrocycle 1 synthon to organize halogen bond donors by co-crystal formation	30
Figure 2.3 Packing diagrams for halogen bonded co-crystals	35
Figure 2.4 Views from the X-ray structure of 1 ·(<i>m</i> -DITFB) ₂ ·DMSO.....	37

Figure 2.5 Computed surface electrostatic potential maps comparing the potential values of the XB acceptor atom and the XB donor atoms	38
Figure 2.6 FT-IR profile of 1 and co-crystals in the range 4000-650 cm ⁻¹	39
Figure 2.7 XPS survey scans for 1 , 1 ·(<i>o</i> -DITFB) ₂ , 1 ·(<i>m</i> -DITFB) ₂ ·DMSO and 1 · <i>p</i> -DITFB recorded with monochromatic Al K α photon source	40
Figure 2.8 High resolution core level spectra of C(1s) and N(1s)	42
Figure 2.9 High resolution core level spectra of O(1s) and I(3d)	43
Figure 2.10 ¹ H NMR (400 MHz, DMSO-d ₆) of pyridyl <i>bis</i> -urea macrocycle 2	46
Figure 2.11 ¹ H NMR (400 MHz, DMSO-d ₆) of host 1	47
Figure 2.12 X-ray structures of the co-crystal dimers used in the theoretical calculations	50
Figure 3.1 The chemical structures of the molecular components and the resulting conformational changes of the pyridyl <i>bis</i> -urea macrocycle 1 upon salt formation	61
Figure 3.2 Views from the crystal structure of 2	65
Figure 3.3 Hydrogen bonding network in the crystal structure of 2	66
Figure 3.4 Views from the crystal structure of 3	68
Figure 3.5 Packing diagrams of the crystal structure of 3	68
Figure 3.6 FT-IR profiles of co-formers (1 & H ₂ NDS) and DMSO-solvated salts (2 & 3) in the range 4000-650 cm ⁻¹	70
Figure 4.1 Self-assembled phenylethyne <i>bis</i> -urea macrocycle	83
Figure 4.2 Guest molecules and possible arrangements inside host 2	84
Figure 4.3 1D channels extended along the crystallographic b axis of host 2	86
Figure 4.4 GCMC simulation outcome of host-guest complex 7	89
Figure 4.5 Host 2 activation and the sorption of dye 6 into host 2 crystals	89
Figure 4.6 Methods of loading of dye into host 2 channels	91
Figure 4.7 Comparison of ¹ H NMR (400 MHz, DMSO-d ₆) spectra from host 2 loading experiments with thiophene dye 6	92

Figure 4.8 Absorption and emission studies of dye 6 in solution.....	93
Figure 4.9 Diffuse reflectance spectra and fluorescence emission spectra.....	94
Figure 4.10 Fluorescence decays: host 2 (blue), host-guest complex 7 (red) and green is IRF.	96
Figure 4.11 Normal-transmission WAXS diffractograms of 2 and 7 demonstrating morphological integrity of the host fiber	97
Figure 4.12 Excitation(A) and emission (B) polarization measurements.....	100
Figure 4.13 Host-guest composites consisting of two dyes	101
Figure 4.14 ¹³ C NMR spectrum of macrocycle 1 dissolved in DMSO-d ₆ (100 MHz).....	103
Figure 4.15 ¹ H NMR spectrum of macrocycle 1 dissolved in DMSO-d ₆ (400 MHz).....	104
Figure 5.1 X-ray crystal structures of bipyridyl <i>bis</i> -urea macrocycle coordination complexes	117
Figure 5.2 Conformations of calix[4]arenes	119
Figure 5.3 Comparison of the host 2 and its coordination complex with NaClO ₄	120
Figure 5.4 X-ray crystal structures of the macrocycle 2 ·Cd complex	121
Figure 5.5 Macrocycle incorporating cyclic urea units	124
Figure 5.6 Room temperature ¹ H NMR (400 MHz) of macrocycle 4 in (a) chloroform-d and (b) acetonitrile-d ₃	125
Figure 5.7 ¹ H NMR (400 MHz, TCE) of macrocyclic ligand 4 at 125 °C.....	126
Figure 5.8 ¹³ C NMR (101 MHz, CD ₃ CN) of macrocyclic ligand 4	126
Figure 5.9 ¹ H NMR (400 MHz, CD ₃ CN) of macrocyclic ligand 5	127
Figure 5.10 ¹³ C NMR (101 MHz, CD ₃ CN) of macrocyclic ligand 5	128
Figure 5.11 Components of the structure of macrocyclic ligand 4	130
Figure 5.12 Packing diagram of macrocycle 4	130
Figure 5.13 Comparison of the solid-state crystal structures of ligand 4 and its constitutional isomer 1	131

Figure 5.14 Components of the structure of macrocyclic ligand 5	132
Figure 5.15 Packing diagram of macrocycle 5	133
Figure 5.16 Components of the crystal structure of $[\text{Cu}_2\text{I}_2(\mathbf{4})_2 \cdot (\text{CH}_3\text{CN})_{1.63(1)}]$	135
Figure 5.17 Coordination network of $[\text{Cu}_2\text{I}_2(\mathbf{4})_2 \cdot (\text{CH}_3\text{CN})_{1.63(1)}]$	136
Figure 5.18 Components of the crystal structure of $[\text{Ag}(\mathbf{4})(\text{NO}_3)(\text{H}_2\text{O})_{2.5}]$	137
Figure 5.19 1D chains showing the side and top views of the coordination environments of Ag(I) ions in $[\text{Ag}(\mathbf{4})(\text{NO}_3)(\text{H}_2\text{O})_{2.5}]$	137
Figure 5.20 2D layers in crystal structure of $[\text{Ag}(\mathbf{4})(\text{NO}_3)(\text{H}_2\text{O})_{2.5}]$	138
Figure 5.21 Packing diagram of $[\text{Ag}(\mathbf{4})(\text{NO}_3)(\text{H}_2\text{O})_{2.5}]$	138
Figure 5.22 FT-IR profiles of ligand 4 and coordination complexes	140
Figure 5.23 Solid state UV-visible diffuse reflectance and photoluminescence spectra.	142
Figure D.1 ^1H NMR (400 MHz, DMSO- d_6) of macrocycle ML2 at 100 °C	168
Figure D.2 ^{13}C NMR (101 MHz, DMSO- d_6) of macrocycle ML2 at 100 °C.....	170
Figure D.3 HSQC spectrum (400 MHz, DMSO- d_6) of macrocycle ML2 at 100 °C.....	170
Figure D.4 X-ray crystal structure of ML2	172
Figure D.5 Comparison of the assembly motifs in macrocycles ML1 and ML2 in the solid state	172

CHAPTER 1
INTRODUCTION

1.0 Introduction

Molecular recognition is known to play a key function in biological and chemical systems and offers scientists methods to design functional materials.¹⁻³ Specific applications of molecular recognition range from enzymatic activity to DNA base pairing in biological systems as well as synthetic molecular motors, sensors, ion receptors.⁴ The recognition properties of molecules traditionally have been studied in different media; (i) solution phase and (ii) nano/materials interfaces.² However, the fast growing pharmaceutical and opto-electronic industries require new materials that will have better physicochemical properties than the original single compounds. This requires better understanding of these recognition properties in the solid state. One of the best ways to achieve this is through the application of molecular recognition principles by means of co-crystallization of molecular components with the desired properties. The development of these organic solid-state materials is reliant on the understanding of the supramolecular interactions between the individual molecules. Even though the exact definition of a co-crystal has been a topic of debate, most chemists would agree that co-crystals consist of two or more components in a definite stoichiometric ratio held together by noncovalent interactions within a single crystal lattice.⁵⁻⁷ These intermolecular interactions between molecules form the basis for molecular recognition.

Hydrogen bonding (HB) and halogen bonding (XB) are arguably the most useful supramolecular synthetic tools due to their strength, selectivity, and directionality.⁸ Even though these two interactions have very different physical and chemical characteristics, they share a common electrostatic foundation which heavily influences non-covalent interaction geometries. In any hydrogen bond, $X-H \cdots A$, a hydrogen atom acts as a bridge

between two atoms X and A. These atoms always tend to be negatively charged (electronegative), which gives the hydrogen bond an electrostatic character, as the electropositive hydrogen atom holds the negative atoms in thrall. If X and A are both quite electronegative, for example in $\text{N-H}\cdots\text{O}$, the hydrogen bond is ‘strong’ or ‘conventional’ ($20\text{-}40\text{ kJ mol}^{-1}$). But if either or both X and A are of moderate to weak electronegativity, such as in $\text{C-H}\cdots\text{O}$, the hydrogen bond is ‘weak’ or ‘non-conventional’ ($2\text{-}20\text{ kJ mol}^{-1}$).⁹

In comparison, halogen bond is an attractive directional interaction between a halogen atom (XB donor) and a donor of electronic density (a neutral or anionic Lewis base with an N, O, S, P or halogen functionality) as XB acceptor.¹⁰ In this case the halogen atom is covalently bound to a molecule R-X, where R can be another atom, including X, an organic or inorganic residue and the halogen bond acceptor can be the lone pair of a Lewis base, or the π electrons of an unsaturated system.^{11,12} Typical halogen interactions are $\text{X}\cdots\text{O}$, $\text{X}\cdots\text{N}$, $\text{X}\cdots\text{X}$, and $\text{X}\cdots\pi$, where the interaction energy follows the trend $\text{I} > \text{Br} > \text{Cl} > \text{F}$.¹³ This trend is influenced by the polarizability and the presence of electron-withdrawing substituents that are capable of activating the halogen bond donor atom through electron depletion¹⁴ and therefore introducing an element of tunability.¹⁵ Several computational studies on halogen bonding suggest that this interaction depend strongly on both electrostatic and dispersion effects. Studies of electrostatic potentials of halogen-containing molecules show that they have a very anisotropic charge distribution, with an equatorial ring of negative potential and a region of positive potential along the extension of the R-X bond that is on the side of X opposite to R, termed the σ -hole which then interacts with a nucleophilic site.^{16,17} Thus, the halogen bonds are directional, with the typical $\text{R-X}\cdots\text{Y}$ (Y is any nucleophilic site) bond angles close to 180° . The halogen bond

interactions can be compared through measurement of their atomic separation distance and then subtraction of sum of the two atoms' van der Waals radii.^{11, 18} The stronger the interaction is, the shorter the X...Y distance is.

Our group has focused on urea-based compounds as a reliable motif for directing supramolecular structures. Ureas, especially those with aryl substituents, are significantly strong hydrogen-bond donors and acceptors, and can direct the self-assembly of molecular structures in both solution and in the solid state. The dominant self-assembly motif in urea-based compounds is a chain of bifurcated N-H...O hydrogen bonds between N-H donors and the C=O acceptor which has been extensively explored for the construction of a variety of interesting crystalline solids.¹⁹⁻²⁰ As shown in Figure 1.1, N,N'-diphenyl urea compounds can theoretically exist in four planar conformations, i.e. ZZ, EZ, ZE and EE isomers.²¹ The ZZ is the favored conformer due to its stability.²² No evidence has been reported for the existence of the EE isomer. The EZ and ZE isomers are equivalent since the two aryl substituents are identical.²²

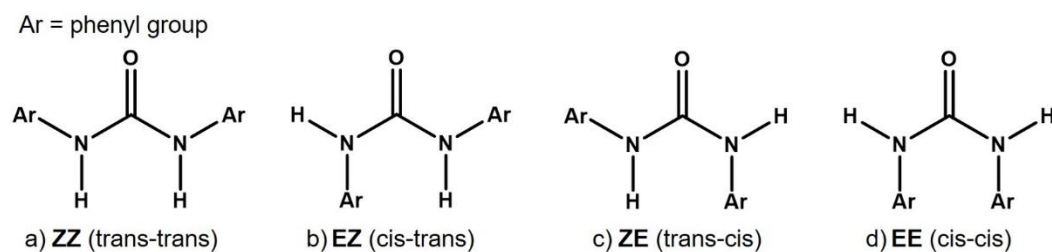


Figure 1.1 Four possible conformations of N,N'-diphenyl urea compounds.

Etter *et al.* studied the molecular recognition properties of diarylureas by co-crystallizing them with guest molecules. Their studies demonstrating that in the absence of guest molecules and steric hindrance most diarylureas will self-assemble through the three centered urea hydrogen bonding motif.²³ This is illustrated in Figure 1.2a for N, N'-

diphenyl urea, where it adopts a conformation with two *trans* amide bonds to favor the three centered urea self-association. *Cis-trans* ureas have also been occasionally observed although they are thought to be less favorable energetically. The substitution pattern of the urea can lead to different arrangements of molecules in the solid state.²³⁻²⁴ Relying on the robustness of the urea motif chemists have been able to design a variety of urea containing monomers that self-assemble into sheets, tapes, fibers or tubular structures. For example, Guichard and co-workers reported a cyclic compound containing four urea groups that self-assemble into a tubular structure with a C_4 symmetry through backbone-backbone hydrogen-bonding interactions so that the two N-H hydrogen atoms of each urea fragment interact with a urea carbonyl oxygen atom of a neighboring macrocycle (Figure 1.2b).²⁵ Also well-known are the *bis*-urea macrocycles from the Shimizu's group that self-assemble into high fidelity columnar structures (Figure 1.2c).²⁶

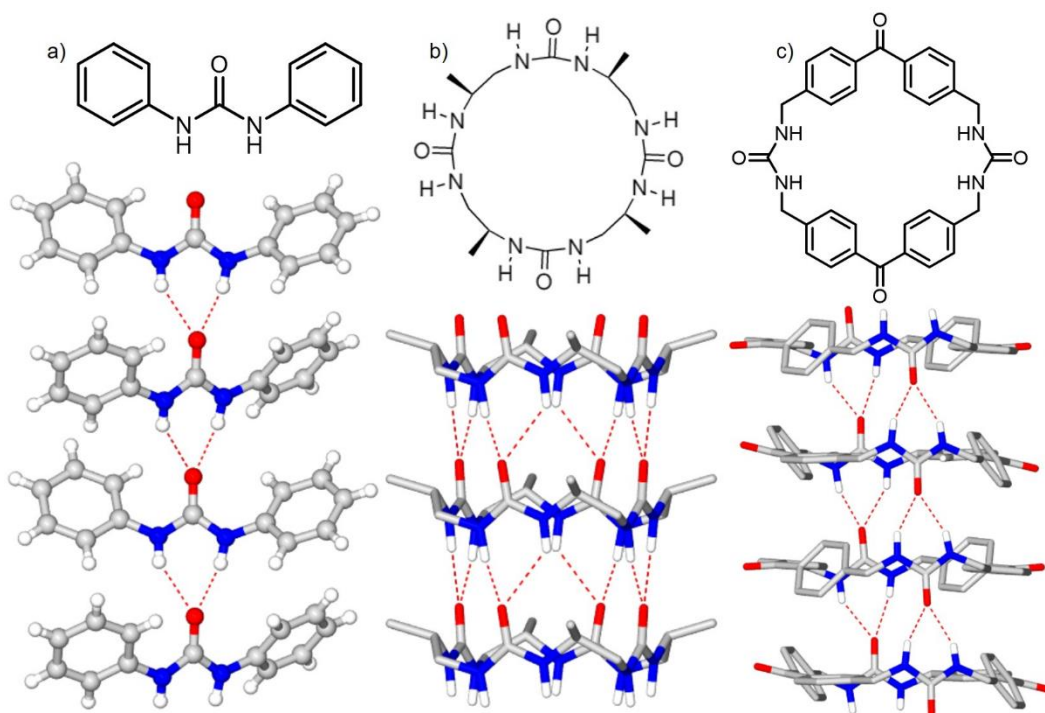


Figure 1.2 Common hydrogen bond motif found in self-assembled structures of urea compounds. a) *N, N'*-diphenyl urea, b) Cyclourea macrocycle (c) Benzophenone *bis*-urea macrocycle. The intermolecular hydrogen bonds are marked as dashed lines. The solvent

molecules and H atoms (in the crystal structures of b and c), except those of the NH groups, are omitted for clarity.

N-functionalized Lewis basic building blocks (such as pyridine and related polypyridines) have been recognized as valuable crystal engineering tools. This is because the pyridine group can be utilized as an acceptor in hydrogen/halogen bonds and can act as coordinating site for metal ions. Further N-functionalization of the aryl groups attached to the urea group can improve the recognition properties of these compounds for both organic and inorganic guests. For example, pyridyl-derivatized ureas (symmetrical), have been used as hosts for dicarboxylic acids, diols, diiodoacetylenes and also as ligands for the controlled spacing of metal atoms in crystals.²⁷⁻²⁹ In this case they act as a 'bridge' between coordination complexes and supramolecular assembly. However, combining these two groups in one molecule generates a challenge in predicting their supramolecular structures in the solid state. This challenge stems from increased number of possible interactions as well as the energetics between these interactions. Here, we have the urea N-Hs acting as HB donors while the urea carbonyl O and the pyridyl N are potential HB acceptor. The hydrogen bond parameters of the urea group are very impressive with $\alpha = 3.0$ and $\beta = 8.3$, while the pyridine group has a β value of 7.0.³⁰ Typically the best donor, as indicated by the α value will pair with the best acceptor, which displays the largest β value. When two donors (or acceptors) show similar α or β values a competition can occur. Geometric fit or match can also influence the final assembly. Depending on the proximity of these groups in the molecule, different supramolecular assemblies can be obtained when they co-crystallize with other molecules. Therefore, the design of pyridyl ureas that determine the assembly structure and organizational pattern of guest molecules is very important.

When ureas are constrained into macrocyclic structures, as in the case *bis*-urea macrocycles, the three-centered urea-urea interaction guides the assembly of these disk-like macrocycles into columnar structures. The Shimizu group designed and synthesized *bis*-urea macrocycles that can act as supramolecular building blocks. These macrocycles are constructed from two urea groups and two rigid C-shaped spacers and afford columnar structures with high fidelity and affords crystalline solids (Figure 1.3). For example, the *bis*-urea macrocycle assembled by bifurcated hydrogen bonds between the urea N-H and the carbonyl O is shown schematically in Figure 1.3. The columnar assembly of phenylethynylene *bis*-urea macrocycle host has a larger channel with a diameter of $\sim 9 \text{ \AA}$. This macrocyclic host has functioned as a nanoreactor and host for several guest molecules. The *bis*-urea macrocycle system has demonstrated several applications such as the uptake³¹⁻³², transport³³ and organization of guests³⁴, and as containers to facilitate photocycloaddition³⁵⁻³⁷ and photo-oxidation reactions. In chapter 4, we investigated the loading of a small dye, 5-(dimethylamino)-5'-nitro-2,2-bithiophene, into the 1D channels of self-assembled phenylethynylene *bis*-urea macrocyclic host.³⁸

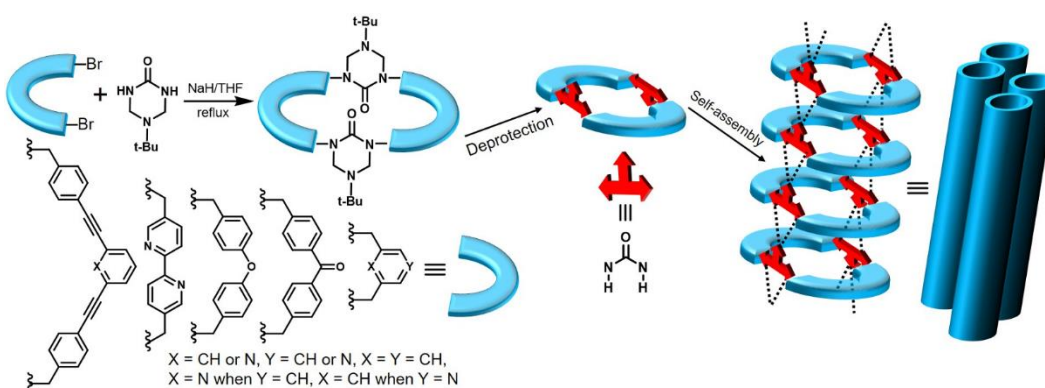


Figure 1.3 Schematic of the synthetic route and self-assembly of the *bis*-urea macrocycles. The protecting groups are removed with diethanolamine under acidic conditions. Self-assembly of *bis*-urea macrocycles is achieved by dissolving the macrocycle (10 mg in 2 mL of hot glacial acetic acid, DMSO, or DMF) followed by hot filtration and slow cooling, by vapor diffusion of MeOH, H₂O, or hexanes into solutions of the macrocycle

This introductory chapter discusses the pyridyl *bis*-urea macrocycles and how they compare to their linear dipyridylurea analogues in terms of ;1) flexibility, 2) the impact of the presence/absence and position of the pyridyl N on self-assembly, and 3) ability to pre-organize guest molecules into crystalline materials. Also, the pyridyl *bis*-urea macrocycles are compared to macrocyclic analogues without pyridyl units.

1.1 Dipyridylureas in crystals and co-crystals

Ureas and pyridines have been exploited extensively in crystal engineering for their ability to engage in non-covalent interactions (e.g., hydrogen bonding, halogen bonding, π - π forces) bonding with complementary molecules. Combining these functional groups within one building block extends their potentials in creating diverse crystalline solid-state materials. Since most functional materials are solids, and most solids are crystalline, the strive for the ‘controlled arrangement of things on a small scale’ is essentially an effort to design and construct crystals from preformed molecular building blocks.³⁹ The urea N-H \cdots O tape synthon is strong and can persist even in the presence of other strong hydrogen-bonding functional groups, such as COOH and CONH₂.⁴⁰ Symmetrical or asymmetrical N,N'-disubstitution of the urea can provide a wide variety of building blocks for the construction of crystalline organic solids, a strategy that has been extensively utilized since the early crystallographic studies of disubstituted ureas in the late 1960s.¹⁹ This feature has been explored in pyridine-substituted ureas (Figure 1.4a) as hosts to control the spacing of small organic guest molecules such as diacetylenes and dicarboxylic acids as well as metal ions.^{29, 41} DeHaven et. al., studied the homomeric and halogen bonded co-crystals of these flexible dipyridyl ureas.⁴² As expected, the crystal structures of these dipyridyl ureas all exhibited the typical three-centered urea-urea hydrogen-bonding motif, suggesting that the

position and proximity of the pyridyl N with respect to the urea moiety does not influence the urea-urea assembly (Figure 1.4b-d). Using computational tools, they ranked best donor / best acceptor sites using electrostatics calculations for each of the three dipyridylureas with regioisomers of diiodotetrafluorobenzene (DITFB). Ten of the eleven halogen bonded co-crystals displayed the key urea hydrogen bonding motif. The majority of the structures exhibited 1:1 dipyridylurea:DITFB stoichiometries and displayed the typical urea assembly as well as short pyridyl to DITFB halogen bonds with an average N...I halogen bond length of 80.6% of the van der Waals radii.⁴² Figure 1.5 shows crystal structures of sample halogen bonded co-crystals of these dipyridylureas and the *p*-diiodotetrafluorobenzene isomer (*p*-DITFB).

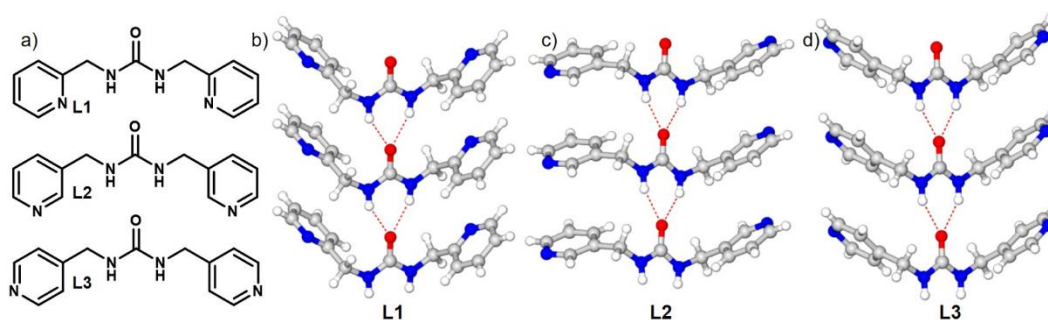


Figure 1.4 Linear dipyridylurea compounds. a) Dipyridylureas; N,N'-bis(2-pyridyl)methylurea (**L1**), N,N'-bis(3-pyridyl)methylurea (**L2**) and N,N'-bis(4-pyridyl)methylurea (**L3**). b) Crystal structure of dipyridylureas (**L1** – **L3**) depicting the urea three-center hydrogen bonding synthon (solvent molecules omitted for clarity).

The MacGillivray, Fowler and Lauher's groups have reported excellent work on [2 + 2] photoreactions of olefin- and pyridine-containing molecules by co-crystallization with template compounds such as resorcinol, *bis*(pyridyl)ureas and *bis*(pyridyl)oxalamides.^{41, 43-44} Dipyridylureas act as excellent templates for solid state [2 + 2] photoreactions and can be recovered by separation from the products. Since the urea group is capable of independently forming defined one-dimensional hydrogen-bonded α -networks where each

urea molecule donating two hydrogens, chelating the carbonyl oxygen of the next molecule in the network. These hydrogen bonds have predictable and persistent symmetries and intermolecular repeat distances which could leave the basic pyridyl N atoms available for interaction with guest molecules.

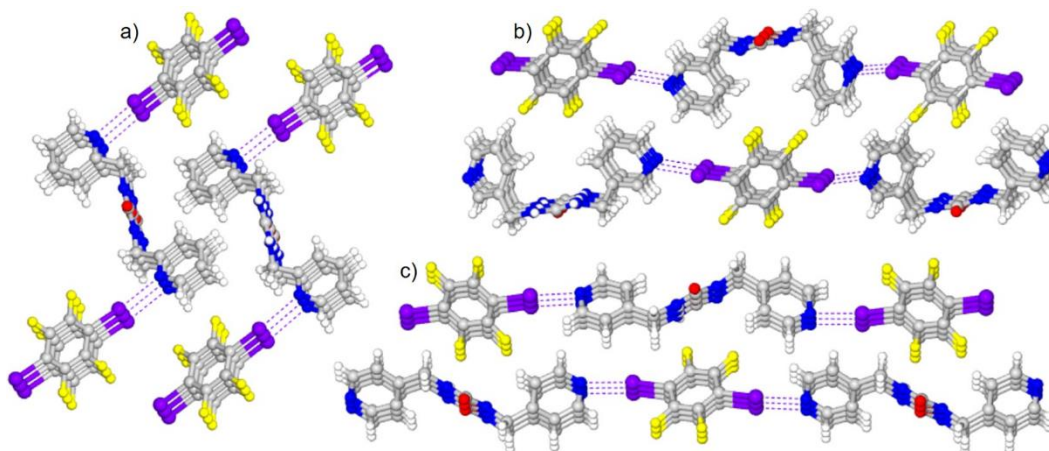


Figure 1.5 Crystal structures of co-crystals of dipyriddyureas with *p*-diodotetrafluorobenzene (*p*-DITFB).⁴² a) **L1**· *p*-DITFB, b) **L2**· *p*-DITFB and c) **L3**· *p*-DITFB. purple dashed lines represent the halogen bonds.

Goroff and co-workers in 2005 used dipyriddyureas **L2** and **L3** as co-crystallizing hosts for diiodopolyynes.⁴³ By slow evaporation of a 1:1 mixture of the host and guest dissolved in warm methanol, they obtained quality crystals that were studied by single crystal X-ray diffraction (Figure 1.6). The Fowler and Lauher groups used **L3** to prepare co-crystals with diacetylene dicarboxylic acid or diol, featuring a two dimensional β -network (Figure 1.7).²⁹ A β -network has two degrees of translational symmetry and is characterized by its layer group symmetry.⁴⁵ These co-crystals contain the two predicted structural motifs of the initial design: the urea units' form hydrogen-bonding networks in one dimension, while the iodine atoms are in close contact with the pyridine Ns, controlling the alignment in the second dimension and leading to a layered material.

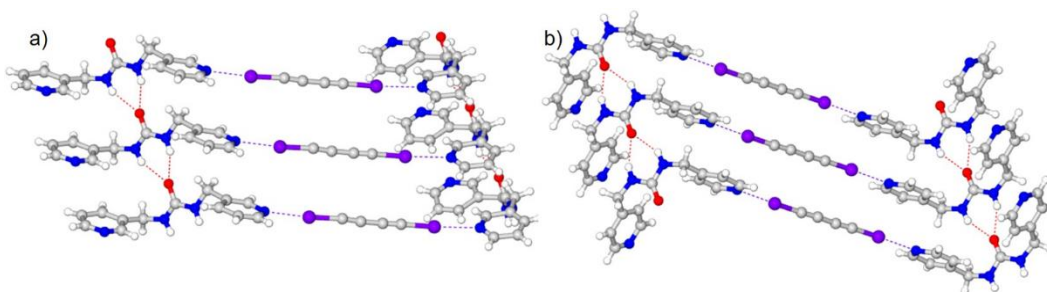


Figure 1.6 X-ray crystal structure of co-crystals of a) 1,4-diiodobuta-1,3-diyne with dipyritylurea (**L2**). b) 1,4-diiodobuta-1,3-diyne with dipyritylurea (**L3**).⁴³

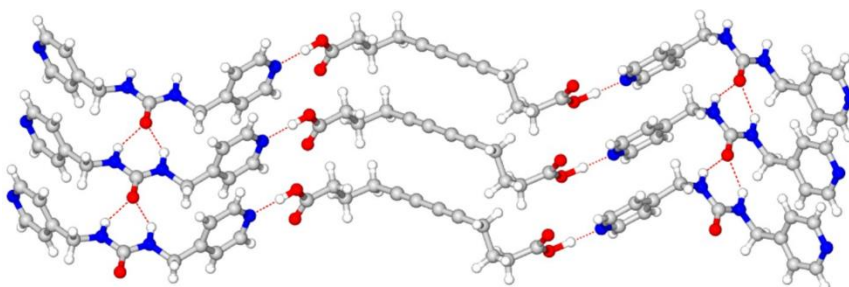


Figure 1.7 X-ray crystal structure of co-crystal of diacetylene diacetic acid with dipyritylurea (**L3**) showing a two-dimensional β -network.²⁹

1.2 Dipyritylureas as building blocks for metallo-assemblies

Several classes of ligands have been widely used in the construction of coordination polymers with a wide range of 1-, 2-, and 3-D infinite solid-state networks as well as metallo-macrocycles and metallo-cages.⁴⁶ A key step in the rational design of these coordination polymers is the control of the linking ligands between metal centers. Polypyridyls have been shown to be an important class of ligand in linkage control.⁴⁷⁻⁴⁸ It is also possible to incorporate highly directional hydrogen bonds as a means of controlling self-assembly in such supramolecular systems. In this case, the hydrogen bonding and/or other non-covalent interactions (π - π interactions) is used to pre-organize a group of building blocks in a suitable geometry to yield the targeted assembly.

The important role of incorporating hydrogen bonding motifs in the crystal engineering study for metal-containing pyridylurea systems have been demonstrated by several research groups (eg. Dastidar and Peng groups).^{28, 49} The dipyritylurea ligands

(Figure 1.4) mentioned above are very flexible because of the methylene bridges between the urea and pyridyl groups. The pyridyl groups can therefore rotate around these methylene bridges to bind metals with different coordination numbers, increasing the supramolecular complexity in the solid state. Figure 1.8 shows 2D coordination complexes of Zn and Hg using dipyridylureas **L2** and **L3** respectively. This is an indication that the urea group can direct the assembly and spacing of the metal centers in such metal-organic structures.

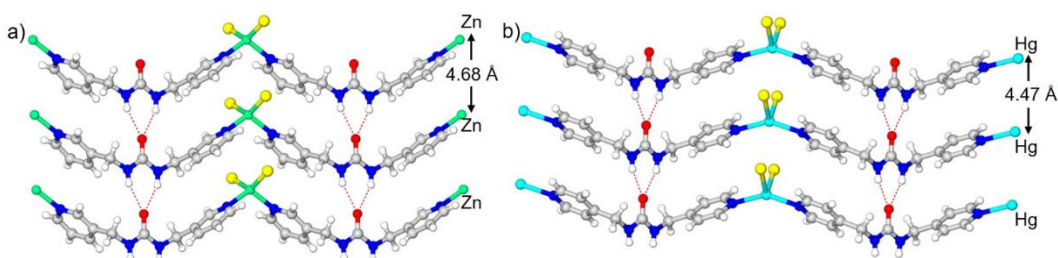


Figure 1.8 a) Two-dimensional hydrogen-bonded frameworks of coordination polymers. a) $[\text{Zn}(\mu\text{-L2})\text{Cl}_2]_n^{49}$ b) $[\text{Hg}(\mu\text{-L3})\text{Cl}_2]_n^{28}$ Metal centers are coordinated by two pyridyl N atoms and two chloride ions forming 1D chains. The 1D chains were further self-assembled via urea...urea synthon to form a 2D network.

1.3 Pyridyl functionalized *bis*-urea macrocycles

A series of *bis*-urea macrocycles have been reported by the Shimizu group that combine urea groups with two C-shaped spacers. Those systems in which the urea groups are ordered approximately perpendicular to a relatively planar macrocycle system, exhibit high fidelity assembly into columnar structures. This assembly is driven through the urea-urea hydrogen bonding motif and through additional aromatic interactions. The macrocycles are synthesized from protected ureas and brominated C-shaped spacers. This modular synthesis is advantageous for functionalizing and tuning the size of the macrocyclic system. Thus, we have explored the feasibility of incorporating interior orthogonal functional groups such as alcohols and pyridines within these *bis*-urea self-assemblies by modifying

the C-shaped spacers. These functional groups offer additional sites for interactions to anchor guests within the channels or potentially act as catalytic sites. Also, these groups could compete with the urea-urea hydrogen bonding motif if they contain lone pairs of electrons of sufficient hydrogen bond acceptor ability (or basicity), leading to the discovery of new supramolecular assemblies. Three macrocycles (**1-3**) containing pyridine group have been reported thus far by the Shimizu group (Figure 1.9). I recently synthesized pyridyl macrocycle **4** (unpublished) which is covered in chapter 5 and appendix D. These macrocycles show different assemblies in the solid state.

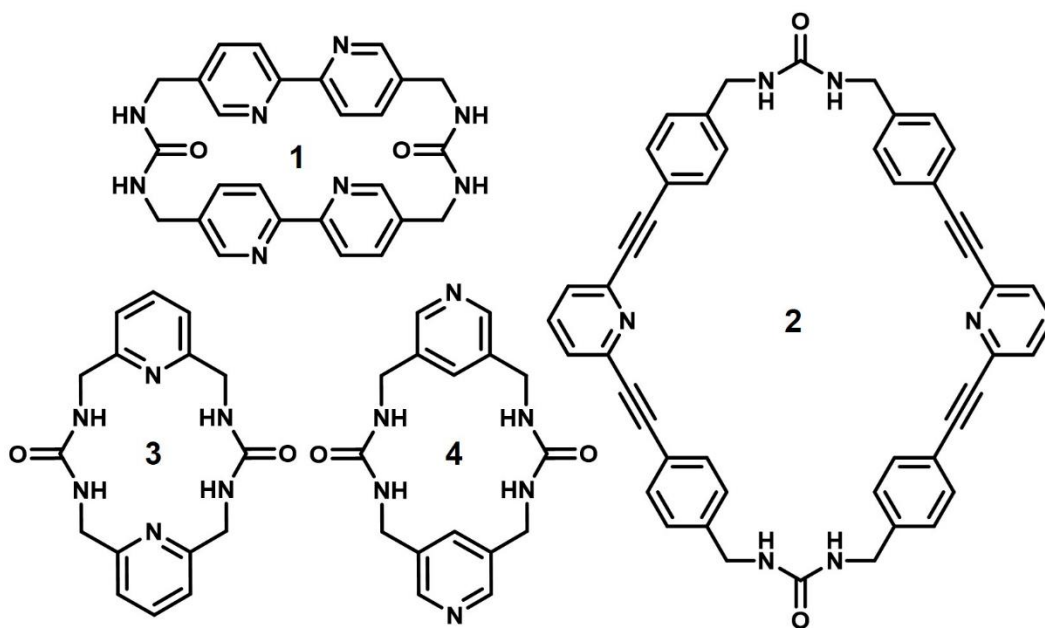


Figure 1.9 Pyridyl functionalized *bis*-urea macrocycles synthesized in the Shimizu group.

First, the bipyridine *bis*-urea macrocycle (**1**) exhibits conformational mobility, which is depicted in Figure 1.10a with black curved arrows. By rotation, the pyridines can flip into two coordination modes where the nitrogens point to the interior (*endo*) or exterior (*exo*) of the macrocycle³¹ According to single crystal X-ray diffraction data it does not form columnar assemblies (Figure 1.10b). Here instead of bifurcated urea-urea hydrogen bonds, a $\text{N(H)}_{(\text{urea})} \cdots \text{N}_{(\text{pyridyl})}$ hydrogen bond is observed where one N-H of each urea group

forms a hydrogen bond with the pyridyl N of a neighboring macrocycle. This macrocycle was utilized as a ligand to prepare coordination complexes, particularly an exocyclic diruthenium complex which was applied as a photosensitizer in the radical cation Diels-Alder reaction between *trans*-anethole and isoprene.⁵⁰

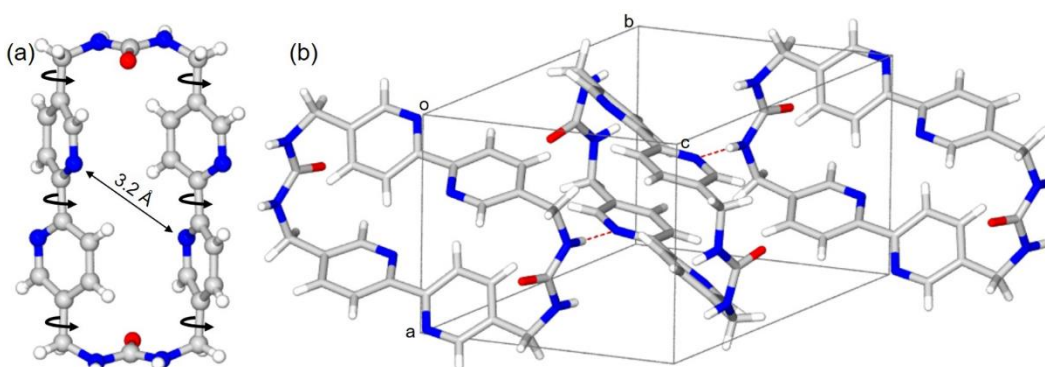


Figure 1.10 X-ray crystal structure of bipyridine *bis*-urea macrocycle. (a) macrocycle **1** and (b) packing diagram displaying $\text{N(H)}_{(\text{urea})} \cdots \text{N}_{(\text{pyridyl})}$ hydrogen bonds (red dashed line).

Secondly, a pyridyl-phenylethyne *bis*-urea macrocycle (**2**) was reported by Salpage et. al., also containing an interior pyridine group.⁵¹ The self-assembled structure of this macrocycle showed a markedly different structure from its phenylethyne counterpart. Where the phenylethyne macrocycle is relatively flat with the urea groups oriented approximately perpendicular to the plane of the macrocycle, the pyridyl derivative is saddle shaped. The crystal structure revealed the expected *bis*-urea macrocycle as a solvate; however, **2** was not planar but folded into a bowl or saddle conformation with C₂ point symmetry (Figure 1.11a). Here, the two urea groups remain oriented in the same direction. This folded architecture assembles through typical bifurcated urea hydrogen bonds ($\text{N(H)} \cdots \text{O}$ distances of 2.81–2.87 Å) with four neighboring macrocycles to afford 2D assemblies of interdigitated cycles (Figure 1.11b). Even though the self-assembly of macrocycle **2** is not columnar it still created channels with pore size of 4.5 Å which is considerably reduced when compared with the pyridine-free phenylethyne macrocycle

self-assembled structure (Figure 1.11c). However, the activated material was able to absorb isoprene and facilitated its polymerization by mild UV irradiation.⁵¹

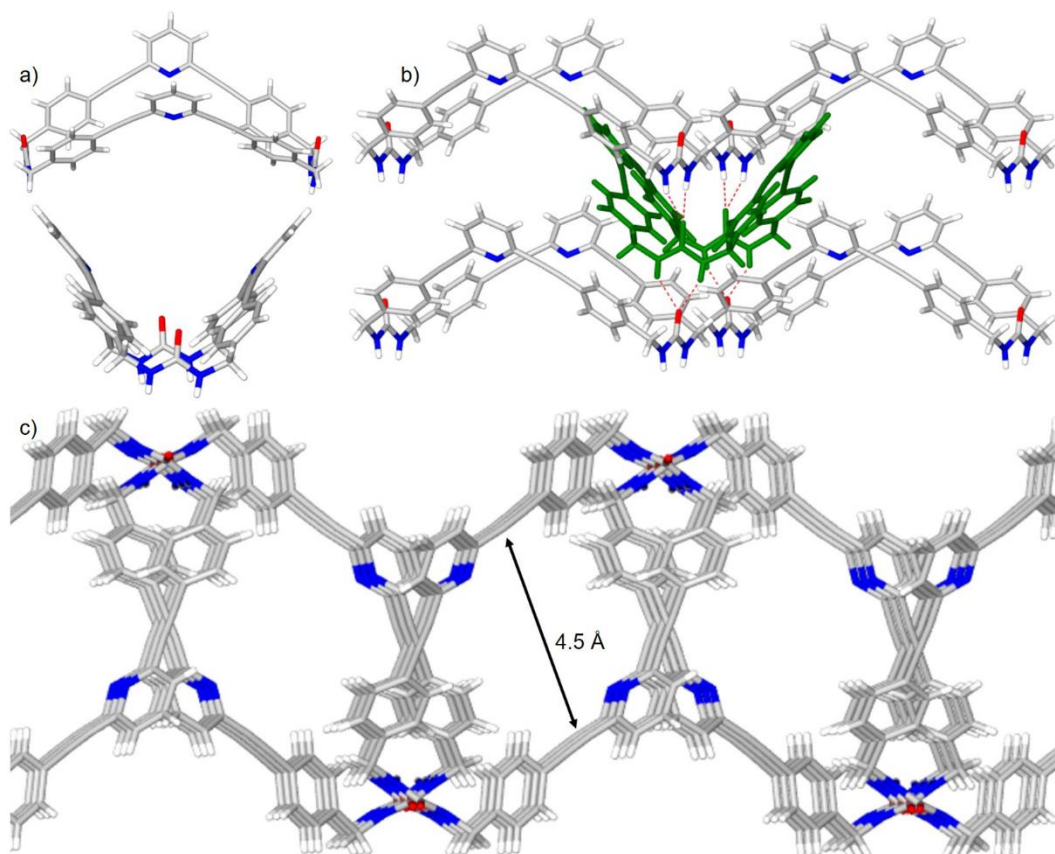


Figure 1.11 Assembly of pyridyl-phenylethynylene *bis*-urea macrocycle (**2**). (a) Saddle formation of macrocycle **2**. (b) A single macrocycle forms bifurcated urea hydrogen bonds with four neighboring cycles with N(H)···O distances of 2.81–2.87 Å. This interdigitated assembly twists the urea groups 62.5° (c) 2D zigzag layers form along the a-axis with adjacent layers packing in an anti-parallel fashion to afford 1D channels along the b-axis with a channel diameter of 4.5 Å.⁵¹

Roy et. al., synthesized the third pyridyl *bis*-urea macrocycle **3** (Figure 1.8), which is the basis for chapters 2 & 3 of this dissertation work. This macrocycle is much smaller compared to the bipyridine macrocycle **1** and the pyridyl-phenylethynylene **2**. Single crystal X-ray diffraction studies revealed a columnar assembly with two different hydrogen bonds (N-H···N and N-H···O) where the urea NHs interacts with the urea carbonyl oxygen and the pyridine nitrogen. This macrocycle contains basic interior nitrogen atoms with no

central cavity and one lone pair on each urea carbonyl oxygen which can be used to form hydrogen/halogen bonding to other molecules.

Therefore, our interest in the smaller pyridyl *bis*-urea macrocycle (**3**) was to leverage on its accessible unsatisfied lone pairs and solid columns to organize small organic guest molecules (hydrogen bond and halogen bond donors) in the solid state through co-crystallization. This has been demonstrated in chapters 2-3. The organization and spatial arrangement of the guests are controlled through noncovalent intermolecular interactions. Further efforts to co-crystallize **3** with reactive molecules and ions led us to redesign **3** by modifying the C-shaped spacer to position the pyridyl N on the exterior of the macrocycle. We expected as the nitrogen is moved from interior to exterior, we would observe the normal urea assembly motif and providing a stronger and more accessible nitrogen to utilize as a binding site. This would increase the size of guests that can be bound as the guests occupy an external and more flexible binding site. Synthesis details of **4** is very similar to the previously reported pyridyl *bis*-urea macrocycle **3** and are presented in chapter 5 and appendix D. In chapter 5, the protected intermediate of **4** was used to synthesize coordination polymers of Cu(I) and Ag(I).

As shown in Figure 1.12, **4** self-assembles differently from **3** but in a similar fashion to the *m*-xylene *bis*-urea macrocycle (**MX**).⁵² The *m*-xylene *bis*-urea macrocycle has no pyridine nitrogen, where **3** and **4** are constitutional isomers, differing only in the position of the pyridyl N. **MX** and **4** self-assemble through the predicted three-centered urea-urea hydrogen bonding motif into the typical columnar structures. In contrast, macrocycle **3** self-assembles through two different hydrogen bonds (N-H...N and N-H...O) where the urea NHs interacts with the urea carbonyl oxygen and the pyridyl N. The newest addition

to the *bis*-urea macrocycle library (**4**) has its pyridyl Ns poised on the exterior of its columnar assembly that potentially can form interactions with guest molecules in solid-state complexes. Considering the fact that N atom is less electronegative than the O atom, this macrocycle (**4**) should be able to bind more guest molecules including metal ions than the accessible carbonyl O lone pair in **3**.

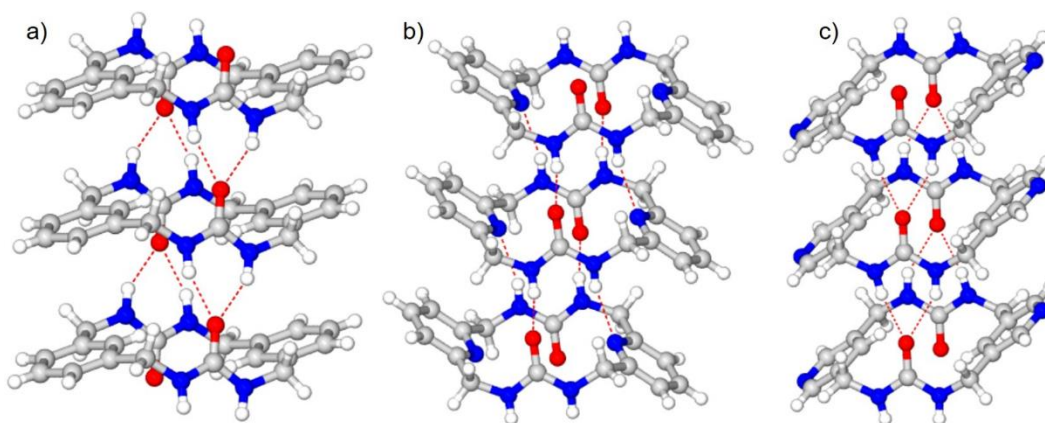


Figure 1.12 Hydrogen-bonded columns of self-assembled *bis*-urea macrocycles. a) *m*-xylene *bis*-urea macrocycle (**MX**), b) pyridyl *bis*-urea macrocycle (**3**) and c) pyridyl *bis*-urea macrocycle (**4**).

1.4 Conclusion

In summary, the urea functional group is an excellent hydrogen bonding motif that scientists have utilized to construct diverse supramolecular architectures similar to what is found in nature. It has been incorporated into several organic molecules and used in the synthesis of highly ordered porous solid-state materials such as hydrogen-bonded organic frameworks (HOFs) via non-covalent interactions. These materials have broad applications in areas such as sensing, drug delivery, heterogeneous catalysis, proton conduction and gas storage. However, due to reversibility of the non-covalent in some of these porous organic materials they are not very stable and collapses upon removal of the solvent of crystallization. Therefore, to make highly stable materials will require rational and strategic design of the monomer molecules such that removal of solvent guests has limited influence

on the stability of the supramolecular assembly. For example, incorporating multiple urea groups into the same molecule or combining the urea group with other functionalities that boost the strength of the non-covalent interactions. Our group has shown that macrocyclic monomers bearing two urea groups can efficiently form porous channels or cylinders via N–H···O stacking. It is also clear that these *bis*-urea macrocycles can be functionalized, in this case with pyridyl groups. The functionalization of these macrocycles definitely affected how the macrocycles assemble in the solid state. But it also opens up their scope of application. The following chapters will discuss the design, syntheses and applications of these *bis*-urea macrocycles.

1.5 References

1. Gellman, S. H., Introduction: Molecular Recognition. *Chem. Rev.* **1997**, *97* (5), 1231-1232.
2. Ariga, K.; Ito, H.; Hill, J. P.; Tsukube, H., Molecular recognition: from solution science to nano/materials technology. *Chem. Soc. Rev.* **2012**, *41* (17), 5800-5835.
3. Persch, E.; Dumele, O.; Diederich, F., Molecular Recognition in Chemical and Biological Systems. *Angew. Chem. Int. Ed.* **2015**, *54* (11), 3290-3327.
4. Užarević, K.; Halasz, I.; Đilović, I.; Bregović, N.; Rubčić, M.; Matković-Čalogović, D.; Tomišić, V., Dynamic Molecular Recognition in Solid State for Separating Mixtures of Isomeric Dicarboxylic Acids. *Angew. Chem. Int. Ed.* **2013**, *52* (21), 5504-5508.
5. Desiraju, G. R., Crystal and co-crystal. *CrystEngComm* **2003**, *5* (82), 466-467.
6. Bond, A. D., What is a co-crystal? *CrystEngComm* **2007**, *9* (9), 833-834.

7. Pagire, S. K.; Korde, S. A.; Whiteside, B. R.; Kendrick, J.; Paradkar, A., Spherical Crystallization of Carbamazepine/Saccharin Co-Crystals: Selective Agglomeration and Purification through Surface Interactions. *Crystal Growth & Design* **2013**, *13* (10), 4162-4167.
8. Aakeroy, C. B.; Welideniya, D.; Desper, J., Ethynyl hydrogen bonds and iodoethynyl halogen bonds: a case of synthon mimicry. *CrystEngComm* **2017**, *19* (1), 11-13.
9. Desiraju, G. R., Chemistry beyond the molecule. *Nature* **2001**, *412*, 397.
10. Metrangolo, P.; Meyer, F.; Pilati, T.; Resnati, G.; Terraneo, G., Halogen Bonding in Supramolecular Chemistry. *Angew. Chem. Int. Ed.* **2008**, *47* (33), 6114-6127.
11. Politzer, P.; Murray, J. S.; Clark, T., Halogen bonding: an electrostatically-driven highly directional noncovalent interaction. *PCCP* **2010**, *12* (28), 7748-7757.
12. Mukherjee, A.; Tothadi, S.; Desiraju, G. R., Halogen Bonds in Crystal Engineering: Like Hydrogen Bonds yet Different. *Acc. Chem. Res.* **2014**, *47* (8), 2514-2524.
13. Bishop, R., Organic crystal engineering beyond the Pauling hydrogen bond. *CrystEngComm* **2015**, *17* (39), 7448-7460.
14. Aakeröy, C. B.; Wijethunga, T. K.; Desper, J., Practical crystal engineering using halogen bonding: A hierarchy based on calculated molecular electrostatic potential surfaces. *J. Mol. Struct.* **2014**, *1072*, 20-27.
15. Gilday, L. C.; Robinson, S. W.; Barendt, T. A.; Langton, M. J.; Mullaney, B. R.; Beer, P. D., Halogen Bonding in Supramolecular Chemistry. *Chem. Rev.* **2015**, *115* (15), 7118-7195.

16. Chudzinski, M. G.; Taylor, M. S., Correlations between Computation and Experimental Thermodynamics of Halogen Bonding. *The Journal of Organic Chemistry* **2012**, *77* (7), 3483-3491.
17. Riley, K. E.; Murray, J. S.; Politzer, P.; Concha, M. C.; Hobza, P., Br \cdots O Complexes as Probes of Factors Affecting Halogen Bonding: Interactions of Bromobenzenes and Bromopyrimidines with Acetone. *Journal of Chemical Theory and Computation* **2009**, *5* (1), 155-163.
18. Priimagi, A.; Cavallo, G.; Metrangolo, P.; Resnati, G., The Halogen Bond in the Design of Functional Supramolecular Materials: Recent Advances. *Acc. Chem. Res.* **2013**, *46* (11), 2686-2695.
19. Custelcean, R., Crystal engineering with urea and thiourea hydrogen-bonding groups. *Chem. Commun.* **2008**, (3), 295-307.
20. Reddy, L. S.; Basavoju, S.; Vangala, V. R.; Nangia, A., Hydrogen Bonding in Crystal Structures of N,N'-Bis(3-pyridyl)urea. Why Is the N-H \cdots O Tape Synthons Absent in Diaryl Ureas with Electron-Withdrawing Groups? *Crystal Growth & Design* **2006**, *6* (1), 161-173.
21. C. Singha, N.; N. Sathyanarayana, D., ¹H and ¹³C NMR spectra of some unsymmetric N,N[prime or minute]-dipyridyl ureas: spectral assignments and molecular conformation. *Journal of the Chemical Society, Perkin Transactions 2* **1997**, (2), 157-162.
22. Meng, S.; Tang, Y.; Yin, Y.; Yin, X.; Xie, J., A theoretical study of molecular conformations and gelation ability of N,N[prime or minute]-dipyridyl urea compounds in ethanol solution: DFT calculations and MD simulations. *RSC Advances* **2013**, *3* (39), 18115-18127.

23. Etter, M. C.; Urbanczyk-Lipkowska, Z.; Zia-Ebrahimi, M.; Panunto, T. W., Hydrogen bond-directed cocrystallization and molecular recognition properties of diarylureas. *J. Am. Chem. Soc.* **1990**, *112* (23), 8415-8426.
24. Etter, M. C.; Reutzel, S. M., Hydrogen bond directed cocrystallization and molecular recognition properties of acyclic imides. *J. Am. Chem. Soc.* **1991**, *113* (7), 2586-2598.
25. Semetey, V.; Didierjean, C.; Briand, J. P.; Aubry, A.; Guichard, G., Self-Assembling Organic Nanotubes from Enantiopure Cyclo-N,N'-Linked Oligoureas: Design, Synthesis, and Crystal Structure. *Angew. Chem. Int. Ed.* **2002**, *41* (11), 1895-1898.
26. Shimizu, L. S.; Salpage, S. R.; Korous, A. A., Functional Materials from Self-Assembled *Bis-urea* Macrocycles. *Acc. Chem. Res.* **2014**, *47* (7), 2116-2127.
27. Schauer, C. L.; Matwey, E.; Fowler, F. W.; Lauher, J. W., Controlled Spacing of Metal Atoms via Ligand Hydrogen Bonds. *J. Am. Chem. Soc.* **1997**, *119* (42), 10245-10246.
28. Tzeng, B.-C.; Huang, Y.-C.; Chen, B.-S.; Wu, W.-M.; Lee, S.-Y.; Lee, G.-H.; Peng, S.-M., Crystal-Engineering Studies of Coordination Polymers and a Molecular-Looped Complex Containing Dipyridyl-Amide Ligands. *Inorg. Chem.* **2007**, *46* (1), 186-195.
29. Kane, J. J.; Liao, R.-F.; Lauher, J. W.; Fowler, F. W., Preparation of layered diacetylenes as a demonstration of strategies for supramolecular synthesis. *J. Am. Chem. Soc.* **1995**, *117* (48), 12003-12004.
30. Hunter, C. A., Quantifying Intermolecular Interactions: Guidelines for the Molecular Recognition Toolbox. *Angew. Chem. Int. Ed.* **2004**, *43* (40), 5310-5324.

31. Tian, L.-l.; Wang, C.; Dawn, S.; Smith, M. D.; Krause, J. A.; Shimizu, L. S., Macrocycles with Switchable exo/endo Metal Binding Sites. *J. Am. Chem. Soc.* **2009**, *131* (48), 17620-17629.
32. Roy, K.; Wang, C.; Smith, M. D.; Pellechia, P. J.; Shimizu, L. S., Alkali Metal Ions As Probes of Structure and Recognition Properties of Macrocyclic Pyridyl Urea Hosts. *J. Org. Chem.* **2010**, *75* (16), 5453-5460.
33. Bowers, C. R.; Dvoyashkin, M.; Salpage, S. R.; Akel, C.; Bhasse, H.; Geer, M. F.; Shimizu, L. S., Crystalline *Bis*-urea Nanochannel Architectures Tailored for Single-File Diffusion Studies. *ACS Nano* **2015**, *9* (6), 6343-6353.
34. Roy, K.; Wang, C.; Smith, M. D.; Dewal, M. B.; Wibowo, A. C.; Brown, J. C.; Ma, S.; Shimizu, L. S., Guest induced transformations of assembled pyridyl *bis*-urea macrocycles. *Chem. Commun.* **2011**, *47* (1), 277-279.
35. Dawn, S.; Dewal, M. B.; Sobransingh, D.; Paderes, M. C.; Wibowo, A. C.; Smith, M. D.; Krause, J. A.; Pellechia, P. J.; Shimizu, L. S., Self-Assembled Phenylethynylene *Bis*-urea Macrocycles Facilitate the Selective Photodimerization of Coumarin. *J. Am. Chem. Soc.* **2011**, *133* (18), 7025-7032.
36. Yang, J.; Dewal, M. B.; Profeta, S.; Smith, M. D.; Li, Y.; Shimizu, L. S., Origins of Selectivity for the [2+2] Cycloaddition of α,β -unsaturated Ketones within a Porous Self-assembled Organic Framework. *J. Am. Chem. Soc.* **2008**, *130* (2), 612-621.
37. Yang, J.; Dewal, M. B.; Shimizu, L. S., Self-Assembling *Bis*-urea Macrocycles Used as an Organic Zeolite for a Highly Stereoselective Photodimerization of 2-Cyclohexenone. *J. Am. Chem. Soc.* **2006**, *128* (25), 8122-8123.

38. Kittikhunnatham, P.; Som, B.; Rassolov, V.; Stolte, M.; Würthner, F.; Shimizu, L. S.; Greytak, A. B., Fluorescence Polarization Measurements to Probe Alignment of a Bithiophene Dye in One-Dimensional Channels of Self-Assembled Phenylethynylene *Bis*-Urea Macrocycle Crystals. *The Journal of Physical Chemistry C* **2017**, *121* (33), 18102-18109.
39. Braga, D.; Grepioni, F.; Maini, L.; d'Agostino, S., Making crystals with a purpose; a journey in crystal engineering at the University of Bologna. *IUCrJ* **2017**, *4* (Pt 4), 369-379.
40. Nguyen, T. L.; Fowler, F. W.; Lauher, J. W., Commensurate and Incommensurate Hydrogen Bonds. An Exercise in Crystal Engineering. *J. Am. Chem. Soc.* **2001**, *123* (44), 11057-11064.
41. Lauher, J. W.; Fowler, F. W.; Goroff, N. S., Single-Crystal-to-Single-Crystal Topochemical Polymerizations by Design. *Acc. Chem. Res.* **2008**, *41* (9), 1215-1229.
42. DeHaven, B. A.; Chen, A. L.; Shimizu, E. A.; Salpage, S. R.; Smith, M. D.; Shimizu, L. S., Synergistic effects of hydrogen and halogen bonding in co-crystals of dipyridylureas and diiodotetrafluorobenzenes. *Supramol. Chem.* **2018**, *30* (4), 315-327.
43. Goroff, N. S.; Curtis, S. M.; Webb, J. A.; Fowler, F. W.; Lauher, J. W., Designed Cocrystals Based on the Pyridine–Iodoalkyne Halogen Bond. *Org. Lett.* **2005**, *7* (10), 1891-1893.
44. MacGillivray, L. R.; Papaefstathiou, G. S.; Friščić, T.; Hamilton, T. D.; Bučar, D.-K.; Chu, Q.; Varshney, D. B.; Georgiev, I. G., Supramolecular Control of Reactivity in the Solid State: From Templates to Ladderanes to Metal–Organic Frameworks. *Acc. Chem. Res.* **2008**, *41* (2), 280-291.

45. Coe, S.; Kane, J. J.; Nguyen, T. L.; Toledo, L. M.; Winger, E.; Fowler, F. W.; Lauher, J. W., Molecular Symmetry and the Design of Molecular Solids: The Oxalamide Functionality as a Persistent Hydrogen Bonding Unit. *J. Am. Chem. Soc.* **1997**, *119* (1), 86-93.
46. Kitagawa, S.; Kitaura, R.; Noro, S. i., Functional Porous Coordination Polymers. *Angew. Chem. Int. Ed.* **2004**, *43* (18), 2334-2375.
47. Zhang, J.-W.; Kan, X.-M.; Li, X.-L.; Luan, J.; Wang, X.-L., Transition metal carboxylate coordination polymers with amide-bridged polypyridine co-ligands: assemblies and properties. *CrystEngComm* **2015**, *17* (21), 3887-3907.
48. Steel, P. J., Ligand Design in Multimetallic Architectures: Six Lessons Learned. *Acc. Chem. Res.* **2005**, *38* (4), 243-250.
49. Banerjee, S.; Adarsh, N. N.; Dastidar, P., Solvent-Driven Structural Diversities in ZnII Coordination Polymers and Complexes Derived from *Bis*-pyridyl Ligands Equipped with a Hydrogen-Bond-Capable Urea Backbone. *Crystal Growth & Design* **2012**, *12* (12), 6061-6067.
50. Salpage, S. R.; Paul, A.; Som, B.; Banerjee, T.; Hanson, K.; Smith, M. D.; Vannucci, A. K.; Shimizu, L. S., Structural, electrochemical and photophysical properties of an exocyclic di-ruthenium complex and its application as a photosensitizer. *Dalton Transactions* **2016**, *45* (23), 9601-9607.
51. Salpage, S. R.; Xu, Y.; Som, B.; Sindt, A. J.; Smith, M. D.; Shimizu, L. S., Pyridyl-phenylethynylene *bis*-urea macrocycles: self-assembly and utility as a nanoreactor for the selective photoreaction of isoprene. *RSC Advances* **2016**, *6* (100), 98350-98355.

52. Shimizu, L. S.; Smith, M. D.; Hughes, A. D.; Shimizu, K. D., Self-assembly of a bis-urea macrocycle into a columnar nanotube. *Chem. Commun.* **2001**, (17), 1592-1593.

CHAPTER 2

PILLARS OF ASSEMBLED PYRIDYL *BIS*-UREA MACROCYCLES: A ROBUST SYNTHON TO ORGANIZE DIODOTETRAFLUOROBENZENE¹

¹ **Som, B.**; Salpage, S. R.; Son, J.; Gu, B.; Karakalos, S. G.; Smith, M. D.; Shimizu, L. S., Pillars of assembled pyridyl *bis*-urea macrocycles: a robust synthon to organize diiodotetrafluorobenzenes. *CrystEngComm* **2017**, *19* (3), 484-491. Reprinted here with permission of publisher.

2.0 Abstract

Columnar assembled pyridyl *bis*-urea macrocycles **1** provide a strong 1D supramolecular synthon to construct hierarchical assemblies. These 1D pillars contain ditopic symmetrical acceptors in the form of basic oxygen lone pairs. In this chapter, we probe this synthon with a series of activated halogen bond donors, the regio-isomers of diiodotetrafluorobenzenes, which vary the relative orientation of the halogen bond formers. Irrespective of the initial stoichiometry, each donor only formed one type of co-crystal with **1**. In each case, similar strong pillars of assembled **1** were observed that organize the donors through the C=O \cdots I interaction, which were significantly shorter than the sum of the van der Waals radii of the atoms involved and among the shortest reported for neutral organic molecules. These studies suggest that this synthon can utilize both hydrogen and halogen bonding orthogonally to build complex structures. Finally, X-ray photoelectron spectroscopy (XPS) was evaluated as a technique to characterize the new halogen bonded complexes. To the best of our knowledge, this is the first application of XPS to analyze O \cdots I halogen bonding complexes. XPS core level shifts strongly indicated the formation of halogen bonding interactions and suggest this technique can be widely applied for solid-state halogen bonded materials.

2.1 Introduction

Halogen bonding is an important tool to control the organization of small molecules into supramolecular assemblies, producing superior properties for materials that have applications in areas as diverse as non-linear optics (NLO) and pharmaceuticals.¹⁻³ The C–X \cdots N supramolecular synthon is the most widely studied among the halogen bond supramolecular synthons, often used in the engineering of organic co-crystals due to its

robustness.⁴ The N···I halogen bond has been frequently used to drive the self-assembly of solid-state architectures, which are stable at room temperature and in air.⁵⁻⁸ Typical examples include the alignment of stilbene and diacetylene derivatives through crystal engineering to favor topochemical [2 + 2] photodimerization⁹ in the solid-state and topotactic polymerization.¹⁰ However, there are fewer reports of donor–acceptor complexes utilizing the O···I halogen bond, especially the C=O···I supramolecular synthon in crystal engineering.¹¹⁻¹⁴ Here, we test a robust 1D pillar whose exterior is lined with basic oxygen lone pair as a synthon to co-crystallize guests through C=O···I interactions into predictable structures. The Shimizu group developed a pyridyl *bis*-urea macrocycle **1** that assembles through two different hydrogen bonds (N–H···N and N–H···O) where the urea NHs interacts with the urea carbonyl oxygen and the pyridine nitrogen (Figure 2.1 a & b).¹⁵⁻¹⁶ As a consequence, two oxygen lone pairs per macrocycle are poised on the exterior of the rods that potentially can form interactions with guests in solid-state complexes. These crystalline materials have been applied as sorbents for alcohols through intermolecular interactions in solid to solid transformations.¹⁵⁻¹⁶ Alternatively, **1** can be used directly to organize hydrogen bond donating guests through co-crystallization to give structures similar to those obtained by vapor treatment. The available oxygen lone pair should also act as halogen bond acceptors. Indeed, a protected derivative of **1** co-crystallized with pentafluoriodobenzene, exhibiting unusually short I···O distances (2.719(2) Å, 78% of the sum of vdw radii); however, this compound lacked the urea hydrogen bonding sites and could not assemble into columns.¹⁷ In this chapter, we investigate strong pillars of self-assembled **1** as a co-crystal former for ditopic halogen bond donors (Figure 2.1c) to test the robustness of this synthon and probe its ability to form

co-crystals with three regioisomers of diiodotetrafluorobenzene: 1,2-diiidotetrafluorobenzene (*o*-DITFB), 1,3-diiidotetrafluorobenzene (*m*-DITFB), 1,4-diiidotetrafluorobenzene (*p*-DITFB).

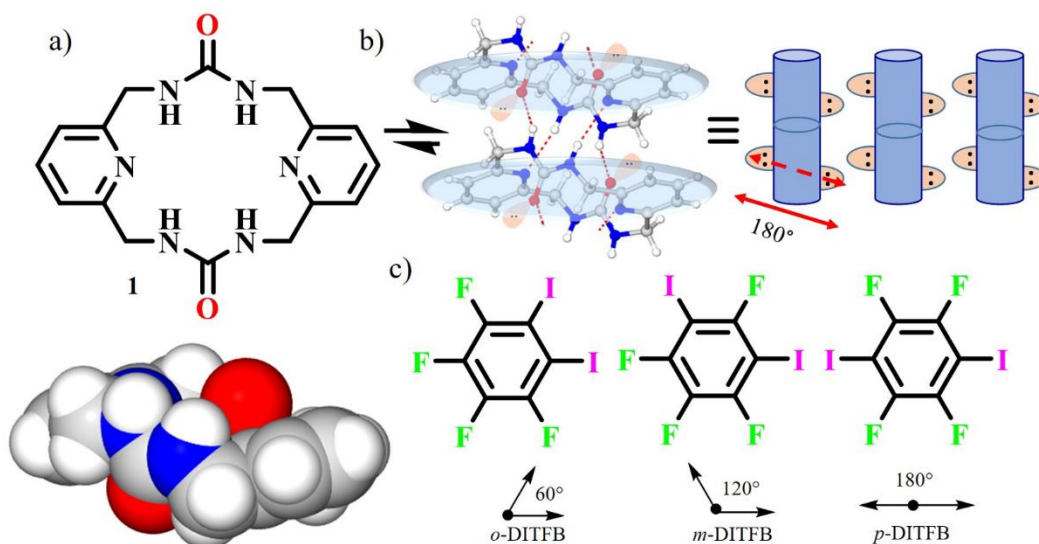


Figure 2.1 Testing pyridyl *bis*-urea macrocycle **1** as a co-crystal former for ditopic halogen bond donors: (a) structure of macrocycle **1** and space filling model from X-ray structure. (b) Self-assembly of **1** forms pillars by hydrogen bonding leaving two oxygen lone pair from each macrocycle unsatisfied. (c) Regioisomers of the diiodotetrafluorobenzene offer ditopic donors that vary the relative orientation of the halogen bond formers.

The halogen bond donors selected present different positions and spatial disposition of the iodine atoms to test: 1) the stoichiometry of the co-formers, 2) the packing of crystalline solids and 3) the strength of the O \cdots I halogen bond in the co-crystals versus the hydrogen bonding motif of the pillars. Of particular interest, was the question of whether the formation of halogen bonds would modulate the hydrogen bonded structure of the pillars. The formation of halogen bonding in these cocrystals was confirmed by several techniques such as single crystal X-ray diffraction (SCXRD), theoretical calculations, Fourier transform infrared spectroscopy (FT-IR), and X-ray photoelectron spectroscopy (XPS).

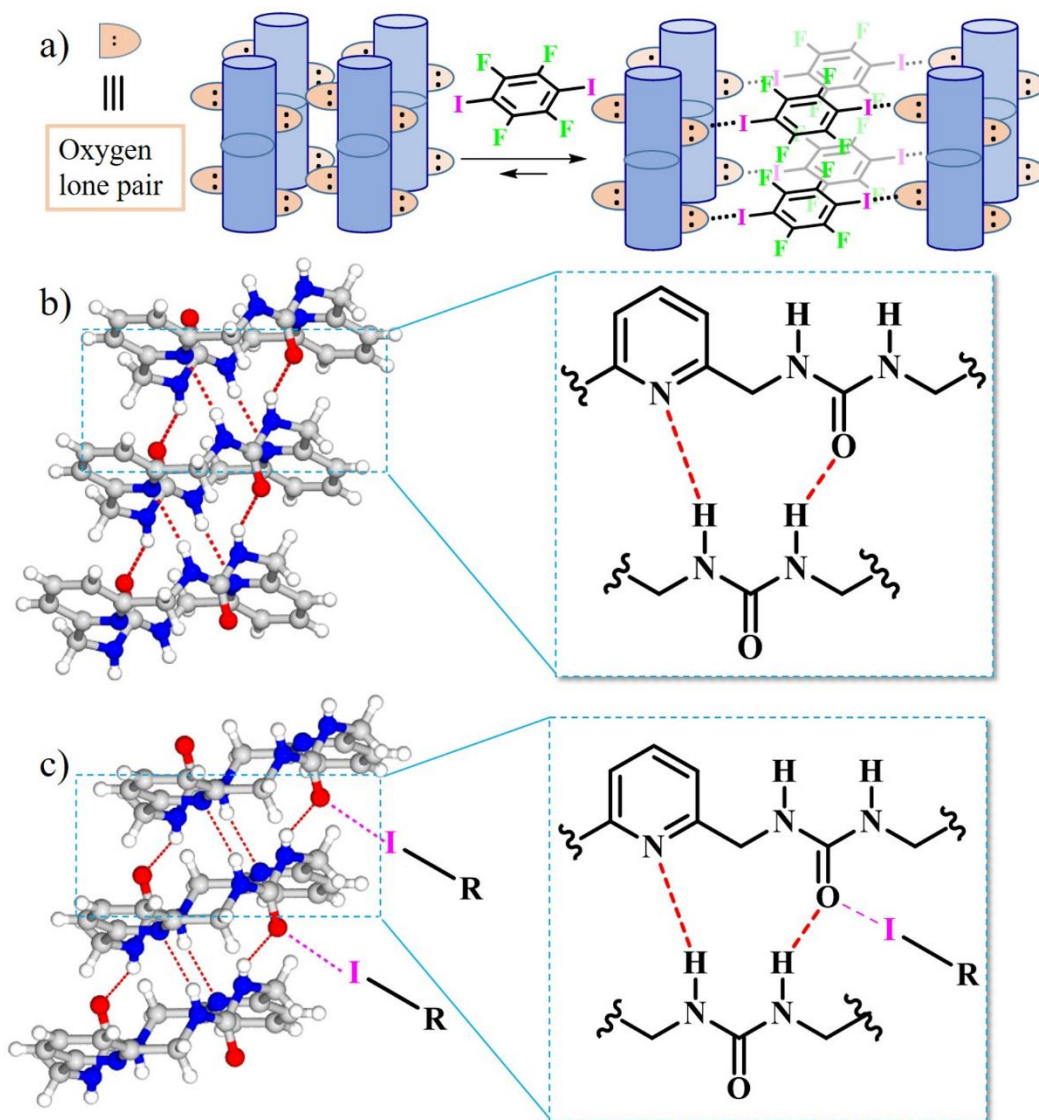


Figure 2.2 The utility of the assembled macrocycle **1** synthon to organize halogen bond donors by co-crystal formation. (a) Schematic assembly of **1** into pillars leaves unsatisfied exterior lone pair, which may interact with ditopic halogen bond donors such as *p*-DITFB. (b) View along the pillar of assembled **1** illustrates two hydrogen bonds: N(H)⋯O (2.90 Å) and N(H)⋯N (3.08 Å). (c) Expected hydrogen and halogen bonding interactions in co-crystals.

2.2 Results and discussion

We investigated the utility of the assembled **1** synthon to organize halogen bond donors by co-crystal formation. Ureas typically self-associate through a 3-centered urea–urea hydrogen bonding motif.¹⁸ However, the close proximity of the pyridyl and the urea groups

within **1** modulated this assembly. Figure 2.2b illustrates the pillars of **1**, which are held together through two different hydrogen bond acceptors: the urea oxygen (N(H)⋯O, 2.904(2) Å) and the pyridyl nitrogen (N(H)⋯N, 3.082(2) Å).¹⁹ Along a single pillar, the oxygen atoms on the macrocyclic assembly of **1** are oriented on opposite sides, one pointing up and the other pointing down. This arrangement results in the available oxygen lone pairs being approximately linear to each other (Figure 2.1b). In this homogeneous assembly, each oxygen is acting as a single hydrogen bond acceptor and assembled **1** is best described as a potential ditopic halogen bond acceptor. Therefore, we expect A⋯D⋯A⋯D⋯ type assemblies when **1** is co-crystallized with ditopic halogen bond donors (Figure 2.2a). Samples of macrocycle **1** in DMSO (3 mg, 0.5 mL) were mixed with ditopic halogen bond donors in both 1 : 1 and 1 : 2 ratio. Prior work focused on slow evaporation methods, which were unsuccessful with **1**.¹⁷ Water was vapor diffused into these solutions. X-ray quality crystals of **1**·(*o*-DITFB)₂, **1**·(*m*-DITFB)₂·DMSO and **1**·*p*-DITFB were obtained from multiple solutions; however, despite the different ratios each donor only formed one type of co-crystal with **1**. The details of crystallographic data are listed in Table 1. In each structure, the 1D pillars display a similar structure as that of the parent crystal structure of **1**. Comparison of the structure of the three co-crystals with **1** highlights the assembled columns of **1** as the key organizing element. Table 2 shows the N(H)⋯O distances in the co-crystals are slightly shorter than in **1**, ranging from 2.801(7) Å in **1**·(*m*-DITFB)₂·DMSO up to 2.878(4) Å in **1**·(*o*-DITFB)₂. The effect of co-crystal formation on the pillar's N(H)⋯N interaction varied. It was unchanged for **1**·(*o*-DITFB)₂ (3.083(4) Å versus 3.082(2) Å for **1**), significantly shorter for one of the pillars of **1**·(*m*-DITFB)₂·DMSO (3.067(8) Å) and longer in the case of **1**·*p*-DITFB and the second pillar

of $\mathbf{1} \cdot (m\text{-DITFB})_2 \cdot \text{DMSO}$ (3.121(4) and 3.117(8) Å respectively). In each co-crystal, C=O \cdots I interactions ranging from 2.760(4) to 2.853(4) Å were observed that were significantly shorter than the sum van der Waals radii of the atoms involved and are among the shortest reported for neutral organic molecules.¹⁹ (the next part is a little difficult to follow. You could make it into a new paragraph and insert the experimental information here.) To further estimate the strength of the O \cdots I interaction, their interaction energies in the co-crystals were calculated by Q-Chem quantum chemistry package in the electronic ground-state using dispersion corrected density function theory (DFT-D). (Add reference) Taking the basis set super position error (BSSE) into account reduces the uncorrected values by 2–3 kJ mol⁻¹ where ΔE represent the uncorrected halogen bond interaction energy values and ΔE_{CP} corresponds to the corrected energy values using the Boys–Bernardi counterpoise (CP) technique (Table 2). These values are similar to those calculated for similar interactions involving haloperfluorobenzenes.²⁰ The O \cdots I lengths correlate with the interaction energy values with shorter halogen bond lengths corresponding to higher interaction energies. The interaction energy of *p*-DITFB is calculated to be slightly stronger than the *o*-DITFB derivative (–31.51 kJ mol⁻¹ vs. –30.00 kJ mol⁻¹), and it indeed has a shorter O \cdots I interaction. For the *m*-DITFB, the orientation of the two independent columns gave rise two different O \cdots I interactions with one longer and one shorter than that of the para-derivative. However, the theoretical calculation involving this contact was still lower compared to the computed strength of O \cdots I in $\mathbf{1} \cdot (p\text{-DITFB})$ probably due to the involvement of secondary interactions in this particular co-crystal.²¹

Macrocycle **1** formed a 1 : 2 co-crystal with *o*-DITFB, crystallizing in the triclinic system as **1**·(*o*-DITFB)₂ (space group P-1).

Table 2.1 Crystallographic data and structure refinement parameters of co-crystals **1**·(*o*-DITFB)₂, **1**·(*m*-DITFB)₂·DMSO, and **1**·*p*-DITFB

	1 ·(<i>o</i> -DITFB) ₂	1 ·(<i>m</i> -DITFB) ₂ ·DMSO	1 · <i>p</i> -DITFB
Empirical formula	C ₂₈ H ₁₈ F ₈ I ₄ N ₆ O ₂	C ₃₀ H ₂₄ F ₈ I ₄ N ₆ O ₃ S	C ₂₂ H ₁₈ F ₄ I ₂ N ₆ O ₂
Formula weight	1130.08	1208.21	728.22
Temperature/K	100(2)	100(2)	100(2)
Crystal system	triclinic	monoclinic	triclinic
Space group	P-1	P2 ₁ /c	P-1
<i>a</i> /Å	4.6564(3)	4.5773(3)	4.5613(5)
<i>b</i> /Å	12.7812(9)	36.882(3)	10.2296(11)
<i>c</i> /Å	14.2764(9)	21.7673(14)	13.7303(15)
α /°	104.509(2)	90	80.280(3)
β /°	96.086(2)	91.029(2)	83.693(3)
γ /°	97.186(2)	90	87.814(3)
Volume/ Å ³	807.70(9)	3674.1(4)	627.52(12)
Z	1	4	1
ρ_{calc} (g/cm ³)	2.323	2.184	1.927
μ /mm ⁻¹	3.943	3.532	2.568
F(000)	528.0	2280.0	350.0
Crystal size/mm ³	0.22 × 0.04 × 0.02	0.6 × 0.04 × 0.02	0.16 × 0.04 × 0.02
2 θ range/°	5.028 - 54.444	4.346 - 50.052	4.63 - 50.052
Reflections collected	31377	104296	12506
Independent reflections	3550	6502	2215
R _{int}	0.0510	0.1435	0.0547
R _{σ}	0.0306	0.0603	0.0381
No. of parameters	225	488	173
No. of restraints	1	12	0
GoF on F ²	1.062	1.103	1.063
Final R ₁ [<i>I</i> > 2 σ (<i>I</i>)]	0.0247	0.0454	0.0242
Final wR ₂ [<i>I</i> > 2 σ (<i>I</i>)]	0.0476	0.0643	0.0416
Final R ₁ [all data]	0.0350	0.0755	0.0313
Final wR ₂ [all data]	0.0506	0.0698	0.0428
$\Delta\rho$ min, max / e Å ⁻³	0.79/-0.71	0.88/-0.76	0.44/-0.54

There is one centrosymmetric macrocycle and two *o*-DITFB molecules per unit cell. There are layers of *o*-DITFB interpenetrated between columnar layers of **1**. The orientation of the halogen bond acceptor atoms (oxygen) in the macrocycle unit are approximately linear in the *ab* plane. Only one iodine atom of *o*-DITFB participates in a halogen bond (XB) with

oxygen atom of the urea carbonyl group. This XB interaction with **1** is almost linear with C–I···O angle of 169.8(1)° and O···I distance is 2.846(2) Å, 81% of the sum of the van der Waals radii. The second iodine atom weakly interacts with another iodine atom on a nearby *o*-DITFB molecule forming a network in which the columnar macrocyclic structures are separated by columns of *o*-DITFB molecules (Figure 2.3a). The short I···I contact (I1···I1) observed in **1**·(*o*-DITFB)₂ has a I···I distance of 3.903(2) Å (Figure 2.3a) compared with sum of the van der Waals radii of 3.96 Å. This halogen–halogen interaction can be best described as a dispersive type I interaction where the angles $\theta_1(\text{C–I}\cdots\text{I})/\theta_2(\text{I}\cdots\text{I–C})$ are obtuse.²²⁻²³ Crystallization of **1** and *p*-DITFB yielded a 1 : 1 co-crystal **1**·*p*-DITFB in the triclinic space group P-1 (No. 2). The asymmetric unit consists of half of one **1** molecule and half of one *p*-DITFB molecule. Both components are located on crystallographic inversion centers. In the structure, layers of *p*-DITFB are interpenetrated between columnar layers of **1**. The hydrogen-bonded columns of the macrocycles are linked by N–H···N and N–H···O H-bonds are very similar in structure to ‘guest free’ form of **1** and are separated by columnar stacks of *p*-DITFB molecules. Both columns run along the crystallographic *a*-axis (Figure 2.3b). These separate columns are linked to each other *via* C–I···O=C halogen bonding that form a 1D infinite linear chains where the molecules of **1** are arranged alternately with *p*-DITFB molecules to generate an alternating chain of the A···D···A···D··· style in the *b*–*c* plane, where A and D stand for XB acceptor **1** and donor *p*-DITFB. The O···I distance in the crystal structure of **1**·*p*-DITFB is 2.825(2) Å with a C–I···O angle of 178.68(9)° (Figure 2.3b). This is remarkably linear and directional compared to that of **1**·(*o*-DITFB)₂, which shows that a linear symmetric halogen bond donor easily favors the formation of linear long chain assemblies propagated by C–I···O halogen bonds.

Table 2.2 Comparison of hydrogen and halogen bond distances, and DFT calculated energies of the halogen bonds

	N(H)···O (Å)	N(H)···N (Å)	O···I (Å)	C—I···O Angle (°)	ΔE (kJ/mol)	ΔE^{CP} (kJ/mol)
1	2.904(2)	3.082(2)				
1 ·(<i>o</i> -DITFB) ₂	2.878(4)	3.083(4)	2.846	169.83	-33.04	-30.00
1 ·(<i>m</i> -DITFB) ₂ ·DMSO	2.801(7)	3.067(8)	2.760	176.74	-33.96	-30.74
	2.846(7)	3.117(8)	2.853	172.63	-33.72	-30.40
1 · <i>p</i> -DITFB	2.839(4)	3.121(4)	2.825	178.68	-34.91	-31.51

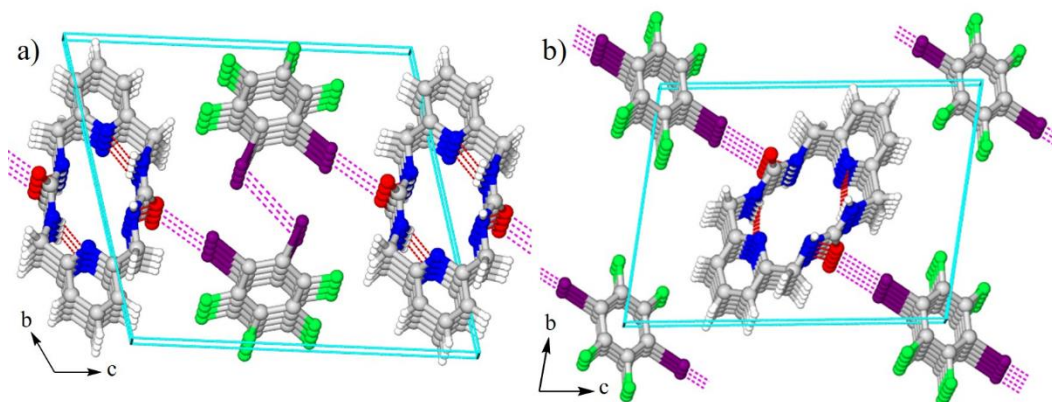


Figure 2.3 Packing diagrams for halogen bonded co-crystals. (a) **1**·(*o*-DITFB)₂, (b) **1**·*p*-DITFB. The purple dotted lines represent the halogen bonds (I···O and I···I) whilst the red dotted lines represent hydrogen bonds within the macrocyclic assembly.

Co-crystallization of **1** with *m*-DITFB consistently formed a three component crystal with a 1 : 2 : 1 ratio of **1** : *m*-DITFB : DMSO, regardless of the initial stoichiometry. The compound crystallizes in the space group P21/c. The asymmetric unit consists of half each of two independent macrocycles, both located on crystallographic inversion centers, two complete *m*-DITFB molecules and one DMSO molecule. There are two independent centrosymmetric macrocycles of **1**, forming infinite hydrogen-bonded 1D columns along the *a*-axis direction. The columns are separated by a double layer of *m*-DITFB and DMSO molecules (Figure 2.4). As can be seen from Table 2, the two columnar systems have slightly different spacing between the macrocyclic units and thus accounts for the two

different C=O...I interactions observed in the crystal structure. These columns are connected through a type II I...I interaction between two halogen bond donor molecules. Again, the strong pillars of **1** are a clear organizing synthon. The two independent macrocycles resulted in two different O...I interactions (O1...I2 and O2...I4) with O...I distances of 2.760(4) and 2.853(4) Å respectively, as shown in Fig. 4. In addition, a third intermolecular XB involving the XB donor and the DMSO molecule (O3...I3) has an O...I distance of 2.892(4) Å. These represent 78–82% of the sum of the van der Waals radii. A type II I...I interaction between I1 and I4 has a distance of 3.770(1) Å which is shorter than the one observed in **1**·(*o*-DITFB)₂ by 0.133 Å. Unlike the type I halogen–halogen interaction which arises from packing of the crystal structure, type II is considered a halogen bond and arises from an electrophile–nucleophile pairing where $\theta_1 \approx 180^\circ$ and $\theta_2 \approx 90^\circ$.²²⁻²³ The halogen bond angles in **1**·(*m*-DITFB)₂·DMSO are also more linear than that of **1**·(*o*-DITFB)₂ (see Table 2.2). In all the co-crystal structures, the diiodotetrafluorobenzenes were organized into column-like structures through offset face-to-face π – π stacking.²⁴⁻²⁶ This provided segregated columns of **1** and the diiodotetrafluorobenzene molecules which are then linked together by the C–I...O=C halogen bonds. The interplanar distances between two diiodotetrafluorobenzenes range from 3.365 Å to 3.526 Å. Distances between centroids and tilted angles were 4.561–4.656 Å and 50.27–63.49° respectively. Figure 2.5 illustrates the electrostatic potential values of the acceptor, macrocycle **1**, and the three XB donors. The electrostatic potential map of macrocycle **1** suggests that the two hydrogens on the urea group are the most electrophilic, and these are utilized in the columnar assembly via hydrogen bonding. Macrocycle **1**

contains two potential halogen bond acceptor atoms (N and O). The most nucleophilic and accessible is the oxygen, which also has the highest negative electrostatic surface.

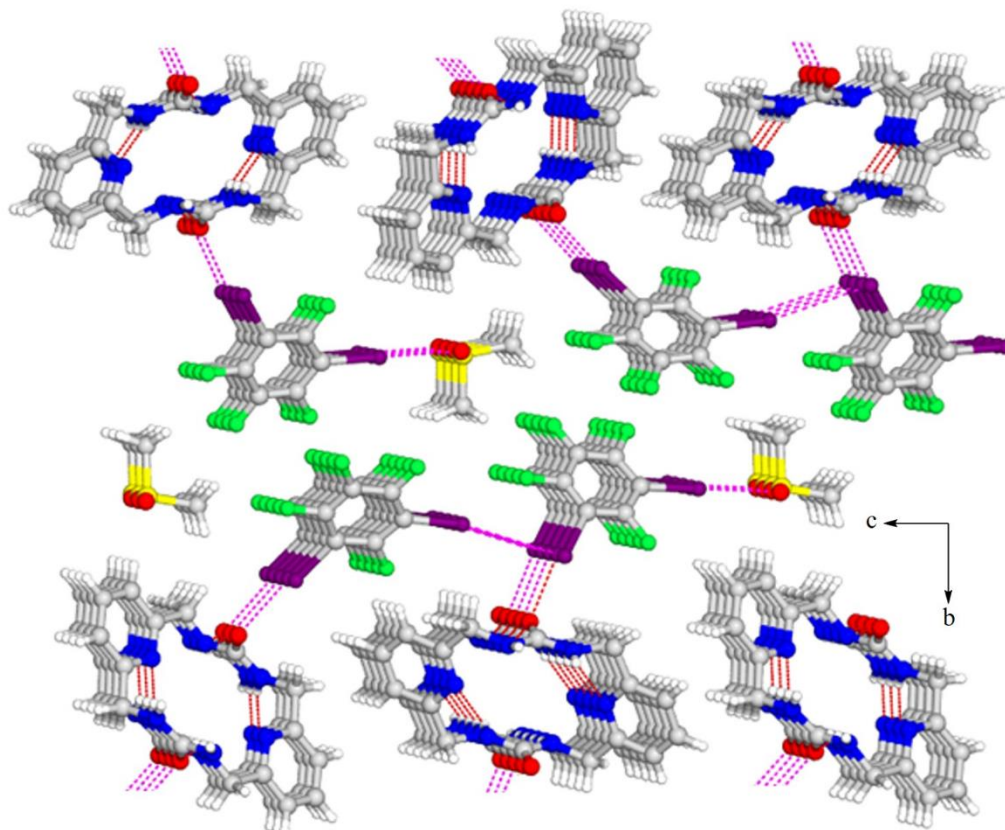


Figure 2.4 Views from the X-ray structure of $1 \cdot (m\text{-DITFB})_2 \cdot \text{DMSO}$. The purple dotted lines represent the halogen bonds ($\text{I} \cdots \text{O}$ and $\text{I} \cdots \text{I}$) while the red dotted lines represent hydrogen bonds within the macrocyclic assembly.

The electrostatic potential surfaces qualitatively indicate the favorable interaction sites between the urea oxygen acceptor on **1** and the σ -holes of the XB donors in the respective DITFB isomers (Figure 2.5b–d), which are marked with significant positive surface areas. The iodine in *p*-DITFB displayed a more positive electrostatic surface than the other two halogen bond donors even though they all have the same number of activating fluorine atoms. This is because the electron density depends on both the composition and the chemical connectivity of atoms in the molecule. Similar calculations done by Aakerøy and co-workers have shown that *p*-DITFB isomer has the highest surface electrostatic potential

when compared to its other two isomers.²⁷ Since halogen bonds are largely electrostatic in nature, the strength of this interaction is expected to be greatest between **1** and *p*-DITFB.²⁸ We turned to solid-state FT-IR spectroscopy to probe the hydrogen and halogen bonding interactions in these systems further. The formation of co-crystals *via* halogen bonding resulted in slightly shorter the N(H)···O distances in the cocrystals between 2.801(7) Å in **1**·(*m*-DITFB)₂·DMSO up to 2.878(4) Å in **1**·(*o*-DITFB)₂.

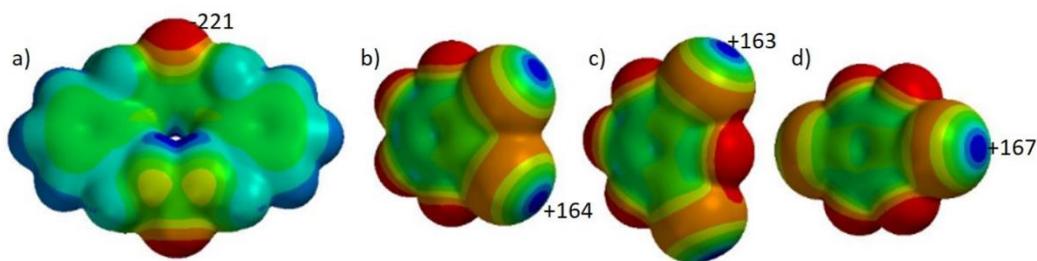


Figure 2.5 Computed surface electrostatic potential maps comparing the potential values of the XB acceptor atom and the XB donor atoms. a) **1**, b) *o*-DITFB c) *m*-DITFB, and d) *p*-DITFB.

In all co-crystals, we observed a shift in the $\nu(\text{C}=\text{O})$ band towards lower wavenumbers by $\sim 20 \text{ cm}^{-1}$ (1650 cm^{-1} in **1** versus $1626\text{--}1628 \text{ cm}^{-1}$ in co-crystals) and decreased intensities, reflecting a weakening of the C=O bond (Figure 2.6). This is reflected in the slight increased bond length of the C=O group from 1.238 in **1** to between 1.239 to 1.251 in the co-crystals (Table 3). The effect of co-crystal formation on the N(H)···N distance varied; however, in the IR the two N–H bands in **1** ($3263, 3320 \text{ cm}^{-1}$) corresponding to the two hydrogen bonds in **1** have shifted and been transformed into a single band in the case of the co-crystals (Table 3). The existence of these shifted bands relative to the starting material **1** is direct evidence of the decrease of electron density on **1** resulting from the $n \rightarrow \sigma^*$ electron donation from the oxygen to the iodine atoms (C=O···I interaction).²⁹ Also, the approach of the XB donor along the direction of the lone-pair on the oxygen further confirms the electrostatic nature of this interaction.³⁰

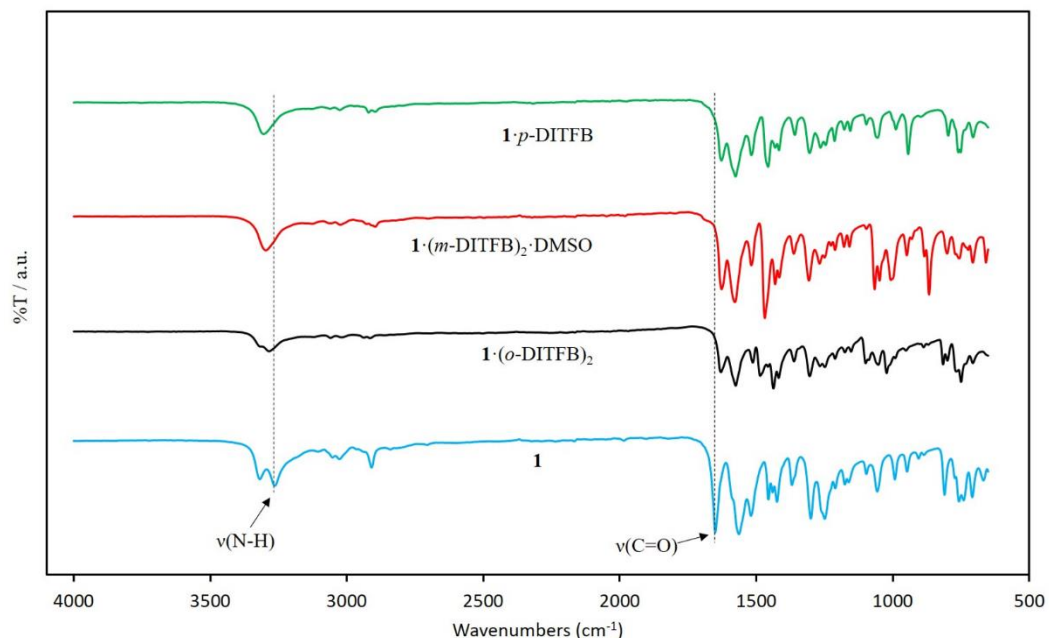


Figure 2.6 FT-IR profile of **1** and co-crystals in the range 4000–650 cm^{-1} .

Table 2.3 Comparison of C=O bond lengths, and indicative FT-IR peaks for host **1** and its co-crystals

	Bond length C=O (Å)	IR bands	
		$\nu_{\text{C=O}}$ (cm^{-1})	$\nu_{\text{N-H}}$ (cm^{-1})
1	1.238	1650	3263, 3320
1·(o-DITFB)₂	1.239	1629	3284
1·(m-DITFB)₂·DMSO	1.243, 1.251	1628	3296
1·p-DITFB	1.247	1626	3304

XPS is an effective spectroscopic method to investigate chemical environments due to changes in binding energy (BE). This method is not applied as frequently to intermolecular interactions and to the best of our knowledge, no $\text{O}\cdots\text{I}$ halogen bonding complex has been analyzed by XPS. Thus, we were interested in comparing the X-ray structure data with XPS analysis. We examined the detailed XPS spectra of the core level peaks for four samples, **1**, **1·(o-DITFB)₂**, **1·(m-DITFB)₂·DMSO**, **1·p-DITFB** and specifically the I(3d) core level peaks for **1·(o-DITFB)₂**, **1·(m-DITFB)₂·DMSO** and **1·p-DITFB**. Initially, a general chemical analysis of the surfaces was carried out by recording the XPS survey

spectra of the four samples, **1**, **1**·(*o*-DITFB)₂, **1**·(*m*-DITFB)₂·DMSO and **1**·*p*-DITFB. Indeed, sample **1** showed photoemission from C, O, and N only, while four additional peaks were observed in each of the co-crystals that corresponding to the F(1s), I(3d3/2), I(3d5/2), and I(4d) features (Figure 2.7).³¹

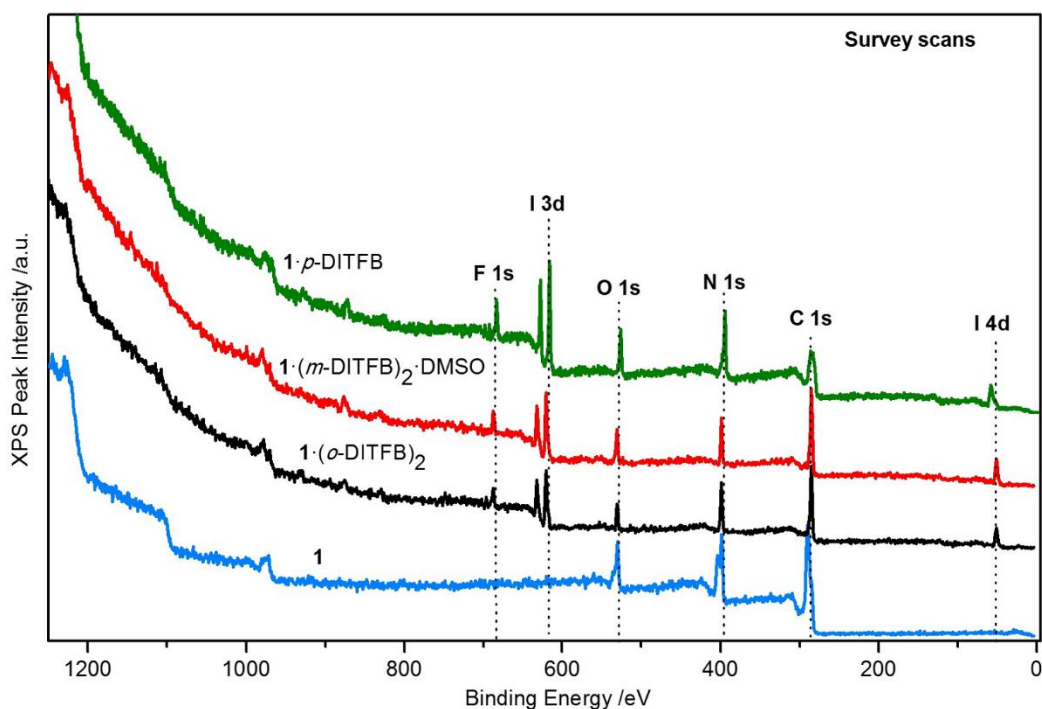


Figure 2.7 XPS survey scans for **1**, **1**·(*o*-DITFB)₂, **1**·(*m*-DITFB)₂·DMSO and **1**·*p*-DITFB recorded with monochromatic Al K_α photon source.

This suggested that the XB donors are fully incorporated in the co-crystals and that there is no contamination by the synthesis procedure or during the measurement. Figure 2.8a shows the deconvolution of the C(1s) core level peak of the three samples. The C(1s) spectrum for sample **1**, consists of four components. The binding energy of C(1s) contributions is well studied in the literature.³²⁻³⁴ The peak at 284.8 eV BE is attributed to the C–C bond, for all samples. The main difference of the two co-crystals compared to **1**, is that the characteristic BE (288.5 eV) for the C=O double bond is not observed, but a C(1s) component can be detected at 287.0 eV that can be attributed to a C–O bond. This

C(1s) peak at 287.0 eV includes contributions of the C–F and C–I bonds of the co-crystals. The XPS C(1s) peak for the C–N bond, is expected according to the literature, between 285–288 eV BE.³⁵ The deconvolution of the C(1s) XPS peaks showed that initially the component for the C–N bond is recorded at 286.2 eV BE, and suggests that after the formation of halogen bonds the C–N bond shifts towards lower BE to 285.2 eV. In summary, the XPS binding energy for C(1s) is very sensitive to the electronic changes that take place around the C=O. The N(1s) peak is detected initially at 400.0 eV BE as expected for the N–C=O bond.³⁶ After the creation of the co-crystals N 1s peak shifts towards 398.5 eV BE close to a pyridine-like nitrogen (Figure 2.8b).³⁷ The F(1s) core level peaks were recorded only for **1**·(*o*-DITFB)₂, **1**·(*m*-DITFB)₂·DMSO, and **1**·*p*-DITFB and were found at 687.3 eV BE as expected for the C–F bond.³⁴ The recorded O(1s) core level peaks of the four samples are shown in Figure 2.9a. Initially, for sample **1**, the O(1s) BE was measured at 531.5 eV as expected for O=C–N groups.³² The O(1s) peak shifted to lower BEs of 530.4 eV for **1**·(*o*-DITFB)₂, **1**·(*m*-DITFB)₂·DMSO and **1**·*p*-DITFB, which is the characteristic binding energy for the I–O bond.³⁸⁻⁴⁰ This suggests that the O···I halogen bonding interaction is comparable to the O–I bond as observed by XPS. Typically, higher binding energy indicates higher oxidation state due to lower electron density around the atom or ion.⁴¹⁻⁴³ Too few examples of O···I halogen bonded complexes have been examined by XPS to determine if this is a general trend or a signature of the hydrogen and halogen bonded co-crystals under study.

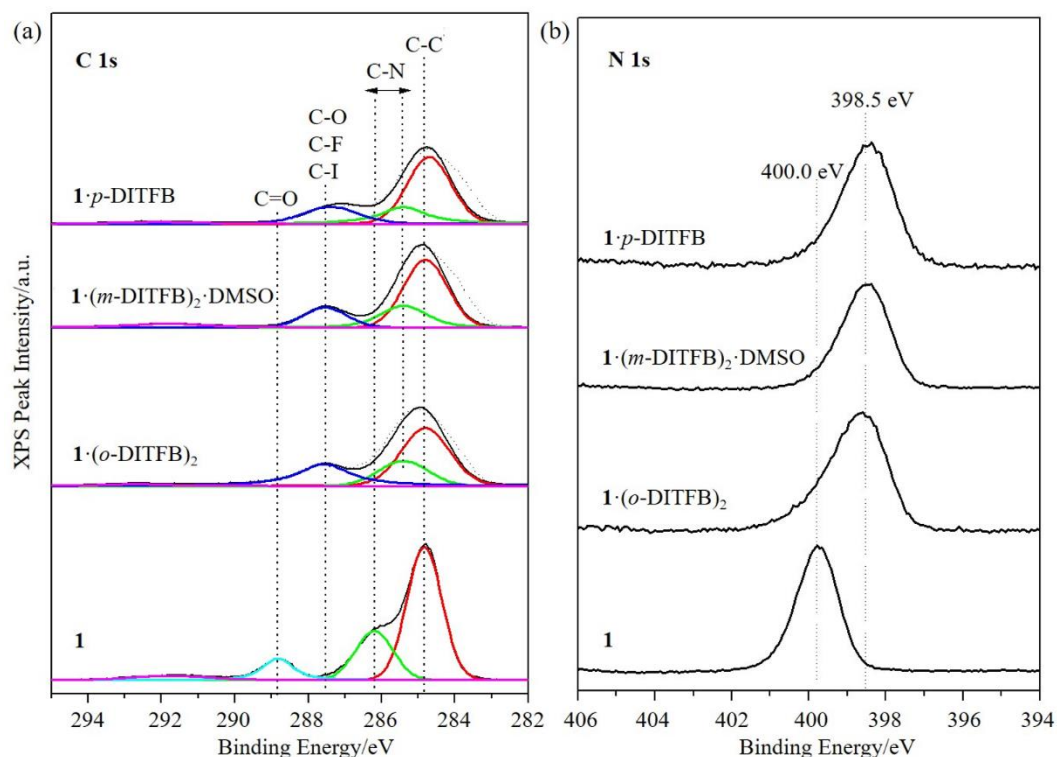


Figure 2.8 High resolution core level spectra of C(1s) and N(1s). (a) C(1s) XPS core level peaks for **1**, **1·(o-DITFB)₂**, **1·(m-DITFB)₂·DMSO** and **1·p-DITFB** (b) N(1s) XPS core level peaks for **1**, **1·(o-DITFB)₂**, **1·(m-DITFB)₂·DMSO** and **1·p-DITFB** recorded with monochromatic Al K α photon source.

The I(3d) core level peaks were recorded for the two co-crystals (Figure 2.9b), and were found at 620.6 eV BE, which again is characteristic for the I–O bond.³⁸⁻⁴⁰ The shift of the O(1s) photoelectron peak towards lower binding energy (530.4 eV), in combination with the binding energy recorded for I(3d) (620.6 eV), upon creation of the co-crystals strongly supports the creation of halogen bonding. As expected, the electronic changes of the C=O bond and the formation of halogen bonds in the co-crystals, affects the N(1s) core level peak of the three samples, which can be detected in a range between 398.5–400.0 eV BE (Figure 2.8b).

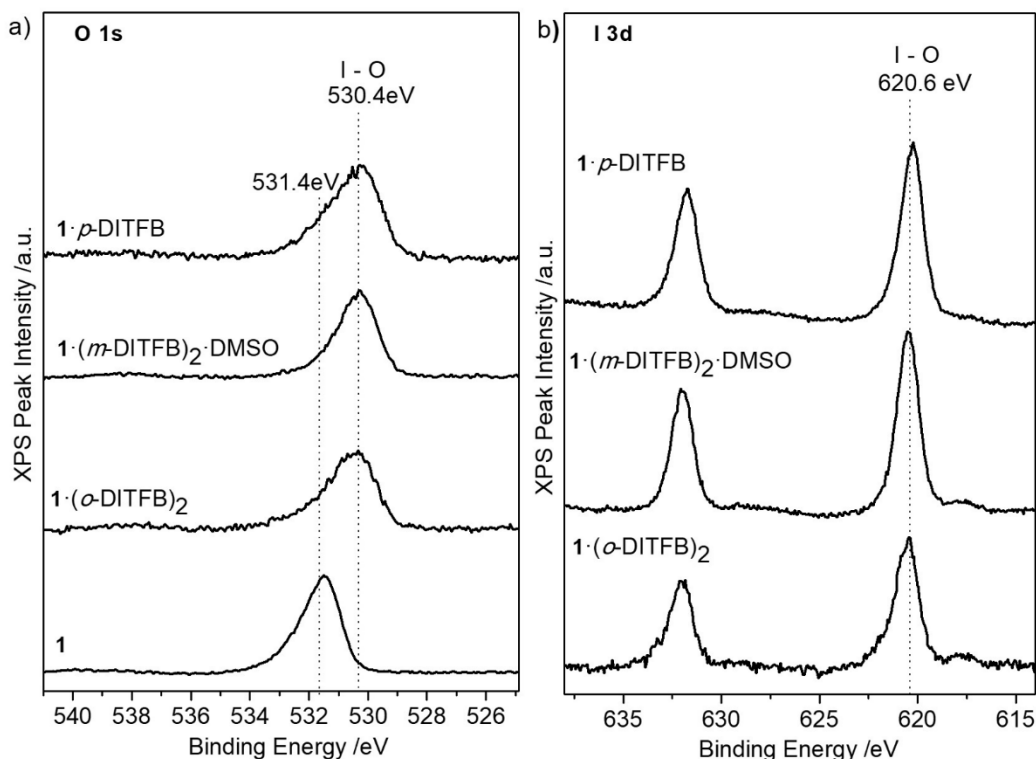


Figure 2.9 High resolution core level spectra of O(1s) and I(3d). (a) O(1s) XPS core level peaks for **1**, **1**·(*o*-DITFB)₂, **1**·(*m*-DITFB)₂·DMSO and **1**·*p*-DITFB (b) I(3d) XPS core level peaks for **1**·(*o*-DITFB)₂, **1**·(*m*-DITFB)₂·DMSO and **1**·*p*-DITFB recorded with monochromatic Al K α X-ray source.

2.3 Conclusions

In summary, we have established the ability of the pillars of assembled pyridyl *bis*-urea macrocycle (host **1**) to absorb and organize small organic molecules in the solid-state through non-covalent interactions. Here, these robust pillars function as ditopic XB acceptors forming co-crystals with three regioisomers of diiodotetrafluorobenzene. The co-crystals exhibit different stoichiometry and crystal packing, which is attributed to the altered geometry of XB donor atoms (iodine) in the donor molecules. The most symmetrical XB donor *p*-DITFB gave rise to a 1 : 1 donor–acceptor co-crystal utilizing the C=O \cdots I synthon. On the other hand, *o*-DITFB and *m*-DITFB isomers resulted in 1 : 2 donor–acceptor co-crystals {**1**·(*o*-DITFB)₂ and **1**·(*m*-DITFB)₂·DMSO} where both

C=O...I and type I/II iodine–iodine interactions were observed. DMSO in the structure of **1**·(*m*-DITFB)₂·DMSO acted as a second XB acceptor molecule. The O...I interaction length range from 2.760(4) to 2.853(4) Å representing an 18–22% reduction of the sum of the van der Waals radii of the atoms involved. DFT calculations estimated the O...I strength to increase from 30.00 kJ mol⁻¹ in **1**·(*o*-DITFB)₂ to 31.51 kJ mol⁻¹ in **1**·*p*-DITFB. Further analysis of the crystals by IR and XPS spectroscopies confirmed the presence of the C=O...I synthon in the co-crystals. The XPS binding energy of the C(1s) of the C=O provided a very sensitive indicator of halogen bond formation. Indeed, without comparison to the X-ray diffraction data, the XPS might be interpreted as indicating the breaking of the C=O bond. However, the bond distance of C to O from the X-ray structures are still in the range expected for the carbonyl and IR also confirms the carbonyl stretch while weakened is still retained. These data should be of interest for future applications of XPS analysis in halogen bonding systems. In conclusion, the introduction of a halogen bonding interactions to form complex supramolecular architectures did not affect the strong assembled pillars of host **1**. Thus, the pyridyl urea hosts should be predictable synthon for orienting guest molecules through non-covalent interactions into co-crystalline materials and could be applicable for controlling their subsequent reactivity.

2.4 Experimental

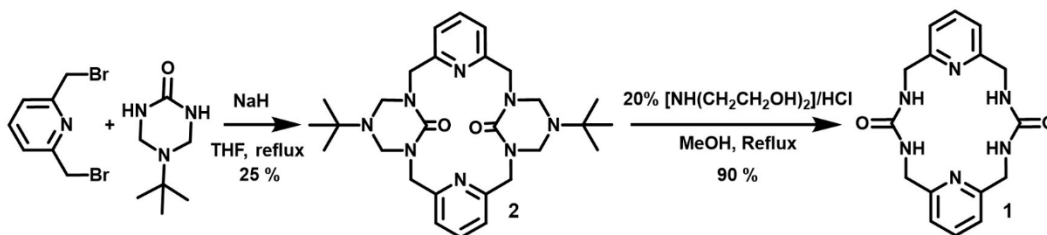
2.4.1 Materials and methods

The pyridyl *bis*-urea macrocycle (**1**) was synthesized as previously reported.¹⁵⁻¹⁶ All reagents, solvents and donors 1,2-diiodotetrafluorobenzene (*o*-DITFB), 1,3-diiodotetrafluorobenzene (*m*-DITFB), 1,4-diiodotetrafluorobenzene (*p*-DITFB) were purchased from Alfa Aesar and used as received. ¹H NMR were recorded on Varian

Mercury/VX 400 NMR spectrometer. FT-IR spectra were obtained with a Perkin Elmer Spectrum 100 FT-IR Spectrometer over the range 4000–650 cm^{-1} with 2 cm^{-1} resolution and 32 scans per sample.

2.4.2 Synthesis and characterization of pyridyl bis-urea macrocycle 1

Scheme 2.1 Synthesis of host **1**.



Compound **1** was synthesized in two steps. Triazinanone⁴⁴ (1.00 g, 6.4 mmol) prepared as previously described and NaH (460 mg, 19.2 mmol) were weighed into a three-neck round bottom flask under nitrogen, 300 mL of dry THF added and the suspension heated to reflux for 1.5 hours. After cooling to room temperature, a solution of **2**, 6-bis(bromomethyl)pyridine (1.69 g, 6.4 mmol) in THF (100 ml) was added dropwisely. The reaction mixture was then stirred and heated to reflux overnight under nitrogen. Upon completion, the reaction mixture was quenched with 50 mL water and then the solution volume was reduced *in vacuo* to 75 mL. The solution was diluted with 50 mL water and then extracted with chloroform (3 × 100 mL). The combined organic layers were washed with brine and dried over anhydrous MgSO₄. Purificaion of crude product by silica gel chromatography with a dichloromethane : methanol : ammonium hydroxide (9: 0.5:0.5) eluent gave **2** as a white solid (0.413 g, 25 %). In this case the compound was pre-adsorbed onto the silica, dried and loaded on the top of the column. The solvents (dichloromethane : methanol : ammonium hydroxide) were mixed together in a separatory funnel affording two layers and only the bottom organic portion was used to run the column. The purity of the

compound was confirmed by proton-NMR (Figure 2.10). ^1H NMR (400 MHz, DMSO) δ = 7.56 (t, J = 7.4 Hz, 1H), 7.05 (d, J = 7.4 Hz, 2H), 5.07 (t, J = 14.5 Hz, 4H), 4.36 (d, J = 11.7 Hz, 2H), 3.94 (d, J = 16.5 Hz, 2H), 1.20 (s, 9H).

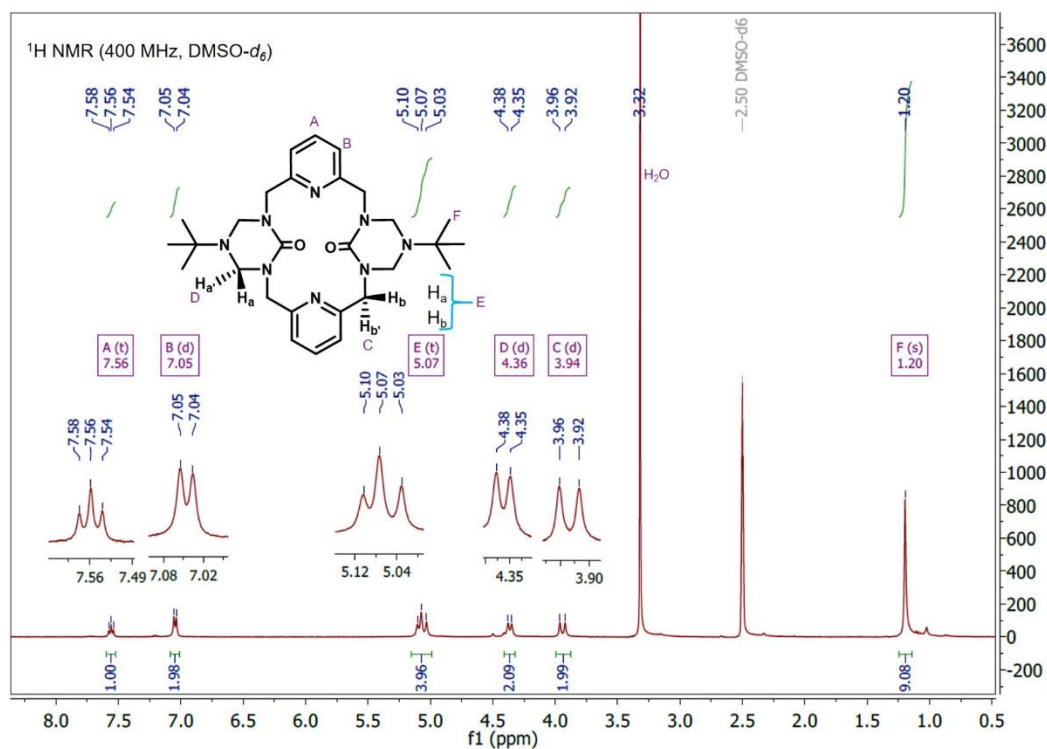


Figure 2.10 ^1H NMR (400 MHz, DMSO- d_6) of protected pyridyl *bis*-urea macrocycle **2**.

Triazinanone protected *bis*-urea macrocycle (**2**) (0.260 g, 4.99×10^{-1} mmol) was heated to reflux in 50 mL of a freshly prepared 1:1 mixture of 20% [diethanolamine/water solution adjusted to pH ~ 2 with conc. HCl]: MeOH for 24 h. After 24 hours, small amount of the reaction mixture was taken out into a test tube, equal amount of dichloromethane was added and the mixture shaken for a few minutes. The dichloromethane layer was then used for TLC to confirm completion of the reaction. No spot for the starting material from this DCM layer on the TLC indicates completion of the reaction. The methanol was removed in vacuo resulting a light brown aqueous solution. A white solid precipitated out of solution upon cooling in an ice-bath. The solid was collected by suction filtration,

washed with 45 mL H₂O and dried in vacuo to obtain the product as white powder (0.163 g, 93%). The ¹H NMR matches that reported in the literature (Figure 2.11).¹⁵ ¹H NMR (400 MHz, DMSO) δ = 7.68 – 7.62 (m, 1H), 7.16 (d, *J* = 8.2 Hz, 2H), 6.93 (s, 1H), 4.33 (d, *J* = 5.0 Hz, 4H).

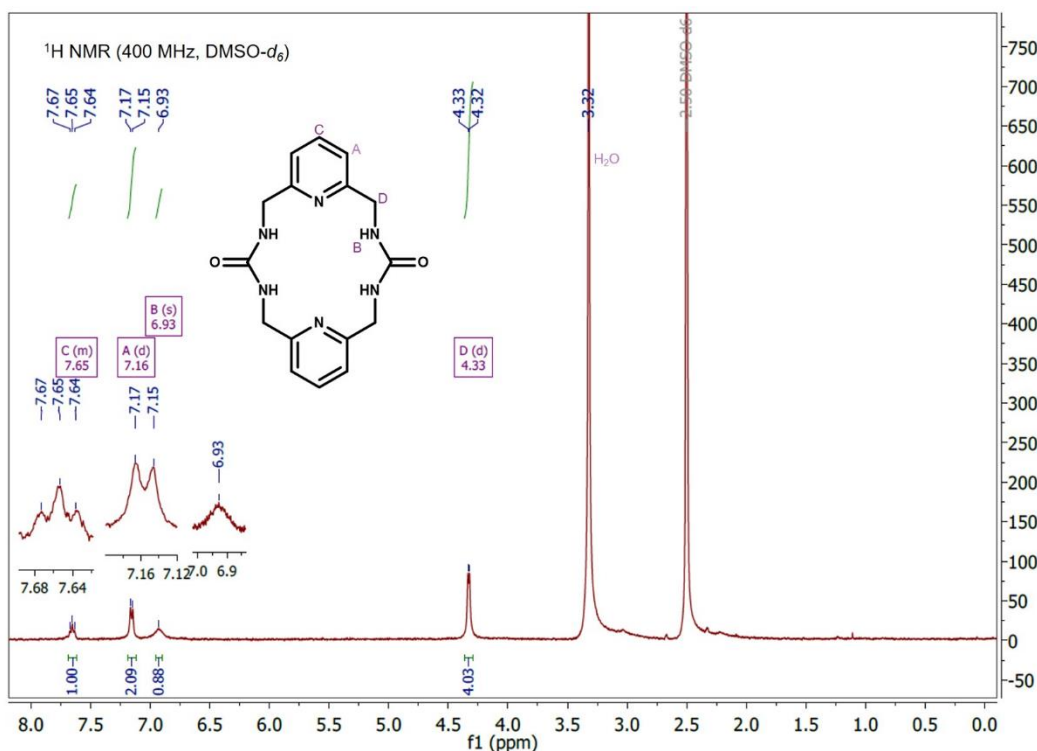


Figure 2.11 ¹H NMR (400 MHz, DMSO-*d*₆) of host **1**.

2.4.3 Co-crystal synthesis

Co-crystals of **1** with the ditopic halogen bond donors were obtained by two methods. Method 1. Macrocycle **1** (3.0 mg, 9.2 μmol) was mixed with two equivalents of the donors (7.4 mg, 18.4 μmol) in 0.5 mL DMSO which was slightly heated to dissolve completely followed by vapor diffusion of water into the DMSO solution over a period of 1–2 weeks. Co-crystals **1**·(*o*-DITFB)₂ and **1**·(*m*-DITFB)₂·DMSO were obtained as clusters of fine colorless needles. Method 2. Macrocycle **1** (3.0 mg, 9.2 μmol) and donor (3.7 mg, 9.2 μmol) were mixed in 1 : 1 molar ratio in 0.5 mL DMSO and slightly heated to dissolve

completely. Water was then vapor diffused into the DMSO solution. Fine colorless crystals (needles) of **1**·*p*-DITFB were obtained after 3–5 days.

2.4.4 X-ray crystallography

Single-crystal XRD data of co-crystal **1**·(*o*-DITFB)₂, **1**·(*m*-DITFB)₂·DMSO, and **1**·*p*-DITFB were collected at 100(2) K using a Bruker D8 QUEST diffractometer equipped with a PHOTON 100 CMOS area detector and an Incoatec microfocus source (Mo K α radiation, $\lambda = 0.71073 \text{ \AA}$).⁴⁵ The raw area detector data frames were reduced and corrected for absorption effects using the SAINT+ and SADABS programs.⁴⁶ Final unit cell parameters were determined by least-squares refinement of large sets of strong reflections taken from each data set. The structures were solved with SHELXT.⁴⁷⁻⁴⁹ Subsequent difference Fourier calculations and full-matrix least-squares refinement against F² were performed with SHELXL-2014⁴⁷⁻⁴⁹ using OLEX2.31 Twinning was diagnosed in **1**·(*o*-DITFB)₂ using the Bruker Cell_Now program, which indexed all reflections to two domains related by a two-fold axis of rotation about the crystallographic [100] direction. The best twin refinement was obtained by integrating only the major triclinic domain, solving the structure and then creating a SHELX HKLF-5 format reflection file using the TwinRotMat program in PLATON.⁴⁹ The derived twin law is (1 0 0/-0.667 -1 0/-0.667 0 -1), and the major twin fraction refined to 0.755(1). Also, non-merohedral twinning in **1**·*p*-DITFB, evident from the diffraction pattern was resolved using the TwinRotMat program in PLATON.³² The twin law derived is (-1 0 0/-0.334 0.334 0.666/-0.334 1.334 -0.334), corresponding to a two-fold rotation perpendicular to the (110) plane. The major twin volume refined to 0.845(1). All non-hydrogen atoms were refined with anisotropic displacement parameters. Hydrogen atoms bonded to carbon were located in difference

maps before being included as riding atoms. In **1**·(*o*-DITFB)₂ and **1**·(*m*-DITFB)₂·DMSO the urea hydrogens were located in difference maps and refined isotropically with their N–H distances restrained to be approximately equal. However, in **1**·*p*-DITFB the urea hydrogens were located in difference maps and refined freely.

2.4.5 Computations

Electrostatic potential surfaces for the halogen bond donor molecules and the acceptor were calculated with density functional B3LYP level of theory with 6-311++G** basis set in vacuum. All calculations were done using Spartan10 software⁵⁰ where all molecules were geometry optimized with maxima and minima in the electrostatic potential surface (0.002 isovalue). Interaction energy calculations for the cocrystals were carried out by Q-CHEM⁵¹ quantum chemistry package in the electronic ground-state using dispersion corrected density functional theory (DFT-D). Single crystal XRD structures of the co-crystals/co-crystal fragments (Figure 2.12) were imported into the software and their energies calculated using B97D⁵² with 6-311++G** basis set. Interaction energies (ΔE) were then determined as the energy difference between the complex (co-crystal dimer) and the sum of the energy of its components (acceptor and donor).

$$\Delta E = E_{\text{complex}} - (E_{\text{acceptor}} + E_{\text{donor}})$$

The basis set superposition error (BSSE) was taken into account by means of the Boys–Bernardi counterpoise (CP) technique.⁵³

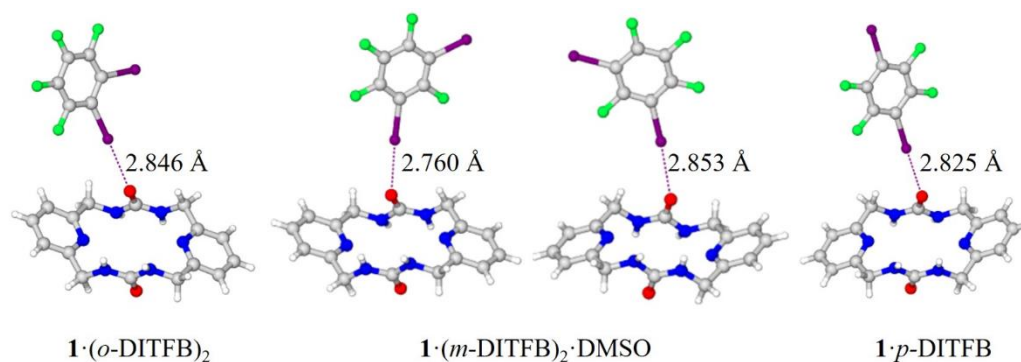


Figure 2.12. X-ray structures of the co-crystal dimers used in the theoretical calculations.

2.4.6 X-ray photoelectron spectroscopy

X-ray photoelectron spectroscopy measurements were performed on the samples using a Kratos AXIS Ultra DLD XPS system with a monochromatic Al K α source operated at 15 keV and 150 W and a hemispherical energy analyzer. The X-rays were incident at an angle of 45° with respect to the surface normal and the pass energy was fixed at 160 eV for the survey scans and 40 eV for the core level peaks. All samples were dried under vacuum for three hours before submitting them for XPS analysis. The samples are then placed as received in a load lock chamber, attached to the main ultra-high vacuum system for XPS measurements. The load lock chamber is pumped down by two turbo-molecular pumps overnight, before the introduction of the samples to the main chamber. XPS survey spectra were acquired on **1**, $1 \cdot (o\text{-DITFB})_2$, $1 \cdot (m\text{-DITFB})_2 \cdot \text{DMSO}$ and $1 \cdot p\text{-DITFB}$ using a Kratos AXIS Ultra DLD XPS system with a monochromatic Al K α source operated at 15 keV and 150 W, and the analysis was performed below 1×10^{-9} mbar. High resolution core level spectra were measured with a pass energy of 40 eV for three samples, **1**, $1 \cdot (o\text{-DITFB})_2$, $1 \cdot (m\text{-DITFB})_2 \cdot \text{DMSO}$ and $1 \cdot p\text{-DITFB}$. Analysis of the data was carried out with XPSPEAK41 software. The XPS experiments were performed while using an electron beam, directed on the sample, for charge neutralization.

2.5 References

1. Metrangolo, P.; Meyer, F.; Pilati, T.; Resnati, G.; Terraneo, G., Halogen Bonding in Supramolecular Chemistry. *Angew. Chem. Int. Ed.* **2008**, *47* (33), 6114-6127.
2. Priimagi, A.; Cavallo, G.; Metrangolo, P.; Resnati, G., The Halogen Bond in the Design of Functional Supramolecular Materials: Recent Advances. *Acc. Chem. Res.* **2013**, *46* (11), 2686-2695.
3. Zhu, W.; Zheng, R.; Zhen, Y.; Yu, Z.; Dong, H.; Fu, H.; Shi, Q.; Hu, W., Rational Design of Charge-Transfer Interactions in Halogen-Bonded Co-crystals toward Versatile Solid-State Optoelectronics. *J. Am. Chem. Soc.* **2015**, *137* (34), 11038-11046.
4. Hidalgo, P. I.; Leal, S.; Jimenez, C. A.; Vohringer-Martinez, E.; Herrera, B.; Pasan, J.; Ruiz-Perez, C.; Bruce, D. W., Extending the halogen-bonded supramolecular synthon concept to 1,3,4-oxadiazole derivatives. *CrystEngComm* **2016**, *18* (1), 42-47.
5. Berger, G.; Soubhye, J.; Meyer, F., Halogen bonding in polymer science: from crystal engineering to functional supramolecular polymers and materials. *Polymer Chemistry* **2015**, *6* (19), 3559-3580.
6. Metrangolo, P.; Neukirch, H.; Pilati, T.; Resnati, G., Halogen Bonding Based Recognition Processes: A World Parallel to Hydrogen Bonding†. *Acc. Chem. Res.* **2005**, *38* (5), 386-395.
7. Meyer, F.; Dubois, P., Halogen bonding at work: recent applications in synthetic chemistry and materials science. *CrystEngComm* **2013**, *15* (16), 3058-3071.
8. Walsh, R. B.; Padgett, C. W.; Metrangolo, P.; Resnati, G.; Hanks, T. W.; Pennington, W. T., Crystal Engineering through Halogen Bonding: Complexes of

Nitrogen Heterocycles with Organic Iodides. *Crystal Growth & Design* **2001**, *1* (2), 165-175.

9. Caronna, T.; Liantonio, R.; Logothetis, T. A.; Metrangolo, P.; Pilati, T.; Resnati, G., Halogen Bonding and $\pi\cdots\pi$ Stacking Control Reactivity in the Solid State. *J. Am. Chem. Soc.* **2004**, *126* (14), 4500-4501.

10. Crihfield, A.; Hartwell, J.; Phelps, D.; Walsh, R. B.; Harris, J. L.; Payne, J. F.; Pennington, W. T.; Hanks, T. W., Crystal Engineering through Halogen Bonding. 2. Complexes of Diacetylene-Linked Heterocycles with Organic Iodides. *Crystal Growth & Design* **2003**, *3* (3), 313-320.

11. Aakeroy, C. B.; Wijethunga, T. K.; Desper, J., Constructing molecular polygons using halogen bonding and bifurcated N-oxides. *CrystEngComm* **2014**, *16* (1), 28-31.

12. Bertolotti, F.; Cavallo, G.; Metrangolo, P.; Nayak, S. K.; Resnati, G.; Terraneo, G., C-halogen...O supramolecular synthons: in situ cryocrystallisation of 1,2-dihalotetrafluoroethane/HMPA adducts. *Supramol. Chem.* **2013**, *25* (9-11), 718-727.

13. Kratzer, P.; Ramming, B.; Romisch, S.; Maas, G., The iodine-oxygen halogen bond: solid-state structures of 3-iodopropiolamides. *CrystEngComm* **2015**, *17* (24), 4486-4494.

14. Syssa-Magalé, J.-L.; Boubekour, K.; Schöllhorn, B., First molecular self-assembly of 1,4-diiodo-tetrafluoro-benzene and a ketone via (O \cdots I) non-covalent halogen bonds. *J. Mol. Struct.* **2005**, *737* (2-3), 103-107.

15. Roy, K.; Wang, C.; Smith, M. D.; Dewal, M. B.; Wibowo, A. C.; Brown, J. C.; Ma, S.; Shimizu, L. S., Guest induced transformations of assembled pyridyl *bis*-urea macrocycles. *Chem. Commun.* **2011**, *47* (1), 277-279.

16. Roy, K.; Wibowo, A. C.; Pellechia, P. J.; Ma, S.; Geer, M. F.; Shimizu, L. S., Absorption of Hydrogen Bond Donors by Pyridyl *Bis*-Urea Crystals. *Chem. Mater.* **2012**, *24* (24), 4773-4781.
17. Geer, M. F.; Mazzuca, J.; Smith, M. D.; Shimizu, L. S., Short, strong halogen bonding in co-crystals of pyridyl *bis*-urea macrocycles and iodoperfluorocarbons. *CrystEngComm* **2013**, *15* (46), 9923-9929.
18. Shimizu, L. S.; Salpage, S. R.; Korous, A. A., Functional Materials from Self-Assembled *Bis*-urea Macrocycles. *Acc. Chem. Res.* **2014**, *47* (7), 2116-2127.
19. Aakeröy, C. B.; Wijethunga, T. K.; Desper, J.; Đaković, M., Crystal Engineering with Iodoethynylnitrobenzenes: A Group of Highly Effective Halogen-Bond Donors. *Crystal Growth & Design* **2015**, *15* (8), 3853-3861.
20. Politzer, P.; Lane, P.; Concha, M. C.; Ma, Y.; Murray, J. S., An overview of halogen bonding. *J. Mol. Model.* **2007**, *13* (2), 305-311.
21. Riley, K. E.; Murray, J. S.; Fanfrlík, J.; Řezáč, J.; Solá, R. J.; Concha, M. C.; Ramos, F. M.; Politzer, P., Halogen bond tunability I: the effects of aromatic fluorine substitution on the strengths of halogen-bonding interactions involving chlorine, bromine, and iodine. *J. Mol. Model.* **2011**, *17* (12), 3309-3318.
22. Pedireddi, V. R.; Reddy, D. S.; Goud, B. S.; Craig, D. C.; Rae, A. D.; Desiraju, G. R., The nature of halogen [three dots, centered] halogen interactions and the crystal structure of 1,3,5,7-tetraiodoadamantane. *Journal of the Chemical Society, Perkin Transactions 2* **1994**, (11), 2353-2360.
23. Pigge, F. C.; Vangala, V. R.; Swenson, D. C., Relative importance of X[three dots, centered]O[double bond, length as m-dash]C vs. X[three dots, centered]X halogen bonding

as structural determinants in 4-halotriarylbenzenes. *Chem. Commun.* **2006**, (20), 2123-2125.

24. Gao, H. Y.; Shen, Q. J.; Zhao, X. R.; Yan, X. Q.; Pang, X.; Jin, W. J., Phosphorescent co-crystal assembled by 1,4-diiidotetrafluorobenzene with carbazole based on C-I[three dots, centered][small pi] halogen bonding. *J. Mater. Chem.* **2012**, *22* (12), 5336-5343.

25. Nguyen, S. T.; Rheingold, A. L.; Tschumper, G. S.; Watkins, D. L., Elucidating the Effects of Fluoro and Nitro Substituents on Halogen Bond Driven Assemblies of Pyridyl-Capped π -Conjugated Molecules. *Crystal Growth & Design* **2016**, *16* (11), 6648-6653.

26. Shen, Q. J.; Wei, H. Q.; Zou, W. S.; Sun, H. L.; Jin, W. J., Cocrystals assembled by pyrene and 1,2- or 1,4-diiidotetrafluorobenzenes and their phosphorescent behaviors modulated by local molecular environment. *CrystEngComm* **2012**, *14* (3), 1010-1015.

27. Aakeröy, C. B.; Wijethunga, T. K.; Desper, J.; Đaković, M., Electrostatic Potential Differences and Halogen-Bond Selectivity. *Crystal Growth & Design* **2016**, *16* (5), 2662-2670.

28. Politzer, P.; Laurence, P. R.; Jayasuriya, K., Molecular electrostatic potentials: an effective tool for the elucidation of biochemical phenomena. *Environ. Health Perspect.* **1985**, *61*, 191-202.

29. Metrangolo, P.; Resnati, G., Halogen Bonding: A Paradigm in Supramolecular Chemistry. *Chemistry - A European Journal* **2001**, *7* (12), 2511-2519.

30. Aakeroy, C. B.; Sinha, A. S.; Chopade, P. D.; Desper, J., Halogen bonding or close packing? Examining the structural landscape in a series of Cu(ii)-acac complexes. *Dalton Transactions* **2011**, *40* (45), 12160-12168.

31. Bomben, K. D.; Moulder, J. F.; Sobol, P. E.; Stickle, W. F., Handbook of X-ray photoelectron spectroscopy. *A Reference Book of Standard Spectra for Identification and Interpretation of XPS Data* **1992**.
32. Briggs, D.; Beamson, G., Primary and secondary oxygen-induced C1s binding energy shifts in x-ray photoelectron spectroscopy of polymers. *Anal. Chem.* **1992**, *64* (15), 1729-1736.
33. Cai, W.; Lin, Z.; Strother, T.; Smith, L. M.; Hamers, R. J., Chemical Modification and Patterning of Iodine-Terminated Silicon Surfaces Using Visible Light. *The Journal of Physical Chemistry B* **2002**, *106* (10), 2656-2664.
34. Yuichi, H.; Tomoya, I.; Hiroyuki, I.; Kazuhiro, K.; Shinji, M., X-Ray Photoelectron Spectroscopy Study of Synchrotron Radiation Irradiation of a Polytetrafluoroethylene Surface. *Japanese Journal of Applied Physics* **2003**, *42* (4R), 1722.
35. Moulder, J. F.; Chastain, J.; King, R. C., *Handbook of x-ray photoelectron spectroscopy : a reference book of standard spectra for identification and interpretation of XPS data*. Physical Electronics: Eden Prairie, Minn., 1995.
36. Stevens, J. S.; Byard, S. J.; Seaton, C. C.; Sadiq, G.; Davey, R. J.; Schroeder, S. L. M., Proton transfer and hydrogen bonding in the organic solid state: a combined XRD/XPS/ssNMR study of 17 organic acid-base complexes. *PCCP* **2014**, *16* (3), 1150-1160.
37. Weidenthaler, C.; Lu, A.-H.; Schmidt, W.; Schüth, F., X-ray photoelectron spectroscopic studies of PAN-based ordered mesoporous carbons (OMC). *Microporous Mesoporous Mater.* **2006**, *88* (1-3), 238-243.

38. Iwanek, E.; Ulkowska, U.; Gliński, M., Surface studies of magnesium oxide-based catalysts modified with X₂ or MgX₂ (X = Br, I). *Surf. Interface Anal.* **2015**, *47* (11), 1001-1008.
39. Rajendra Kumar, G.; Dennyson Savariraj, A.; Karthick, S. N.; Selvam, S.; Balamuralitharan, B.; Kim, H.-J.; Viswanathan, K. K.; Vijaykumar, M.; Prabakar, K., Phase transition kinetics and surface binding states of methylammonium lead iodide perovskite. *PCCP* **2016**, *18* (10), 7284-7292.
40. Sherwood, P. M. A., X-ray photoelectron spectroscopic studies of some iodine compounds. *Journal of the Chemical Society, Faraday Transactions 2: Molecular and Chemical Physics* **1976**, *72* (0), 1805-1820.
41. Houbenov, N.; Milani, R.; Poutanen, M.; Haataja, J.; Dichiarante, V.; Sainio, J.; Ruokolainen, J.; Resnati, G.; Metrangolo, P.; Ikkala, O., Halogen-bonded mesogens direct polymer self-assemblies up to millimetre length scale. *Nature Communications* **2014**, *5*, 4043.
42. Stevens, J. S.; Byard, S. J.; Schroeder, S. L. M., Salt or Co-Crystal? Determination of Protonation State by X-Ray Photoelectron Spectroscopy (XPS). *J. Pharm. Sci.* **2010**, *99* (11), 4453-4457.
43. Wang, F.; Ma, N.; Chen, Q.; Wang, W.; Wang, L., Halogen Bonding as a New Driving Force for Layer-by-Layer Assembly. *Langmuir* **2007**, *23* (19), 9540-9542.
44. Mitchell, A. R.; Pagoria, P. F.; Coon, C. L.; Jessop, E. S.; Poco, J. F.; Tarver, C. M.; Breithaupt, R. D.; Moody, G. L., Nitroureas 1. Synthesis, scale-up and characterization of K-6. *Propellants, Explosives, Pyrotechnics* **1994**, *19* (5), 232-239.

45. APEX2 Version 2014.9-0, SAINT+ Version 8.34A and SADABS Version 2014/4. Bruker Analytical X-ray Systems, Inc., Madison, Wisconsin, USA, 2014.
46. Sheldrick, G., A short history of SHELX. *Acta Crystallographica Section A* **2008**, *64* (1), 112-122.
47. Sheldrick, G., SHELXT - Integrated space-group and crystal-structure determination. *Acta Crystallographica Section A* **2015**, *71* (1), 3-8.
48. Spek, A., Single-crystal structure validation with the program PLATON. *J. Appl. Crystallogr.* **2003**, *36* (1), 7-13.
49. Spek, A., Structure validation in chemical crystallography. *Acta Crystallographica Section D* **2009**, *65* (2), 148-155.
50. Spartan'10, Version 1.1.0, Wavefunction, Inc., Irvine, 2010
51. Shao, Y.; Gan, Z.; Epifanovsky, E.; Gilbert, A. T. B.; Wormit, M., Advances in molecular quantum chemistry contained in the Q-Chem 4 program package. *Mol. Phys.* **2015**, *113* (2), 184-215.
52. Grimme, S., Semiempirical GGA-type density functional constructed with a long-range dispersion correction. *J. Comput. Chem.* **2006**, *27* (15), 1787-1799.
53. Boys, S. F.; Bernardi, F., The calculation of small molecular interactions by the differences of separate total energies. Some procedures with reduced errors. *Mol. Phys.* **1970**, *19* (4), 553-566.

CHAPTER 3

SYNTHESIS OF MOLECULAR SALTS FROM A PYRIDYL *BIS*-UREA MACROCYCLE AND NAPHTHALENE-1,5-DISULFONIC ACID²

² **Som, B.;** Shue, J. R.; Smith, M. D.; Shimizu, L. S., Temperature-induced pseudopolymorphism of molecular salts from a pyridyl *bis*-urea macrocycle and naphthalene-1,5-disulfonic acid. *Acta Crystallographica Section C* **2018**, 74 (1), 75-81. Reprinted here with permission of publisher.

3.0 Abstract

Molecular salts, often observed as co-crystals, play an important role in pharmaceuticals and material science where salt formation is used to tune the properties of APIs and improve the stability of solid-state materials. Salt formation *via* proton transfer reaction typically alters hydrogen bonding motifs and influences supramolecular assembly patterns. In this chapter, we report molecular salts formed by a pyridyl *bis*-urea macrocycle (**1**) and naphthalene-1,5-disulfonic acid (H₂NDS) to afford two salt co-crystal solvates, **2** (H₂**1**²⁺·NDS²⁻·2DMSO) and **3** (H₂**1**²⁺·NDS²⁻·DMSO). This follows the ΔpK_a rule such that there is a proton transfer from the H₂NDS to (**1**) forming the molecular salts through hydrogen bonding. Prior to the salt formation, (**1**) is relatively planar and assembles in high fidelity to columnar structures. The salt co-crystal solvates were obtained upon slow cooling of dimethylsulfoxide-acetonitrile solutions of the molecular components at two temperatures (90 and 120 °C). The proton transfer to (**1**) significantly alters the macrocycle conformation, changing the formerly planar macrocycle into a step-shape conformation with *trans-cis* ureas in (**2**) or a bowl-shape conformation with *trans-trans* ureas in (**3**) respectively.

3.1 Introduction

Chemists employ non-covalent interactions including hydrogen and halogen bonding, ionic interactions, charge-transfer interactions (π-stacking), and van der Waals forces to engineer solid-state supramolecular materials and to probe structure-property relationships.¹⁻³ Efficient and high fidelity control of solid-state structure can directly impact applications in agrochemicals,⁴ optoelectronics,⁵⁻⁶ conductivity,⁷ and pharmaceuticals.⁸⁻⁹ To implement building blocks that present multiple hydrogen bond

donors and acceptors into organized supramolecular frameworks, one must consider the acidities of these groups, assess their propensity for proton transfer and evaluate the subsequent assembly of the into salts or co-crystals. Ureas and pyridines have been exploited extensively for crystal design. In the presence of acids, the pyridyl group can be protonated, generating a further hydrogen bond donor strong enough to compete with urea N-H groups. Herein, we evaluate the protonation of the pyridyl N atoms in the pyridyl *bis*-urea macrocycle (**1**), using naphthalene-1,5-disulfonic acid (H₂NDS) and report the structures of two DMSO-solvate salts (DMSO is dimethyl sulfoxide) formed upon slow cooling of the DMSO-acetonitrile solutions of the molecular components to room temperature (Figure 3.1).

Organic acids, such as carboxylic¹⁰, sulfonic¹¹ and phosphonic¹²⁻¹³ acids have been used in assembling multicomponent salts and co-crystals with basic amines and amides forming complex supramolecular architectures. In salts, a proton transfer occurs between the molecular components affording cations and anions, whereas the co-crystals typically contain only neutral molecules held together by non-covalent interactions. The formation of salt *versus* co-crystal involving these organic acids is governed by the ΔpK_a rule,¹⁴⁻¹⁵ where $\Delta pK_a = [pK_a(\text{base}) - pK_a(\text{acid})]$. According to this rule the difference of pK_a values should be at least 3 units for salt formation to occur. Control over the assembled structure is possible as these acids are directional in their reaction and subsequent recognition of N-containing basic building blocks.¹¹ Several researchers have predicted co-crystal or salt formation between carboxylic acids and pyridines using the ΔpK_a rule.¹⁵ For example, Price and co-workers have reported a series of crystal structures formed from simple

subsequent assembly of these salts and/or co-crystals. Naphthalene-1,5-disulfonic acid (H₂NDS) was selected for this study because of its acidity ($pK_a = -3.67, -2.64$)²⁰ and its rigid extended conjugated system, which present a contrast to the small alcohols evaluated previously. Macrocycle (**1**) has two possible sites for protonation with the pyridyl nitrogen being the more basic site ($pK_a \sim 6.60$ for the conjugate acid similar to 2,6-lutidine)²¹ *versus* the urea carbonyl ($pK_a \sim -3$, conjugate acid). As a chromophore, the optoelectronic properties of H₂NDS should be impacted by controlled organization into solid-state structures. Herein, we test if acid H₂NDS will: i) hydrogen bond to only the exterior O atoms of (**1**) to form alternating pillars of (**1**) and H₂NDS or ii) transfer its acidic protons to the pyridyl N atoms in (**1**) (ΔpK_a is 10.27) and form a salt. Specifically, we were interested in how the protonated pyridines induce conformational changes in the macrocycle and alter the assembly. The mono- and disolvated salts of (**1**) and H₂NDS *i.e.*, (**2**) and (**3**) (as determined by single crystal X-ray diffraction) were grown from 1:1/1:2 stoichiometric mixtures of **1** and H₂NDS dissolved in DMSO-acetonitrile solution (1/1.5, *v/v*) by slow cooling (Figure 3.1). The crystals were further characterized in the solid-state by FT-IR. These characterizations clearly showed the expected protonation of the *bis*-urea pyridyl macrocycle. However, the protonation gave rise to conformational changes in the macrocyclic system in both DMSO-solvated salts. The ionic species and solvent molecules that constituted these salts in the solid state are shown in (Figure 3.1).

3.2 Results and discussion

Herein, we investigated the ability of (**1**) to form salts with H₂NDS and analyzed the subsequent assembly of these building blocks into crystalline structures. Given the differences in their pK_a values ($\Delta pK_a \sim 10.3$), we expected that the acid H₂NDS should

transfer its acidic protons to the pyridyl N atoms in (**1**) and form a salt. This proton transfer alters the numbers of hydrogen-bond donors in (**1**), affording pyridinium N-H groups ($pK_a \sim 6.6$) in addition to the urea NH's. The protonated pyridines are expected to be the best hydrogen bond donor. In addition, multiple hydrogen bond acceptors are present including the sulfonate anions (NDS^{2-}), the urea carbonyl oxygen, and unprotonated pyridine nitrogens (if remaining). Favorable complementarity in terms of the pairing of hydrogen bond donors and acceptors as well as the similar size and rigidity of these building blocks, led us to investigate their co-crystallization. Macrocycle (**1**) and H_2NDS were mixed in 1:1 ratio and crystals were obtained by liquid assisted grinding (LAG) followed by slow cooling (at a rate of $1\text{ }^\circ\text{C/h}$) in DMSO-acetonitrile (1/1.5, v/v) solution from 120 or $90\text{ }^\circ\text{C}$ to room temperature respectively affording salt co-crystal solvate (**2**) and (**3**). Changing the ratio of the co-formers from 1:1 to 1:2 with an increasing amount of H_2NDS still only gave (**2**) and (**3**) when slow cooled from $120\text{ }^\circ\text{C}$ and $90\text{ }^\circ\text{C}$ respectively. Temperature appeared to be a key driving force for selecting a particular crystal form and varying the temperature during the co-crystallization process resulted in two salt co-crystal solvates that displayed different hydrogen bonding networks. The details of crystallographic data are listed in Table 3.1.

DMSO-solvated salt 2 ($H_2\mathbf{1}^{2+} \cdot NDS^{2-} \cdot 2DMSO$) was obtained from the 1:1 mixture of (**1**) and H_2NDS . A proton transfer occurred during this process from H_2NDS to the pyridine N3 of the macrocycle; this generates protonated pyridyl rings of the N_{py} -diprotonated pyridyl *bis*-urea macrocycle ($H_2\mathbf{1}^{2+}$) and one naphthalene-1,5-disulfonate (NDS^{2-}) anion. The unit cell contains one $H_2\mathbf{1}^{2+}$ and one NDS^{2-} anion, which are located on crystallographic inversion centers, as well as two DMSO molecules (Figure 3.2a).

Table 3.1 Crystallographic data and structure refinement parameters of salt co-crystals (2) and (3)

	2 (H ₂ 1 ²⁺ ·NDS ²⁻ ·2DMSO)	3 (H ₂ 1 ²⁺ ·NDS ²⁻ ·DMSO)
Empirical formula	C ₃₀ H ₃₈ N ₆ O ₁₀ S ₄	C ₂₈ H ₃₂ N ₆ O ₉ S ₃
Formula weight	770.90	692.77
Temperature/K	100(2)	200(2)
Crystal system	triclinic	monoclinic
Space group	P-1	P2 ₁ /c
a/Å	8.5763(4)	8.9076(4)
b/Å	9.7305(5)	25.5878(11)
c/Å	11.4194(5)	13.6411(6)
α/°	111.3790(10)	90
β/°	108.656(2)	105.644(2)
γ/°	93.040(2)	90
Volume/ Å ³	825.08(7))	2994.0(2)
Z	1	4
ρ _{calc} (g/cm ³)	1.552	1.537
μ/mm ⁻¹	0.356	0.314
F(000)	404.0	1448.0
Crystal size/mm ³	0.24 × 0.08 × 0.01	0.22 × 0.18 × 0.14
Radiation	MoKα (λ = 0.71073)	MoKα (λ = 0.71073)
2θ range/°	4.58 to 60.092	4.346 - 50.052
Index ranges	-12 ≤ h ≤ 12, -13 ≤ k ≤ 13, -16 ≤ l ≤ 16	-11 ≤ h ≤ 11, -32 ≤ k ≤ 32, -17 ≤ l ≤ 17
Reflections collected	24789	52398
Independent reflections	4807	6634
R _{int}	0.0272	0.0645
R _σ	0.0246	0.0336
No. of parameters	240	442
No. of restraints	0	0
GoF on F ²	1.047	1.029
Final R ₁ [I > 2σ (I)]	0.0343	0.0386
Final wR ₂ [I > 2σ (I)]	0.0870	0.0822
Final R ₁ [all data]	0.0439	0.0596
Final wR ₂ [all data]	0.0907	0.0906
Δρ min, max / e Å ⁻³	0.61/-0.41	0.48/-0.38

The pyridinium groups of H₂1²⁺ are excellent hydrogen bond donors and form the shortest hydrogen bond in the structure with DMSO acceptors (N⁺(H)····O distance = 2.773(2) Å). Figure 3.2b illustrates the NDS²⁻ dianion, which acts as a ditopic hydrogen bond acceptor using one oxygen atom on each sulfonate group to form hydrogen bonds that bridge two macrocycles through their urea NH groups with relatively long N(H)····O⁻ interactions of 3.229(2) Å forming a second 1D chain. The NDS²⁻ units are arranged along the *a*-axis in a parallel-displaced fashion at a distance of 8.576(4) Å indicating no π-π stacking interaction between the units. These weaker hydrogen bonding interactions join the anions to the

cation/solvent tapes, making a 2D network parallel to the crystallographic (011) plane as shown in the packing diagram (Figure 3.2c). Individual macrocycles are linked through hydrogen bonds to neighbouring macrocycles *via* an $R_2^2(8)$ hydrogen bond motif²²⁻²³ with an N(H)···O distance of 2.871(2) Å (Figure 3.3). This forms 1D chains of $(H_21^{2+})(DMSO)_2$ units along the *a*-axis direction, which is the dominant structural motif.

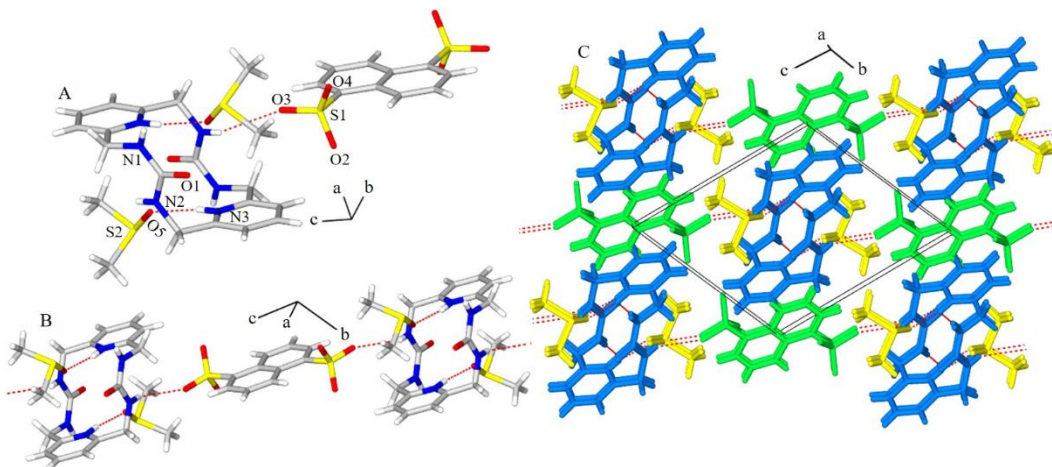


Figure 3.2 Views from the crystal structure of **2**. (A) Unit cell consists of one H_21^{2+} , one NDS^{2-} di-anion, and two DMSO molecules. (B) Illustration of the hydrogen bonded chains with alternating H_21^{2+} and NDS^{2-} . (C) Color-coded views of the crystal packing down the *a*-axis. H_21^{2+} in blue, NDS^{2-} in green, DMSO in yellow. Hydrogen bonds shown as dotted red lines.

Evidence of the proton transfer and $H_21^{2+} \cdot NDS^{2-} \cdot 2DMSO$ salt formation pronouncedly changes the assembly motif and structure of the macrocyclic units when compared to the known columns/pillars of the free (**1**), which is nearly planar and shows a *trans-trans* urea conformation.¹⁷ Upon protonation, the macrocycle adopts a step-shape conformation when viewed down the *a*-axis. Here, the urea groups adopted *trans-cis* conformations with the carbonyl groups pointing in opposite directions and parallel to each other (Figure 3.2a). The carbon-nitrogen (C-N and C=N) bond distances in the pyridyl groups of the macrocycle range from 1.345(17) to 1.359(16) Å with a C-N-C angle of 122.99(12)°, compared to 1.3397(17) to 1.3492(17). Å with a C-N-C angle of 118.16(11)° in the free

1.¹⁷ This slight increase in bond length and widening of bond angles is due to protonation of the nitrogen atom in the pyridyl groups of **1**. In the anion, the sulfur-oxygen bond lengths reflect the deprotonated SO₃⁻ moiety with S-O distances ranging from 1.4486(11) to 1.4611(11) Å.²⁴⁻²⁵ These changes in bond lengths and angles are indicative of the proton transfer between H₂NDS and (**1**).

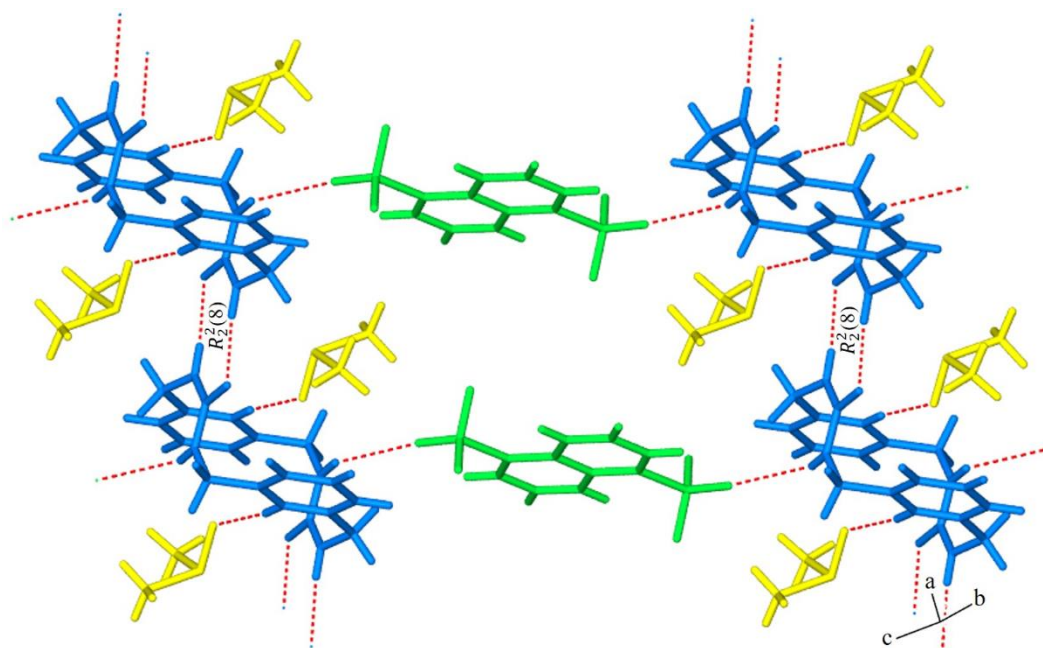


Figure 3.3 Hydrogen bonding network in the crystal structure of **2**. Macrocycles are connected in the *a*-axis direction via $R_2^2(8)$ hydrogen-bonded synthons. Dotted red lines represent hydrogen bonds.

Table 3.2 Geometrical data for hydrogen bonding in salt co-crystals **2** and **3**

Molecular salt	D	H	A	d(D-H)/Å	d(H-A)/Å	d(D-A)/Å	D-H-A/°	Symmetry codes
2	N1	H1	O1(<i>i</i>)	0.845(19)	2.029(19)	2.8712(15)	174.4(18)	(<i>i</i>) 2- <i>x</i> , 1- <i>y</i> , 1- <i>z</i>
	N2	H2	O3(<i>ii</i>)	0.85(2)	2.55(2)	3.2286(16)	136.9(17)	(<i>ii</i>) 1- <i>x</i> , 1- <i>y</i> , 1- <i>z</i>
	N3	H3	O5	0.86(2)	1.94(2)	2.7733(15)	163.0(2)	
3	N1	H1	O31(<i>i</i>)	0.82(2)	2.15(2)	2.892(2)	151.0(2)	(i) 1+ <i>x</i> , + <i>y</i> , + <i>z</i>
	N2	H2	O31(<i>i</i>)	0.84(2)	2.18(2)	2.940(2)	151.0(2)	
	N3	H3	O2	0.86(3)	2.14(3)	2.823(2)	136.0(2)	
	N3	H3	O11	0.86(3)	2.62(3)	2.851(2)	96.8(19)	
	N4	H4	O31	0.84(2)	2.04(2)	2.839(2)	158.0(2)	
	N5	H5	O31	0.83(2)	2.19(2)	2.934(2)	150.0(2)	
	N6	H6	O2	0.85(3)	2.37(3)	2.912(2)	122.0(2)	
	N6	H6	O21	0.85(3)	2.30(3)	2.833(2)	121.0(2)	

DMSO-solvated salt 3 ($\text{H}_2\mathbf{1}^{2+} \cdot \text{NDS}^{2-} \cdot \text{DMSO}$) was obtained as clusters of colorless wedge-shaped crystals, from which individual single crystals were cleaved apart for X-ray diffraction studies. The crystals visibly fractured when placed in the diffractometer cold stream at 100 K. Crystal integrity was maintained upon flash-cooling the crystals to 200 K, at which temperature data were collected. The temperature at which the material undergoes the crystallinity-destroying transition is not known. The asymmetric unit consists of one complete $\text{H}_2\mathbf{1}^{2+}$ cation, half each of two NDS^{2-} anions and one DMSO molecule (Figure 3.4a). Both NDS^{2-} anions are located on crystallographic inversion centers. Unlike (2), *DMSO-solvated salt 3* features both intramolecular and intermolecular hydrogen bonds. The macrocycle in the $\text{H}_2\mathbf{1}^{2+}$ cation adopts a bowl-shaped conformation compared to the step-shape observed in the previous structure. The bowl-shaped conformation (Figure 3.4b) is stabilized by intramolecular hydrogen bonding from the two pyridinium N-H groups to the urea carbonyl oxygen atoms with $\text{N}^+(\text{H}) \cdots \text{O}$ distances of 2.823(2) and 2.912(2) Å. The pyridinium N-H groups also form short contacts with the sulfonates of the NDS^{2-} anion with $\text{N}(\text{H}) \cdots \text{O}^-$ interactions of 2.833(2) and 2.851(2) Å. This forms 2D layers parallel to the crystallographic *ab* plane. The urea groups adopt the *trans-trans* conformation with their carbonyl groups pointing in opposite directions (Figure 4b). One of the carbonyl oxygens (O2) is pulled much farther into the macrocycle as a result of the intramolecular hydrogen bonding within the macrocycle while the other oxygen (O1) does not form any additional interactions (Figure 3.4c). The DMSO molecule plays an essential role by acting as an acceptor for all the urea NHs, forming four short interactions with $\text{N}(\text{H}) \cdots \text{O}$ ranging from 2.839(2) to 2.940(2) Å. This links the $\text{H}_2\mathbf{1}^{2+}$ cations into 1D chains along the *a*-axis (Figure 3.5a). Also the NDS^{2-} anion hydrogen

bonding forms 2D layers parallel to the crystallographic *ab* plane (Figure 3.5b). The hydrogen bond parameters found in both salts are shown in Table 3.2.

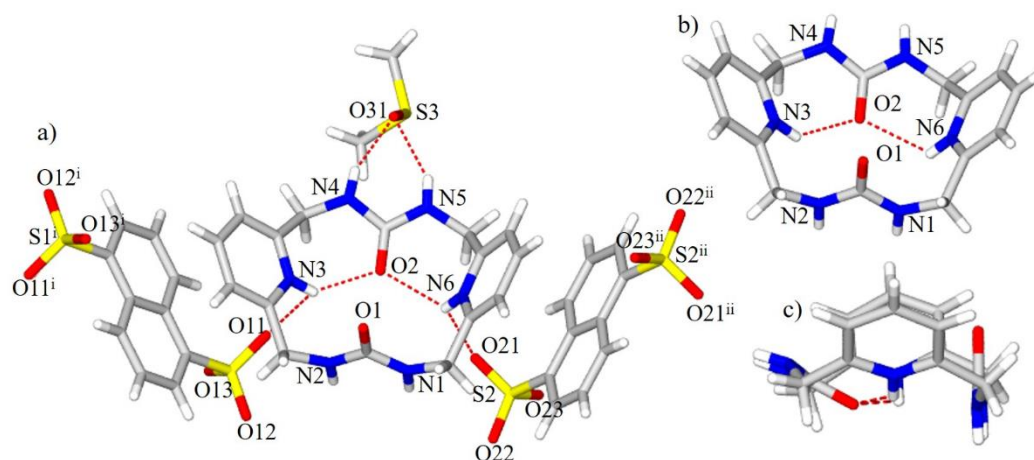


Figure 3.4 Views from the crystal structure of (3). (a) Salt (3) shows both intra and intermolecular hydrogen bonds. Displacement ellipsoids drawn at the 60% probability level. (b) Illustration of bowl shaped H_2I^{2+} cation highlighting intramolecular hydrogen bonds. (c) One of the urea carbonyl oxygen is pulled further into the macrocycle cavity due to intramolecular hydrogen bonding. Superscripts denote symmetry-equivalent atoms. Dotted red lines represent hydrogen bonds.

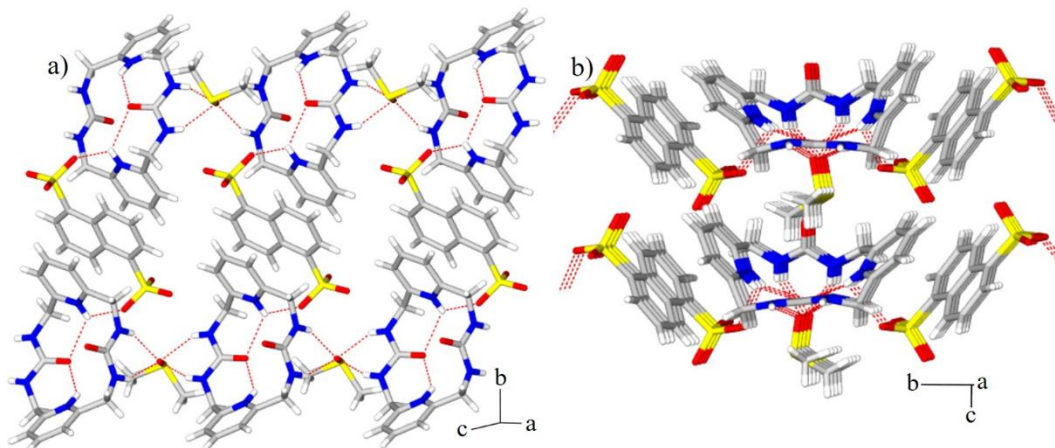


Figure 3.5 Packing diagrams of the crystal structure of (3). a) Role of DMSO as an acceptor of four hydrogen bonds involving all four urea NHs linking H_2I^{2+} cations into chains along the *a*-axis. b) [100] view of the packing. NDS²⁻ anion hydrogen bonding forms 2D layers parallel to the crystallographic *ab* plane. Dotted red lines represent hydrogen bonds.

We used solid-state FT-IR spectroscopy to probe the new hydrogen bonding interactions and protonation state changes in the DMSO-solvated salts looking for shifts in the key vibrational bands ($\nu_{\text{N-H}}$, $\nu_{\text{C=O}}$, and $\nu_{\text{C=N}}$) from the individual components (Figure S1 & Table

S1, ESI). There are multiple broad bands around 3400-2800 cm^{-1} which can be attributed to the N-H bands of the urea as well as new bands from the protonated pyridyl groups in the DMSO-solvated salts. There is a higher degree of broadening in this region of the DMSO-solvated salts spectra than the free macrocycle. The carbonyl stretching frequency in the free (**1**) shifts from 1650 cm^{-1} to 1671 cm^{-1} in DMSO-solvated salt (**2**), suggesting a stronger C=O bond in the salt. The shift to higher wavenumbers is expected as (**1**) forms columnar structures through hydrogen bonding where the urea N-H groups interacts with the urea carbonyl oxygen and the pyridine nitrogen, while (**2**) is assembled through amide type interactions, which use only one of the carbonyl oxygen lone pairs. Two carbonyl bands are observed for DMSO-solvated salt (**3**) at 1661 and 1688 cm^{-1} . These two distinct carbonyl peaks are attributed to the two different carbonyl groups observed in the single crystal X-ray diffraction data. The band at 1661 cm^{-1} likely corresponds to the carbonyl group that acts as an H-bond acceptor, while the band at 1688 cm^{-1} probably corresponds to the carbonyl group not involved in hydrogen bonding. Interestingly, this did not translate into significant changes in the C=O bond length, suggesting that IR is more sensitive to the hydrogen bonding network. According to the crystal structure data, the C=O bond length is 1.238(15) Å in (**1**), 1.243(16) Å in (**2**) and 2.224(2), 2.236(2) Å in salt (**3**). Also, the C=N stretching frequency shifted to slightly lower wavenumbers in the DMSO-solvated salts, indicating a slight weakening of these bonds as a result of protonating the pyridyl nitrogens. Other new bands are evident and are attributed to the characteristic sulfonate (SO_3^-) asymmetric and symmetric frequencies. The IR spectra show that the characteristic vibrations of $\nu_{\text{as}}(\text{SO}_3^-)$ in the DMSO-solvated salts are in the range of 1206-1175 cm^{-1} whereas $\nu_{\text{s}}(\text{SO}_3^-)$ stretching vibrations are in the range 1029-1022 cm^{-1} . These are

comparable to those of the sulfonic acid, which are observed around 1194-1118 cm^{-1} and 1063-914 cm^{-1} respectively.

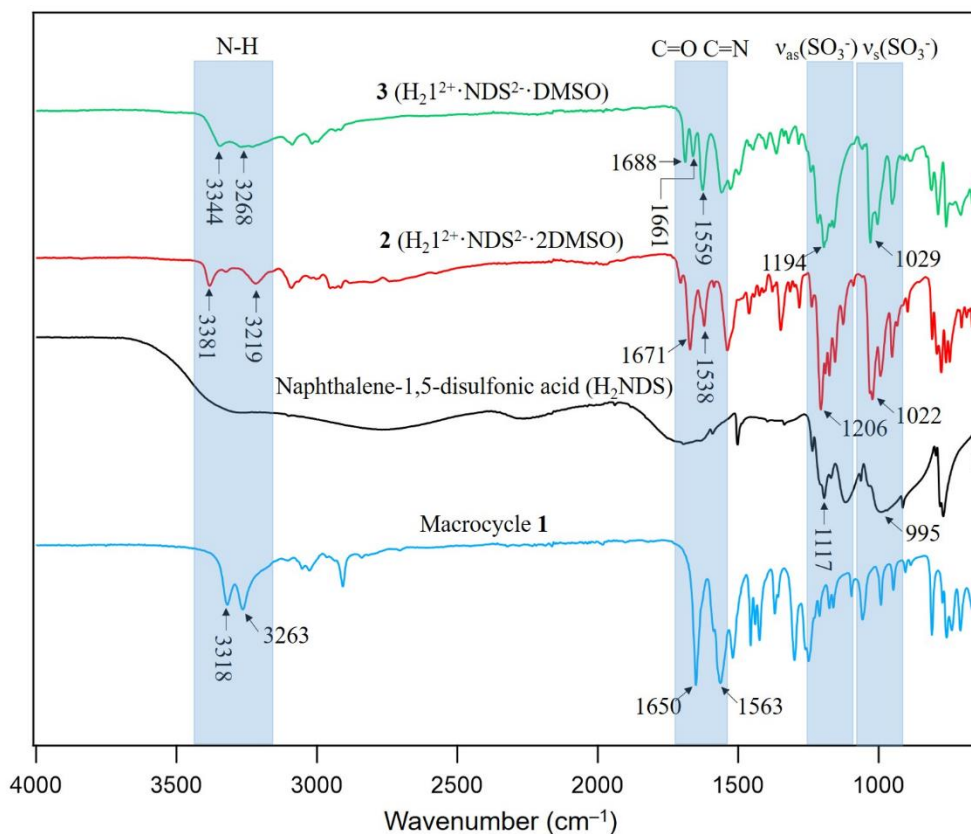


Figure 3.6. FT-IR profiles of co-formers (**1** & H_2NDS) and DMSO-solvated salts (**2** & **3**) in the range 4000–650 cm^{-1} .

3.3 Conclusion

In summary, two new DMSO-solvated salts were synthesized and their structures determined by single crystal X-ray diffraction and FT-IR. These two molecular salts were obtained by crystallization at two different temperatures (90 and 120 °C). As expected from ΔpK_a values, DMSO-solvated salts were obtained. Protonation of both pyridyl nitrogens of macrocycle (**1**) altered its conformation and disrupted the columnar assembly that is typically observed in the free macrocycle. This gave rise to two different macrocycle conformers, step-shaped and bowl-shaped, that exhibited different hydrogen bonding patterns. Both salts contain the same number of diprotonated pyridyl *bis*-urea macrocycle

(H₂1²⁺) cations and naphthalene-1,5-disulfonate (NDS²⁻) anions but differ in the number of solvent molecules. Both new structures display unsatisfied lone pairs on the macrocyclic carbonyl oxygen of (1), which could be employed to direct further assembly in more complex molecular salts.

3.4 Experimental

Pyridyl *bis*-urea macrocycle (1) was synthesized as reported previously.¹⁷ All other reagents and naphthalene-1,5-disulfonic acid (H₂NDS) were purchased from Sigma-Aldrich and VWR respectively, and used as received. ¹H NMR were recorded on a Varian Mercury/VX 300 NMR spectrometer. FT-IR spectra were recorded on a Perkin Elmer Spectrum 100 FT-IR Spectrometer over the range 4000–650 cm⁻¹ at a spectral resolution of 4 cm⁻¹ and 32 scans per sample.

3.4.1 Preparation of salt solvates (2) and (3)

Macrocycle (1) (5.0 mg, 0.015 mmol) and naphthalene-1,5-disulfonic acid (8.8 mg, 0.031 mmol) were weighed into a small mortar with a drop of DMSO and ground for 20 mins. The DMSO was then allowed to dry and the mixture ground a second time (20 mins). The fine powdered mixture was dissolved in DMSO-acetonitrile solution (1/1.5, *v/v*) in a pressure tube at 120 °C (**Method 1**) and slowly cooled to room temperature at 1 °C/h to afford colorless prism-shape crystals (2) suitable for X-ray diffraction in 4-5 days. **Method 2**, the fine powdered mixture was dissolved in DMSO-acetonitrile solution (1/1.5, *v/v*) in a pressure tube at heating at 90 °C then slowly cooled to room temperature at 1 °C/h resulting in another salt co-crystal (3) that was also characterized by single crystal X-ray diffraction. Using equimolar amounts of the co-formers gave the same crystals as the 1:2 molar mixtures. Both crystal forms decompose at 285 °C.

3.4.2 X-ray Crystal Structure Determination

Molecular salt 2 [(C₁₆H₂₀N₆O₂)(C₁₀H₆O₆S₂)(C₂H₆SO)₂]. X-ray intensity data from a colorless triclinic prism were collected at 100(2) K using a Bruker D8 QUEST diffractometer equipped with a PHOTON 100 CMOS area detector and an Incoatec microfocus source (Mo K α radiation, $\lambda = 0.71073 \text{ \AA}$).²⁶ The raw area detector data frames were reduced and corrected for absorption effects using the SAINT+ and SADABS programs.²⁶ Final unit cell parameters were determined by least-squares refinement of 9898 reflections taken from the data set. The structure was solved by direct methods with SHELXT.² Subsequent difference Fourier calculations and full-matrix least-squares refinement against F^2 were performed with SHELXL-2014²⁷⁻²⁸ using OLEX2.²⁹

The compound crystallizes in the triclinic system. The space group $P-1$ (No. 2) was confirmed by structure solution. The asymmetric unit consists of half of one C₁₆H₂₀N₆O₂²⁺ cationic cycle, half of one naphthalene-1,5-disulfonate (C₁₀H₆O₆S₂²⁻) anion and one DMSO molecule. The cycle and naphthalene-1,5-disulfonate species are located on crystallographic inversion centers. All non-hydrogen atoms were refined with anisotropic displacement parameters. Hydrogen atoms bonded to carbon were located in Fourier difference maps before being placed in geometrically idealized positions included as riding atoms with $d(\text{C-H}) = 0.95 \text{ \AA}$ and $U_{\text{iso}}(\text{H}) = 1.2U_{\text{eq}}(\text{C})$ for aromatic hydrogen atoms, $d(\text{C-H}) = 0.99 \text{ \AA}$ and $U_{\text{iso}}(\text{H}) = 1.2U_{\text{eq}}(\text{C})$ for methylene hydrogen atoms and $d(\text{C-H}) = 0.98 \text{ \AA}$ and $U_{\text{iso}}(\text{H}) = 1.5U_{\text{eq}}(\text{C})$ for methyl hydrogens. The methyl hydrogens were allowed to rotate as a rigid group to the orientation of maximum observed electron density. Hydrogen atoms bonded to nitrogen were located in difference maps and refined freely. The largest

residual electron density peak in the final difference map is 0.61 e-/Å³, located 0.71 Å from S1.

Molecular salt 3 [(C₁₆H₂₀N₆O₂)(C₁₀H₆O₆S₂)(C₂H₆SO)]. Crystals formed as clusters of colorless wedge-shaped crystals, from which individual single crystals were cleaved apart. The crystals visibly fractured when placed in to the diffractometer cold stream at 100 K. Crystal integrity was maintained upon flash-cooling the crystals to 200 K, at which temperature data were collected. The temperature at which the material undergoes the crystallinity-destroying transition is not known. X-ray intensities were measured using a Bruker D8 QUEST diffractometer equipped with a PHOTON-100 CMOS area detector and an Incoatec microfocus source (Mo K α radiation, $\lambda = 0.71073$ Å). The raw area detector data frames were reduced and corrected for absorption effects using the Bruker APEX3, SAINT+ and SADABS programs.³⁰⁻³¹ Final unit cell parameters were determined by least-squares refinement of 9930 reflections taken from the data set. The structure was solved with SHELXT.^{28, 32} Subsequent difference Fourier calculations and full-matrix least-squares refinement against F^2 were performed with SHELXL-2017^{28, 32} using OLEX2.²⁹

The compound crystallizes in the monoclinic system. The pattern of systematic absences in the intensity data was consistent with the space group $P2_1/n$, which was confirmed by structure solution. The asymmetric unit consists of one complete C₁₆H₂₀N₆O₂²⁺ cation, half each of two C₁₀H₆O₆S₂²⁻ anions and one C₂H₆SO molecule. Both C₁₀H₆O₆S₂⁻ anions are located on crystallographic inversion centers. All non-hydrogen atoms were refined with anisotropic displacement parameters. Hydrogen atoms bonded to carbon were located in Fourier difference maps before being placed in geometrically

idealized positions and included as riding atoms with $d(\text{C-H}) = 0.95 \text{ \AA}$ and $U_{\text{iso}}(\text{H}) = 1.2U_{\text{eq}}(\text{C})$ for aromatic hydrogen atoms, $d(\text{C-H}) = 0.99 \text{ \AA}$ and $U_{\text{iso}}(\text{H}) = 1.2U_{\text{eq}}(\text{C})$ for methylene hydrogen atoms, and $d(\text{C-H}) = 0.98 \text{ \AA}$ and $U_{\text{iso}}(\text{H}) = 1.5U_{\text{eq}}(\text{C})$ for methyl hydrogens. The methyl hydrogens were allowed to rotate as a rigid group to the orientation of maximum observed electron density. The six unique hydrogen atoms bonded to nitrogen were located in difference maps and refined freely. The largest residual electron density peak in the final difference map is 0.48 e-/\AA^3 , located 1.01 \AA from C31.

3.5 References

1. Aakeröy, C. B.; Beatty, A. M.; Helfrich, B. A., "Total Synthesis" Supramolecular Style: Design and Hydrogen-Bond-Directed Assembly of Ternary Supermolecules. *Angew. Chem. Int. Ed.* **2001**, *40* (17), 3240-3242.
2. Desiraju, G. R., Crystal Engineering: A Holistic View. *Angew. Chem. Int. Ed.* **2007**, *46* (44), 8342-8356.
3. Hosseini, M. W., Molecular Tectonics: From Simple Tectons to Complex Molecular Networks. *Acc. Chem. Res.* **2005**, *38* (4), 313-323.
4. Powell, K. A.; Croker, D. M.; Rielly, C. D.; Nagy, Z. K., PAT-based design of agrochemical co-crystallization processes: A case-study for the selective crystallization of 1:1 and 3:2 co-crystals of p-toluenesulfonamide/triphenylphosphine oxide. *Chem. Eng. Sci.* **2016**, *152*, 95-108.
5. Anthony, S. P.; Varughese, S.; Draper, S. M., Switching and tuning organic solid-state luminescence via a supramolecular approach. *Chem. Commun.* **2009**, (48), 7500-7502.

6. Yan, D.; Delori, A.; Lloyd, G. O.; Friščić, T.; Day, G. M.; Jones, W.; Lu, J.; Wei, M.; Evans, D. G.; Duan, X., A Cocrystal Strategy to Tune the Luminescent Properties of Stilbene-Type Organic Solid-State Materials. *Angew. Chem. Int. Ed.* **2011**, *50* (52), 12483-12486.
7. Goud, N. R.; Matzger, A. J., Impact of Hydrogen and Halogen Bonding Interactions on the Packing and Ionicity of Charge-Transfer Cocrystals. *Crystal Growth & Design* **2017**, *17* (1), 328-336.
8. Schultheiss, N.; Newman, A., Pharmaceutical Cocrystals and Their Physicochemical Properties. *Crystal Growth & Design* **2009**, *9* (6), 2950-2967.
9. Bolla, G.; Nangia, A., Pharmaceutical cocrystals: walking the talk. *Chem. Commun.* **2016**, *52* (54), 8342-8360.
10. Ivasenko, O.; Perepichka, D. F., Mastering fundamentals of supramolecular design with carboxylic acids. Common lessons from X-ray crystallography and scanning tunneling microscopy. *Chem. Soc. Rev.* **2011**, *40* (1), 191-206.
11. Du, M.; Jiang, X.-J.; Tan, X.; Zhang, Z.-H.; Cai, H., Co-crystallization of a versatile building block 4-amino-3,5-bis(4-pyridyl)-1,2,4-triazole with R-isophthalic acids (R = -H, -NH₂, -SO₃H, and -COOH): polymorphism and substituent effect on structural diversity. *CrystEngComm* **2009**, *11* (3), 454-462.
12. Kong, D.; Yao, J.; Clearfield, A.; Zon, J., Hydrogen-Bonded Structures Formed from the Reaction of 1,3,5-Benzene-triphosphonic Acid and Adamantane. *Crystal Growth & Design* **2008**, *8* (8), 2892-2898.

13. Lie, S.; Maris, T.; Wuest, J. D., Molecular Networks Created by Charge-Assisted Hydrogen Bonding in Phosphonate, Phosphate, and Sulfonate Salts of *Bis*(amidines). *Crystal Growth & Design* **2014**, *14* (7), 3658-3666.
14. Cruz-Cabeza, A. J., Acid-base crystalline complexes and the pKa rule. *CrystEngComm* **2012**, *14* (20), 6362-6365.
15. Lemmerer, A.; Govindraj, S.; Johnston, M.; Motloun, X.; Savig, K. L., Co-crystals and molecular salts of carboxylic acid/pyridine complexes: can calculated pKa's predict proton transfer? A case study of nine complexes. *CrystEngComm* **2015**, *17* (19), 3591-3595.
16. Mohamed, S.; Tocher, D. A.; Vickers, M.; Karamertzanis, P. G.; Price, S. L., Salt or Cocrystal? A New Series of Crystal Structures Formed from Simple Pyridines and Carboxylic Acids. *Crystal Growth & Design* **2009**, *9* (6), 2881-2889.
17. Roy, K.; Wang, C.; Smith, M. D.; Dewal, M. B.; Wibowo, A. C.; Brown, J. C.; Ma, S.; Shimizu, L. S., Guest induced transformations of assembled pyridyl *bis*-urea macrocycles. *Chem. Commun.* **2011**, *47* (1), 277-279.
18. Roy, K.; Wibowo, A. C.; Pellechia, P. J.; Ma, S.; Geer, M. F.; Shimizu, L. S., Absorption of Hydrogen Bond Donors by Pyridyl *Bis*-Urea Crystals. *Chem. Mater.* **2012**, *24* (24), 4773-4781.
19. Som, B.; Salpage, S. R.; Son, J.; Gu, B.; Karakalos, S. G.; Smith, M. D.; Shimizu, L. S., Pillars of assembled pyridyl *bis*-urea macrocycles: a robust synthon to organize diiodotetrafluorobenzenes. *CrystEngComm* **2017**, *19* (3), 484-491.
20. Xu, Y.; Jiang, L.; Mei, X., Supramolecular structures and physicochemical properties of norfloxacin salts. *Acta Crystallographica Section B* **2014**, *70* (4), 750-760.

21. Groenenboom, M. C.; Saravanan, K.; Zhu, Y.; Carr, J. M.; Marjolin, A.; Faura, G. G.; Yu, E. C.; Dominey, R. N.; Keith, J. A., Structural and Substituent Group Effects on Multielectron Standard Reduction Potentials of Aromatic N-Heterocycles. *The Journal of Physical Chemistry A* **2016**, *120* (34), 6888-6894.
22. Bernstein, J.; Davis, R. E.; Shimoni, L.; Chang, N.-L., Patterns in Hydrogen Bonding: Functionality and Graph Set Analysis in Crystals. *Angewandte Chemie International Edition in English* **1995**, *34* (15), 1555-1573.
23. Etter, M. C.; MacDonald, J. C.; Bernstein, J., Graph-set analysis of hydrogen-bond patterns in organic crystals. *Acta Crystallographica Section B* **1990**, *46* (2), 256-262.
24. Deng, Z.-P.; Huo, L.-H.; Zhao, H.; Gao, S., A Co-Crystal Strategy to Tune the Supramolecular Patterns and Luminescent Properties: Ten Well-Designed Salts Assembled by Arenedisulfonic Acid with Diverse Diamines. *Crystal Growth & Design* **2012**, *12* (6), 3342-3355.
25. Gaytán-Barrientos, N. S.; Morales-Morales, D.; Herrera-Ruiz, D.; Reyes-Martínez, R.; Rivera-Islas, J., Sulfonate salts of the therapeutic agent dapsone: 4-[(4-aminophenyl)sulfonyl]anilinium benzenesulfonate monohydrate and 4-[(4-aminophenyl)sulfonyl]anilinium methanesulfonate monohydrate. *Acta Crystallographica Section C: Structural Chemistry* **2016**, *72* (4).
26. APEX2 Version 2014.9-0, SAINT+ Version 8.34A and SADABS Version 2014/4. Bruker Analytical X-ray Systems, Inc., Madison, Wisconsin, USA, 2014.
27. Sheldrick, G., A short history of SHELX. *Acta Crystallographica Section A* **2008**, *64* (1), 112-122.

28. Sheldrick, G., SHELXT - Integrated space-group and crystal-structure determination. *Acta Crystallographica Section A* **2015**, *71* (1), 3-8.
29. Dolomanov, O. V.; Bourhis, L. J.; Gildea, R. J.; Howard, J. A. K.; Puschmann, H., OLEX2: a complete structure solution, refinement and analysis program. *J. Appl. Crystallogr.* **2009**, *42* (2), 339-341.
30. APEX3 Version 2016.5-0 and SAINT+ Version 8.37A. Bruker AXS, Inc., Madison, Wisconsin, USA, 2016.
31. Krause, L.; Herbst-Irmer, R.; Sheldrick, G. M.; Stalke, D., Comparison of silver and molybdenum microfocus X-ray sources for single-crystal structure determination. *J. Appl. Crystallogr.* **2015**, *48* (1), 3-10.
32. Sheldrick, G., Crystal structure refinement with SHELXL. *Acta Crystallographica Section C* **2015**, *71* (1), 3-8.

CHAPTER 4

ABSORPTION OF FLUORESCENT DYES BY A SELF-ASSEMBLED PHENYLETHYNYLENE *BIS*-UREA MACROCYCLIC HOST³

³ Parts of this chapter are published in *The Journal of Physical Chemistry C* **2017**, *121* (33), 18102-18109.

4.0 Abstract

Host-guest complexes have attracted much attention in supramolecular chemistry for their optoelectronic applications. This is especially true for confined dye molecules in 1-dimensional (1D) channels, where encapsulation typically modulates the optical properties of the individual dyes. Herein, we investigated the loading of a small dye, 5-(dimethylamino)-5'-nitro-2,2-bithiophene, into 1D channels of self-assembled phenylethyneylene *bis*-urea macrocyclic host. In particular, we were interested in understanding how the guest is aligned inside the host and how the binding alters the overall properties of the host-guest complex. The complex was prepared by soaking the crystalline host in an acetonitrile solution of the dye for 24 hours to give a purple solid. This complex was then characterized by ^1H NMR, UV-visible absorption and fluorescence emission spectroscopies, and wide-angle X-ray scattering. The guest alignment studies were carried out in collaboration with Dr. Vitaly Rassalov, Dr. Andrew B. Greytak and graduate student Preecha Kittikhunnatham using linear polarization fluorescence microscopy and time-dependent density functional theory (TDDFT) calculations at the B3LYP/TZ2P level of theory. The guest fluorescence was shown to be polarized along the fiber axis with emission polarization values up to 0.729, indicating a high degree of orientational order within the 1D channels. The observed behavior is consistent with calculated results for the guest orientation and electronic transition dipole moment. The results indicate the value of functional fluorescent probes as a measure of guest confinement in low-dimensional environments.

4.1 Introduction

A host with a one-dimensional (1D) channel imposes a strict arrangement upon the guest molecules and facilitates the impacts of structural constraints on the chemical and photophysical properties of the guest.¹⁻² The incorporation of dyes into channels generates new highly functional composite materials with altered photophysics.³ Encapsulation of dye molecules inside the channels enhances their stability and, in many cases, prevents aggregation and fluorescence quenching. Often molecular orientation measurements,⁴⁻⁵ photosensitization, and diffusion experiments⁶⁻⁸ of the dye molecules can be carried out inside the channels. The absorption and diffusion of guest molecules into pores and channels are influenced by size-selective and chemical environment processes that generate new host-guest species or complexes. Simple 1D hosts are ideal for probing these process as they are readily modeled and display two entrances that can be opened or closed with no nodes or branching.⁹ The field of dye-host composite materials has been dominated by inorganic host systems such as zeolites and metal-organic frameworks (MOFs). In comparison, few crystalline organic materials have been employed. Of these, perhydrotriphenylene (PHTP) and tris(o-phenylenedioxy)cyclotriphosphazene (TPP) display 1D channels with diameters ranging from 4.5 – 5.0 Å¹⁰⁻¹² and have been shown to act as ordering nanocontainers giving different organizational patterns of guest molecules (particularly dyes) in their channels.¹³ These ordered hybrid materials display highly anisotropic responses to light, which is a vital property for their use in non-linear optics (NLO) applications such as second harmonic generation, dichroic filters, and light waveguides.¹⁴

In this chapter, we focus on screening small organic dyes as guests for the 1D channels of nanoporous host prepared by the crystallization of phenylethyne *bis*-urea macrocycle **1**. Our goal is to investigate the effects of encapsulation on these dyes and to develop methods to monitor the orientation of these dyes inside the channels. In particular, we are interested in understanding the structure of the encapsulated complexes and correlating this structure with the changes in the photophysical properties before and after encapsulation. Also of interest is to identify the important host–guest interactions that contribute to the structure of dye-host complexes. A key requirement for systematically influencing properties and reactivity that one is able to control supramolecular organization of guests within these confined nanochannels.

Bis-urea **1** self-assembles by slow cooling from DMSO to give needle-like single crystals.¹⁵ According to X-ray diffraction analysis (Figure 4.1), the macrocycles self-assemble into columnar structures by bifurcated urea-urea hydrogen bonding with each column enclosing a 1D channel. The solvent of crystallization (DMSO) is always retained in these 1D channels. Activation by heating removes the included DMSO to generate host **2** with accessible pore openings of $\sim 9 \text{ \AA}$ in diameter (Figure 4.1 b-c). Shimizu's group has demonstrated that this host can absorb a variety of guest molecules from organic solvents (hexane, dichloromethane and acetonitrile) to afford solid state host-guest complexes. Upon UV-irradiation, the encapsulated guests can undergo reactions. Subsequent sonication of the crystalline complexes in dichloromethane or chloroform releases the products. Using such a protocol, the group demonstrated stereoselective photodimerization of encapsulated coumarins, chromones, and acenaphthalene.¹⁶⁻¹⁷ These studies showed that host **2** is able to direct the organization of guest molecules inside its

channels. In this case the reactive guests were bound in close proximity within the channels satisfying the geometric requirements needed to enable such photodimerization reactions. The coumarins (coumarin, 6- and 7-methyl coumarin) were found to selectively form the *anti*-HH photodimers with a good-to-excellent selectivity of 84-97%.¹⁶ Chromone and 6-fluorochromone on the other hand afforded the *anti*-HT photodimers in 87-99% selectivity.¹⁷ These reactions in confinement are remarkable not only for their selectivity, since some of these guest molecules are unreactive in the solid-state by themselves. These studies demonstrate that guests are organized within the 1D channels of host **2**.

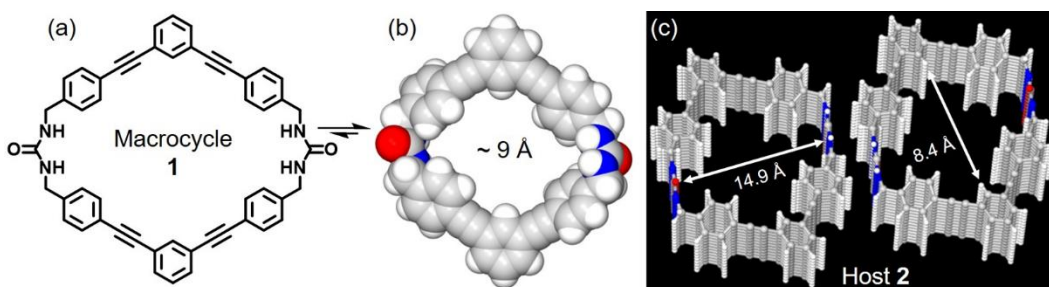


Figure 4.1 Self-assembled phenylethynylene *bis*-urea macrocycle. (a) Chemical structure of phenylethynylene *bis*-urea macrocycle **1**; (b) space filling model of single macrocycle from X-ray structure. (c) view down the *b* axis of self-assembled host **2**. The solvent (DMSO) in the structure was omitted for clarity.

In this work, we studied the uptake and orientation as well as the effect of confinement on the spectral and new photophysical properties of fluorescent dyes in a 1D nanoporous phenylethynylene *bis*-urea macrocyclic host (**2**). A number of relatively small, linear dyes (Figure 4.2a) were screened for absorption into the columnar channels of the host including 7-dimethylamino-4-methylcoumarin (**3**), 7-amino-4-methylcoumarin (**4**), acridine yellow (**5**) and 5-(dimethylamino)-5'-nitro-2,2'-bithiophene (**6**). Coumarins (**3-4**) have widespread applications, especially in industrial use as dye lasers.¹⁸ Acridine yellow on the other hand is usually used in biological systems as a fluorescent stain or fluorescent probe. Bithiophene dye (**6**) was provided by Prof. Frank Wuerthner's group and shows

distinct solvatochromism, which is the ability of a chemical substance to change color due to a change in solvent polarity.¹⁹ These dyes present different backbones, dimensions, substituents and polarity (Table 4.1) and enable us to probe the following questions: 1) What dyes load into the channels of **2**? 2) Are the photophysical properties of the dyes modulated within the host-guest complex? 3) How are the dye molecules arranged inside the host channels? (Figure 4.2b). The dyes were loaded into the host from solution (degassed acetonitrile) where the activated host **2** crystals were soaked in the dye solution overnight. All the dyes except for **4** have their long axes larger than the host channel inner diameter. This varying molecular dimensions and polarity of the guest can lead to different organizations of the guest inside host **2** channels (Figure 4.2b). The pink oval with double headed arrow as shown in Figure 4.2 represents the electronic transition dipole moment (ETDM) of the guest dyes. Valuable information can be obtained experimentally through optical spectroscopy or by advanced fluorescence microscopy techniques which are related to the orientation of the ETDM of the molecules with respect to host channel axis.

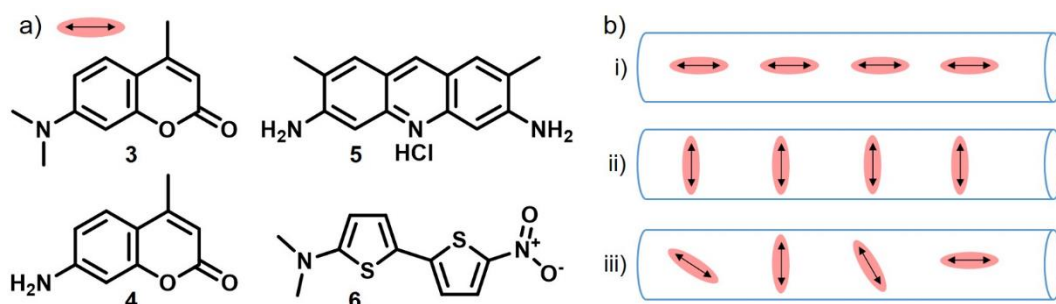


Figure 4.2 Guest molecules and possible arrangements inside host **2** channels. a) Guest molecules. (b) Three of many possible orientations of molecules in 1D channels. (i) Orientation of molecules which align their ETDM parallel and (ii) perpendicular to the channel axis. (iii) Representative orientations of molecules with different packing.

Table 4.1 Molecular dimensions and polarity of guests.

Guest	Dimensions (Å)	Volume (Å ³)	Polarity (D)	CSD reference code
3	9.20 x 4.30	260.02	5.34 ²⁰	ZENMAG
4	7.85 x 4.80	211.25	6.8 ²¹	WIKDEZ
5	11.88 x 5.42		6.33 ²²	
6	11.70 × 3.50	281.14	7.95	YAPMEH

The dimensions (estimated) of **3**, **4** and **6**, and the volume were obtained from data available on the Cambridge Structural Database (CSD). The dimensions of dye **5** were estimated in Spartan. Polarity values were taken from literature.

Using ¹H NMR we found that only the bithiophene dye (**6**) successfully loaded into the 1D channels of host **2**. After initial characterization of the host-guest complex **7** by NMR, diffuse reflectance and fluorescence spectroscopic techniques, fluorescence lifetime and wide-angle X-ray scattering (WAXS), we investigated the guest orientations inside the host by computational and fluorescence polarization methods in collaboration with Dr. Vitaly Rassalov, Dr. Andrew B. Greytak and his graduate student Preecha Kittikhunnatham. These further studies helped us determine the guest orientation inside the channel. The fluorescence intensity of the guest molecules with linearly or plane polarized transition dipoles varies depending on the orientation of the guest electronic transition dipole moments with respect to the polarization of the excitation light and/or emission filter. This technique has been used to study guests in both organic and inorganic hosts as well as in biological complexes.^{4, 23-24} Key features of this technique are its sensitivity and high spatial resolution, which provide relevant information about the host-guest complex even for small single crystals.

4.2 Results and discussion

The phenylethynylene *bis*-urea macrocycle (**1**), is made up of two rigid C-shaped phenylethynylene spacers linking two urea motifs which self-assembles by slow cooling from DMSO to give needle-like (fiber-like) single crystals. X-ray diffraction demonstrates that the self-assembly consists of macrocycles stacked in a columnar fashion with each column enclosing a 1D channel. The encapsulated solvent can be removed without collapsing the assembly structure. These channels can then be reloaded with different guests. Figure 4.3a shows the columns in which the *bis*-urea macrocycles are held together by three centered urea hydrogen bonds. Additional stabilization was provided by edge to face aryl stacking and by stacking interactions between the alkyne and the phenyl on the neighboring macrocycle.¹⁵

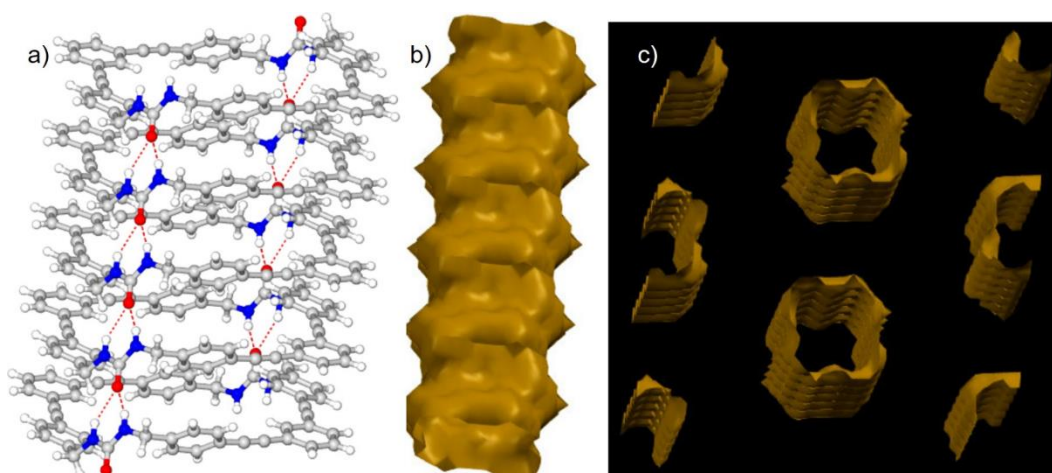


Figure 4.3 1D channels extended along the crystallographic b axis of host **2**. (a) Self-assembly of phenylethynylene *bis*-urea macrocycle **1** affords columns that are held together through the urea hydrogen-bonding motif (solvents of crystallization are omitted). (b) A representation of the interior channel surface of a single column of host **2** along the b-axis. (c) A similar top view of the interior channel surface looking down the b-axis of host **2**.

The pore space in host **2** columns is almost round with a cross-sectional diameter of $\sim 9 \text{ \AA}$.

Figure 4.3 b-c shows the void space in the columns after removal of the solvent of crystallization, the calculated void volume is 491.1 \AA^3 per unit cell (21% of the total unit

cell volume).¹⁵ The 1D channels are separated by a distance of ~9 - 10 Å, which can ensure lateral and electronic separation of guests. Interior of the channel in host **2** is lined with aromatic groups and polar urea groups providing a suitable environment to absorb guests with varying polarity and complementary size.

In this study, guest molecules were selected based on their sizes (Table 4.1 shown above). The coumarin molecules were of interest based on previous loading of similar coumarin derivatives into host **2**. The other two dyes **5** and **6** were selected since they have long axis greater than the channel diameter of host **2**. Initial attempts were made to simulate the loading of these guests into host **2** using the Monte Carlo for complex chemical systems (MCCCS) towhee plug-in built into Scienomics' materials processes and simulations (MAPS) platform. Calculations with guest **3-5** failed several times and were discontinued however some success was made with dye **6**. Here, we saw insertion of dye **6** into the channels of host **2** (Figure 4.4). The dye appears to align its long axis along the channel axis as was expected. In most of the channels, the dyes are ordered in a head to tail fashion and the dye distribution was not uniform in all the channels. Figure 4.4 shows the ordering of the dye (space filling model) in a single column channel and the energy minimization profile during the simulation. The energy minimization in this case went from a lower value to a higher value without reaching a plateau, which is the opposite of previous reports where the simulations were carried out with some coumarin derivatives. This is because the insertion of the dye molecules into the host takes a longer time and each insertion increases the energy, requiring a much longer run time for it to stabilize to lower energies.

Additionally, Dr. Vitaly Rassalov carried out DFT using crystal structure data of the host and guest. The guest geometry was optimized at the PBEsol-D3/DZP level,

keeping the host geometry frozen. Next he carried out a TDDFT calculation at the B3LYP/TZ2P level to confirm the orientation of the lowest-energy electronic transition dipole moment (ETDM) in the guest. These calculations indicate that the guest molecule **6** is aligned approximately parallel to the host channel axis and that a minimum of four macrocycles are needed to fully encapsulate one dye molecule.²⁵ These results are similar to our Grand Canonical Monte Carlo (GCMC) simulations. Both suggest that the guest molecule is slightly off center due to favorable interactions with the host sidewalls. In comparison to guests previously loaded into host **2**, the bithiophene dye **6** is more polar (7.95 D) and has a longer molecular axis. Based on the simulation and computation done, about 4-5 macrocycles are needed to completely encapsulate one dye **6** molecule. Quantification of the host:guest ratio by ¹H NMR gave ~ 11:1. This suggests that only 50% of host **2** channels were occupied the guest dye **6**.

4.2.1 Host 2 preparation and activation

Macrocycle **1** was synthesized according to literature procedure¹⁵ and recrystallized from DMSO (50 mg / 10 mL) using a slow cooling from 120 to 25 °C to give microcrystalline needles (host **2**). The recrystallized host **2** usually have encapsulated solvent in its channels after the crystallization process. The solvent was removed by TGA to afford the empty host **2** (activated). Our experimental findings suggest that the activated host the same structure as the DMSO filled host and is assembled through bifurcated hydrogen bonding of the urea groups.¹⁵ The TGA showed a two-step desorption curve corresponding to a total weight loss 14%; 9.1% weight loss between 30 and 80 °C, and 4.9 % between 80 and 130 °C (Figure 4.5a).

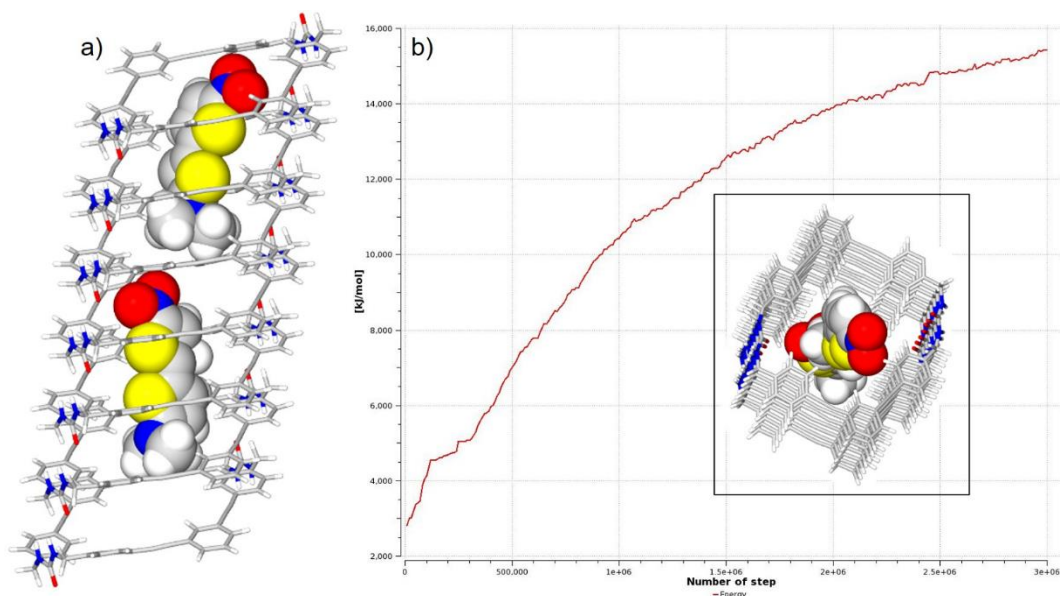


Figure 4.4 GCMC simulation outcome of host-guest complex **7**. a) Arrangement of dye **6** molecules along the channel axis of a single column. b) Energy minimization profile during the simulation with a picture insert showing the top view of the channel along the y axis.

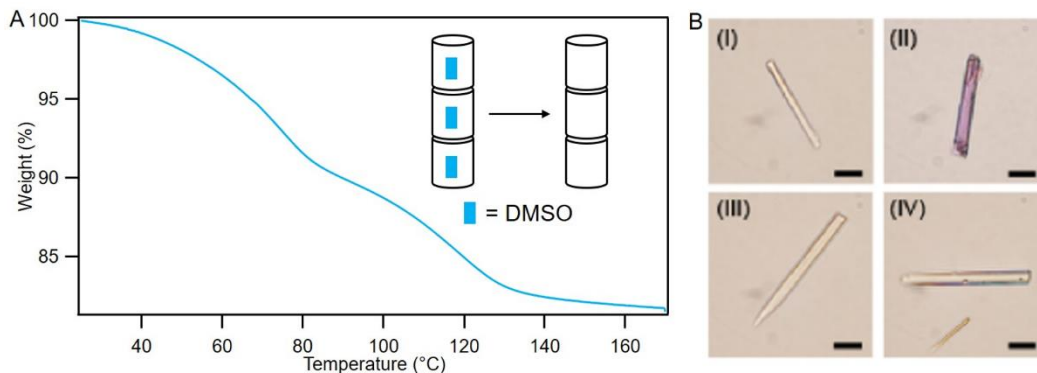


Figure 4.5 Host **2** activation and the sorption of dye **6** into host **2** crystals. (A) Activation of host **2** by TGA shows a two-step desorption curve corresponding to the removal of DMSO guest. (B) (I, II) Activated crystals before and after exposure to **3**. (III, IV) Unactivated crystals before and after exposure to **6**. Scale bars 10 μm .

4.2.2 Host-guest complex (**7**) preparation

All the dye molecules selected were expected to have favorable interactions with the host walls since it is made of both aromatic benzene rings and polar urea groups. The guests were loaded in the empty host by soaking the activated host in solutions of the guest at room temperature for 12–24 h. Incorporation of the guests into the empty channels of host **2** was carried out by soaking the activated host **2** in a degassed acetonitrile solution of the

dyes using two methods (Figure 4.6). Method 1 - the crystalline activated host **2** (3-5 mg) was soaked in dye solution (1.0 mM) for 12-24 h. After overnight loading followed by filtration the samples were washed with hexane and air-dried in the hood (Figure 4.6a). For solution of dye **6** equilibrated with host **2**, the crystals changed from white/colorless to purple in color to the naked eye. Figure 4.5b shows the transmission micrographs of the activated crystals of host **2** before and after exposure to guest. A second approach was taken to monitor and analyze the loading of dye **6** into host **2** by modifying the loading procedure where small aliquots of the loading solution were taken out, diluted and their UV-vis absorption recorded (Method 2, Figure 4.6b) at 30 minutes' intervals. In order to ensure that more dye is loaded into the channels of host **2**, the amount of dye in solution was twice the amount (in terms of moles) of solid host **2**. The depletion of dye molecules from solution should translate into a decrease in the absorbance of the dye suggesting it is loading into the host **2** channels. Unfortunately, minimal changes and large fluctuations were observed in some cases with UV-monitoring. Thus, the first method displayed reproducible loading of dye **6** into the host channels.

Our first concern was to probe if the dye was loaded in the crystals or was interacting with the exterior and more of a surface phenomenon. Thus, we equilibrated sample of the unactivated host **2** (host **2**·DMSO, 3-5 mg) the dye solution (1.0 mM). The unactivated host crystals displayed no change in color before and after exposure to the dye solution. This suggests that majority of the dye molecules in complex **7** (host **2**·dye **6**) are loaded into the channels of the activated host **2** and are not simply adsorbed on the surface of the crystals. In summary, loading, as defined as the uptake of dye into the channels of host **2**, was observed for dye **6**, while no loading was observed for dyes **3-5**. The different

loading behavior could be due to several factors such as polarity, pH, or temperature. Future studies should investigate changing these parameters to see if dyes **3-5** can be loaded into host **2** channels.

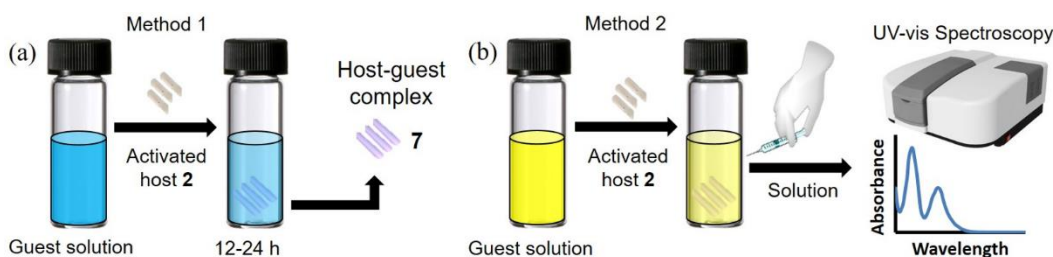


Figure 4.6 Methods of loading of dye into host **2** channels. (a) method 1, the host (3-5 mg) is soaked in guest solution (1.0 mM) for 12-24 hours; (b) method 2, host is soaked in guest solution and the loading monitored by UV-vis spectroscopy (every 30 mins) until equilibrium is reached.

^1H NMR analysis was used to determine the host:guest ratio as well as confirm that the dye was absorbed by host **2**. Samples of the host-guest complexes (5 mg) were dissolved in $\text{DMSO-}d_6$ (1.0 mL) then analyzed by ^1H NMR (Figure 4.7). Integrating and averaging two key peaks CH2 (in host **2**) and CH3 (in dye **6**) gave a loading ratio of 11:1 (Host **2** : dye **6**). The peaks corresponding to the dye appeared in the ^1H NMR spectrum of host-guest complex **7** but were absent in the ^1H NMR spectrum of unactivated host **2** treated with a solution of the dye. These suggest that the dye molecule can diffuse into the empty host channel, but cannot diffuse into the host channel filled with DMSO molecules. In these spectra, the proton peaks for macrocycle **1** appeared at 7.64 (s, 2H, Ar-H), 7.55 (m, $J=20.0$ Hz, 12H, Ar-H), 7.47 (t, $J=16.0$ Hz, 2H, Ar-H), 7.28 (d, $J=8.0$ Hz, 8H, Ar-H), 6.69 (t, $J=12.0$ Hz, 4H, -NH), 4.28 (d, $J=8.0$ Hz, 8H, -CH₂). [Figure 4.7 b-d]. on the other hand, proton peaks for the dye were observed at 7.98 (d, $J = 4.6$ Hz, 1H), 7.52 (d, $J = 4.3$ Hz, 1H), 7.05 (d, $J = 4.5$ Hz, 1H), 6.05 (d, $J = 4.3$ Hz, 1H), 3.02 (s, 6H) [Figure 4.7 a-b].

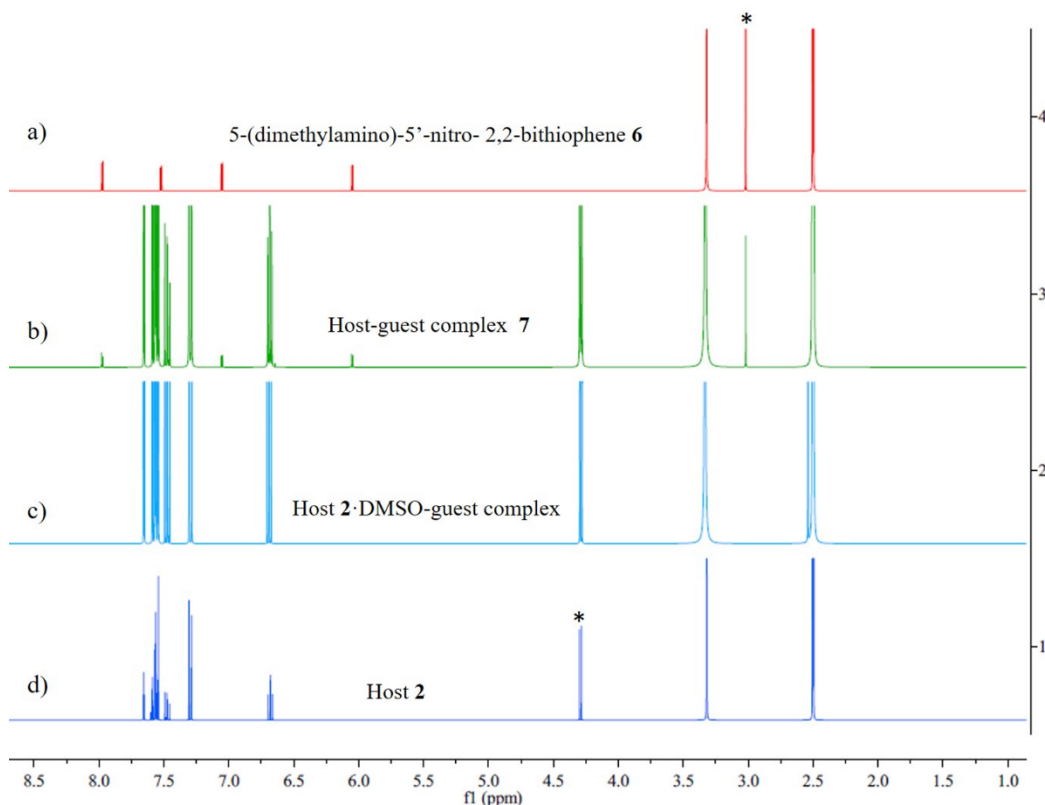


Figure 4.7 Comparison of ^1H NMR (400 MHz, $\text{DMSO-}d_6$) spectra from host **2** loading experiments with thiophene dye **6**. ^1H NMR spectrum of a) dye **6**, b) host-guest complex **7**, (c) unactivated host **2** treated with dye **6** solution, and (d) activated host **2**.

4.2.3 General photophysical characterization

Solvatochromic dyes can be used to probe the polarity of different media.¹⁹ The small bithiophene dye **6** is polar (7.95 D) and displays a marked solvatochromism. Figure 4.8a compares the absorption spectra of **6** (0.01 mM) in four solvents of different polarities. In non-polar hexane (1.89 D), dye **6** displays an absorbance maximum with the shortest wavelength $\lambda_{\text{max}} = 465$ nm. While in polar DMSO (47 D), the dye absorbs at much longer wavelengths with $\lambda_{\text{max}} = 562$ nm. This shift to longer wavelengths correlates well with solvent polarity as measured by the π^* scale from $\lambda_{\text{max}} = 467$ nm in hexanes ($\pi^* = -0.08$) to $\lambda_{\text{max}} = 498$ nm in diethyl ether (Et_2O , $\pi^* = 0.27$) to $\lambda_{\text{max}} = 533$ nm in acetonitrile (CH_3CN , $\pi^* = 0.75$) to $\lambda_{\text{max}} = 562$ nm in dimethyl sulfoxide (DMSO, $\pi^* = 1.00$). Our results are

similar to previous literature reports on this dye.²⁶ Upon loading into the host, the absorption spectra of encapsulated dye **6** should be modulated. Thus, we expect the dye's absorption maximum in the complex will provide a measure of the interior environment of the host channels.

The fluorescence of dye **6** was also investigated by recording the photoluminescence (PL). The spectra were recorded in the same set solvents and concentrations (0.01 mM) at or close to the absorption maximum of dye **6** in each solvent (same concentrations). From inspection of Figure 4.8b, several trends are apparent. First, we observed a bathochromic shift in the PL spectra that is correlated roughly with polarity. The dye displays the lowest wavelength emission in non-polar hexanes with $\lambda_{\text{max}} = 521$ nm in hexanes. The emission wavelength is shifted towards longer wavelengths in solvents of increasing polarity with $\lambda_{\text{max}} = 693$ nm in DMSO ($\lambda_{\text{exc}} \sim 530\text{--}550$ nm). Also apparent is the significant drop in intensity in highly polar solvents. In Et₂O and DMSO, the photoluminescence intensity of the dye **6** decreases. Furthermore, no photoluminescence peak was detected for **6** in CH₃CN (0.01 mM) using $\lambda_{\text{Exc}} = 530$ nm.

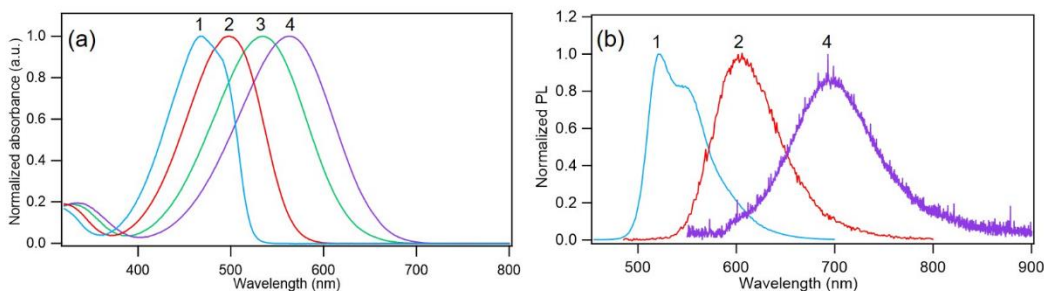


Figure 4.8 Absorption and emission studies of dye **6** in solution. (a) Solvatochromism of **6** in (1) hexanes, (2) Et₂O, (3) CH₃CN, and (4) DMSO. (b) Photoluminescence (PL) spectra of dye **6** in various solvents displaying positive solvatochromism; (1) a solution of the dye in hexane ($\lambda_{\text{max}} = 521$ nm, excitation at 450 nm), (2) a solution of the dye in Et₂O ($\lambda_{\text{max}} = 572$ nm, excitation at 480 nm), and (3) a solution of the dye in DMSO ($\lambda_{\text{max}} = 693$ nm, excitation at 530–550). Note: PL spectrum of dye **3** in CH₃CN was also measured (excitation at 530), but the PL signal was not detected in our condition. The PL spectrum of the dye in DMSO was measured through a 590 nm long-pass filter.

Next, the host-complex was characterized in the solid state by UV-visible and fluorescence spectroscopies. Figure 4.9 compares the solid-state UV-visible diffuse reflectance and fluorescence spectra of the host and host-guest complex. Host **2** exhibits an absorption band with $\lambda_{\text{max}} = 322$ nm whilst the dye-loaded host spectrum has two broad bands at 327 nm and 552 nm. The absorption maxima of host **2** in solution (DMSO) was previously reported to be 286 and 305 nm,¹⁵ whilst the guest (dye) displays a marked solvatochromism in organic solvents (Figure 4.8). The absorption spectrum of the dye-loaded host **2** clearly indicates a new band which is attributed to the incorporated dye and a slight redshift (~ 5 nm) in the band associated with host **2**.

The fluorescence emission spectra of the host and host-guest complex were recorded by exciting both samples at 280 nm. This lower wavelength was chosen to preferentially excite the host, since it is well below the absorption maximum of the dye both in the solid state and in representative organic solvents.

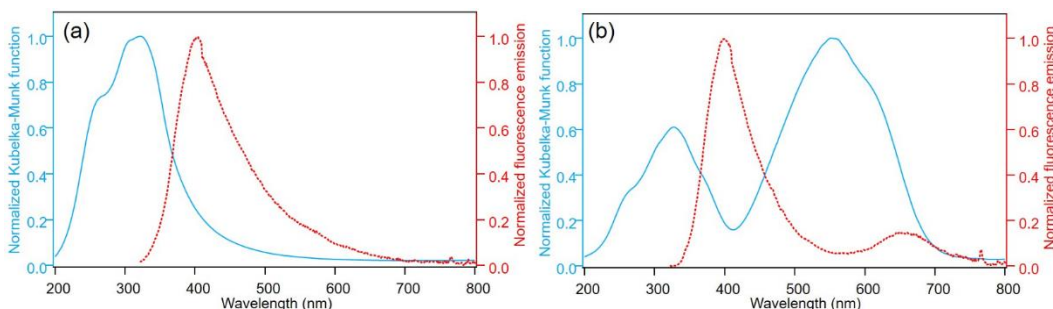


Figure 4.9 Diffuse reflectance spectra (solid blue) and fluorescence emission spectra (dotted red) of (a) self-assembled phenylethynylene *bis*-urea macrocycle columnar structure **2**, and (b) host-guest complex **7**.

Under these conditions host **2** displays an emission maximum at 404 nm. In comparison, the solid host-guest complex **7** displays two emission maxima at 400 and 649 nm with the longer wavelength emission showing a larger intensity. The peak at 649 nm is attributed to the guest and lies within the range found for **6** in polar solvents such as DMSO. It is

interesting that such a low excitation wavelength still successfully excited the guest inside the host channels. This emission can arise both from direct excitation and by energy transfer (ET) from the host.

To verify if energy transfer takes place from the host to the guest, we measured the fluorescence lifetimes of the host **2** and the host-guest complex **7**. The fluorescence lifetimes were measured using a Mini- τ lifetime spectrometer from Edinburgh Instruments equipped with a 300.6 nm picosecond-pulsed-light-emitting diode (EPLD 300). This excitation wavelength is well below the absorption maximum of the dye and should only excite the host. In the case of efficient nonradiative energy transfer from the host (donor) to the guest(acceptor), a reduction in the average decay lifetime of the host is expected. Analysis of the curves with a reconvolution fit supported a triexponential decay model in each case and revealed a shortening of the amplitude-weighted average lifetimes from 1.27 (in host **2**) to 1.08 ns (in host-guest complex **7**) as shown in Table 4.2 and Figure 4.10. The ET efficiency (Φ_{ET}) was determined based on donor lifetimes (host **2**) in the presence and absence of the acceptor molecules (dye **6**). Estimated Φ_{ET} energy was found to be $\sim 15\%$. This suggests that energy transfer occurs within host-guest complex **7** with excitation wavelength of 280 nm and explains the origin of the observed emission peak of the dye in this fluorescence emission.

Table 4.2 Fluorescence life times of host **2** and host-guest complex **7**

	Host 2	Host-guest complex 7
$B_1(X 10^{-2})$	8.16	9.29
$B_2(X 10^{-2})$	2.37	1.94
$B_3(X 10^{-2})$	0.23	0.17
τ_1 (ns)	0.68	0.63
τ_2 (ns)	2.56	2.36
τ_3 (ns)	8.86	11.12
τ_{av} (ns)	1.27	1.08
χ^2	1.19	1.27

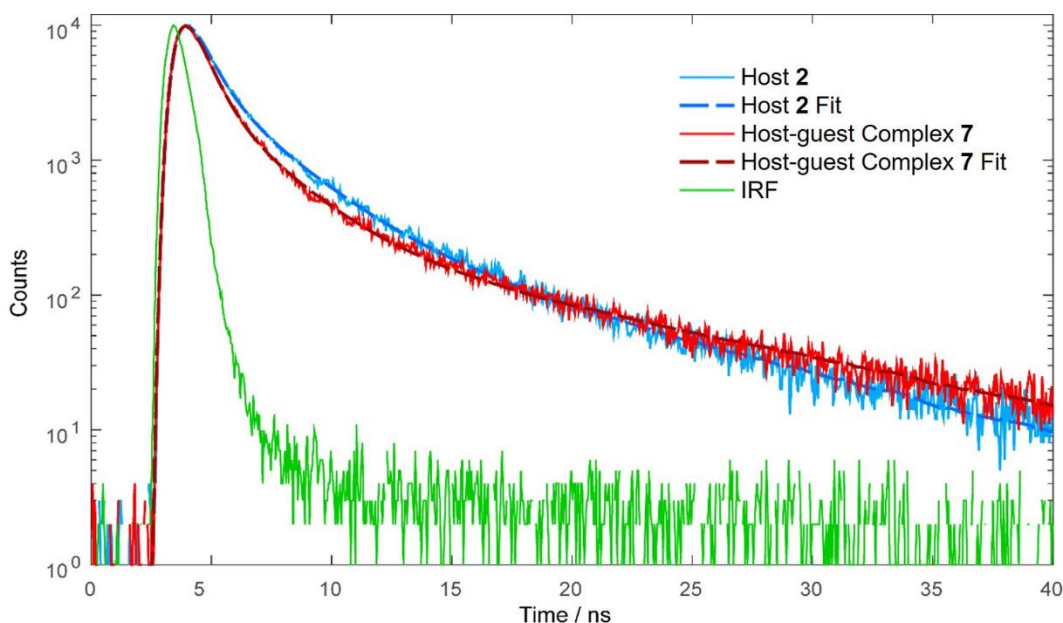


Figure 4.10 Fluorescence decays: host **2** (blue), host-guest complex **7** (red) and green is IRF. Dashed lines are fits of the decays which were fitted with a triexponential function. The samples were excited at 300 nm. The emissions were measured through 430-475 nm band-pass filter.

4.2.4 Wide angle X-ray diffraction scattering (WAXS)

Typically, we use PXRD and single crystal X-ray diffraction to evaluate structure; however, our sample size was limited. Thus, to further understand and evaluate the crystallinity of the host and host-guest complex, their structures were probed by wide-angle X-ray scattering (WAXS) at the South Carolina SAXS Collaborative (SCSC) center. Figure 4.11 compares the WAXS patterns. Upon incorporation of the dye, the WAXS patterns of the dye-loaded host **2** samples show characteristic peaks of host **2**; however, the relative intensities of the peaks differ from pure host **2**. A very slight shifting of some of the peaks was also observed (~ 0.5 - 1.0). This suggests that the high crystallinity of the host is maintained upon uptake of the dye into the 1D channels while accommodating some changes in the overall structure.

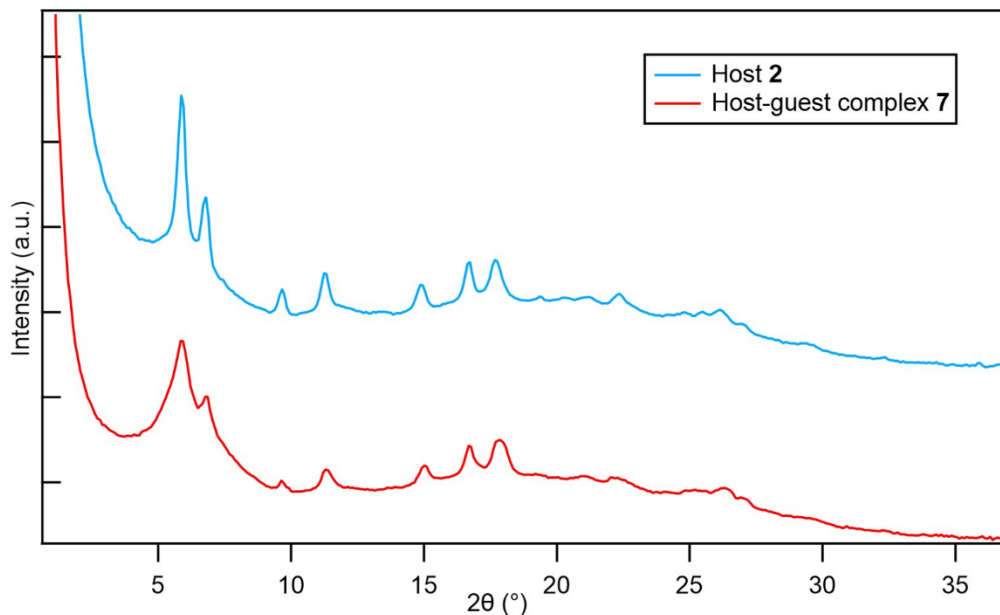


Figure 4.11 Normal-transmission WAXS diffractograms of **2** and **7** demonstrating morphological integrity of the host fiber. 2θ positions ($^{\circ}$) of major peaks; (**2**): 5.94, 7.05, 9.64, 11.21, 15.01, 16.87, 17.90, 21.45, 24.46, 26.25, (**7**): 5.94, 6.77, 9.64, 11.30, 15.01, 16.69, 17.80, 21.08, 22.11, 26.25

4.2.5 Guest alignment studies

By comparing the lengths of the guest dyes with the diameter of the 1D channels in the host, a number of orientations of the guest molecules are plausible. For guests with lengths longer than the diameter of the host 1D channel, a limited number of accessible orientations can be achieved. We examined how the dye molecules are arranged inside the host channels in collaboration with Preecha Kittikhunnatham, Dr. Andrew B. Greytak, and Dr. Vitaly Rassalov. Dr. Vitaly Rassalov using DFT calculations with ADF2014 to investigate the loading of the dyes within the host channel. First, a model of the host was generated by importing the atomic coordinates from the single crystal X-ray structure of the host. Next, the coordinates of the solvent guests were omitted and the structure was truncated to five macrocycles of a single column. Similarly coordinates of the guest **6** was obtained from the CSD data base and used for the calculation. The model host-guest complex was then optimized at the PBEsol-D3/DZP level, keeping the host geometry frozen. The guest

molecule **6** is expected to adopt a lengthwise orientation inside the host channels (Figure 4.2) since the long axis of the guest molecule **6** is larger than the host channel inner diameter (11 vs 9 Å internuclear distance). Next, a time-dependent density functional theory (TDDFT) calculation at the B3LYP/TZ2P level of theory to confirm the orientation of the lowest-energy transition dipole moment (ETDM) in the guest. This calculation showed that the ETDM of the guest in the optimized structure is nearly parallel to the plane defined by the urea oxygen atoms of the host and is canted by an angle $\alpha = 9.5^\circ$ from the channel axis, as represented by the arrow in Figure 4.2b (i). Further calculations were carried out at room temperature, since thermal population of higher energy geometries can occur at room temperature. To evaluate this possibility, we performed a geometry optimization calculation with the molecule constrained to interact with the two opposing sides of the host channel. This calculation yielded a guest structure in which the calculated EDTM is tilted at an angle $\alpha = 30^\circ$ from the channel axis and with the ground state energy only 175 K, or 0.35 kcal/ mol, above the optimized minimum. These calculations indicated that there are likely many similar states within the thermally accessible energy from the minimum, which can result in a broad distribution of ETDM orientations with $\alpha \leq 30^\circ$ at room temperature.

Secondly, Preecha Kittikhunnatham and Dr. Greytak developed a polarimetric fluorescence microscopy method to probe the orientation of dye **6** inside the host channels. Polarized fluorescence microscopy has been used extensively in the field of life sciences, e.g., the location, molecular orientations, and behavior inside lipid and cell membranes.²⁷ It is, however, also a highly attractive methodology to investigate molecules inside 1D channel host systems (such as zeolite L) that provide an ideal architecture to investigate

molecular orientation and interaction.²⁸⁻²⁹ The phenylethynylene *bis*-urea macrocyclic host **2** fits well into this category of materials. Taking into account the diffuse reflectance and fluorescence data of host **2**, our collaborators selected appropriate excitation and emission channels for polarimetric fluorescence microscopy of individual macrocycle fibers cast on glass substrates. A green excitation filter cube (530–550 nm excitation band-pass; 570 nm dichroic mirror, 590 nm emission long-pass filter) was used to selectively excite the guest. For comparison, a UV excitation filter cube (330–385 nm excitation band-pass; 400 nm dichroic, 420 nm emission long-pass) was used to excite the host and guest together with separation of host and guest emission signals possible through the use of a color camera. These excitation and emission conditions were combined with linear polarizers to perform fluorescence excitation and emission polarization measurements to assess the orientation of the dye within the 1D channels. Figure 4.12A shows the fluorescence micrographs where linearly polarized light is used to excite the sample. Excitation polarization is sensitive to the anisotropy of the transition dipole alignment in the absorbing state: thus the excitation rate is greatest when the polarizer is parallel to the excitation dipole and reaches a minimum when they are perpendicular. By applying a polarized light parallel to axis of the fiber-like host-guest complex crystals a huge anisotropic response to the linear polarized light is observed in this material [Figure 4.12A (ii)]. Application of polarized light perpendicular to the fiber axis almost quenches the fluorescence [Figure 4.12A (iv)]. To correct for any effects of photobleaching, uneven detector response or instability of the light source throughout the experiment, they ensured that the fluorescence intensities were normalized by comparison to matching images recorded both polarizers removed [Figure 4.12A (i) and (iii)].

Next, the excitation polarization anisotropy was analyzed in greater detail by plotting I_{θ}/I_{max} as a function of the angle θ_1 between the direction of the polarized excitation and the direction of the fiber axis [Figure 4.12A (v)], where I_{θ} is the ratio of fluorescence intensity of the fiber when excited by linearly polarized light to fluorescence intensity of the fiber excited by unpolarized light and I_{max} is the maximum value of I_{θ} . From the plot, a large oscillation is evident. I_{θ}/I_{max} is highest when the direction of the polarized excitation is parallel to the fiber axis ($\theta_1 \approx 0^\circ$), whereas I_{θ}/I_{max} is minimized when the direction of the polarized excitation is perpendicular to the fiber axis ($\theta_1 \approx 90^\circ$). A similar response was observed for the emission polarization in the host-guest sample using the green (guest selective) excitation channel (Figure 4.12B) which indicates strongly polarized light emitted from the host-guest complex **7**.

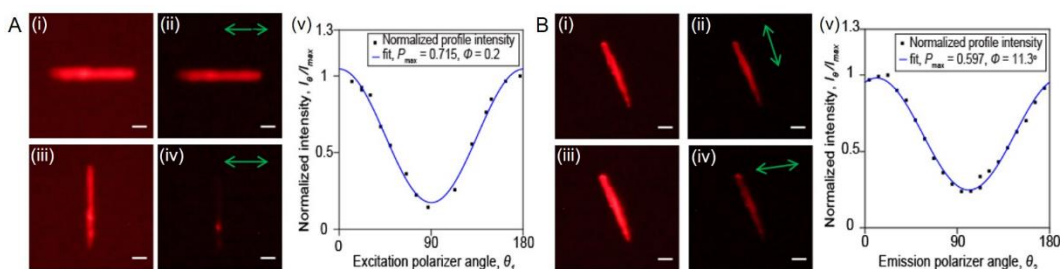


Figure 4.12 Excitation(A) and emission (B) polarization measurements. A; (i-iv) Micrographs of a single host-guest complex fiber recorded with varying excitation conditions (scale bars are 10 μm). Panels (i) and (iii) were recorded with an unpolarized condition, while panels (ii) and (iv) were recorded with polarized excitation with orientation indicated by green arrows. (v) Plot of I_{θ}/I_{max} (determined from averaged line profiles) versus θ_1 , shown with least-squares fit to the equation $I(\theta)/I_{max} = I_n + I_p \cos^2(\theta - \phi)$. B; Micrographs of a single host-guest complex fiber recorded with varying excitation conditions (scale bars are 10 μm). Panels (i) and (iii) were recorded with an unpolarized condition, while panels (ii) and (iv) were recorded with polarized observation with orientation indicated by green arrows. (v) Plot of I_{θ}/I_{max} (determined from averaged line profiles) versus θ_2 , shown with least-squares fit to the equation $I(\theta)/I_{max} = I_n + I_p \cos^2(\theta - \phi)$. where I_n and I_p represent the relative intensities of a “normal” (unpolarized) component of the signal and of a component that is linearly polarized with a maximum at $\theta = \phi$, respectively. Arrows indicate the direction of the polarized light. Reprinted with permission from reference 25. Copyright (2017) America Chemical Society.

4.3 Future Plans

Our preliminary data showed host **2** is able to absorb polar guest dyes such as 5-(dimethylamino)-5'-nitro-2,2'-bithiophene with only 50% occupation of the host channels. It will be interesting to see if a second guest (dye) can be inserted into the channels with dye **6**. This will lead to host-guest composites consisting of two dyes. This will be particularly important for dyes that can act as donor-acceptor pairs. This is achievable when the dyes enter the channels at about the same speed. If the spectral properties of the dyes are such that the emission spectra of one dye (donor) has a large overlap integral with the excitation spectra of the other dye (acceptor), Förster-type energy transfer from one dye to the other may be observed.

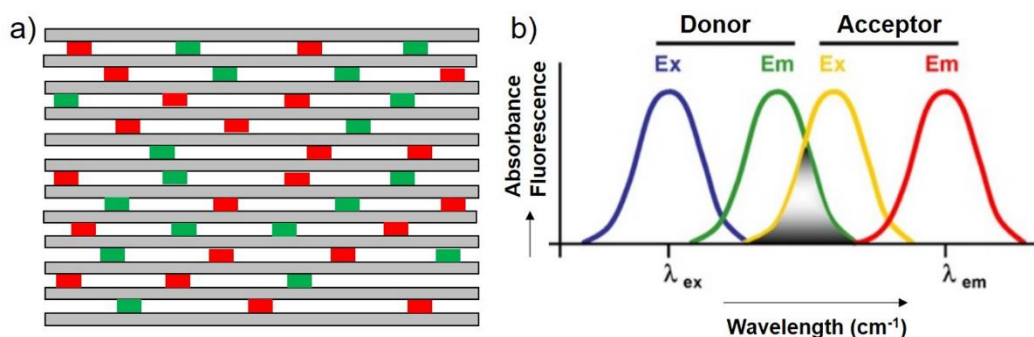


Figure 4.13 Host-guest composites consisting of two dyes. a) Cartoon picture of host **2** crystals loaded with two different dye molecules. b) Diagram of the overlapping spectra of a pair of FRET donor and acceptor.

4.4 Conclusions

In this chapter, we demonstrated our phenylethynylene *bis*-urea macrocycle that self-assembles into nanotubes with 1D channels can absorb a molecular fluorophore 5-(dimethylamino)-5'-nitro-2,2'-bithiophene **6** into its channels. Solution ¹H NMR of the host-guest complex gave a host:guest ratio of ~ 11:1 which is lower compared the computational results of ~ 5:1 indicating only 50 % of the host channels were occupied. WAXS patterns of the host-guest complex in the solid state showed that host **2** maintains

its crystalline integrity upon incorporation of the guest dye. Polarized fluorescence microscopy measurements indicate that the ETDMs of the guests exhibit a net alignment parallel to the long axis of individual micrometer-scale crystals. A TDDFT calculation allows the EDTM to be indexed to the guest's molecular structure, and geometry optimization by DFT indicates that, while the minimized structure is tilted at $\sim 9.5^\circ$ from the channel axis, larger angles up to 30° are thermally accessible, which is sufficient to explain the maximum polarization values measured. Also, the ET efficiency (Φ_{ET}) was determined based on donor lifetimes (host **2**) in the presence and absence of the acceptor molecules (dye **6**) to be $\sim 15\%$. These studies further deepen the understanding of host-guest systems (especially organic hosts) and should facilitate the rational design of advanced host-guest composite materials for applications in non-linear optics (NLO).

4.5 Experimental

4.5.1 Materials and General Procedures

All chemicals were purchased from Aldrich or VWR and used as received. Phenylethynylene *bis*-urea macrocycle was synthesized according to previously described procedures (Scheme 4.1) and 5-(dimethylamino)-5'-nitro-2,2'-bithiophene dye was provided by Prof. Dr. Frank Würthner group at the Center for Nanosystems Chemistry (CNC) and Institut für Organische Chemie, Universität Würzburg, 97074 Würzburg, Germany. ^1H NMR and ^{13}C NMR spectra of macrocycle **1** were recorded on Varian Mercury/VX 300 NMR (Figure 4.14 and Figure 14.15). Thermogravimetric analysis (TGA) was carried out using a TA Instruments SDT-Q600 simultaneous DTA-TGA. Solid-state diffuse-reflectance spectra were recorded using a PerkinElmer Lambda 35 UV-visible scanning spectrophotometer equipped with an integrating sphere.

Fluorescence spectroscopy was carried out on an Edinburgh FS5 instrument equipped with a 150 W continuous wave xenon lamp source for excitation. Fluorescence lifetimes were measured using a Mini- τ lifetime spectrometer from Edinburgh Instruments equipped with a 300.6 nm picosecond-pulsed-light-emitting diode (ELED 300). Wide-angle X-ray scattering (WAXS) was carried out using a SAXSLab Ganesha instrument. A Xenocs GeniX 3D microfocus source was used with a Cu target to generate a monochromatic beam with a 0.154 nm wavelength. A 300 K Pilatus detector (Dectris) was used to collect the two-dimensional (2D) WAXS patterns.

Scheme 4.1 An overview of phenylethynylene *bis*-urea macrocycle synthesis

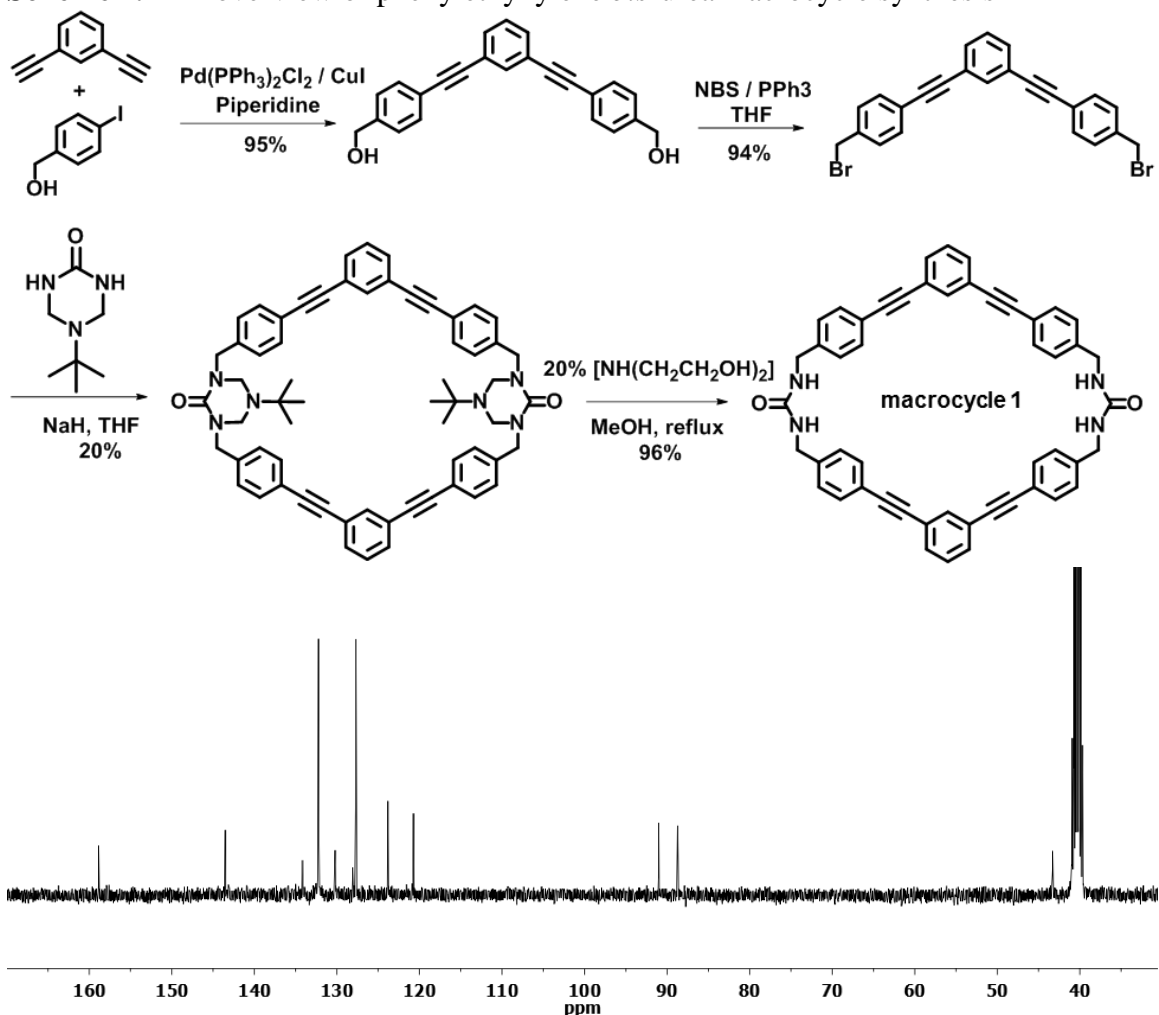


Figure 4.14 ^{13}C NMR spectrum of macrocycle **1** dissolved in $\text{DMSO}-d_6$ (100 MHz): 158.9, 134.5, 134.2, 132.3, 130.2, 128.1, 127.7, 123.8, 120.7, 91.0, 88.7, and 43.3.

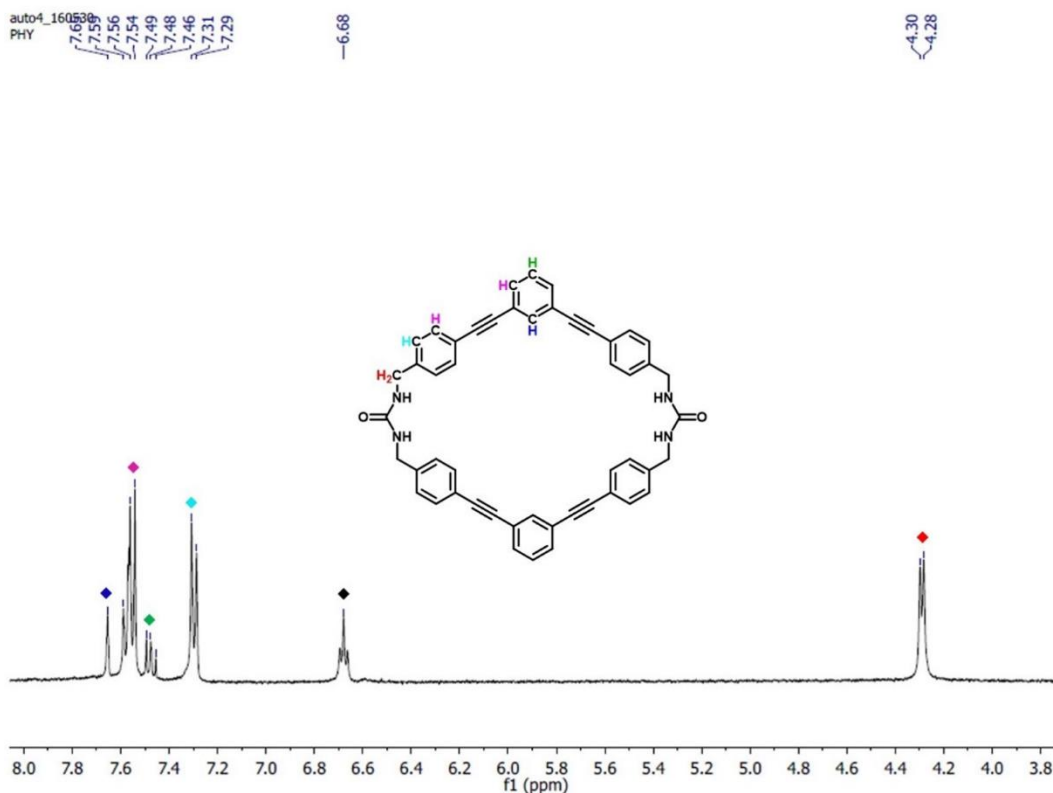


Figure 4.15 ^1H NMR spectrum of macrocycle **1** dissolved in $\text{DMSO-}d_6$ (400 MHz): 7.64 (s, 2H, Ar-H), 7.55 (m, $J=20.0$ Hz, 12H, Ar-H), 7.47 (t, $J=16.0$ Hz, 2H, Ar-H), 7.28 (d, $J=8.0$ Hz, 8H, Ar-H), 6.69 (t, $J=12.0$ Hz, 4H, -NH), 4.28 (d, $J=8.0$ Hz, 8H, -CH₂).

4.5.2 Preparation of Host 2

Host **2** was synthesized according to a previously reported procedure.¹⁵ Recrystallization of 150 mg of the phenylethyne *bis*-urea macrocycle in 30 mL DMSO by slow cooling afforded the self-assembled host **2**. Here the macrocycle was heated (at 120 °C) in an oil bath to dissolve completely in hot DMSO, then ramped to cool at a rate of 1 °C/h to room temperature producing microcrystalline needle of host **2** containing solvent DMSO molecules within the channels. Thermogravimetric analysis was carried out on a TA Instruments SDT Q600 under helium with a flow rate of 100 mL/min to remove the solvent of crystallization in the channels of host **2**. The samples were heated from 25 °C to 180 °C at a rate of 4 °C/min and kept at isotherm for 10 minutes.

4.5.3 Thermogravimetric analysis calculation

The ratio of macrocycle **1** to DMSO in host fibers prior to activation was calculated to be 1:2 using the formulas below:

$$\text{Moles of host} = \frac{\text{Final weight (g)}}{724.2845 \left(\frac{\text{g}}{\text{mol}}\right)}$$

$$\text{Moles of guest} = \frac{\text{Initial weight} - \text{Final weight (g)}}{\text{Guest molecular weight} \left(\frac{\text{g}}{\text{mol}}\right)}$$

$$\text{Host : Guest} = \frac{\text{Moles of host}}{\text{Moles of guest}}$$

4.5.4 Loading of bithiophene dye into Host 2

The bithiophene dye was loaded into host **2** by directly soaking the emptied crystals of host **2** (3.8 mg, 5.24 μmol) in a 0.94 mM acetonitrile (degassed) solution of the dye (11.0 μmol) overnight. The crystals were suction filtered, washed with cyclohexane, and dried under vacuum to give a purple colored material. ^1H NMR of the complex was taken to determine the host-guest ratio. Two key peaks CH_2 (in host **2**) and CH_3 (in the dye) were used to determine the loading ratio by integrating the area under these peaks. These calculations gave a loading ratio of 10.84:1 (Host **2** : bithiophene dye **6**).

4.5.5 Treatment of unactivated host 2 crystals with dye

Host **2**·DMSO crystals (3.8 mg, 5.24 $\times 10^{-6}$ mol) equilibrated with 0.94 mM acetonitrile (degassed) solution of the dye (1.10 $\times 10^{-5}$ mol) overnight. The crystals remained whitish upon filtration and were air-dried in the hood.

4.5.6 Wide angle X-ray diffraction scattering

Wide-angle X-ray scattering were carried out using a SAXSLab Ganesha at the South Carolina SAXS Collaborative (SCSC) at the University of South Carolina. A Xenocs

GeniX 3D microfocus source was used with a Cu target to generate a monochromatic beam with a 0.154 nm wavelength. The samples were packed into metal rings and sandwiched between two sheets of Kapton film. The instrument was calibrated using a silver behenate reference with the first order scattering vector $q^* = 1.076 \text{ nm}^{-1}$, where $q = 4\pi\lambda^{-1} \sin \theta$ with a total scattering angle of 2θ . A 300 K Pilatus detector (Dectris) was used to collect the two-dimensional (2D) WAXS patterns. Diffraction intensity versus q (scattering vector) plots were obtained by radial integration of the two-dimensional (2D) WAXS patterns.

4.5.7 Fluorescence emission

Emission spectra of host **2** and host-guest complex **7** (solid samples) were recorded on an Edinburgh FS5 fluorescence spectrometer equipped with a 150 W Continuous Wave Xenon Lamp source for excitation. The samples were placed inside a 0.5 mm quartz sample holder using the front-facing module. Host **2** and host-guest complex **7** were excited at 280 nm.

4.5.8 Fluorescence lifetime calculations

Fluorescence decay lifetimes of host **2** and host-guest complex **7** were measured using a Mini- τ lifetime spectrometer from Edinburgh Instruments equipped with a 300.6 nm picosecond-pulsed-light-emitting diode (EPLD 300). The lifetimes and decay profiles are shown in Figure 4.8 and Table 4.2. The amplitude-weighted average lifetime τ_{av} is the appropriate measure by which to describe fluorescence resonant energy transfer. Accordingly, the decays were fit with a triexponential function ($n = 3$), where τ_i and B_i are respective lifetimes and amplitudes of each component, and these fit parameters were used to calculate τ_{av} :

$$\text{Fit: } A + B_1 \cdot e^{(-t/\tau_1)} + B_2 \cdot e^{(-t/\tau_2)} + B_3 \cdot e^{(-t/\tau_3)}$$

$$\tau_{av} = \frac{B_1\tau_1 + B_2\tau_2 + B_3\tau_3}{B_1 + B_2 + B_3}$$

The energy transfer efficiency, Φ_{ET} was calculated using the following equation:

$$\Phi_{ET} [\%] = \frac{k_{et}}{k_r + k_{nr} + k_{et}} = \frac{k_{et}}{k_o + k_{et}}$$

The k_o and k_{et} values are obtained from the decay lifetimes for donor molecule (τ_D) and donor molecule in the presence of acceptor (τ_{D-A}), which are $\tau_D = 1/k_o$ and $\tau_{D-A} = 1/(k_o + k_{et})$, respectively. The calculated Φ_{ET} was 14.8%.

4.5.9 Grand Canonical Monte Carlo (GCMC) simulations

All GCMC simulations were performed using the Monte Carlo for Complex Chemical Systems (MCCCS) Towhee plug-in built into Scienomics' Materials Processes and Simulations (MAPS) platform.³⁰ First, an amorphous guest system was built using the Amorphous Builder plug-in within MAPS, and the chemical potentials of the guest dye **6** was calculated via a 1×10^4 step canonical MC simulation with MCCCS Towhee for systems containing 100 guest molecules using the Widom insertion method and the Dreiding force field. The chemical potential of guest dye **6** was found to be 89180. Next, a periodic simulation cell was constructed by importing the atomic coordinates from the X-ray structure of host **2** into MAPS.¹⁵ The calculations of host-guest complex **7** was performed using the above calculated chemical potential value of dye **6**. The calculation was conducted via GCMC simulations for 3×10^6 steps, where the chemical potential (μ) of dye **6** was kept constant and the system was maintained at standard ambient constant temperature (T, 298.15K) and constant volume (V). Moves and associated probability of Grand Canonical Monte Carlo simulations are shown in Table 4.3 and Table 4.4.

Table 4.3. Moves and associated probability of Canonical Monte Carlo simulations for guest dye 6 chemical potential calculations.

Move	Probability of move	Guest		
Configurational bias single box molecule reinsertion move	0.2	1.0		
Move	Probability of move	Guest	Guest	Guest
Configurational bias partial molecule regrowth	0.4	1.0	1.0	
Move	Probability of move	Guest	Maximum displacement	Acceptance rate
Intramolecular single atom translation	0.6	1.0	0.5	0.5
Move	Probability of move	Guest	Maximum displacement	Acceptance rate
Center of mass molecule translation	0.8	1.0	0.5	0.5
Move	Probability of move	Guest	Maximum displacement	Acceptance rate
Rotation about the center of mass	1.0	1.0	0.05	0.5

Table 4.4 Moves and associated probability of Grand Canonical Monte Carlo simulations for host-guest complex 7.

Move	Probability of move	Host 2	Guest		
Configurational bias grand canonical insertion/deletion move	0.4	0	1.0		
Move	Probability of move	Host 2	Guest		
Configurational bias two box molecule transfer move	0.01	0	1.0		
Move	Probability of move	Host 2	Guest	Host 2	Guest
Configurational bias partial molecule regrowth	0.7	0	1.0	0.5	1.0
Move	Probability of move	Host 2	Guest	Maximum displacement	Acceptance rate
Intramolecular single atom translation	0.8	0.3	1.0	0.5	0.5
Move	Probability of move	Host 2	Guest	Maximum displacement	Acceptance rate
Center of mass molecule translation	0.9	0	1.0	0.5	0.5
Move	Probability of move	Host 2	Guest	Maximum displacement	Acceptance rate
Rotation about the center of mass	1.0	0	1.0	0.05	0.5

4.6 References

1. Minkowski, C.; Pansu, R.; Takano, M.; Calzaferri, G., Energy Collection, Transport, and Trapping by a Supramolecular Organization of Dyes in Hexagonal Zeolite Nanocrystals. *Adv. Funct. Mater.* **2006**, *16* (2), 273-285.
2. Gigli, L.; Arletti, R.; Vitillo, J. G.; Alberto, G.; Martra, G.; Devaux, A.; Vezzalini, G., Thionine Dye Confined in Zeolite L: Synthesis Location and Optical Properties. *The Journal of Physical Chemistry C* **2015**, *119* (28), 16156-16165.
3. Alarcos, N.; Cohen, B.; Ziólek, M.; Douhal, A., Photochemistry and Photophysics in Silica-Based Materials: Ultrafast and Single Molecule Spectroscopy Observation. *Chem. Rev.* **2017**, *117* (22), 13639-13720.
4. Gasecka, A.; Dieu, L. Q.; Brühwiler, D.; Brasselet, S., Probing Molecular Order in Zeolite L Inclusion Compounds Using Two-Photon Fluorescence Polarimetric Microscopy. *The Journal of Physical Chemistry B* **2010**, *114* (12), 4192-4198.
5. Fois, E.; Tabacchi, G.; Calzaferri, G., Orientation and Order of Xanthene Dyes in the One-Dimensional Channels of Zeolite L: Bridging the Gap between Experimental Data and Molecular Behavior. *The Journal of Physical Chemistry C* **2012**, *116* (31), 16784-16799.
6. Sozzani, P.; Comotti, A.; Simonutti, R.; Meersmann, T.; Logan, J. W.; Pines, A., A Porous Crystalline Molecular Solid Explored by Hyperpolarized Xenon. *Angew. Chem. Int. Ed.* **2000**, *39* (15), 2695-2699.
7. Anedda, R.; Soldatov, D. V.; Moudrakovski, I. L.; Casu, M.; Ripmeester, J. A., A New Approach to Characterizing Sorption in Materials with Flexible Micropores. *Chem. Mater.* **2008**, *20* (9), 2908-2920.

8. Cheng, C.-Y.; Bowers, C. R., Direct Observation of Atoms Entering and Exiting l-Alanyl-l-valine Nanotubes by Hyperpolarized Xenon-129 NMR. *J. Am. Chem. Soc.* **2007**, *129* (45), 13997-14002.
9. Calzaferri, G., Nanochannels: Hosts for the Supramolecular Organization of Molecules and Complexes. *Langmuir* **2012**, *28* (15), 6216-6231.
10. Kobr, L.; Zhao, K.; Shen, Y.; Comotti, A.; Bracco, S.; Shoemaker, R. K.; Sozzani, P.; Clark, N. A.; Price, J. C.; Rogers, C. T.; Michl, J., Inclusion Compound Based Approach to Arrays of Artificial Dipolar Molecular Rotors. A Surface Inclusion. *J. Am. Chem. Soc.* **2012**, *134* (24), 10122-10131.
11. Hoss, R.; König, O.; Kramer-Hoss, V.; Berger, U.; Rogin, P.; Hulliger, J., Crystallization of Supramolecular Materials: Perhydrotriphenylene (PHTP) Inclusion Compounds with Nonlinear Optical Properties. *Angewandte Chemie International Edition in English* **1996**, *35* (15), 1664-1666.
12. Tsuwi, J.; Berger, R.; Labat, G.; Couderc, G.; Behrnd, N.-R.; Ottiger, P.; Cucinotta, F.; Schürmann, K.; Bertoni, M.; Viani, L.; Gierschner, J.; Cornil, J.; Prodi-Schwab, A.; De Cola, L.; Wübbenhorst, M.; Hulliger, J., Alignment and Relaxation Dynamics of Dye Molecules in Host–Guest Inclusion Compounds As Probed by Dielectric Spectroscopy. *The Journal of Physical Chemistry A* **2010**, *114* (26), 6956-6963.
13. Bruhwiler, D.; Calzaferri, G.; Torres, T.; Ramm, J. H.; Gartmann, N.; Dieu, L.-Q.; Lopez-Duarte, I.; Martinez-Diaz, M. V., Nanochannels for supramolecular organization of luminescent guests. *J. Mater. Chem.* **2009**, *19* (43), 8040-8067.
14. Sola-Llano, R.; Martínez-Martínez, V.; Fujita, Y.; Gómez-Hortigüela, L.; Alfayate, A.; Uji-i, H.; Fron, E.; Pérez-Pariente, J.; López-Arbeloa, I., Formation of a Nonlinear

Optical Host–Guest Hybrid Material by Tight Confinement of LDS 722 into Aluminophosphate 1D Nanochannels. *Chemistry - A European Journal* **2016**, *22* (44), 15700-15711.

15. Dawn, S.; Dewal, M. B.; Sobransingh, D.; Paderes, M. C.; Wibowo, A. C.; Smith, M. D.; Krause, J. A.; Pellechia, P. J.; Shimizu, L. S., Self-Assembled Phenylethynylene *Bis*-urea Macrocycles Facilitate the Selective Photodimerization of Coumarin. *J. Am. Chem. Soc.* **2011**, *133* (18), 7025-7032.

16. Dawn, S.; Salpage, S. R.; Koscher, B. A.; Bick, A.; Wibowo, A. C.; Pellechia, P. J.; Shimizu, L. S., Applications of a *Bis*-Urea Phenylethynylene Self-Assembled Nanoreactor for [2 + 2] Photodimerizations. *The Journal of Physical Chemistry A* **2014**, *118* (45), 10563-10574.

17. Salpage, S. R.; Donevant, L. S.; Smith, M. D.; Bick, A.; Shimizu, L. S., Modulating the reactivity of chromone and its derivatives through encapsulation in a self-assembled phenylethynylene *bis*-urea host. *Journal of Photochemistry and Photobiology A: Chemistry* **2016**, *315*, 14-24.

18. Esnal, I.; Duran-Sampedro, G.; Agarrabeitia, A. R.; Banuelos, J.; Garcia-Moreno, I.; Macias, M. A.; Pena-Cabrera, E.; Lopez-Arbeloa, I.; de la Moya, S.; Ortiz, M. J., Coumarin-BODIPY hybrids by heteroatom linkage: versatile, tunable and photostable dye lasers for UV irradiation. *PCCP* **2015**, *17* (12), 8239-8247.

19. Reichardt, C., Solvatochromic Dyes as Solvent Polarity Indicators. *Chem. Rev.* **1994**, *94* (8), 2319-2358.

20. Sharma, V. K.; Saharo, P. D.; Sharma, N.; Rastogi, R. C.; Ghoshal, S. K.; Mohan, D., Influence of solvent and substituent on excited state characteristics of laser grade

coumarin dyes. *Spectrochimica Acta Part A: Molecular and Biomolecular Spectroscopy* **2003**, *59* (6), 1161-1170.

21. Zhao, W.; Pan, L.; Bian, W.; Wang, J., Influence of Solvent Polarity and Hydrogen Bonding on the Electronic Transition of Coumarin 120: A TDDFT Study. *ChemPhysChem* **2008**, *9* (11), 1593-1602.

22. Aaron, J. J.; Maafi, M.; Párkányi, C.; Boniface, C., Quantitative treatment of the solvent effects on the electronic absorption and fluorescence spectra of acridines and phenazines. The ground and first excited singlet-state dipole moments. *Spectrochimica Acta Part A: Molecular and Biomolecular Spectroscopy* **1995**, *51* (4), 603-615.

23. Komorowska, K.; Brasselet, S.; Dutier, G.; Ledoux, I.; Zyss, J.; Poulsen, L.; Jazdyk, M.; Egelhaaf, H. J.; Gierschner, J.; Hanack, M., Nanometric scale investigation of the nonlinear efficiency of perhydrotriphenylene inclusion compounds. *Chem. Phys.* **2005**, *318* (1), 12-20.

24. Huber, S.; Ruiz, A. Z.; Li, H.; Patrinoiu, G.; Botta, C.; Calzaferri, G., Optical spectroscopy of inorganic–organic host–guest nanocrystals organized as oriented monolayers. *Inorg. Chim. Acta* **2007**, *360* (3), 869-875.

25. Kittikhunnatham, P.; Som, B.; Rassolov, V.; Stolte, M.; Würthner, F.; Shimizu, L. S.; Greytak, A. B., Fluorescence Polarization Measurements to Probe Alignment of a Bithiophene Dye in One-Dimensional Channels of Self-Assembled Phenylethynylene Bis-Urea Macrocycle Crystals. *The Journal of Physical Chemistry C* **2017**, *121* (33), 18102-18109.

26. Effenberger, F.; Wuerthner, F.; Steybe, F., Synthesis and Solvatochromic Properties of Donor-Acceptor-Substituted Oligothiophenes. *The Journal of Organic Chemistry* **1995**, *60* (7), 2082-2091.
27. Gasecka, A.; Han, T.-J.; Favard, C.; Cho, B. R.; Brasselet, S., Quantitative Imaging of Molecular Order in Lipid Membranes Using Two-Photon Fluorescence Polarimetry. *Biophys. J.* **2009**, *97* (10), 2854-2862.
28. Busby, M.; Blum, C.; Tibben, M.; Fibikar, S.; Calzaferri, G.; Subramaniam, V.; De Cola, L., Time, Space, and Spectrally Resolved Studies on J-Aggregate Interactions in Zeolite L Nanochannels. *J. Am. Chem. Soc.* **2008**, *130* (33), 10970-10976.
29. Sprung, C.; Weckhuysen, B. M., Differences in the Location of Guest Molecules within Zeolite Pores As Revealed by Multilaser Excitation Confocal Fluorescence Microscopy: Which Molecule Is Where? *J. Am. Chem. Soc.* **2015**, *137* (5), 1916-1928.
30. Materials and Processes Simulations (MAPS), Copyright Scienomics SARL, Paris, France, 2004–2013.

CHAPTER 5

MULTI-DIMENSIONAL COPPER(I) AND SILVER (I) COORDINATION COMPLEXES OF A PROTECTED PYRIDYL *BIS*-UREA MACROCYCLE⁴

⁴ **Som, B.**; Smith, M. D.; Shimizu, L. S., Multi-dimensional copper(I) and silver (I) coordination complexes of a protected pyridyl *bis*-urea macrocycle. *In preparation*.

5.0 Abstract

Two new protected pyridyl urea macrocycles **4-5** (dimer and trimer) have been synthesized and subsequently used in the syntheses of Cu(I) and Ag(I) coordination polymers. These compounds have been structurally characterized by NMR and IR spectroscopies, and single crystal X-ray diffraction. Two coordination polymers were obtained with protected pyridyl *bis*-urea macrocyclic ligand **4**: $[\text{Cu}_2\text{I}_2(\mathbf{4})_2 \cdot (\text{CH}_3\text{CN})_{1.63(1)}]$ and $[\text{Ag}(\mathbf{4})(\text{NO}_3)(\text{H}_2\text{O})_{2.5}]$. The crystal structure of $[\text{Cu}_2\text{I}_2(\mathbf{4})_2 \cdot (\text{CH}_3\text{CN})_{1.63(1)}]$ shows a 2D coordination network constructed from a rhomboid Cu_2I_2 dimer units with bridging ligand **4** (through the pyridyl N atoms). Complex $[\text{Ag}(\mathbf{4})(\text{NO}_3)(\text{H}_2\text{O})_{2.5}]$ on the other hand formed an intricate 3D structure in which 1D chains formed by N-Ag-N links (angle 154°) between pyridyl N atoms of two adjacent macrocyclic ligands and Ag(I) ion are transformed into 2D layers by longer Ag-O interaction of 2.52 \AA between the Ag(I) centers and carbonyl O atoms of neighboring chains, these 2D layers are then linked together by hydrogen bonding involving interstitial water molecules resulting in the 3D structure. Initial photoluminescence studies showed that only complex $[\text{Cu}_2\text{I}_2(\mathbf{4})_2 \cdot (\text{CH}_3\text{CN})_{1.63(1)}]$ exhibit fluorescence properties in the solid state at ambient temperature.

5.1 Introduction

The design and synthesis of coordination polymers (CPs) have attracted much attention in the last few decades due to their intriguing topological features and functional properties.¹⁻
² These complex materials have potential applications for gas storage/separation,³⁻⁴ catalysis,⁵ molecular magnetism,⁶ luminescent materials and drug delivery. By using crystal engineering tools, scientist have employed several strategies to synthesize a large number of CPs. For example, the judicious choice of organic ligands and metal ions that

have specific directionality gives rise to CPs with diverse solid-state structures (1D, 2D or 3D) and properties. Other factors that influence the structural out-come of CPs include temperature, solvents, pH value, and reactants ratio. Each of these factors increase structurally diversity and sometimes lead to unpredicted structures.⁷⁻⁸ However, from a crystal engineering viewpoint, the focus is centered primarily on the ligand and the coordination geometry around the metal. Organic polycarboxylates (O-donors) and pyridines (N-donors) are among the most used ligands in coordination polymer synthesis. Multi-topic bridging ligands with these functional groups can show different binding abilities to metal ions and therefore can be applied as effective tectons for assembling coordination networks.⁹ The flexibility and position of the donor atoms plays a very important role in these structures.¹⁰ These ligands are usually designed in a linear fashion with different levels of flexibility. For example, in biphenyl-based bicarboxylates or bipyridines ligands the two phenyl (or pyridyl) groups of the ligand can be separated by other groups such as -O-, -CH₂-, and -O-CH₂-, enabling free rotation around these groups to fit the coordination geometry of the metal ions in the assembly process. Coordination of macrocyclic ligands to the metal ions differs from the linear analogues. Macrocyclic ligands, especially ones with coordinating sites directly connected to the cyclic backbone are typically less flexible and are expected to show more rigid properties in the assembly of CPs.

Chapter 1 reviewed the pyridyl *bis*-urea macrocyclic systems that have been synthesized and/or reported by our group. In these functionalized macrocycles the pyridyl N could be in the interior of the macrocycle (*endo*) or on its exterior (*exo*). Incorporating such groups into the macrocycle is important for applications in catalysis and molecular

recognition. Previously, our group has employed protected N-functionalized macrocycles and deprotected N-functionalized macrocycles as ligands to synthesized coordination complexes, and as co-formers in co-crystal synthesis. Silver coordination polymers were synthesized from the protected bipyridine *bis*-urea macrocycle and silver triflate (Figure 5.1a).¹¹⁻¹² The deprotected version of this macrocycle also formed a complex with Cd(NO₃)₂ favoring the *endo*-type structure (Figure 5.1b).¹¹ In this structure the 2,2'-bipyridines adopted a nearly planar conformation with N-C-C-N dihedral angles of 5.2°, and the four N donors point inward for efficient coordination with Cd. The crystal structures of these complexes demonstrated that the bipyridine *bis*-urea macrocycle is flexible and can rotate to access conformations where the metal binding site sits in the interior of the macrocycle (*endo*) or on its exterior (*exo*). A recently reported complex involving this macrocycle is an exocyclic di-ruthenium complex (Figure 5.1c), which functions as a photocatalyst for the radical cation Diels–Alder reaction between trans-anethole and isoprene.¹³

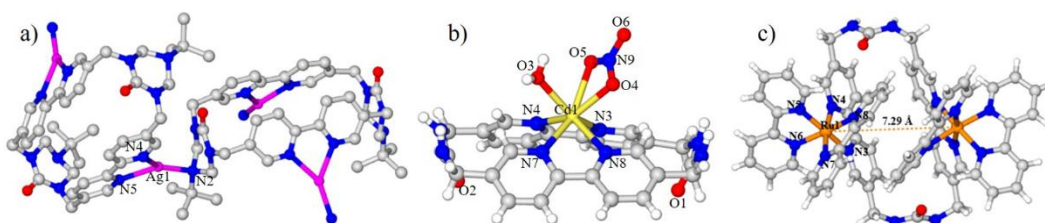
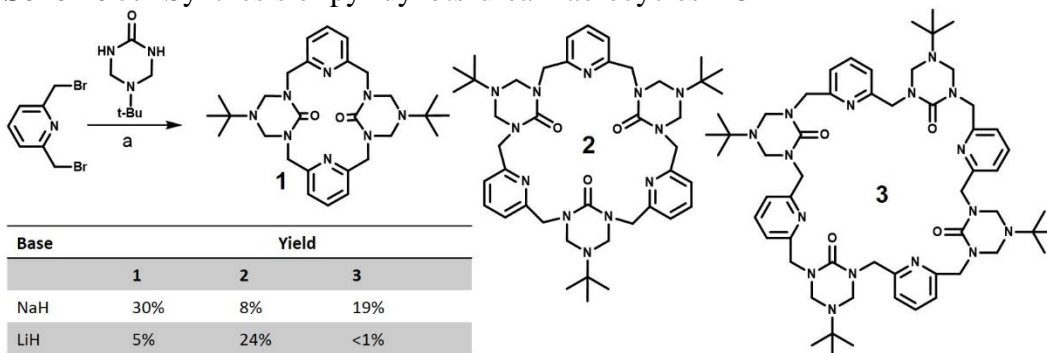


Figure 5.1. X-ray crystal structures of bipyridyl *bis*-urea macrocycle coordination complexes. (a) The coordination environment of the silver atom in protected bipyridyl *bis*-urea macrocycle coordination polymer, {[Ag₂(C₃₈H₄₆N₁₀O₂)](SO₃CF₃)₂·unknown solvate}. (b) Side view of deprotected bipyridine *bis*-urea macrocycle with cadmium, Cd(C₂₆H₂₄N₈O₂)(H₂O)(NO₃)₂ showing *endo* coordination mode. (c) Top view of the bowl-like structure of the cation in [(Ru(C₁₀H₈N₂)₂)₂(C₂₆H₂₄N₈O₂)](Cl)₄(H₂O)₆ synthesized by reacting the deprotected bipyridine *bis*-urea macrocycle with Ru(bpy)₂Cl₂·2H₂O. The macrocycle is in the *exo* binding mode while the ruthenium centers are 7.29 Å apart.¹³

The pyridyl *bis*-urea macrocycle **1** places the pyridyl Ns in the interior of the macrocycle where they are in close proximity to the urea groups.¹⁴ The urea carbonyl is

the better hydrogen bond acceptor as indicated by its β value of 8.3 versus 7.0 for the pyridine. However, the proximity and of the two functional groups (urea and pyridine) within a single macrocycle provided opportunity for the investigation of the structure and molecular recognition properties of the macrocycles both in solution and solid-state. In particular, they were interested in how the two functional groups interact with each other. As shown in Scheme 5.1, the cyclization under basic conditions gave three macrocyclic products: dimer (**1**), trimer (**2**) and tetramer (**3**). These macrocycles and their deprotected versions were characterized by single crystal X-ray diffraction and studied for their ability to bind metal ions.

Scheme 5.1 Synthesis of pyridyl *bis*-urea macrocycles **1-3**



^aReagents and conditions: (a) triazinanone (2.5 mM in THF), base, 80°C (1 h), cooling, followed by dropwise addition of dibromide (1.2 mM in THF), 48 h

The dimer **1** can be considered an analogue of calix[4]arenes, which are of special interest due to their ability to adopt well-defined three-dimensional structures. Calix[4]arenes are commonly discussed in terms of four basic conformations: cone, partial cone, 1,2- and 1,3-alternate (Figure 5.2a).¹⁵⁻¹⁶ The protected dimer **1** and calix[4]arenes are similar in their structures, which contain four six-membered rings that are linked together by methylene groups. Pioneered by the Gutsche group, calixarenes can be readily synthesized in a one-pot synthesis by the condensation of phenols with formaldehyde under

alkaline conditions in relatively good yields.¹⁵ The stability of each conformation has been attributed to hydrogen bonding, steric and electrostatic forces, guest complexation, and to a lesser degree of solvent effects. Thus, the partial or complete replacement of the phenol OH groups by other groups or by hydrogen may fundamentally alter the conformational properties.¹⁷ In comparison, the protected pyridyl *bis*-urea macrocyclic dimer (**1**) in the solid state adopted two conformations, partial cone and 1,3-alternate when crystallized from two different solvent *o*-xylene and DMSO respectively (Figure 5.2b).

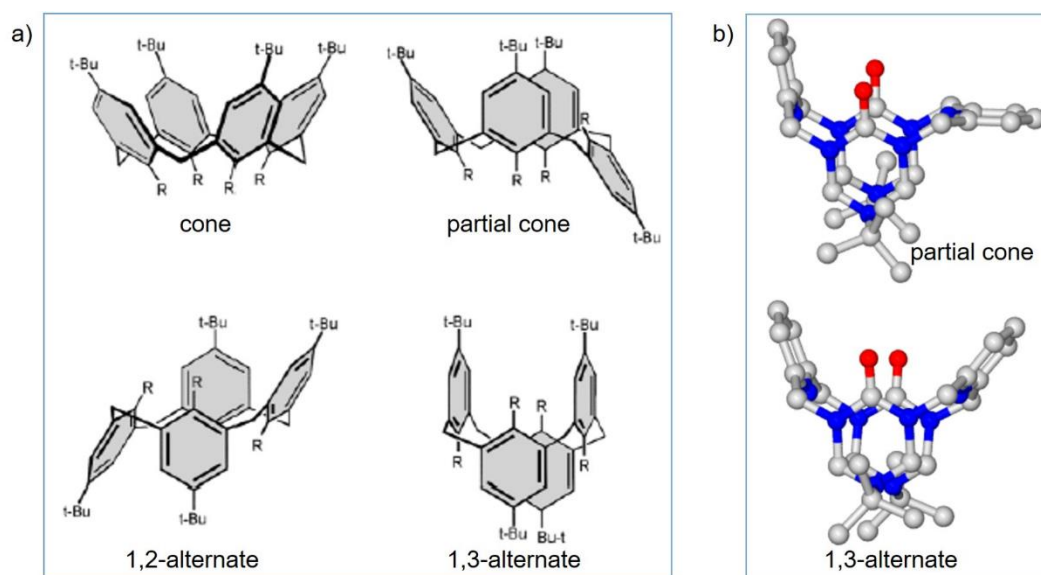


Figure 5.2 Conformations of calix[4]arenes. (a) The four main conformations of calix[4]arenes; cone, partial cone, 1,2-alternate, and 1,3-alternate.¹⁶ (b) Conformations of macrocycle **1** in the solid state.¹⁴ Top; a partial cone conformer was obtained from *o*-xylene, bottom; the 1,3-alternate conformation was obtained from DMSO. Hydrogen atoms are omitted for clarity.

Geer *et al.* reported the co-crystallization of the protected dimer with two halogen bond donors, diiodotetrafluoroethane and iodopentafluorobenzene, by slow evaporation from dichloride methane.¹⁸ These co-crystal structures exhibited very strong halogen bonds as indicated by their I \cdots O distances. The halogen bonds formed were between the carbonyl O of the urea in **1** and the iodine atom of the halogen bond donors. These halogen bonds were on average 78% of the sum of van der Waals radii for I \cdots O (3.50 Å). In

comparison, these halogen bonds are shorter than those reported by Resnati *et al.* for halogen bonds formed between a nitro-oxide and *p*-diiodotetrafluorobenzene with an O...I distance of 2.745 Å.¹⁹

The trimer (**2**) was utilized in binding studies with alkali metal ions and as a ligand to synthesize transition metal complexes.^{14, 20} This investigation was initiated based on the product selectivity of the macrocycles when different bases are used in the synthesis (Scheme 5.1). The low yield of **2** with NaH as base indicates it is binding to the Na⁺ ions and does not bind Li⁺ ions, hence higher yield when LiH is used as base. So dissolving **2** and NaClO₄ (1:1 molar ratio) in methanol/acetonitrile mixture followed by slow evaporation produced **2**·NaClO₄ complex. Single crystal X-ray diffraction studies of the complex showed that the cavity of **2** can accommodate cation guests. Upon complexation with NaClO₄, the macrocycle dramatically flipped its conformation, turning all the carbonyl groups inward to coordinate the Na⁺ ion. This structure had a 1:3 stoichiometry forming a host **2**·NaClO₄ *endo*-type complex (Figure 5.3).¹⁴

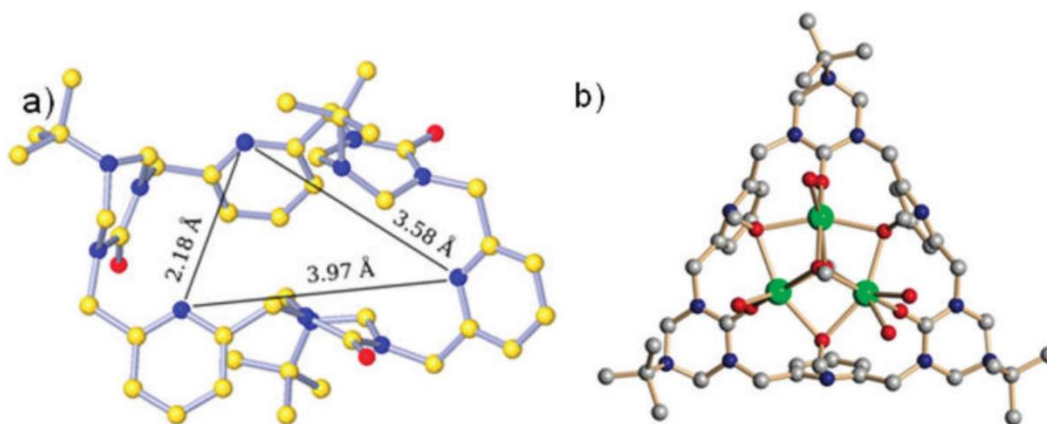


Figure 5.3 Comparison of the host **2** and its coordination complex with NaClO₄: (a) View of the free host from the X-ray crystal structure of macrocycle **2**. Indicated distances are between the van der Waals surfaces of pyridine Ns. (b) Low-quality crystals diffracted well enough to establish the general connectivity of **2**·NaClO₄ complex in which Na⁺ atoms (green) were coordinated to three carbonyl oxygens as well as to oxygens from perchlorate ions and methanol molecules. Reprinted with permission from Reference 14. Copyright (2010) American Chemical Society.

Investigating complexation with a Cd^{2+} ion in $\text{Cd}(\text{ClO}_4)_2 \cdot 6\text{H}_2\text{O}$, they obtained a 1D helical coordination polymer, $[\text{Cd}_3(\mathbf{2})_2(\text{CH}_3\text{CN})_2(\text{H}_2\text{O})_6](\text{ClO}_4)_6 \cdot (\text{CH}_3\text{CN})_{1.4}(\text{H}_2\text{O})_{8.5}$.²⁰ In this structure two macrocyclic ligands (**2**) complexed with three cadmium atoms to form a helicate monomeric structure $[\text{Cd}_3(\mathbf{2})_2(\text{H}_2\text{O})_6(\text{CH}_3\text{CN})_2]^{6+}$, which extends to a 1D polymeric structure *via* hydrogen bonding (Figure 5.4). These complexes demonstrated the flexibility of macrocyclic ligand **2**.

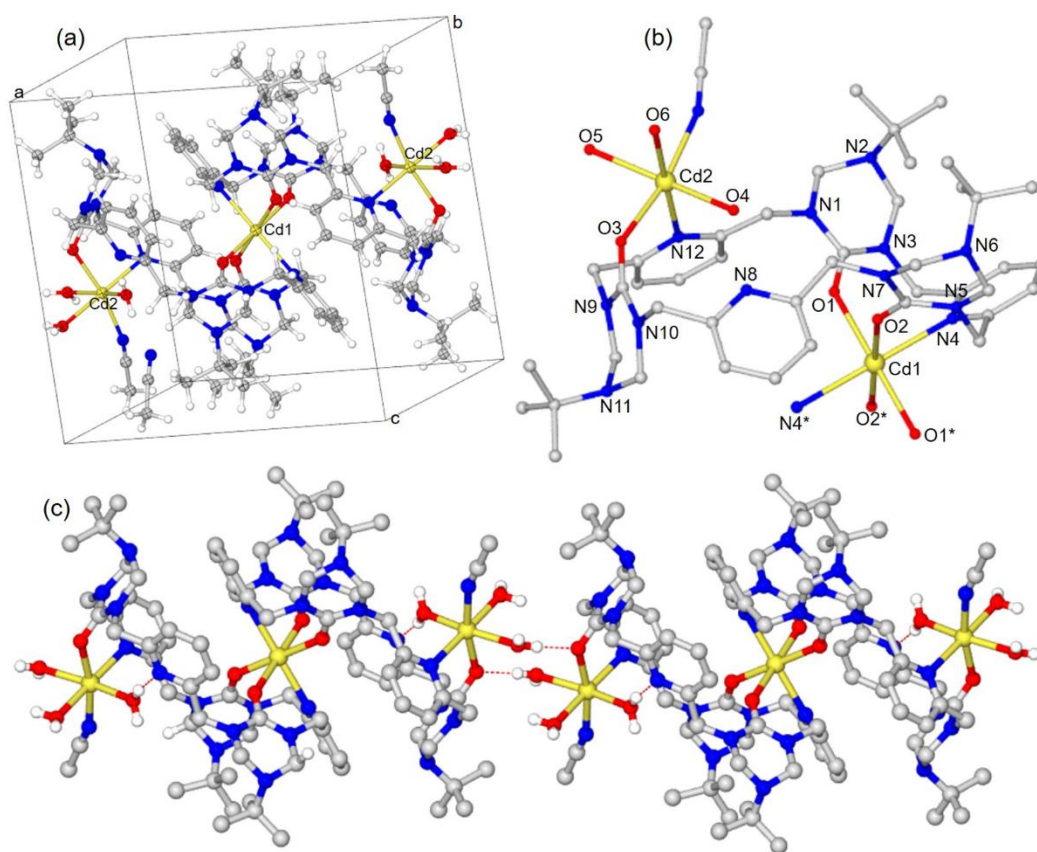


Figure 5.4 X-ray crystal structures of the macrocycle **2**·Cd complex. (a) Structure of the complex where two macrocyclic ligands were connected by central Cd^{2+} and formed a helicate monomeric unit. (b) Details of the ligand conformation showed that the host **3** underwent conformational adjustment and followed the *exo*-type binding mode. (c) monomeric units are bridged by hydrogen bonding in an end-to-end mode to form a 1D chain. Perchlorate ions, some solvents and hydrogen atoms are omitted for clarity.

In this work, we report the synthesis of two new pyridyl urea macrocycles (**4** and **5**) that present exterior pyridines as potential binding sites. This new design should alter

the external hydrogen bond acceptors from the carbonyl O atom in macrocycle **1** to a pyridyl N atom in the new systems. The pyridyl N atom now lies on the exterior of the structures, where it is accessible to guest molecules. The N atom in general is less electronegative than the O atom and is therefore expected to be a better donor of its lone pair of electrons to a wider range of guest species. This switch in the structure should favor formation of different co-crystals, with hydrogen and halogen donors that prefer interaction with aryl nitrogen. In addition, the design increases the distance between the pyridyl N and the urea group, which should reduce competition between the hydrogen bond acceptors (carbonyl O and pyridyl N).

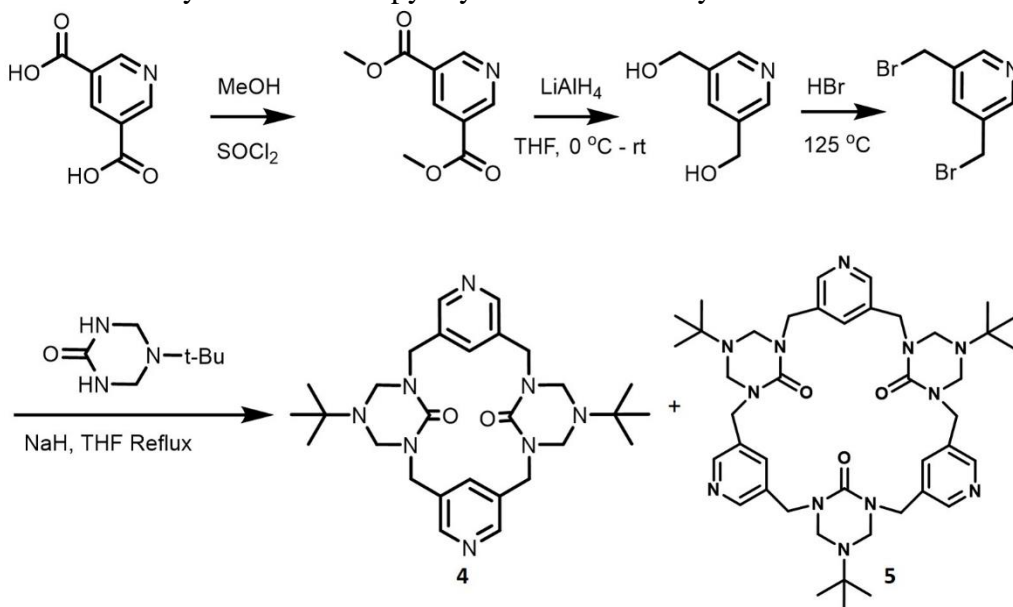
5.2 Synthesis and solution structures of macrocyclic ligand 4-5

Two new pyridyl *bis*-urea macrocyclic ligands (**4-5**) were synthesized in four steps prepared by adopting a modified procedure similar to a previously reported procedure (Scheme 5.2).²¹ The typical approach used in Shimizu's lab, utilizes C-shaped spacers usually in the form of dibromides to react with a protected triazinanone under basic conditions at relatively high dilutions (0.2 mM) in dry tetrahydrofuran (THF) to form cyclic compounds. Here, our required C-shaped spacer (3,5-*bis*(bromomethyl)pyridine hydrobromide) was synthesized in three steps starting with pyridine-3,5-dicarboxylic acid (as shown in scheme 5.2). Esterification of the diacid, reduction of the dicarboxylate by lithium aluminum hydride yielded a diol which was treated with 48% HBr at 125 °C for six hours to yield the C-shaped spacer.

Next, the spacers are typically cyclized with the triazinanone protected urea under basic condition, which usually require four equivalence of sodium hydride as the base. The protecting group serves several functions. It prevents the ureas from self-assembling and

increases the solubility, which aids in purification by column chromatography. The cyclization of 3,5-*bis*(bromomethyl)pyridine hydrobromide with the protected triazinanone was accomplished with an increased amount of sodium hydride (5 equivalents) to afford macrocycle **4** as the major product (30.64% yield) together with macrocycle **5** (10.21% yield). The products were separated by wet loading the crude product (dissolved in minimum CHCl₃) onto a silica gel column then eluting with chloroform/methanol (9:1) solvent mixture. HRMS (ES) calculated for C₂₈H₄₀N₈O₂: [M+H], 521.3347, observed *m/z* 521.3351. NMR of the crude product indicates formation of a tetramer as one of the minor products. However, we are still optimizing the column conditions to see if it can be isolate and characterized.

Scheme 5.2 Synthesis of new pyridyl *bis*-urea macrocycles **4-5**



Macrocycle **4** is similar to a triazinanone macrocycle reported by Dave et al (Figure 5.5).²² By using ¹H-NMR, ¹³C-NMR and 2D correlation experiments they were able to study the structural changes of this macrocycle and compare them to similar structures in solution. Early work indicated that in solution these systems are dominated by conformational

equilibria involving readily interconvertible species with *syn* and *anti* alignments of the urea carbonyl groups (Figure 5.5). Interconversion of these conformers likely occurs by carbonyl through the annulus rotation.²²

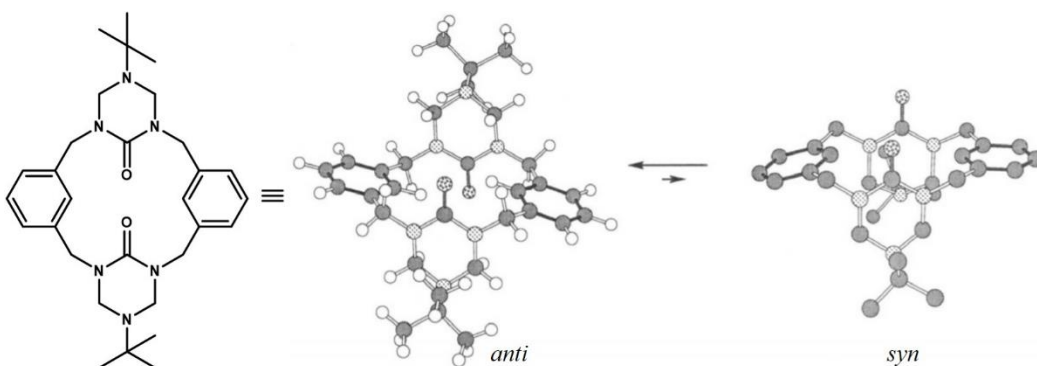


Figure 5.5 Macrocycle incorporating cyclic urea units. Structural studies indicate that these systems in solution are dominated by conformational equilibria involving readily interconvertible species with *syn* and *anti* alignments of the urea carbonyl groups. (Reprinted with permission from Reference 22. Copyright (1995) American Chemical Society).

The structure of dimer macrocycle **4** was investigated by $^1\text{H-NMR}$ and $^{13}\text{C-NMR}$ spectroscopy. Figure 5.6 illustrates proton NMR of **4** recorded at room temperature in chloroform-*d* and in acetonitrile-*d*₃. In both spectra of **4**, the sixteen methylene protons are seen as broad signals at δ 4.22 ppm in chloroform-*d* and 4.20 ppm in acetonitrile-*d*₃. Two sets of signals were expected for these sixteen methylene protons in a ratio of 1:1 representing eight benzylic protons and eight protons from the heterocyclic ring methylene groups. The broadening and only one signal observed for these sixteen methylene protons in the room temperature $^1\text{H-NMR}$ suggest the presence of two or more conformations slowly interconverting on the NMR time scale. A high temperature $^1\text{H NMR}$ was carried out to fully assign these methylene protons. The solvent 1,1,2,2-Tetrachloroethane-*d*₂, was chosen for this experiment as it is a high boiling solvent and dissolves macrocycle **4**.

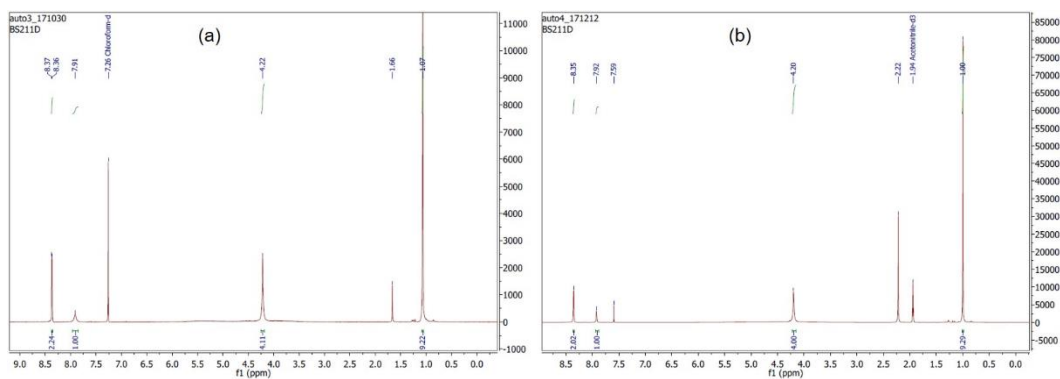


Figure 5.6 Room temperature ^1H NMR (400 MHz) of macrocycle **4** in (a) chloroform- d and (b) acetonitrile- d_3 .

Figure 5.8 shows the ^1H NMR of macrocycle **4** recorded at 125 °C. In this spectrum, we can clearly see two signals for the sixteen methylene protons at δ 4.64 and 4.26 ppm which are assigned to the benzylic protons and the heterocyclic ring methylene protons respectively. The integration ratio of these two sets of methylene protons was 1:1. This suggests that macrocycle **4** exist predominantly in one conformation in solution that slowly interconverts on the NMR time scale. At 125 °C, *t*-butyl protons peak appeared at 1.14 ppm as a singlet while the aromatic protons appeared at 8.40 ppm and 7.98 ppm as singlets (Figure 5.7). When compared to the original protected pyridyl dimer (**1**), these aromatic protons are deshielded probably due to their close proximity to the nitrogen and oxygen atoms which are more electronegative. Integration of all the different proton peaks in this spectrum recorded at 125 °C gave the expected ratio of 2:1:4:4:9 and were fully assigned as shown in Figure 5.8. The ^{13}C NMR spectrum of macrocycle **4** exhibits the requisite number of signals at both room temperature and high temperature (125 °C). Figure 5.8 shows ^{13}C NMR spectrum of macrocycle **4** in acetonitrile- d_3 at room temperature.

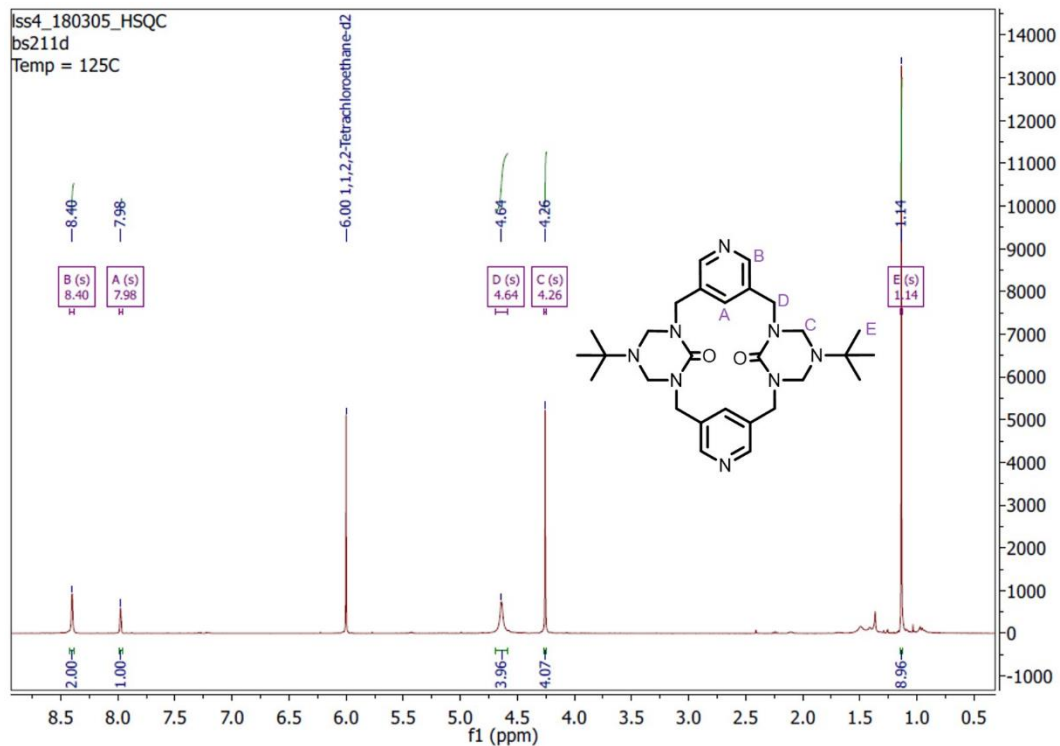


Figure 5.7 ^1H NMR (400 MHz, TCE) of macrocyclic ligand **4** at 125 °C.

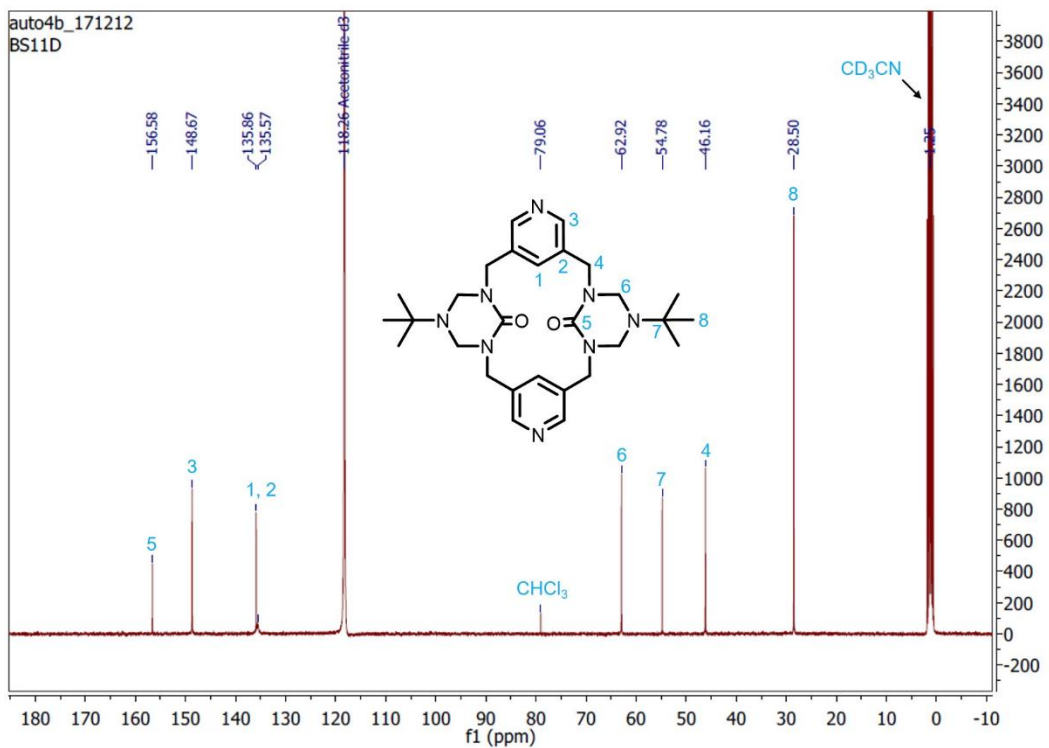


Figure 5.8 ^{13}C NMR (101 MHz, CD_3CN) of macrocyclic ligand **4**.

The ^1H and ^{13}C NMR of macrocycle **5** were both recorded at ambient temperature in acetonitrile- d_3 without much complexity (Figure 5.9 and 5.10). In comparison to the original pyridyl macrocycle (**2**), the aromatic protons are shifted downfield, the methylene protons almost at the same positions whereas the *t*-butyl protons are shifted upfield. In the ^1H NMR spectrum all the expected proton peaks appeared as singlets ($\delta = 8.41, 7.73, 4.50, 4.28, 1.04$ ppm) and were duly assigned with an integration ratio of 2:1:4:4:9. The ^{13}C NMR of macrocycle **5** look more like the original pyridyl macrocycle. HRMS (ES) calculated for $\text{C}_{42}\text{H}_{60}\text{N}_{12}\text{O}_3$: $[\text{M}+\text{H}]$, 781.4984. Observed m/z 781.5001.

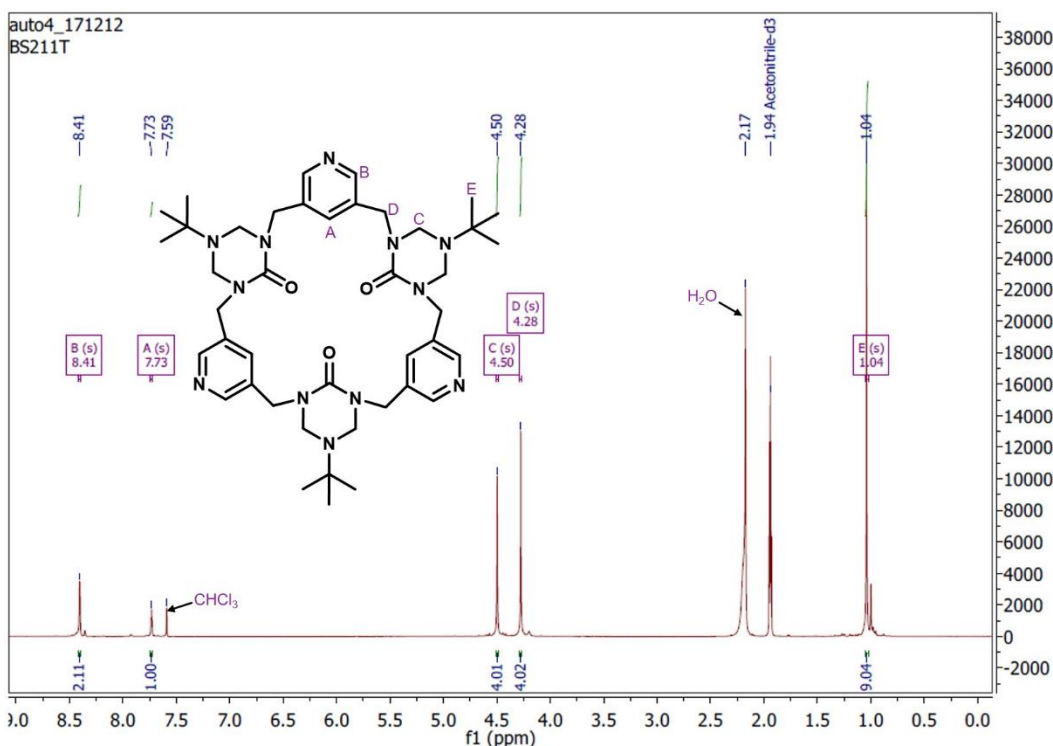


Figure 5.9 ^1H NMR (400 MHz, CD_3CN) of macrocyclic ligand **5**.

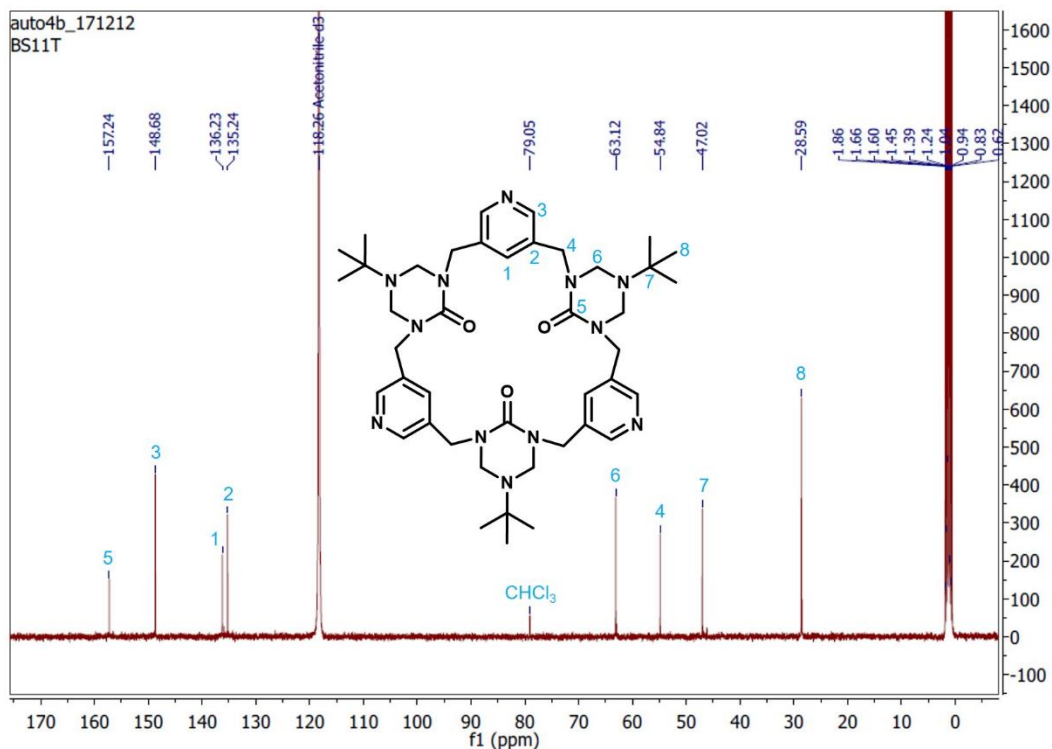


Figure 5.10 ^{13}C NMR (101 MHz, CD_3CN) of macrocyclic ligand **5**.

5.3 X-ray diffraction studies

The solid state structures of macrocycles **4-5**, and coordination complexes $[\text{Cu}_2\text{I}_2(\mathbf{4})_2 \cdot (\text{CH}_3\text{CN})_{1.63(1)}]$ and $[\text{Ag}(\mathbf{4})(\text{NO}_3)(\text{H}_2\text{O})_{2.5}]$ have been determined by single crystal X-ray diffraction analysis. Crystallographic data and structure refinement parameters are summarized in Table 5.1.

5.3.1 Solid state structure of macrocycle **4**

X-ray quality single crystals of macrocycles **4** were crystallized from toluene (3 mg / 1 mL) by slow evaporation to give colorless rhombic plates. The macrocycle (**4**) crystallizes in the triclinic space group $P\bar{1}$ (No. 2) as confirmed by structure solution. The asymmetric unit consists of one complete macrocyclic ligand **4** molecule and half each of two additional ligands **4** molecules, both of which are located on crystallographic inversion

centers. There are three crystallographically independent molecules, two of which are centrosymmetric (Figure 5.11).

Table 5.1 Crystallographic data and structure refinement parameters of macrocyclic ligands **4-5**, and $[\text{Cu}_2\text{I}_2(\mathbf{4})_2 \cdot (\text{CH}_3\text{CN})_{1.63(1)}]$ and $[\text{Ag}(\mathbf{4})(\text{NO}_3)(\text{H}_2\text{O})_{2.5}]$.

	4	5.(toluene)_{0.5}	$[\text{Cu}_2\text{I}_2(\mathbf{4})_2 \cdot (\text{CH}_3\text{CN})_{1.63(1)}]$	$[\text{Ag}(\mathbf{4})(\text{NO}_3)(\text{H}_2\text{O})_{2.5}]$
Empirical formula	C ₂₈ H ₄₀ N ₈ O ₂	C _{45.5} H ₆₄ N ₁₂ O ₃	C _{59.26} H _{84.89} Cu ₂ I ₂ N _{17.63} O ₄	C ₂₈ H _{44.98} AgN ₉ O _{4.49}
Formula weight	520.68	827.08	1489.15	735.42
T/K	100(2)	100(2)	100(2)	100(2)
Crystal system	triclinic	triclinic	triclinic	triclinic
Space group	P-1	P-1	P-1	P1
a/Å	10.6246(5)	10.4105(5)	8.6693(4)	8.9880(3)
b/Å	11.0831(5)	12.8175(6)	13.1139(7)	9.1999(3)
c/Å	22.5999(11)	17.6507(9)	15.1067(8)	10.5400(4)
α/°	90.020(2)	80.247(2)	96.502(2)	70.9060(10)
β/°	90.197(2)	81.253(2)	97.650(2)	88.585(2)
γ/°	94.120(2)	74.289(2)	93.897(2)	76.0530(10)
Volume/Å ³	2654.3(2)	2220.45(19)	1685.20(15)	797.92(5)
Z	4	2	1	1
ρ _{calc} /cm ³	1.303	1.237	1.467	1.530
μ/mm ⁻¹	0.086	0.081	1.604	0.693
F(000)	1120.0	890.0	760.0	383.0
Crystal size/mm ³	0.26 × 0.2 × 0.18	0.4 × 0.24 × 0.06	0.2 × 0.14 × 0.04	0.16 × 0.1 × 0.04
2θ range/°	5.13 to 60.344	4.332 to 52.906	4.414 to 58.256	4.678 to 60.342
Reflections collected	146413	62896	66300	48759
Independent reflections	15682 [R _{int} = 0.0483, R _{sigma} = 0.0352]	9129 [R _{int} = 0.0678, R _{sigma} = 0.0475]	9060 [R _{int} = 0.0433, R _{sigma} = 0.0324]	9401 [R _{int} = 0.0344, R _{sigma} = 0.0319]
Data/restraints	15682/0	9129/15	9060/200	9401/107
Parameters	699	588	491	489
GoF on F ²	1.036	1.019	1.060	1.037
Final R indexes [I >= 2σ(I)]	R ₁ = 0.0449, wR ₂ = 0.1090	R ₁ = 0.0522, wR ₂ = 0.1142	R ₁ = 0.0344, wR ₂ = 0.0703	R ₁ = 0.0276, wR ₂ = 0.0509
Final R indexes [all data]	R ₁ = 0.0635, wR ₂ = 0.1183	R ₁ = 0.0925, wR ₂ = 0.1330	R ₁ = 0.0524, wR ₂ = 0.0773	R ₁ = 0.0329, wR ₂ = 0.0525
Δρ _{max./min.} (e Å ⁻³)	0.42/-0.24	0.35/-0.22	1.04/-0.73	0.32/-0.38

In this structure, the pyridyl groups are positioned in a trans fashion such that **4** can act as a linear bidentate ligand with the exterior nitrogen binding sites (5.11a). These pyridyl N

atoms are poised on the exterior and pointing in opposite directions. On the other hand, the urea carbonyl groups and triazinanone rings are antiparallel to each other. Packing structure of **4** in the solid state is shown in Figure 5.12. The molecules are layered on top each other. There are two layers; one made of molecule A and the other made of alternating molecule B and molecule C.

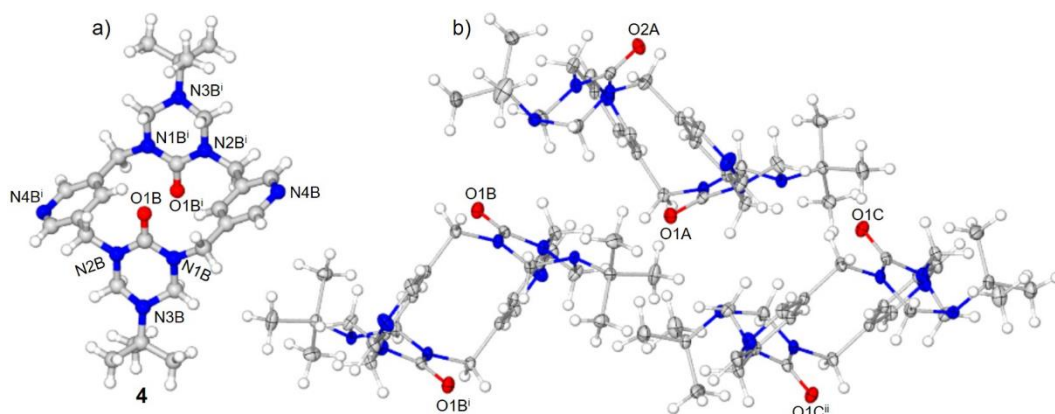


Figure 5.11 Components of the structure of macrocyclic ligand **4**. a) Structure of component B. b) Three crystallographically independent, chemically similar molecules. Molecules B and C are located on crystallographic inversion centers. Superscripts denote symmetry-equivalent atoms. Displacement ellipsoids drawn at the 60% probability level.

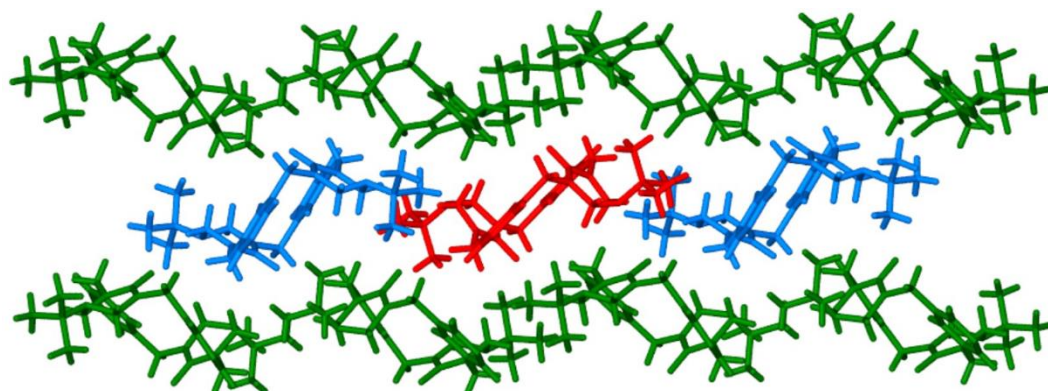


Figure 5.12 Packing diagram of macrocycle **4**. Layered structure made of two types of layers. Layer 1 is made of only molecule A, and layer 2 is made of alternating molecule B and C. Color coded for the crystallographically independent, chemically similar molecules. Molecules A (green), B (blue) and C (red).

All three crystallographically independent macrocycles in the crystal structure of **4** adopted the 1,2-alternate conformation similar to that of calix[4]arenes discussed in section

5.1.^{15, 23-24}. In these structures, the carbonyl groups are parallel and anti to each other while the benzene rings are a little flattened out (Figure 5.13a). In comparison, the previously reported pyridyl-*bis*-urea macrocycle **1**, adopted two conformations; the partial cone and the 1,3-alternate conformations when crystallized from *o*-xylene (polarity of 2.57D) and DMSO (polarity of 47D) respectively (Figure 5.13b-c).¹⁴ in the case of macrocycle **1** it appears the solvent used for the crystallization plays a role type of conformation it adopts. Toluene (2.38 D) which has a similar polarity as *o*-xylene (polarity of 2.57D). Thus, conformational differences between macrocycles **1** and **4** has to do with other factors in addition to solvent polarity. The different location of the pyridyl N in these macrocycles could be a contributory factor. Currently, we are probing the different conformations in macrocycles **1** and **4** by growing crystals of both compounds in the same solvents.

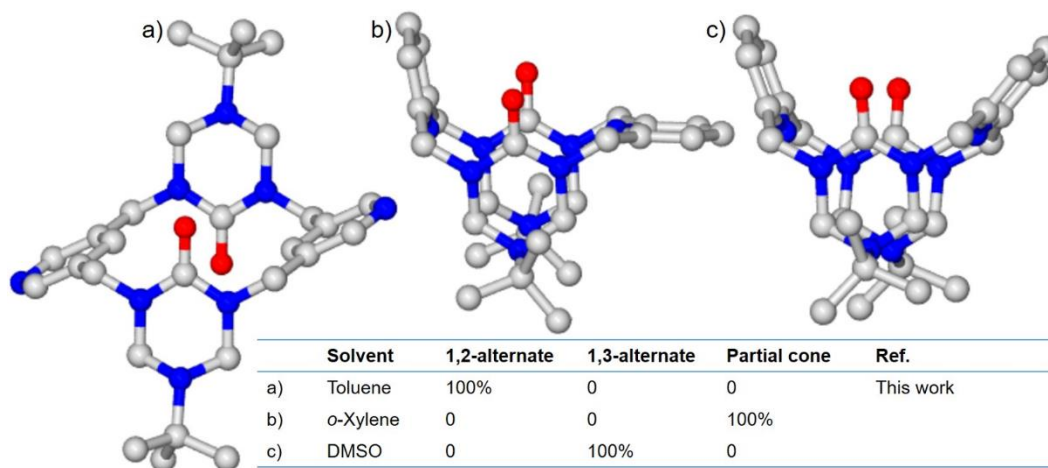


Figure 5.13 Comparison of the solid-state crystal structures of ligand **4** (a) and its constitutional isomer **1** (b & c) reported by Roy *et al.*, 2010, showing different conformations: (a) the 1,2-alternate conformation was observed when crystallized from toluene; (b) a partial cone conformer was observed when crystallized from *o*-xylene; (c) the 1,3-alternate conformation was observed when crystallized from DMSO. Hydrogen atoms omitted for clarity.

5.3.2 Solid state structure of macrocycle **5**

Single crystals of **5** were obtained from toluene (3 mg / 1 mL) by slow evaporation to give colorless plates. This macrocycle crystallizes as a toluene hemisolvate in the triclinic space group $P-1$ (No. 2). The asymmetric unit consists of one macrocycle **5** molecule and half of one toluene molecule (Figure 5.14). The toluene is disordered over a crystallographic inversion center and was refined with half-occupancy. This structure suggests that macrocycle **5** is much more flexible such that it can fold inwards with no specific directionality of the various functional groups. Two pyridyl N atoms and one carbonyl O atom are pointing in one side while the other two carbonyl O atoms and one pyridyl N atom points in the opposite direction. Packing diagram is shown in Figure 5.15.

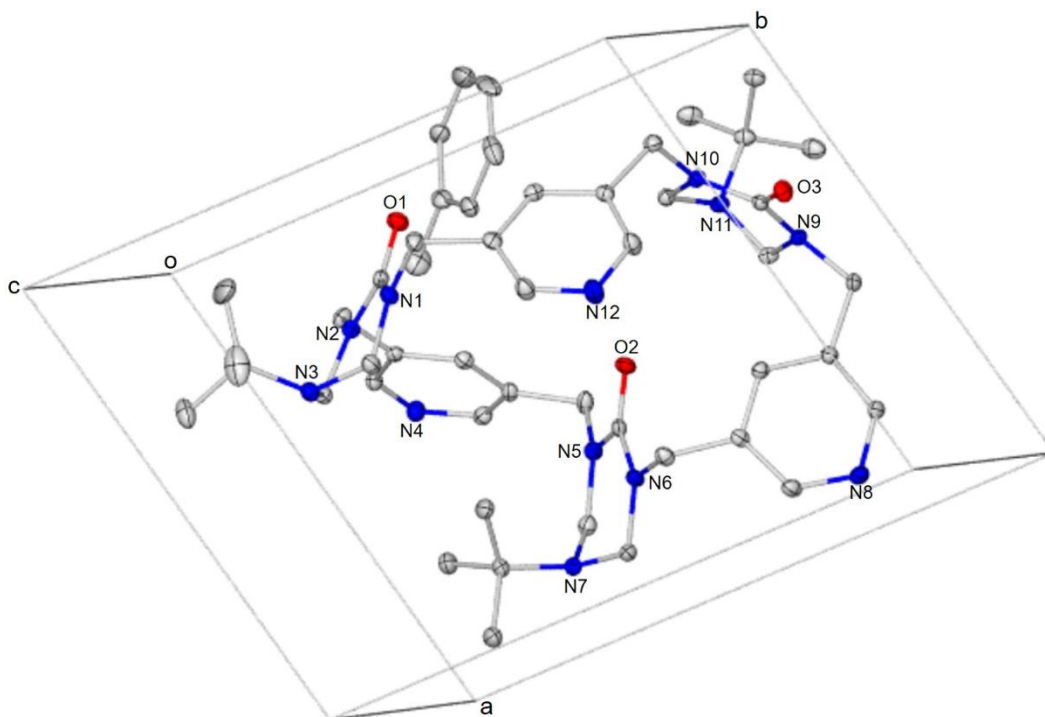


Figure 5.14 Components of the structure of macrocyclic ligand **5**. Hydrogen atoms in crystal structure are omitted for clarity. Displacement ellipsoids drawn at the 30% probability level.

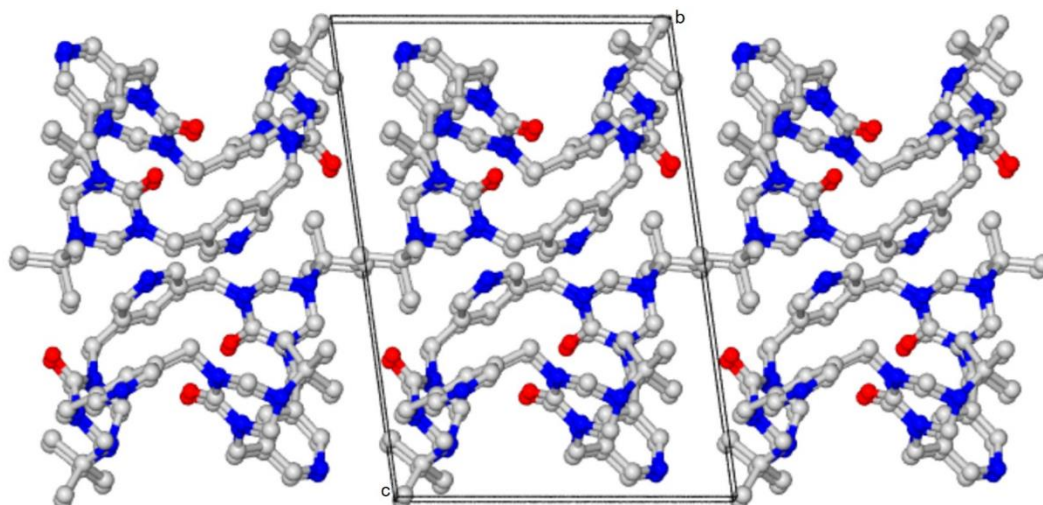


Figure 5.15 Packing diagram of macrocycle **5**. Solvent molecules and hydrogen atoms omitted for clarity.

5.4 Investigation of complex formation between **4** and d^{10} transition metal ions

Structural analysis of macrocycles **4-5** by NMR and single crystal X-ray diffraction revealed that these structures are flexible and should be amenable to rotation and folding to adopt optimal structures for binding metal ions. Our first studies probed these macrocycles as ligands for d^{10} metal ions such as Cu(I) and Ag(I) which are known to form one-, two- and three-dimensional structures in the solid state with interesting properties.

Copper (I) complexes with polypyridines ligands have been intensively investigated because copper is a relatively inexpensive and abundant noble metal, which in its Cu(I) d^{10} electronic configuration has demonstrated tunable photochemical and photophysical properties.²⁵⁻²⁷ Linear N-heterocyclic organic ligands have been utilized to assemble $[Cu_nI_n]$ -based CPs.²⁸ This makes macrocycles **4-5** structurally intriguing as they would generate new ways of networking macrocyclic building units in CPs. Ag(I) ion, with a d^{10} closed-shell electronic configuration shows (i) a dynamic range of coordinative geometries, including linear, trigonal-planar, tetrahedral, and trigonal-pyramidal, with rare occurrences of square-planar, pyramidal, and octahedral geometry,²⁹⁻³¹ and (ii) a tendency

to form an argentophilic interaction,³² both of which may lead to discovery of novel structural motifs. Reaction of ligand **4** with copper(I) iodide and silver(I) nitrate resulted in two coordination polymers $[\text{Cu}_2\text{I}_2(\mathbf{4})_2 \cdot (\text{CH}_3\text{CN})_{1.63(1)}]$ and $[\text{Ag}(\mathbf{4})(\text{NO}_3)(\text{H}_2\text{O})_{2.5}]$. Coordination polymer $[\text{Cu}_2\text{I}_2(\mathbf{4})_2 \cdot (\text{CH}_3\text{CN})_{1.63(1)}]$ was synthesized by mixing dichloromethane solution of ligand **4** and acetonitrile solution of copper(I) iodide for one hour at room temperature. The resulting solid was then dissolved in acetonitrile and slowly evaporated to form single crystals of $[\text{Cu}_2\text{I}_2(\mathbf{4})_2 \cdot (\text{CH}_3\text{CN})_{1.63(1)}]$. In the case of $[\text{Ag}(\mathbf{4})(\text{NO}_3)(\text{H}_2\text{O})_{2.5}]$, both ligand **4** and silver nitrate were each dissolved in hot acetonitrile. The solutions were mixed, cooled and allowed to slowly evaporate over 2-3 days producing crystals. These coordination polymers were characterized by standard techniques including IR, elemental analysis, UV-vis and fluorescence spectroscopies and single crystal X-ray diffraction. The single crystal characterization of the complexes showed that the macrocyclic ligand adopted different conformations with respect to the metal ion. In the copper(I) complex ligand **4** adopted a 1,2-alternate conformation while in the silver(I) complex it adopted a flattened cone conformation.

5.4.1 Copper coordination complex $[\text{Cu}_2\text{I}_2(\mathbf{4})_2 \cdot (\text{CH}_3\text{CN})_{1.63(1)}]$

Ligand **4** (3.0 mg, 5.76×10^{-3} mmol) and AgNO_3 (1.95 mg, 11.5×10^{-3} mmol) were both dissolved in hot acetonitrile (1.0 mL). The solutions were mixed, cooled and allowed to slowly evaporate over 2-3 days producing single crystals suitable for X-ray diffraction studies. Complex $[\text{Cu}_2\text{I}_2(\mathbf{4})_2 \cdot (\text{CH}_3\text{CN})_{1.63(1)}]$ crystallizes in a triclinic space group *P*-1 (No. 2). The asymmetric unit consists of one copper and one iodine atom, half each of two $\text{C}_{28}\text{H}_{40}\text{N}_8\text{O}_2$ ligands and two acetonitrile molecules (Figure 5.16a). There are two crystallographically independent macrocyclic ligands. One of the macrocyclic ligands is

disordered across an inversion center over two orientations and there is some acetonitrile mixed among the disordered ligand atoms. Only the protected urea part is disordered; the $\text{CH}_2(\text{pyridyl})\text{CH}_2$ linker is common to both. The disorder components each has an occupancy of 50% (Figure 5.16b). The single crystal X-ray analysis reveals that $[\text{Cu}_2\text{I}_2(\mathbf{4})_2 \cdot (\text{CH}_3\text{CN})_{1.63(1)}]$ is a 2D sheet coordination polymer built from Cu_2I_2 units linked by the protected macrocyclic ligands ($\mathbf{4}$) through their pyridyl N atoms (Figure 5.17).

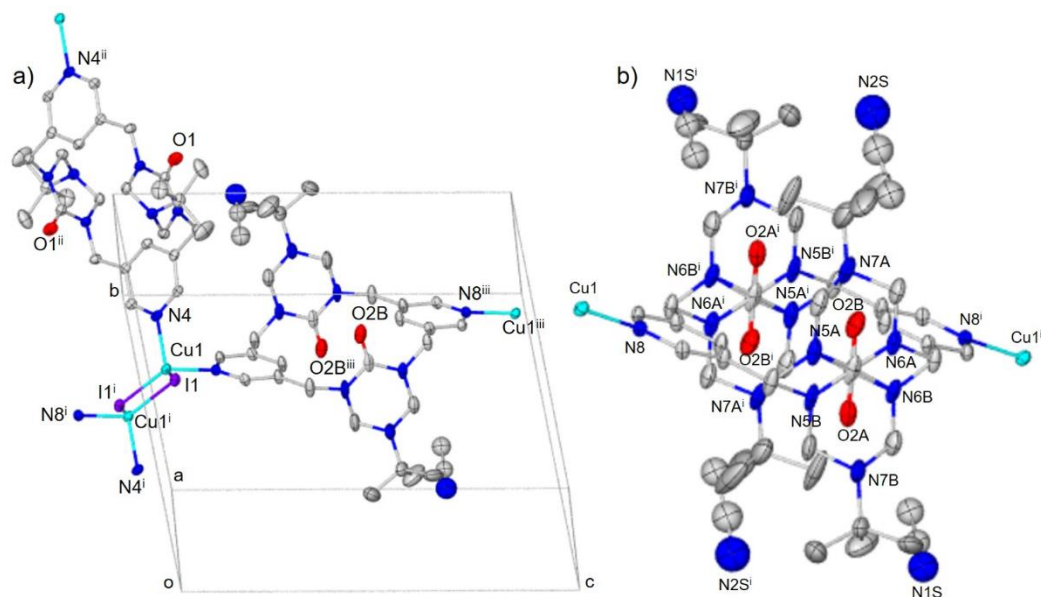


Figure 5.16 a) Components of the crystal structure of $[\text{Cu}_2\text{I}_2(\mathbf{4})_2 \cdot (\text{CH}_3\text{CN})_{1.63(1)}]$, expanded by symmetry containing only one component of the disordered ligand. b) Disorder of one ligand across inversion center, generating two orientations. Both components shown. Each has an occupancy of 50%. Displacement ellipsoids drawn at the 50% probability level. Superscripts denote symmetry-equivalent atoms.

The Cu_2I_2 group is formed as a rhombus and each Cu(I) center is coordinated by two ligands through the pyridyl N atoms creating a tetrahedral coordination geometry around the Cu(I) center with Cu-N bonds of 2.070(2) Å (Cu1-N4) and 2.074(2) Å (Cu1-N8) respectively. Bond lengths of Cu-I are 2.6051(4) and 2.6294(4) Å. The $\text{Cu} \cdots \text{Cu}$ distance is 2.5989(6) Å as a diagonal of the Cu_2I_2 rhombus repeating motif. This $\text{Cu} \cdots \text{Cu}$ distance is shorter than the sum of the van der Waals radii of two Cu atoms (2.8 Å)³³⁻³⁴ and very

close to that in copper metal (2.56 Å), suggesting strong cuprophilic interaction that may significantly affect the photophysical properties. In this structure, ligand **1** acted as a bidentate-bridging ligand coordinating the Cu(I) centers with both pyridyl N atoms.

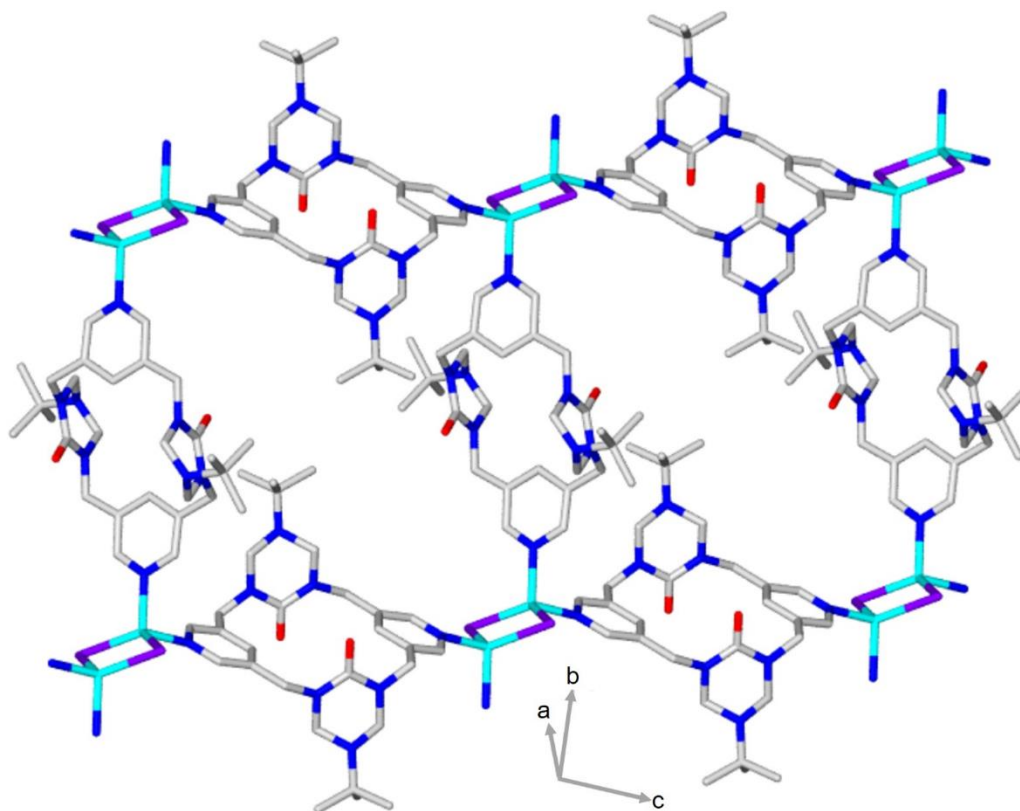


Figure 5.17 Coordination network of $[\text{Cu}_2\text{I}_2(\mathbf{4})_2 \cdot (\text{CH}_3\text{CN})_{1.63(1)}]$ with disorder component B. Macrocyclic ligands link Cu_2I_2 unit through pyridyl N atoms into infinite 2D layers. Solvent molecules are omitted for clarity.

5.4.2 Silver coordination complex $[\text{Ag}(\mathbf{4})(\text{NO}_3)(\text{H}_2\text{O})_{2.5}]$

$[\text{Ag}(\mathbf{4})(\text{NO}_3)(\text{H}_2\text{O})_{2.5}]$ crystallizes in the triclinic system with the acentric group *P*1 (No. 1). Figure 5.18 shows the asymmetric unit of the crystal structure of $[\text{Ag}(\mathbf{4})(\text{NO}_3)(\text{H}_2\text{O})_{2.5}]$. Each Ag(I) center adopts a distorted tetrahedral coordination geometry where the metal center is coordinated by two pyridyl N donors, one carbonyl O donor from ligand **4**, and the O atom of a nitrate anion. In this structure the macrocyclic ligand **4** adopted a flattened cone conformation with the carbonyl groups on the same side. The Ag-N bond distances were 2.167(2) and 2.166(2) Å, while the Ag-O bond distances

are 2.517(18) and 2.529(14) Å respectively. There are 1D chains formed by N-Ag-N links (angle 154°) between pyridyl N atoms of two adjacent macrocyclic ligands and Ag(I) ion (Figure 5.19). A further, longer, Ag-O interaction of 2.52 Å links the Ag centers to a carbonyl O atom of neighboring chain, making 2D layers (Figure 5.20). Furthermore, some hydrogen bonding between the interstitial water molecules and a protecting group N atom exists, forming a 3D structure (Figure 5.21). The nitrate and the interstitial waters are disordered in the crystal structure.

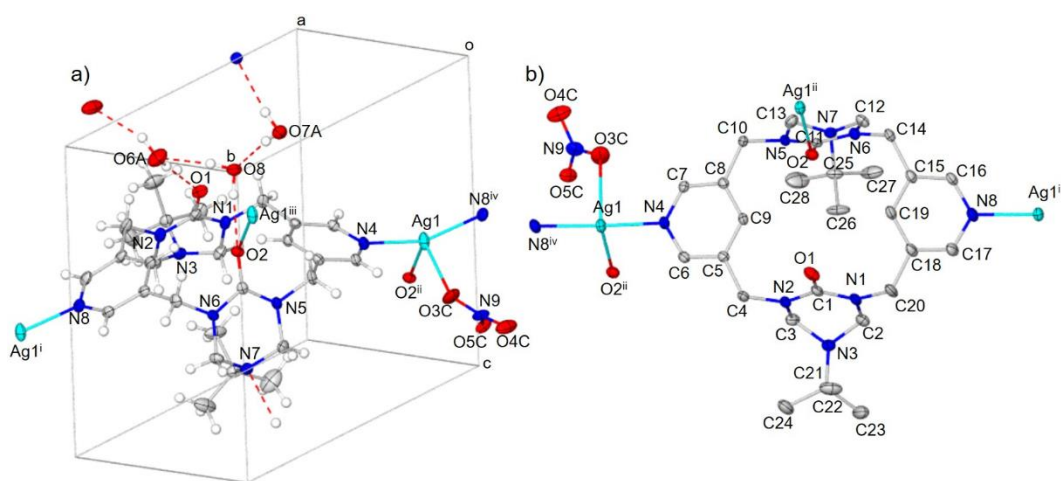


Figure 5.18 Components of the crystal structure of [Ag(4)(NO₃)(H₂O)_{2.5}]. a) Asymmetric unit of the crystal structure of [Ag(4)(NO₃)(H₂O)_{2.5}] with additional atoms to complete Ag and ligand coordination environments. Only one component each of the disordered nitrate and water molecules are shown. Hydrogen bonds are dashed lines. b) Ag and ligand environment, hydrogens and water molecules are omitted for clarity. Displacement ellipsoids drawn at the 50% probability level. Superscripts denote symmetry-equivalent atoms.

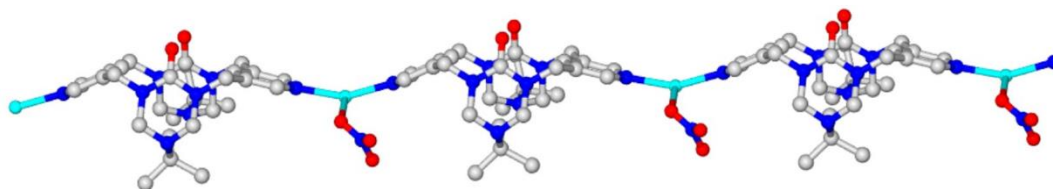


Figure 5.19 1D chains showing the side and top views of the coordination environments of Ag(I) ions in [Ag(4)(NO₃)(H₂O)_{2.5}] along the crystallographic [110] direction. One nitrate disorder component shown. Solvent molecules are omitted for clarity.

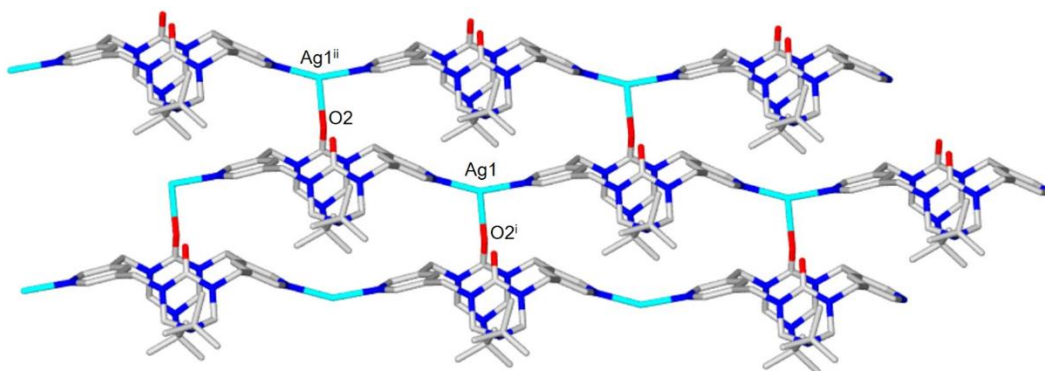


Figure 5.20 2D layers in crystal structure of $[\text{Ag}(\mathbf{4})(\text{NO}_3)(\text{H}_2\text{O})_{2.5}]$. Ag1-O2 interaction between chains creates 2D layers parallel to the crystallographic (001) plane. Solvent molecules and nitrate ions are omitted for clarity.

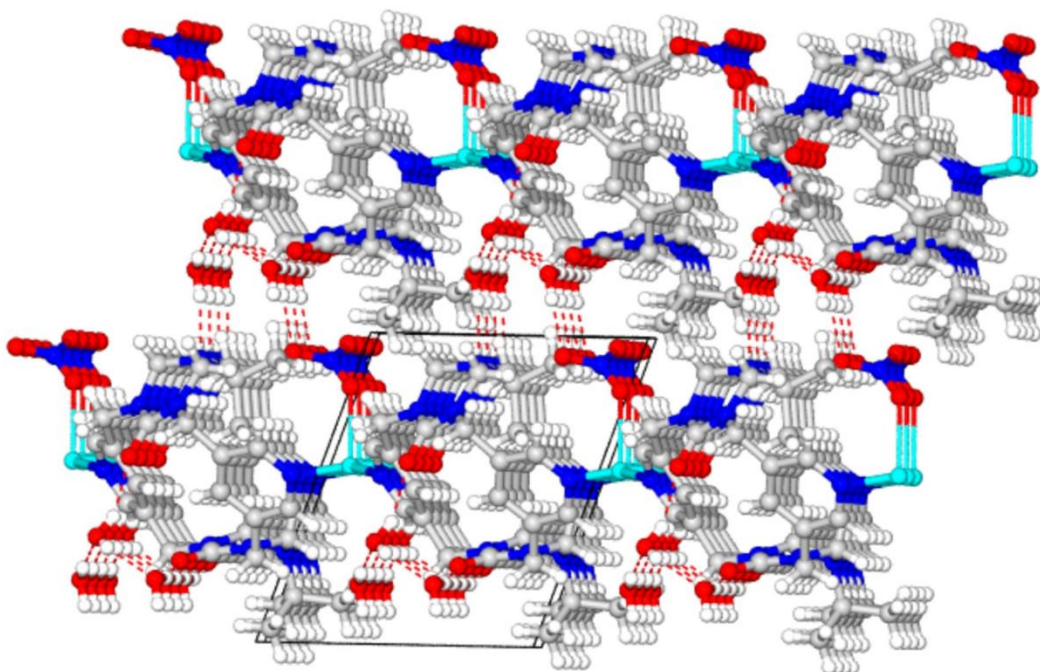


Figure 5.21 Packing diagram of $[\text{Ag}(\mathbf{4})(\text{NO}_3)(\text{H}_2\text{O})_{2.5}]$. OH-N hydrogen bonding (O7---N7) links 2D layers into 3D structure.

5.5 FT-IR spectroscopy

Further investigation on different functionalities present in the ligand structure and the change in electronic states upon complexation are analyzed using FT-IR. Comparison of the solid state infrared (IR) spectra of the synthesized ligand **4** and coordination complexes is shown in (Figures 5.22). The IR spectrum of ligand **4** exhibit a strong band at 1631 cm^{-1}

¹ which is attributed to the carbonyl (C=O) group. Upon coordination the intensity of this band decreased considerably in both $[\text{Cu}_2\text{I}_2(\mathbf{4})_2 \cdot (\text{CH}_3\text{CN})_{1.63(1)}]$ and $[\text{Ag}(\mathbf{4})(\text{NO}_3)(\text{H}_2\text{O})_{2.5}]$. In coordination complex $[\text{Cu}_2\text{I}_2(\mathbf{4})_2 \cdot (\text{CH}_3\text{CN})_{1.63(1)}]$ the band is split in two at 1615 and 1638 cm^{-1} , indicating two different carbonyl groups are present in the complex. This is reasonable as the single crystal X-ray structure of $[\text{Cu}_2\text{I}_2(\mathbf{4})_2 \cdot (\text{CH}_3\text{CN})_{1.63(1)}]$ (Figure 5.16) displays two crystallographically independent macrocyclic ligands of **4**. A similar splitting of the carbonyl group was observed in the spectrum of $[\text{Ag}(\mathbf{4})(\text{NO}_3)(\text{H}_2\text{O})_{2.5}]$ at 1615 and 1632 cm^{-1} corresponding to a coordinating carbonyl group (C=O-Ag) and an uncoordinated carbonyl group (C=O) respectively. Another key functional group in the structure of ligand **4** is the C=N (pyridine) group. The absorption band of this group shifted to higher wavenumbers (by 7-10 cm^{-1}) in complexes indicating coordination to metal centers (Table 5.2). Broad bands are observed at 3479 cm^{-1} for $[\text{Cu}_2\text{I}_2(\mathbf{4})_2 \cdot (\text{CH}_3\text{CN})_{1.63(1)}]$ and 3409 cm^{-1} for $[\text{Ag}(\mathbf{4})(\text{NO}_3)(\text{H}_2\text{O})_{2.5}]$, which are absent in the spectrum of ligand **4**. These bands are attributed to the interstitial solvent molecules (CH_3CN and H_2O) present in the structures of $[\text{Cu}_2\text{I}_2(\mathbf{4})_2 \cdot (\text{CH}_3\text{CN})_{1.63(1)}]$ and $[\text{Ag}(\mathbf{4})(\text{NO}_3)(\text{H}_2\text{O})_{2.5}]$ respectively.

Table 5.2 FT-IR peak positions of key functional groups in ligand **4** and its coordination polymers, $[\text{Cu}_2\text{I}_2(\mathbf{4})_2 \cdot (\text{CH}_3\text{CN})_{1.63(1)}]$ and $[\text{Ag}(\mathbf{4})(\text{NO}_3)(\text{H}_2\text{O})_{2.5}]$.

	IR bands (cm^{-1})	
	$\nu_{\text{C=O}}$	$\nu_{\text{C=N}}$
Ligand 4	1631	1503
$[\text{Cu}_2\text{I}_2(\mathbf{4})_2 \cdot (\text{CH}_3\text{CN})_{1.63(1)}]$	1615, 1638	1511
$[\text{Ag}(\mathbf{4})(\text{NO}_3)(\text{H}_2\text{O})_{2.5}]$	1615, 1632	1513

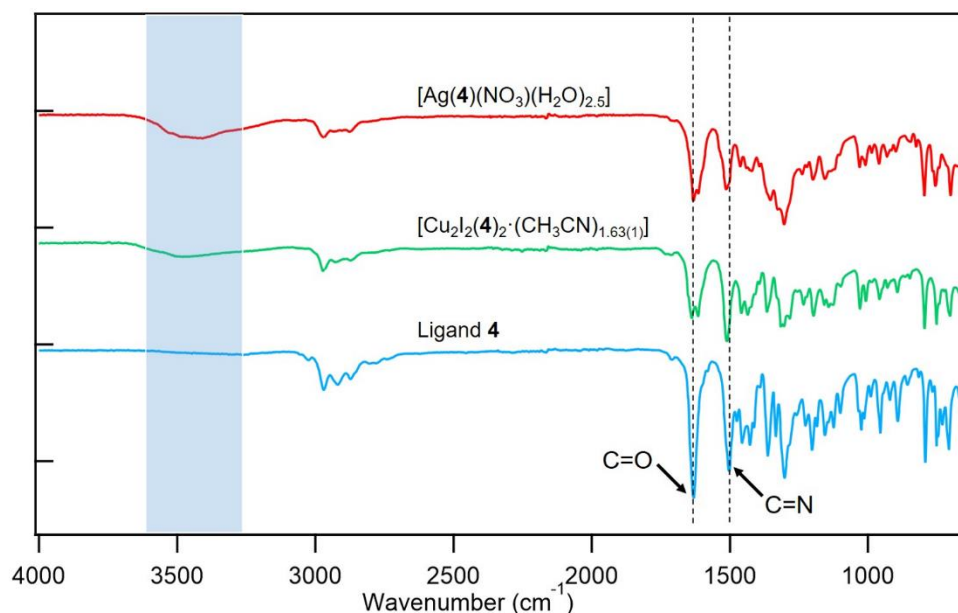


Figure 5.22 FT-IR profiles of ligand **4** and coordination complexes in the range 4000–650 cm^{-1} .

5.6 Photophysical studies of coordination complexes

The photophysical properties of d^{10} metal complexes, especially Cu(I) species are well-studied because many Cu(I) complexes are emissive. Therefore, we investigated the photophysical properties of these new complexes in the solid state. Figure 5.23a shows the UV-vis diffuse reflectance spectra of ligand **4** and complexes that were recorded in the solid state at room temperature. All three compounds exhibit a transition band at 230-300 nm corresponding to intraligand $\pi \rightarrow \pi^*$ or $n \rightarrow \pi^*$ transitions of the macrocyclic ligand **4**. This band is however slightly shifted compared to that of ligand **4** which is in support of coordination to a metal ion. A broad band was observed at 330-500 nm with a true maximum at 395 nm for coordination complex $[\text{Cu}_2\text{I}_2(\mathbf{4})_2 \cdot (\text{CH}_3\text{CN})_{1.63(1)}]$. While a band appearing in the range of 330-600 nm with maximum at 450 nm was observed in the spectrum of coordination complex $[\text{Ag}(\mathbf{4})(\text{NO}_3)(\text{H}_2\text{O})_{2.5}]$. These second bands in $[\text{Cu}_2\text{I}_2(\mathbf{4})_2 \cdot (\text{CH}_3\text{CN})_{1.63(1)}]$ and $[\text{Ag}(\mathbf{4})(\text{NO}_3)(\text{H}_2\text{O})_{2.5}]$ which are absent in the spectrum of ligand **4** is attributed to a mixture of metal-to-ligand charge transfer (MLCT).³⁵

The photoluminescence properties of ligand **4** along with the coordination complexes in the solid state at room temperature were examined. Upon excitation with UV light (330-385 nm) emissions were observed for only ligand **4** and complex $[\text{Cu}_2\text{I}_2(\mathbf{4})_2 \cdot (\text{CH}_3\text{CN})_{1.63(1)}]$ (Figure 5.23b). The emission of ligand **4** was in the range 420-660 nm with λ_{max} at ca. 495 nm (blue luminescence), which is likely attributed to $\pi\text{-}\pi^*$ transitions. Cu_nI_n cluster compounds have been studied by many research groups for their photophysical luminescent properties under different conditions such as temperature, vapors and stress.³⁶⁻³⁸ Photoluminescence in Cu(I) CPs with N donor ligands and various Cu_nI_n geometries such as rhomboid-like, stair step-like, cubane-like, etc. is a phenomenon observed in many cases. Several of these reports show that the emission energies of copper(I)-halide complexes are strongly affected by the N-heteroaromatic ligands and $[\text{Cu}_n\text{I}_n]$ motifs.^{26, 28} The origins of the luminescent may arise from iodide-to-copper(I) charge transfer (XMCT), ligand-to-metal charge transfer (LMCT), halogen-to-ligand charge transfer (XLCT), cluster-centered (CC*) transition, or the admixture of more than one of the above. Computational investigation of the excited state surfaces would be the next step in evaluating the origins of these bands. Complex $[\text{Cu}_2\text{I}_2(\mathbf{4})_2 \cdot (\text{CH}_3\text{CN})_{1.63(1)}]$, which contains a Cu_2I_2 unit, exhibits broad emission between 460 and 680 nm with λ_{max} at ca. 540 nm (green). There is significant red-shifting in the emission of $[\text{Cu}_2\text{I}_2(\mathbf{4})_2 \cdot (\text{CH}_3\text{CN})_{1.63(1)}]$ from that of ligand **4** (λ_{max} at ca. 495 nm) indicating the emission band of $[\text{Cu}_2\text{I}_2(\mathbf{4})_2 \cdot (\text{CH}_3\text{CN})_{1.63(1)}]$ may not be intraligand charge transition in nature.

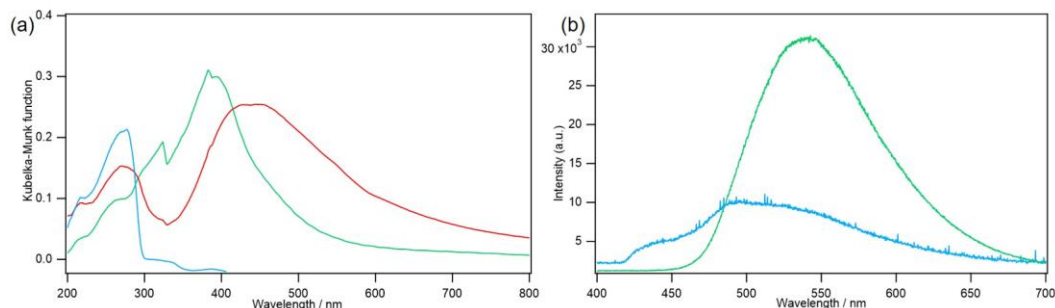


Figure 5.23 Solid state UV-visible diffuse reflectance and photoluminescence spectra. (a) Solid state UV-visible diffuse reflectance spectra of ligand **4** (blue), complex $[\text{Cu}_2\text{I}_2(\mathbf{4})_2 \cdot (\text{CH}_3\text{CN})_{1.63(1)}]$ (green) and complex $[\text{Ag}(\mathbf{4})(\text{NO}_3)(\text{H}_2\text{O})_{2.5}]$ (red). (b) Solid state photoluminescence spectra of ligand **4** (blue) ($\lambda_{\text{ex}} = 330\text{-}385$ nm; $\lambda_{\text{em}} = 495$) and complex $[\text{Cu}_2\text{I}_2(\mathbf{4})_2 \cdot (\text{CH}_3\text{CN})_{1.63(1)}]$ (green) ($\lambda_{\text{ex}} = 330\text{-}385$ nm; $\lambda_{\text{em}} = 540$) at room temperature.

Based on reports of similar copper(I) complexes and the Cu...Cu distance (2.5989(6) Å) within the $[\text{Cu}_2(\mu - \text{I})_2]$ units in $[\text{Cu}_2\text{I}_2(\mathbf{4})_2 \cdot (\text{CH}_3\text{CN})_{1.63(1)}]$, the emission band of the complex likely corresponds to a combination of metal-to-ligand charge transfer (MLCT), iodide-to-ligand charge transfer (XMCT), halogen-to-ligand charge transfer (XLCT) and cluster-centered (CC*) transitions. The existence of a CC* contribution is supported by the probable Cu...Cu interactions, which play a key role in the photoluminescence of Cu(I) complexes. Copper(I) complexes consisting of Cu_2I_2 units are well known to show promising luminescence properties,³⁹⁻⁴⁰ which prompted us to study the luminescence behavior of these complexes. The high-energy luminescence observed at ca. 540 nm further suggests that the transitions are localized on the Cu_2I_2 cluster and are essentially independent of the ligand.⁴¹ Surprisingly the Ag(I) complex of the same ligand did not show any emission properties in the solid-state when irradiated with UV light at room temperature. This probably due to the absence of Ag...Ag interactions and the coordination mode of ligand **4**.

5.7 Conclusion

In summary, the redesigned pyridyl *bis*-urea macrocycles (**4-5**) showed several structural differences when compared to the previously reported pyridyl *bis*-urea macrocycles (**1-3**) which contain the pyridyl N in the interior of the macrocycle. The dimers (**4** and **1**) adopted different conformations in the solid state. Macrocycle **4** adopted 1,2-alternate when crystallized from toluene, whilst **1** adopted the partial cone and the 1,3-alternate conformations when crystallized from *o*-xylene and DMSO respectively. The recognition properties of these redesigned macrocycles is currently ongoing. At the moment we have only screened the ability of macrocycles **4-5** to bind transition metal ions. However, it is in our future plan to test binding with other guest molecules such hydrogen/halogen bond donors, especially with the deported dimer of **4** (see Appendix D).

The smaller ligand **4** was used to prepare coordination polymers based on copper(I) iodide and silver(I) nitrate using solvothermal methods. Single crystal X-ray diffraction was used to confirm the structures of all the compounds. Ligand **4**, a more rigid structure than **5** acted as a multidentate ligand to form coordination complexes with Cu(I) and Ag(I) to give $[\text{Cu}_2\text{I}_2(\mathbf{4})_2 \cdot (\text{CH}_3\text{CN})_{1.63(1)}]$ and $[\text{Ag}(\mathbf{4})(\text{NO}_3)(\text{H}_2\text{O})_{2.5}]$ respectively. In complex $[\text{Cu}_2\text{I}_2(\mathbf{4})_2 \cdot (\text{CH}_3\text{CN})_{1.63(1)}]$, ligand **4** is a bidentate ligand only binding through the pyridyl N atoms. It however behaved as a tridentate in complex $[\text{Ag}(\mathbf{4})(\text{NO}_3)(\text{H}_2\text{O})_{2.5}]$, binding through the pyridyl N atoms and one carbonyl O atom. No coordination complexes of flexible ligand **5** have been obtained at this time. These complexes present extended architectures with interesting dimensionality from 1D to 3D structures. Also, ligand **4** adopted different conformations in the complex of Cu(I) versus that of Ag(I). The 1,2-alternate conformation of ligand **4** in complex $[\text{Cu}_2\text{I}_2(\mathbf{4})_2 \cdot (\text{CH}_3\text{CN})_{1.63(1)}]$ renders the

carbonyl O atoms inert to coordination, which effects the formation of extended 2D networks through the peripheral pyridyl N ligation sites only. On the other hand, the flattened cone conformation of ligand **4** in $[\text{Ag}(\mathbf{4})(\text{NO}_3)(\text{H}_2\text{O})_{2.5}]$ made the carbonyl O atoms more accessible and therefore they were able to participate in coordination to the metal center. Luminescence studies of ligand **4** and complexes in the solid state revealed a blue emission for ligand **4**, green emission for complex $[\text{Cu}_2\text{I}_2(\mathbf{4})_2 \cdot (\text{CH}_3\text{CN})_{1.63(1)}]$ and no emission for complex $[\text{Ag}(\mathbf{4})(\text{NO}_3)(\text{H}_2\text{O})_{2.5}]$ when irradiated with UV light (330 – 385 nm). On the basis of these results, further syntheses and studies of ligand **4** complexes of Cu(I) and Ag(I) containing different anions to determine if that is a structural determinant or has any influence on the luminescence properties of the complexes.

5.8 Experimental

5.8.1 Materials and Methods

Unless otherwise specified, all chemicals were purchased from commercial sources (Sigma-Aldrich, Alfa Aesar, TCI or VWR) and used without further purification. Dimethyl pyridine-3,5-dicarboxylate, 3,5-*bis*(hydroxymethyl)pyridine and 3,5-*bis*(bromomethyl)pyridine hydrobromide were prepared according to published literature procedures respectively.⁴²⁻⁴⁴ Triazinanone was prepared as previously described.⁴⁵ The macrocyclic ligands **4-5** were synthesized according scheme 5.2. ¹H NMR and ¹³C NMR were recorded on Varian Mercury/VX 400 NMR spectrometer. FT-IR spectra were obtained with a Perkin Elmer Spectrum 100 FT-IR Spectrometer over the range 4000-650 cm⁻¹ with 2 cm⁻¹ resolution and 32 scans per sample. Solid-state diffuse-reflectance spectra were recorded using a PerkinElmer Lambda 35 UV–visible scanning spectrophotometer

equipped with an integrating sphere. Emission spectra were recorded by an Ocean Optics USB 4000 spectrometer under 330-385 nm excitation at room temperature.

5.8.2 Synthesis

Dimethyl pyridine-3,5-dicarboxylate. Thionyl chloride (1.3 mL, 17.94 mmol) was added dropwise to a stirring solution of pyridine-3,5-dicarboxylic acid (1.0 g, 5.98 mmol) in dry methanol (10 mL) at 0 °C. The reaction was heated at reflux (3 h) after which the mixture was cooled to room temperature then concentrated *in vacuo*. The residue was diluted with water (100 mL) and extracted with ethyl acetate (100 mL). The aqueous layer was neutralized with 8M NaOH solution and extracted ethyl acetate again (100 mL). The combined organic layers were washed with saturated NaHCO₃ solution and brine, dried over anhydrous Na₂SO₄. Finally, the solvent removed under reduced pressure to give a white solid material (0.8 g, 68% yield). ¹H NMR (300 MHz, CDCl₃): δ = 9.37 (d, *J* = 2.0 Hz, 2H), 8.87 (t, *J* = 2.1 Hz, 1H), 3.99 (s, 6H).

3,5-Bis(hydroxymethyl)pyridine. The dimethyl pyridine-3,5-dicarboxylate (2.10 g, 10.76 mmol) was dissolved in dry THF (150 mL) and added dropwise to a suspension of LiAlH₄ (1.02 g, 26.90 mmol in 150 mL of THF) in an ice/acetone bath (0 °C) under nitrogen. After addition, the resulting yellow mixture was allowed to warm gradually to r.t. then left overnight. Upon completion, the reaction mixture was quenched by sequentially adding H₂O (1 mL), 10% NaOH (2 mL) and H₂O (3 mL). The mixture was suction filtered, and the yellow filtrate dried over anhydrous MgSO₄. Removal of the solvent under reduced pressure followed by drying under vacuum to give a yellow solid crude (1.12 g, 75 % yield). The product was used directly for the next reaction without any further purification.

3,5-Bis(bromomethyl)pyridine Hydrobromide. To the crude 3,5-bis(hydroxymethyl)pyridine (1.12 g, 8.05 mmol) was added to a 250 mL round bottom flask and 48% HBr (15 mL) was slowly and carefully added. The reaction mixture was stirred and heated at 125 °C for 6 hours. The reaction was cooled to room temperature, and 40 mL H₂O was added slowly at room temperature then adjusted the pH to 8 with saturated NaHCO₃. The resulting whitish precipitate was collected by suction filtration and washed with H₂O (10 mL). This crude product was dried under vacuum overnight (1.56 g, 55.86 % yield). ¹H-NMR (300 MHz, CDCl₃): δ = 8.56 (d, *J* = 2.0 Hz, 2H), 7.77 (t, *J* = 2.0 Hz, 1H), 4.47 (s, 4H).

Macrocyclic ligands (4-5). An oven dried 500 mL round bottom flask was filled with a suspension of triazinanone (0.30 g, 1.88 mmol) and NaH (0.39 g, 9.76 mmol) in dry THF (100 mL) was refluxed for 2 hours under nitrogen then cooled to room temperature. To this cooled mixture, a solution of 3,5-bis(bromomethyl)pyridine hydrobromide (0.65 g, 1.88 mmol) in THF (50 mL) was added in one portion. The reaction mixture stirred and heated to reflux under nitrogen for 48 hours while monitoring the reaction with TLC (Scheme 5.1). Upon completion (based on TLC monitoring), the reaction mixture was cooled to room temperature and quenched with water (100 mL). The volume of the resulting solution was reduced by rotary evaporation to a minimum and extracted with DCM (3 x 100 mL). The DCM layers were combined, washed with brine, dried with anhydrous MgSO₄ and the solvent removed under reduced pressure to give a yellow solid. Purification of the crude material (wet loaded) by silica gel chromatography with CHCl₃/MeOH (9:1) afforded macrocycles **4-5** in the elution order of **4** (0.15 g, 30.64 %), **4** (0.05 g, 10.21 %). X-ray quality single crystals were grown by slow evaporation from toluene (3 mg / 1 mL).

Macrocycle **4**; ^1H NMR (400 MHz, TCE) δ 8.40 (s, 2H), 7.98 (s, 1H), 4.64 (s, 4H), 4.26 (s, 4H), 1.14 (s, 9H); ^{13}C NMR (101 MHz, CD_3CN) δ = 156.58, 148.67, 135.86, 62.92, 54.78, 46.16, 28.50: Melting point 268-271 °C. HRMS (ES) calculated for $\text{C}_{28}\text{H}_{40}\text{N}_8\text{O}_2$: [M+H], 521.3347. Observed m/z 521.3351. IR (neat ATR) 2969, 1630, 1503, 1427, 1362, 1302, 1202, 1156, 1025, 955, 893, 793, 752, 707 cm^{-1} . Macrocycle **5**; ^1H NMR (400 MHz, CD_3CN): δ = 8.41 (s, 2H), 7.73 (s, 1H), 4.50 (s, 4H), 4.28 (s, 4H), 1.04 (s, 9H); ^{13}C NMR (101 MHz, CD_3CN) δ = 157.24, 148.68, 136.23, 135.23, 63.12, 54.84, 47.02, 28.59: IR (neat ATR) 2965, 1632, 1500, 1429, 1364, 1304, 1198, 1125, 1029, 796, 754, 708 cm^{-1} . HRMS (ES) calculated for $\text{C}_{42}\text{H}_{60}\text{N}_{12}\text{O}_3$: [M+H], 781.4984. Observed m/z 781.5001.

Complex $[\text{Cu}_2\text{I}_2(\text{C}_{28}\text{H}_{40}\text{N}_8\text{O}_2)_2 \cdot (\text{CH}_3\text{CN})_{1.63(1)}$]. The protected pyridyl macrocyclic ligand (**4**) (10 mg, 0.0192 mmol) was dissolved in dichloromethane (1 mL) and was added to acetonitrile solution of CuI (3.65 mg, 0.0192 mmol in 1.0 mL). The mixture stirred at room temperature for an hour. This resulted in a white powder that was collected by filtration, washed with diethyl ether-acetonitrile mixture and chloroform then dried under vacuum. Yield: 10.4 mg (76 %). X-ray quality single crystals were grown by dissolving 3 mg of the powder obtained from the above synthesis in 10 mL acetonitrile and allowed to slowly evaporate over 5 days. IR (neat ATR) 3479, 2973, 1638, 1511, 1436, 1366, 1304, 1234, 1197, 1143, 1029, 959, 894, 795, 752, 703 cm^{-1} .

Complex $[\text{Ag}(\text{C}_{28}\text{H}_{40}\text{N}_8\text{O}_2)](\text{NO}_3) \cdot (\text{H}_2\text{O})_{2.49(1)}$. Ligand **4** (3.0 mg, 5.76×10^{-3} mmol) and AgNO_3 (1.95 mg, 11.5×10^{-3} mmol) were both dissolved in hot acetonitrile (1.0 mL). The solutions were mixed, cooled and allowed to slowly evaporate over 2-3 days. A cluster of colorless block crystals formed that were suitable for single crystal X-ray diffraction. Yield

70% (2.96 mg). IR (neat ATR) 3409, 2969, 1632, 1513,1420, 1304,1199, 1156, 1031, 960, 932, 900, 796, 757, 701 cm^{-1} .

5.8.3 X-ray Crystal Structure Determination

Ligand 4 ($\text{C}_{28}\text{H}_{40}\text{N}_8\text{O}_2$). X-ray intensity data from a colorless block were collected at 100(2) K using a Bruker D8 QUEST diffractometer equipped with a PHOTON-100 CMOS area detector and an Incoatec microfocus source (Mo $\text{K}\alpha$ radiation, $\lambda = 0.71073 \text{ \AA}$). The raw area detector data frames were reduced and corrected for absorption effects using the Bruker APEX3, SAINT+ and SADABS programs.⁴⁶⁻⁴⁷ Final unit cell parameters were determined by least-squares refinement of 9795 reflections taken from the data set. The structure was solved with SHELXT.⁴⁸⁻⁴⁹ Subsequent difference Fourier calculations and full-matrix least-squares refinement against F^2 were performed with SHELXL-2017⁴⁸⁻⁴⁹ using OLEX2.⁵⁰

The compound crystallizes in the triclinic system. The space group $P-1$ (No. 2) was confirmed by structure solution. The asymmetric unit consists of one complete $\text{C}_{28}\text{H}_{40}\text{N}_8\text{O}_2$ molecule and half each of two additional $\text{C}_{28}\text{H}_{40}\text{N}_8\text{O}_2$ molecules, both of which are located on crystallographic inversion centers. The molecules were numbered similarly except for atom label suffixes A, B, or C. All non-hydrogen atoms were refined with anisotropic displacement parameters. Hydrogen atoms bonded to carbon were located in Fourier difference maps before being placed in geometrically idealized positions and included as riding atoms with $d(\text{C-H}) = 1.00 \text{ \AA}$ and $U_{\text{iso}}(\text{H}) = 1.2U_{\text{eq}}(\text{C})$ for methine hydrogen atoms, $d(\text{C-H}) = 0.95 \text{ \AA}$ and $U_{\text{iso}}(\text{H}) = 1.2U_{\text{eq}}(\text{C})$ for aromatic hydrogen atoms, $d(\text{C-H}) = 0.99 \text{ \AA}$ and $U_{\text{iso}}(\text{H}) = 1.2U_{\text{eq}}(\text{C})$ for methylene hydrogen atoms, and $d(\text{C-H}) = 0.98 \text{ \AA}$ and $U_{\text{iso}}(\text{H}) = 1.5U_{\text{eq}}(\text{C})$ for methyl hydrogens. The methyl hydrogens were allowed to rotate as a rigid

group to the orientation of maximum observed electron density. The largest residual electron density peak in the final difference map is 0.42 e-/Å³, located 0.67 Å from C5C. The crystal was a pseudo-merohedral twin emulating the monoclinic system, to which it is metrically similar. The twin law is (-1 0 0 / 0 -1 0 / 0 0 1), a two-fold axis around [001]. Including this twin law in the refinement lowered the residual from $R1 = 0.083$ to $R1 = 0.045$. The minor twin volume fraction refined to 0.089(2).

Ligand 5 [C₄₂H₆₀N₁₂O₃·(C₇H₈)_{0.5}]. X-ray intensity data from a colorless plate were collected at 100(2) K using a Bruker D8 QUEST diffractometer equipped with a PHOTON-100 CMOS area detector and an Incoatec microfocus source (Mo K α radiation, $\lambda = 0.71073$ Å). The raw area detector data frames were reduced and corrected for absorption effects using the Bruker APEX3, SAINT+ and SADABS programs.⁴⁶⁻⁴⁷ Final unit cell parameters were determined by least-squares refinement of 9906 reflections taken from the data set. The structure was solved with SHELXT.⁴⁸⁻⁴⁹ Subsequent difference Fourier calculations and full-matrix least-squares refinement against F^2 were performed with SHELXL-2017⁴⁸⁻⁴⁹ using OLEX2.⁵⁰

The compound crystallizes in the triclinic system. The space group $P-1$ (No. 2) was confirmed by structure solution. The asymmetric unit consists of one C₄₂H₆₀N₁₂O₃ molecule and half of one toluene molecule. The toluene is disordered over a crystallographic inversion center and was refined with half-occupancy. All toluene ring C-C distances were restrained to be similar. All non-hydrogen atoms were refined with anisotropic displacement parameters. Hydrogen atoms bonded to carbon were located in Fourier difference maps before being placed in geometrically idealized positions and included as riding atoms with $d(\text{C-H}) = 0.95$ Å and $U_{\text{iso}}(\text{H}) = 1.2U_{\text{eq}}(\text{C})$ for aromatic

hydrogen atoms, $d(\text{C-H}) = 0.99 \text{ \AA}$ and $U_{\text{iso}}(\text{H}) = 1.2U_{\text{eq}}(\text{C})$ for methylene hydrogen atoms, and $d(\text{C-H}) = 0.98 \text{ \AA}$ and $U_{\text{iso}}(\text{H}) = 1.5U_{\text{eq}}(\text{C})$ for methyl hydrogens. The methyl hydrogens were allowed to rotate as a rigid group to the orientation of maximum observed electron density. The largest residual electron density peak in the final difference map is 0.35 e-/\AA^3 , located 0.93 \AA from H34A.

Complex $[\text{Cu}_2\text{I}_2(\text{C}_{28}\text{H}_{40}\text{N}_8\text{O}_2)_2 \cdot (\text{CH}_3\text{CN})_{1.63(1)}]$. X-ray intensity data from a colorless rhombic plate were collected at $100(2) \text{ K}$ using a Bruker D8 QUEST diffractometer equipped with a PHOTON-100 CMOS area detector and an Incoatec microfocus source (Mo $K\alpha$ radiation, $\lambda = 0.71073 \text{ \AA}$). The raw area detector data frames were reduced and corrected for absorption effects using the Bruker APEX3, SAINT+ and SADABS programs.⁴⁶⁻⁴⁷ Final unit cell parameters were determined by least-squares refinement of 9531 reflections taken from the data set. The structure was solved with SHELXT.⁴⁸⁻⁴⁹ Subsequent difference Fourier calculations and full-matrix least-squares refinement against F_2 were performed with SHELXL-2018⁴⁸⁻⁴⁹ using OLEX2.⁵⁰

The compound crystallizes in the triclinic system. The space group $P-1$ (No. 2) was confirmed by structure solution. The asymmetric unit consists of one copper and one iodine atom, half each of two $\text{C}_{28}\text{H}_{40}\text{N}_8\text{O}_2$ ligands and two acetonitrile molecules. Both $\text{C}_{28}\text{H}_{40}\text{N}_8\text{O}_2$ ligands are located on inversion centers. One is disordered about the inversion center such that only the protected urea part of the ligand (atoms O2, N5-N7, C15-C17, C25-C28) is affected. The linking *bis*(methylene)pyridyl atoms (N8, C18-C24) are common to both disorder orientations. Atoms of each disorder component were given label suffixes A or B and were refined with fixed occupancies of 0.5. For stability, 1,2 and 1,3 bond distances in the disorder components were restrained to be similar to those in the

ordered protected urea group using SHELX SAME instructions. Each protected urea component is disordered together with an acetonitrile molecule, *i.e.* when a given orientation of the urea disorder component is absent an acetonitrile is present. Two partially occupied acetonitrile molecules were refined: one (N1S-C2S) with occupancies fixed at 0.5 and the other (N2S-C4S) with a refined occupancy of 0.316(8). Appropriate acetonitrile N-C and C-C distance restraints were applied. Similar disorder was observed in the acentric space group *P1* (No. 1). All non-hydrogen atoms were refined with anisotropic displacement parameters except for acetonitrile atoms (isotropic). Hydrogen atoms were placed in geometrically idealized positions and included as riding atoms with $d(\text{C-H}) = 0.95 \text{ \AA}$ and $U_{\text{iso}}(\text{H}) = 1.2U_{\text{eq}}(\text{C})$ for aromatic hydrogen atoms, $d(\text{C-H}) = 0.99 \text{ \AA}$ and $U_{\text{iso}}(\text{H}) = 1.2U_{\text{eq}}(\text{C})$ for methylene hydrogen atoms, and $d(\text{C-H}) = 0.98 \text{ \AA}$ and $U_{\text{iso}}(\text{H}) = 1.5U_{\text{eq}}(\text{C})$ for methyl hydrogens. The methyl hydrogens were allowed to rotate as a rigid group to the orientation of maximum observed electron density. The largest residual electron density peak in the final difference map is $1.04 \text{ e}^{-}/\text{\AA}^3$, located 1.10 \AA from H2SA.

Complex $[\text{Ag}(\text{C}_{28}\text{H}_{40}\text{N}_8\text{O}_2)](\text{NO}_3) \cdot (\text{H}_2\text{O})_{2.49(1)}$. X-ray intensity data from an irregular colorless block were collected at 100(2) K using a Bruker D8 QUEST diffractometer equipped with a PHOTON-100 CMOS area detector and an Incoatec microfocus source (Mo $K\alpha$ radiation, $\lambda = 0.71073 \text{ \AA}$). Crystals of the compound invariably grew as intergrown blocky aggregations from which a suitably single crystalline specimen was cleaved apart. The raw area detector data frames were reduced and corrected for absorption effects using the Bruker APEX3, SAINT+ and SADABS programs.^{47, 51} Final unit cell parameters were determined by least-squares refinement of 9762 reflections taken from the data set. The structure was solved with SHELXT.⁴⁸⁻⁴⁹ Subsequent difference Fourier calculations and

full-matrix least-squares refinement against F^2 were performed with SHELXL-2018⁴⁸⁻⁴⁹ using OLEX2.⁵⁰

The compound crystallizes in the triclinic system. Intensity statistics suggested an acentric structure. The solution program XT returned the acentric group $P1$ (No. 1) as the only reasonable choice. This space group was subsequently confirmed by structure solution and by ADDSYM, which found no missed inversion center.⁵²⁻⁵⁵ The asymmetric unit consists of one silver atom, one $C_{28}H_{40}N_8O_2$ ligand, one nitrate anion and three water molecules. The nitrate anion and water molecules are disordered. The nitrate was modeled using three components A/B/C, whose total occupancy was constrained to sum to one. Occupancies refined to A/B/C = 0.423(4)/0.361(4)/0.216(4). Nitrate N-O and O-O distances were restrained to be approximately equal to those of the same kind (SHELX SADI). Two of the three water molecules (O6 and O7) are disordered over two closely separated sites A/B. The occupancies of the two sites were also constrained to sum to one, and refined to O6A/O6B = 0.905(8)/0.095(8) and O7A/O7B = 0.554(8)/0.446(8). The third water oxygen, O8, refined to a partial occupancy value of 0.490(8). All non-hydrogen atoms were refined with anisotropic displacement parameters. Hydrogen atoms bonded to carbon were located in difference Fourier maps before being placed in geometrically idealized positions and included as riding atoms with $d(C-H) = 0.95 \text{ \AA}$ and $U_{iso}(H) = 1.2U_{eq}(C)$ for aromatic hydrogen atoms, $d(C-H) = 0.99 \text{ \AA}$ and $U_{iso}(H) = 1.2U_{eq}(C)$ for methylene hydrogen atoms, and $d(C-H) = 0.98 \text{ \AA}$ and $U_{iso}(H) = 1.5U_{eq}(C)$ for methyl hydrogens. The methyl hydrogens were allowed to rotate as a rigid group to the orientation of maximum observed electron density. Plausible water hydrogen positions could be located for all but the minor disorder component O6B (10% occupancy). Distance restraints

of $d(\text{O-H}) = 0.85(2) \text{ \AA}$ and $d(\text{H-H}) = 1.35 \text{ \AA}$ were applied and these atoms were refined isotropically. This resulted in reasonable hydrogen-bonding geometries and displacement parameters, giving good support to the located positions. The largest residual electron density peak in the final difference map is 0.32 e-/\AA^3 , located 0.52 \AA from H22C. The final absolute structure (Flack) parameter was $-0.042(5)$.

5.9 References

1. Leong, W. L.; Vittal, J. J., One-Dimensional Coordination Polymers: Complexity and Diversity in Structures, Properties, and Applications. *Chem. Rev.* **2011**, *111* (2), 688-764.
2. Carlucci, L.; Ciani, G.; Proserpio, D. M.; Mitina, T. G.; Blatov, V. A., Entangled Two-Dimensional Coordination Networks: A General Survey. *Chem. Rev.* **2014**, *114* (15), 7557-7580.
3. Farha, O. K.; Özgür Yazaydın, A.; Eryazici, I.; Malliakas, C. D.; Hauser, B. G.; Kanatzidis, M. G.; Nguyen, S. T.; Snurr, R. Q.; Hupp, J. T., De novo synthesis of a metal-organic framework material featuring ultrahigh surface area and gas storage capacities. *Nature Chemistry* **2010**, *2*, 944.
4. Ma, S.; Zhou, H.-C., Gas storage in porous metal-organic frameworks for clean energy applications. *Chem. Commun.* **2010**, *46* (1), 44-53.
5. Zhao, M.; Ou, S.; Wu, C.-D., Porous Metal-Organic Frameworks for Heterogeneous Biomimetic Catalysis. *Acc. Chem. Res.* **2014**, *47* (4), 1199-1207.
6. Dechambenoit, P.; Long, J. R., Microporous magnets. *Chem. Soc. Rev.* **2011**, *40* (6), 3249-3265.

7. Zhang, D.; Xue, Z.-Z.; Pan, J.; Li, J.-H.; Wang, G.-M., Dual Ligand Strategy for Constructing a Series of d10 Coordination Polymers: Syntheses, Structures, Photoluminescence, and Sensing Properties. *Crystal Growth & Design* **2018**, *18* (3), 1882-1890.
8. Mitra, A.; Hubley, C. T.; Panda, D. K.; Clark, R. J.; Saha, S., Anion-directed assembly of a non-interpenetrated square-grid metal-organic framework with nanoscale porosity. *Chem. Commun.* **2013**, *49* (59), 6629-6631.
9. Du, M.; Li, C.-P.; Liu, C.-S.; Fang, S.-M., Design and construction of coordination polymers with mixed-ligand synthetic strategy. *Coord. Chem. Rev.* **2013**, *257* (7), 1282-1305.
10. Wang, S.-L.; Hu, F.-L.; Zhou, J.-Y.; Zhou, Y.; Huang, Q.; Lang, J.-P., Rigidity versus Flexibility of Ligands in the Assembly of Entangled Coordination Polymers Based on Bi- and Tetra Carboxylates and N-Donor Ligands. *Crystal Growth & Design* **2015**, *15* (8), 4087-4097.
11. Tian, L.-I.; Wang, C.; Dawn, S.; Smith, M. D.; Krause, J. A.; Shimizu, L. S., Macrocycles with Switchable exo/endo Metal Binding Sites. *J. Am. Chem. Soc.* **2009**, *131* (48), 17620-17629.
12. Dawn, S.; Salpage, S. R.; Smith, M. D.; Sharma, S. K.; Shimizu, L. S., A trinuclear silver coordination polymer from a bipyridine bis-urea macrocyclic ligand and silver triflate. *Inorg. Chem. Commun.* **2012**, *15*, 88-92.
13. Salpage, S. R.; Paul, A.; Som, B.; Banerjee, T.; Hanson, K.; Smith, M. D.; Vannucci, A. K.; Shimizu, L. S., Structural, electrochemical and photophysical properties

of an exocyclic di-ruthenium complex and its application as a photosensitizer. *Dalton Transactions* **2016**, 45 (23), 9601-9607.

14. Roy, K.; Wang, C.; Smith, M. D.; Pellechia, P. J.; Shimizu, L. S., Alkali Metal Ions As Probes of Structure and Recognition Properties of Macrocyclic Pyridyl Urea Hosts. *The Journal of Organic Chemistry* **2010**, 75 (16), 5453-5460.

15. Böhmer, V., Calixarenes, Macrocycles with (Almost) Unlimited Possibilities. *Angewandte Chemie International Edition in English* **1995**, 34 (7), 713-745.

16. Thondorf, I., Conformational interconversions of partially dehydroxylated calix[4]arenes. A molecular mechanics study [dagger]. *Journal of the Chemical Society, Perkin Transactions 2* **1999**, (8), 1791-1796.

17. Matthews, S. E.; Cecioni, S.; O'Brien, J. E.; MacDonald, C. J.; Hughes, D. L.; Jones, G. A.; Ashworth, S. H.; Vidal, S., Fixing the Conformation of Calix[4]arenes: When Are Three Carbons Not Enough? *Chemistry – A European Journal* **2018**, 24 (17), 4436-4444.

18. Geer, M. F.; Mazzuca, J.; Smith, M. D.; Shimizu, L. S., Short, strong halogen bonding in co-crystals of pyridyl bis-urea macrocycles and iodoperfluorocarbons. *CrystEngComm* **2013**, 15 (46), 9923-9929.

19. Messina, M. T.; Metrangolo, P.; Panzeri, W.; Pilati, T.; Resnati, G., Intermolecular recognition between hydrocarbon oxygen-donors and perfluorocarbon iodine-acceptors: the shortest O...I non-covalent bond. *Tetrahedron* **2001**, 57 (40), 8543-8550.

20. Roy, K.; Smith, M. D.; Shimizu, L. S., 1D coordination network formed by a cadmium based pyridyl urea helical monomer. *Inorg. Chim. Acta* **2011**, 376 (1), 598-604.

21. Roy, K.; Wang, C.; Smith, M. D.; Dewal, M. B.; Wibowo, A. C.; Brown, J. C.; Ma, S.; Shimizu, L. S., Guest induced transformations of assembled pyridyl *bis*-urea macrocycles. *Chem. Commun.* **2011**, 47 (1), 277-279.
22. Dave, P. R.; Doyle, G.; Axenrod, T.; Yazdekhasti, H.; Ammon, H. L., Novel Macrocycles Incorporating Cyclic Urea Units. *The Journal of Organic Chemistry* **1995**, 60 (21), 6946-6952.
23. Macias, A. T.; Norton, J. E.; Evanseck, J. D., Impact of Multiple Cation- π Interactions upon Calix[4]arene Substrate Binding and Specificity. *J. Am. Chem. Soc.* **2003**, 125 (8), 2351-2360.
24. Kim, S. K.; Lynch, V. M.; Hay, B. P.; Kim, J. S.; Sessler, J. L., Ion pair-induced conformational motion in calix[4]arene-strapped calix[4]pyrroles. *Chemical Science* **2015**, 6 (2), 1404-1413.
25. Hasegawa, T.; Kobayashi, A.; Ohara, H.; Yoshida, M.; Kato, M., Emission Tuning of Luminescent Copper(I) Complexes by Vapor-Induced Ligand Exchange Reactions. *Inorg. Chem.* **2017**, 56 (9), 4928-4936.
26. Li, J.-C.; Li, H.-X.; Li, H.-Y.; Gong, W.-J.; Lang, J.-P., Ligand Coordination Site-Directed Assembly of Copper(I) Iodide Complexes of ((Pyridyl)-1-pyrazolyl)pyridine. *Crystal Growth & Design* **2016**, 16 (3), 1617-1625.
27. Kitada, N.; Ishida, T., Polymeric one- and two-dimensional copper(i) iodide complexes showing photoluminescence tunable by azaaromatic ligands. *CrystEngComm* **2014**, 16 (34), 8035-8040.
28. Hu, M.-C.; Wang, Y.; Zhai, Q.-G.; Li, S.-N.; Jiang, Y.-C.; Zhang, Y., Synthesis, Crystal Structures, and Photoluminescent Properties of the Cu(I)/X/ α,ω -

Bis(benzotriazole)alkane Hybrid Family (X = Cl, Br, I, and CN). *Inorg. Chem.* **2009**, *48* (4), 1449-1468.

29. Burchell, T. J.; Eisler, D. J.; Puddephatt, R. J., Hierarchy of Hydrogen Bonding versus Anion Binding in Self-Assembled Network Structures of Silver(I). *Crystal Growth & Design* **2006**, *6* (4), 974-982.

30. Hanton, L. R.; Young, A. G., Square-Planar Silver(I)-Containing Polymers Formed from π -Stacked Entities. *Crystal Growth & Design* **2006**, *6* (4), 833-835.

31. Sun, D.; Zhang, N.; Huang, R.-B.; Zheng, L.-S., Series of Ag(I) Coordination Complexes Derived from Aminopyrimidyl Ligands and Dicarboxylates: Syntheses, Crystal Structures, and Properties. *Crystal Growth & Design* **2010**, *10* (8), 3699-3709.

32. Schmidbaur, H.; Schier, A., Argentophilic Interactions. *Angew. Chem. Int. Ed.* **2015**, *54* (3), 746-784.

33. Kim, T. H.; Shin, Y. W.; Jung, J. H.; Kim, J. S.; Kim, J., Crystal-to-Crystal Transformation between Three CuI Coordination Polymers and Structural Evidence for Luminescence Thermochromism. *Angew. Chem. Int. Ed.* **2008**, *47* (4), 685-688.

34. Peng, R.; Li, M.; Li, D., Copper(I) halides: A versatile family in coordination chemistry and crystal engineering. *Coord. Chem. Rev.* **2010**, *254* (1), 1-18.

35. Ye, Q.; Wang, X.-S.; Zhao, H.; Xiong, R.-G., Highly stable olefin-Cu(I) coordination oligomers and polymers. *Chem. Soc. Rev.* **2005**, *34* (3), 208-225.

36. Kang, G.; Jeon, Y.; Lee, K. Y.; Kim, J.; Kim, T. H., Reversible Luminescence Vapochromism and Crystal-to-Amorphous-to-Crystal Transformations of Pseudopolymorphic Cu(I) Coordination Polymers. *Crystal Growth & Design* **2015**, *15* (11), 5183-5187.

37. Park, H.; Kwon, E.; Chiang, H.; Im, H.; Lee, K. Y.; Kim, J.; Kim, T. H., Reversible Crystal Transformations and Luminescence Vapochromism by Fast Guest Exchange in Cu(I) Coordination Polymers. *Inorg. Chem.* **2017**, *56* (14), 8287-8294.
38. Perruchas, S.; Le Goff, X. F.; Maron, S.; Maurin, I.; Guillen, F.; Garcia, A.; Gacoin, T.; Boilot, J.-P., Mechanochromic and Thermochromic Luminescence of a Copper Iodide Cluster. *J. Am. Chem. Soc.* **2010**, *132* (32), 10967-10969.
39. Zhao, H.; Li, X.; Wang, J.; Li, L.; Wang, R., Synthesis and Crystal Structures of Coordination Complexes Containing Cu₂I₂ Units and Their Application in Luminescence and Catalysis. *ChemPlusChem* **2013**, *78* (12), 1491-1502.
40. Li, H.-H.; Wang, Y.-J.; Dong, H.-J.; Chen, Z.-R.; Wu, Y.-L.; Wang, M.; Huang, S.-W., An organic-inorganic hybrid heterobridging luminescent copper(i) polymer exhibiting thermochromic behavior. *CrystEngComm* **2011**, *13* (6), 1778-1781.
41. Gallego, A.; Castillo, O.; Gómez-García, C. J.; Zamora, F.; Delgado, S., Electrical Conductivity and Luminescence in Coordination Polymers Based on Copper(I)-Halides and Sulfur-Pyrimidine Ligands. *Inorg. Chem.* **2012**, *51* (1), 718-727.
42. Xue, F.; Fang, J.; Delker, S. L.; Li, H.; Martásek, P.; Roman, L. J.; Poulos, T. L.; Silverman, R. B., Symmetric Double-Headed Aminopyridines, a Novel Strategy for Potent and Membrane-Permeable Inhibitors of Neuronal Nitric Oxide Synthase. *J. Med. Chem.* **2011**, *54* (7), 2039-2048.
43. Imaeda, Y.; Tokuhara, H.; Fukase, Y.; Kanagawa, R.; Kajimoto, Y.; Kusumoto, K.; Kondo, M.; Snell, G.; Behnke, C. A.; Kuroita, T., Discovery of TAK-272: A Novel, Potent, and Orally Active Renin Inhibitor. *ACS Medicinal Chemistry Letters* **2016**, *7* (10), 933-938.

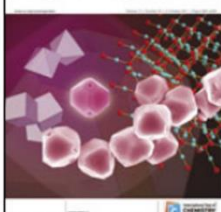
44. Fuller, A. M.; Leigh, D. A.; Lusby, P. J.; Oswald, I. D. H.; Parsons, S.; Walker, D. B., A 3D Interlocked Structure from a 2D Template: Structural Requirements for the Assembly of a Square-Planar Metal-Coordinated [2]Rotaxane. *Angew. Chem. Int. Ed.* **2004**, *43* (30), 3914-3918.
45. Mitchell, A. R.; Pagoria, P. F.; Coon, C. L.; Jessop, E. S.; Poco, J. F.; Tarver, C. M.; Breithaupt, R. D.; Moody, G. L., Nitroureas 1. Synthesis, scale-up and characterization of K-6. *Propellants, Explosives, Pyrotechnics* **1994**, *19* (5), 232-239.
46. APEX3 Version 2016.5-0 and SAINT+ Version 8.37A. Bruker AXS, Inc., Madison, Wisconsin, USA, 2016.
47. Krause, L.; Herbst-Irmer, R.; Sheldrick, G. M.; Stalke, D., Comparison of silver and molybdenum microfocus X-ray sources for single-crystal structure determination. *J. Appl. Crystallogr.* **2015**, *48* (1), 3-10.
48. Sheldrick, G., SHELXT - Integrated space-group and crystal-structure determination. *Acta Crystallographica Section A* **2015**, *71* (1), 3-8.
49. Sheldrick, G., Crystal structure refinement with SHELXL. *Acta Crystallographica Section C* **2015**, *71* (1), 3-8.
50. Dolomanov, O. V.; Bourhis, L. J.; Gildea, R. J.; Howard, J. A. K.; Puschmann, H., OLEX2: a complete structure solution, refinement and analysis program. *J. Appl. Crystallogr.* **2009**, *42* (2), 339-341.
51. APEX3 Version 2016.5-0 and SAINT+ Version 8.38A. Bruker AXS, Inc., Madison, Wisconsin, USA, 2016.
52. Le Page, Y., Computer derivation of the symmetry elements implied in a structure description. *J. Appl. Crystallogr.* **1987**, *20* (3), 264-269.

53. Spek, A., LEPAGE - an MS-DOS program for the determination of the metrical symmetry of a translation lattice. *J. Appl. Crystallogr.* **1988**, 21 (5), 578-579.
54. Spek, A., PLATON, An Integrated Tool for the Analysis of the Results of a Single Crystal Structure Determination. *Acta Crystallographica Section A* **1990**, 46 (s1), c34.
55. Spek, A., Structure validation in chemical crystallography. *Acta Crystallographica Section D* **2009**, 65 (2), 148-155.

APPENDIX A

PERMISSION TO REPRINT: CHAPTER 2

 **Copyright Clearance Center**  **RightsLink**[®]  **Home**  **Create Account**  **Help** 

 	Title: Pillars of assembled pyridyl bis-urea macrocycles: a robust synthon to organize diiodotetrafluorobenzenes	LOGIN If you're a copyright.com user, you can login to RightsLink using your copyright.com credentials. Already a RightsLink user or want to learn more?
	Author: Bozumeh Som, Sahar R. Salpage, Juno Son, Bing Gu, Stavros G. Karakalos, Mark D. Smith, Linda S. Shimizu	
	Publication: CrystEngComm	
	Publisher: Royal Society of Chemistry	
	Date: Dec 14, 2016	

Copyright © 2016, Royal Society of Chemistry

This reuse request is free of charge. Please review guidelines related to author permissions here: <http://www.rsc.org/AboutUs/Copyright/Permissionrequests.asp>

BACK

CLOSE WINDOW

Copyright © 2018 [Copyright Clearance Center, Inc.](#) All Rights Reserved. [Privacy statement](#), [Terms and Conditions](#). Comments? We would like to hear from you. E-mail us at customercare@copyright.com

APPENDIX B

PERMISSION TO REPRINT: CHAPTER 3

From: Sean Conway <sc@iucr.org>
Sent: Wednesday, June 13, 2018 9:26:07 AM
To: SOM, BOZUMEH
Subject: Re: Permission request

Dear Dr Som

Our transfer of copyright information has the following:-

=====

Authors retain the following rights to re-use the article, as long as it is not sold or reproduced, in whole or in part, for commercial purposes, i.e. for monetary gain on the authors' account or on that of a third party, or for indirect financial gain by a commercial entity. These rights apply without needing to seek permission from the IUCr.

Provided that a full bibliographic reference to the article as published in an IUCr journal is made, authors may use all or part of the article and abstract, without revision or modification, in theses and/or dissertations, in personal compilations or other publications of their own work (and may receive a royalty or other payment for such work).

=====

So all is well since you are an author on this paper.

Bets wishes
Sean Conway

On Wednesday, 13 June 2018 12:51:53 BST you wrote:

> I am reproducing this for my dissertation, so I will be using longer passages, and almost all tables and figures from this paper. I therefore think a prior permission for reuse is required.

>

> Thanks,
>
> Bozume Som
> Graduate Research Assistant
> Department of Chemistry & Biochemistry
> University of South Carolina
> Columbia, SC 29208
> bsom@email.sc.edu
> _____
> From: Peter Strickland <ps@iucr.org>
> Sent: Wednesday, June 13, 2018 6:29:58 AM
> To: SOM, BOZUMEH
> Subject: Fwd: Permission request
>
> Dear Dr Som
>
> Thank you for your message
>
> Our conditions for the reuse of material in scientific publications are given at:
>
> <http://journals.iucr.org/services/permissions.html>
>
> If you comply with the conditions at the top of this web page, prior permission for
reuse is not required.
>
> Best wishes
> Sean Conway
> Managing Editor (Acta Cryst. C)
> Email: sc@iucr.org<<mailto:sc@iucr.org>>
>
> ----- Forwarded Message -----
>
> Subject: Permission request
> Date: Tuesday 12 June 2018, 19:12:16
> From: SOM, BOZUMEH <bsom@email.sc.edu>
> To: med@iucr.org <med@iucr.org>
>
> Dear Sir/Madam,
>

> I am writing to request permission to reproduce the material detailed below in my dissertation.

>

> Som, B., Shue, J. R., Smith, M. D. & Shimizu, L. S. (2018). Acta Crystallographica Section C 74, 75-81.

>

> I am the first author of the original work. If you are not the copyright holder for this material, then I would appreciate it if you could let me know who I should contact.

>

> Yours sincerely,

>

> Bozume Som

>

> Graduate Research Assistant

> Department of Chemistry & Biochemistry

> University of South Carolina

> Columbia, SC 29208

> bsom@email.sc.edu

> -----

Best wishes from Chester.

Sean Conway

Managing Editor (Acta Cryst. C)

Email: sc@iucr.org

<http://journals.iucr.org/c>

From: Peter Strickland <ps@iucr.org>

Sent: Wednesday, June 13, 2018 6:29:58 AM

To: SOM, BOZUMEH

Subject: Fwd: Permission request

Dear Dr Som

Thank you for your message.

Our conditions for the reuse of material in scientific publications are given at:

<http://journals.iucr.org/services/permissions.html>

If you comply with the conditions at the top of this web page, prior permission for reuse is not required.

Best wishes

Sean Conway
Managing Editor (Acta Cryst. C)
Email: sc@iucr.org

----- Forwarded Message -----

Subject: Permission request
Date: Tuesday 12 June 2018, 19:12:16
From: SOM, BOZUMEH <bsom@email.sc.edu>
To: med@iucr.org <med@iucr.org>

Dear Sir/Madam,

I am writing to request permission to reproduce the material detailed below in my dissertation.

Som, B., Shue, J. R., Smith, M. D. & Shimizu, L. S. (2018). Acta Crystallographica Section C 74, 75-81.

I am the first author of the original work. If you are not the copyright holder for this material, then I would appreciate it if you could let me know who I should contact.

Yours sincerely,

Bozumeh Som
Graduate Research Assistant
Department of Chemistry & Biochemistry
University of South Carolina
Columbia, SC 29208
bsom@email.sc.edu

From: Sean Conway <sc@iucr.org>
Sent: Tuesday, April 24, 2018 5:14:49 AM
To: SOM, BOZUMEH
Cc: ps@iucr.org
Subject: Permission request

Dear Bozumeh

Thank you for your message.

Our conditions for the reuse of material in scientific publications are given at:

<http://journals.iucr.org/services/permissions.html>

If you comply with the conditions at the top of this web page, prior permission for reuse is not required.

Best wishes
Sean Conway
Managing Editor (Acta Cryst. C)
Email: sc@iucr.org

#####

----- Forwarded Message -----

Subject: Permission request re:
Date: Monday, 23 April 2018, 21:48:14 BST
From: dh@iucr.org
To: sc@iucr.org

Message from "Contact Us" web form from Bozume Som

email: bsom@email.sc.edu

Subject: Permission request re:

Enquiry: type Journals

Comment:

I am writing my PhD dissertation and would like to request permission to reproduce the material detailed below in my dissertation.

Som, B., Shue, J. R., Smith, M. D. & Shimizu, L. S. (2018). Acta Crystallographica Section C 74, 75-81.

I am an author of the original work.

If you are not the copyright holder for this material, then I would appreciate it if you could let me know who I should contact.

Yours faithfully
Bozume Som

APPENDIX C

PERMISSION TO REPRINT: CHAPTER 4



RightsLink®

Home

Create Account

Help



ACS Publications
Most Trusted. Most Cited. Most Read.

Title: Fluorescence Polarization Measurements to Probe Alignment of a Bithiophene Dye in One-Dimensional Channels of Self-Assembled Phenylethylenylene Bis-Urea Macrocycle Crystals

Author: Preecha Kittikhunnatham, Bozumeh Som, Vitaly Rassolov, et al

Publication: The Journal of Physical Chemistry C

Publisher: American Chemical Society

Date: Aug 1, 2017

Copyright © 2017, American Chemical Society

LOGIN

If you're a [copyright.com user](#), you can login to RightsLink using your [copyright.com](#) credentials. Already a [RightsLink user](#) or want to [learn more?](#)

PERMISSION/LICENSE IS GRANTED FOR YOUR ORDER AT NO CHARGE

This type of permission/license, instead of the standard Terms & Conditions, is sent to you because no fee is being charged for your order. Please note the following:

- Permission is granted for your request in both print and electronic formats, and translations.
- If figures and/or tables were requested, they may be adapted or used in part.
- Please print this page for your records and send a copy of it to your publisher/graduate school.
- Appropriate credit for the requested material should be given as follows: "Reprinted (adapted) with permission from (COMPLETE REFERENCE CITATION). Copyright (YEAR) American Chemical Society." Insert appropriate information in place of the capitalized words.
- One-time permission is granted only for the use specified in your request. No additional uses are granted (such as derivative works or other editions). For any other uses, please submit a new request.

BACK

CLOSE WINDOW

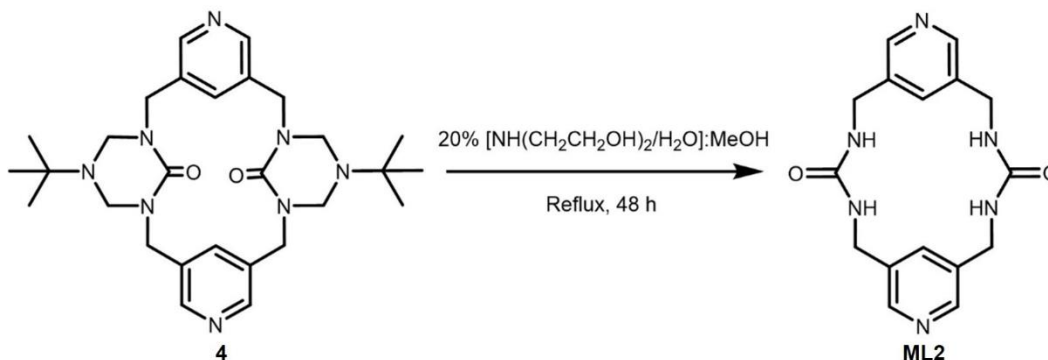
Copyright © 2018 [Copyright Clearance Center, Inc.](#) All Rights Reserved. [Privacy statement](#). [Terms and Conditions](#). Comments? We would like to hear from you. E-mail us at customer@copyright.com

APPENDIX D

DEPROTECTED NEW PYRIDYL *BIS*-UREA MACROCYCLE (**ML2**)

Synthesis of pyridyl *bis*-urea macrocycle (ML2**).** Triazinanone protected *bis*-urea macrocycle **4** (0.12 g, 0.23 mmol) was heated to reflux in 20 mL of a 1:1 mixture of 20% [diethanolamine/water solution adjusted to pH ~ 2 with conc. HCl]: MeOH for 24 h. The methanol was removed in vacuo and cooled in an ice-bath to afford white solid precipitate. The solid was collected by suction filtration, washed with 10 mL H₂O and dried in vacuo to obtain the product as white powder (68 mg, 90 %). The proton NMR of **ML2** was recorded at 100 °C. Heteronuclear Single Quantum Correlation (HSQC) experiments enable us to fully confirm the ¹³C NMR of **ML2**. ¹H NMR (400 MHz, DMSO-d₆) δ = 8.27 (s, 2H), 7.66 (s, 1H), 6.41 (t, J = 5.8 Hz, 2H), 4.32 (d, J = 6.0 Hz, 4H). ¹³C-NMR (101 MHz, DMSO-d₆); δ = 158.51, 146.78, 137.36, 132.04, 40.42. Material turns brown (decomposes) in the temperature range of 283-286 °C.

Scheme D.1 Synthesis of macrocycle **ML2**



Recrystallization: Macrocycle **ML2** (6.0 mg) was heated with a heat gun in a DMSO-acetonitrile (1:1.5 v/v) solution (5 mL) in a pressure tube to dissolve completely. The mixture was then placed in an oil that is heated to 120 °C for 30 minutes before slowly cooling to room temperature at a rate of 1 °C/h. This afforded colorless needles suitable for single crystal X-ray diffraction.

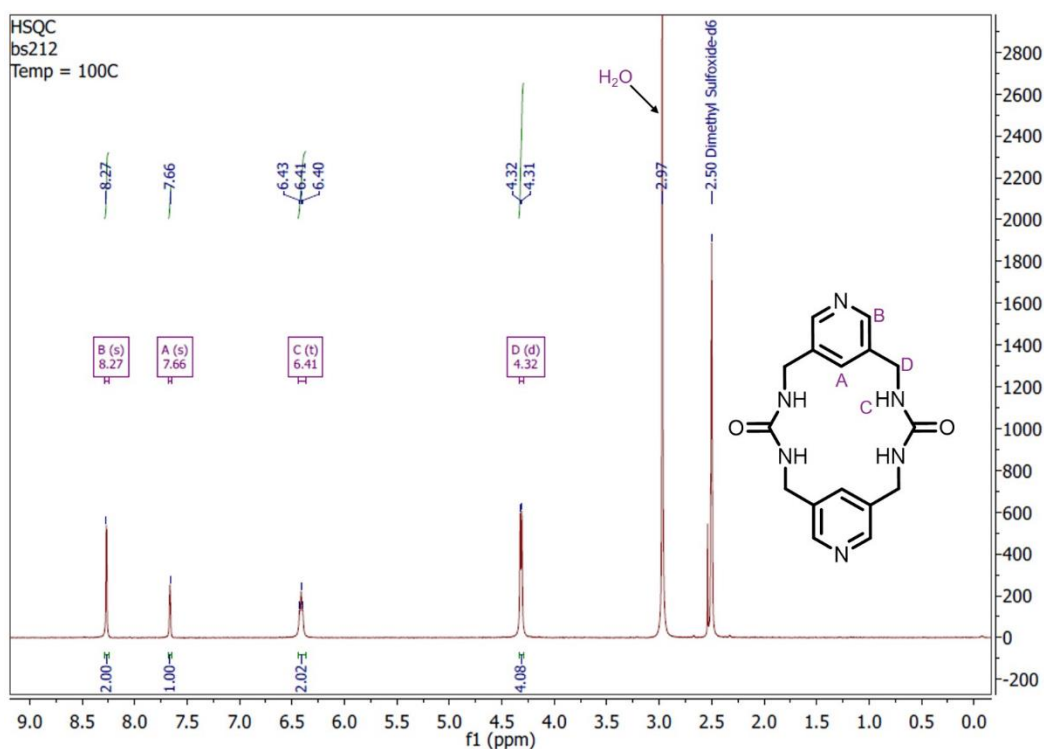


Figure D.1 ¹H NMR (400 MHz, DMSO-d₆) of macrocycle **ML2** at 100 °C

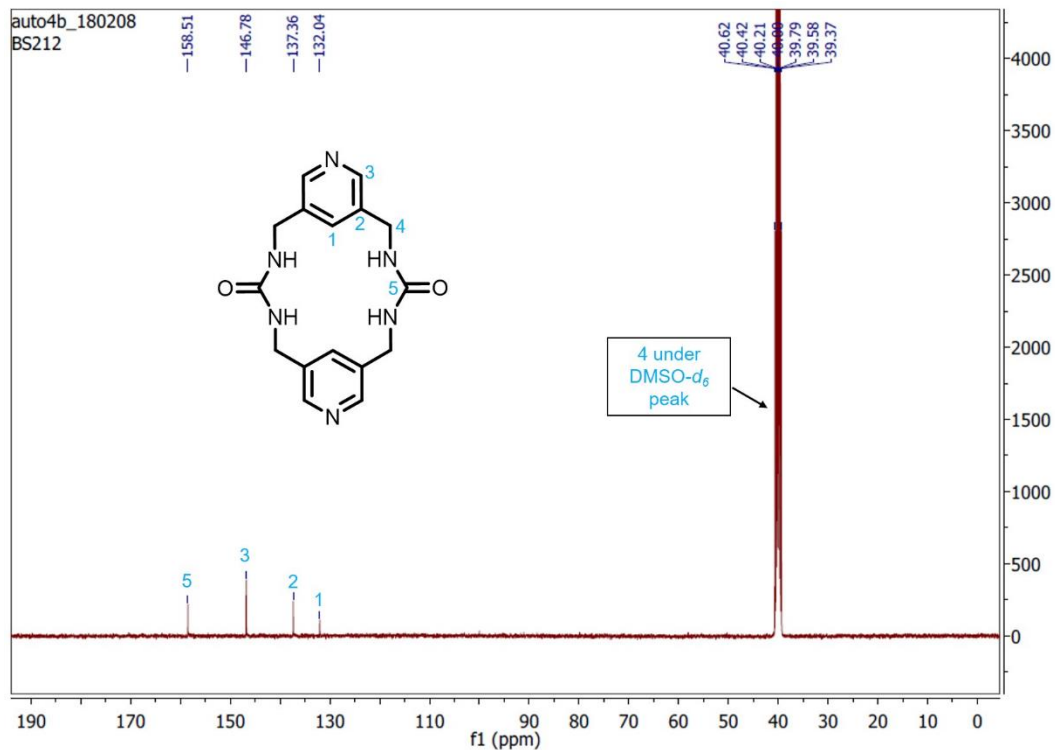


Figure D.2 ^{13}C NMR (101 MHz, $\text{DMSO-}d_6$) of macrocycle **ML2** at 100 °C

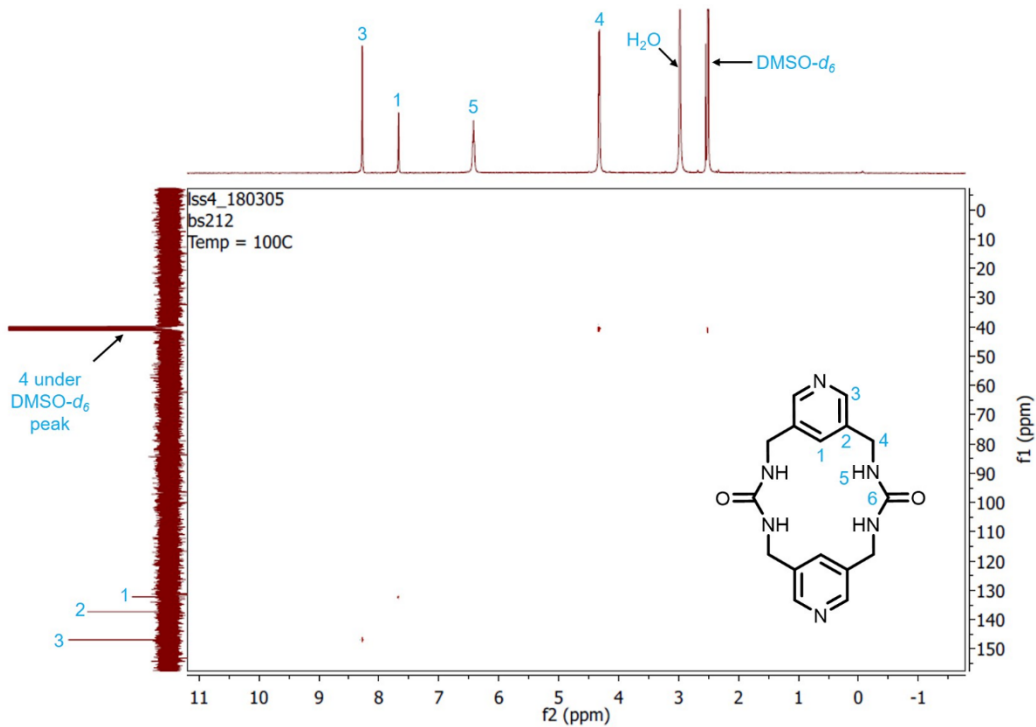


Figure D.3 HSQC spectrum (400 MHz, $\text{DMSO-}d_6$) of macrocycle **ML2** at 100 °C

X-Ray Structure Determination of ML2

X-ray intensity data from a colorless needle were collected at 100(2) K using a Bruker D8 QUEST diffractometer equipped with a PHOTON-100 CMOS area detector and an Incoatec microfocus source (Mo K α radiation, $\lambda = 0.71073 \text{ \AA}$). The raw area detector data frames were reduced and corrected for absorption effects using the Bruker APEX3, SAINT+ and SADABS programs.^{1,2} Final unit cell parameters were determined by least-squares refinement of 9816 reflections taken from the data set. The structure was solved with SHELXT.³ Subsequent difference Fourier calculations and full-matrix least-squares refinement against F^2 were performed with SHELXL-2018³ using OLEX2.⁴

The compound crystallizes in the monoclinic system. The pattern of systematic absences in the intensity data was consistent with the space group $P2_1/c$, which was confirmed by structure solution. The asymmetric unit consists of half of one molecule, which is located on a crystallographic inversion center. All non-hydrogen atoms were refined with anisotropic displacement parameters. Hydrogen atoms bonded to carbon were located in difference Fourier maps before being placed in geometrically idealized positions and included as riding atoms with $d(\text{C-H}) = 0.95 \text{ \AA}$ for aromatic hydrogen atoms and $d(\text{C-H}) = 0.99 \text{ \AA}$, and freely refined isotropic displacement parameters. The two hydrogen atoms bonded to the urea nitrogen atoms were located in difference maps and refined freely. The largest residual electron density peak in the final difference map is $0.36 \text{ e}^-/\text{\AA}^3$, located 0.68 \AA from C3.

(1) **APEX3** Version 2016.5-0 and **SAINT+** Version 8.37A. Bruker AXS, Inc., Madison, Wisconsin, USA, 2016.

(2) **SADABS**-2016/2: Krause, L., Herbst-Irmer, R., Sheldrick G.M. and Stalke D. *J. Appl. Cryst.* **2015**, *48*, 3-10.

(3) (a) **SHELXT**: Sheldrick, G.M. *Acta Cryst.* **2015**, *A71*, 3-8. (b) **SHELXL**: Sheldrick, G.M. *Acta Cryst.* **2015**, *C71*, 3-8.

(4) **OLEX2**: a complete structure solution, refinement and analysis program. Dolomanov, O. V., Bourhis, L. J., Gildea, R. J., Howard J. A. K. and Puschmann, H. *J. Appl. Cryst.* **2009**, *42*, 339-341.

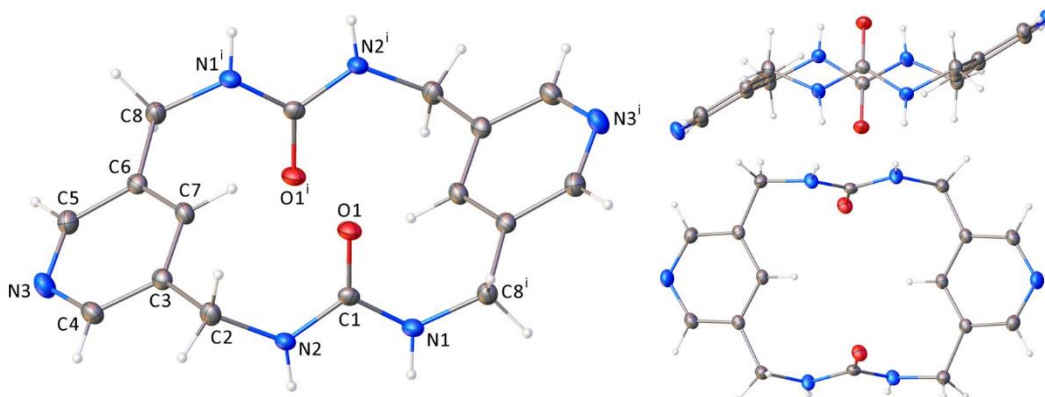


Figure D.4 X-ray crystal structure of **ML2**. Displacement ellipsoid plots of the molecular structure. Displacement ellipsoids drawn at the 60% probability level. Molecule on crystallographic inversion center. Superscripts denote symmetry-equivalent atoms.

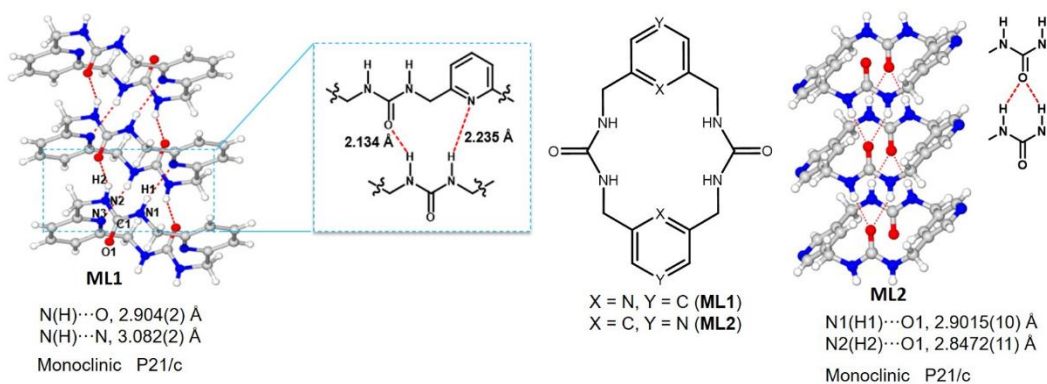


Figure D.5 Comparison of the assembly motifs in macrocycles **ML1** and **ML2** in the solid state.

Table D.1 Crystal data and structure refinement for **ML2**.

Empirical formula	C ₁₆ H ₁₈ N ₆ O ₂
Formula weight	326.36
Temperature/K	100(2)
Crystal system	monoclinic
Space group	P2 ₁ /c
a/Å	4.5960(2)
b/Å	8.0466(4)
c/Å	20.1745(9)
α/°	90
β/°	91.053(2)
γ/°	90
Volume/Å ³	745.97(6)
Z	2
ρ _{calc} /cm ³	1.453
μ/mm ⁻¹	0.101
F(000)	344.0
Crystal size/mm ³	0.6 × 0.06 × 0.06
Radiation	MoKα (λ = 0.71073)
2θ range for data collection/°	5.45 to 60.124
Index ranges	-6 ≤ h ≤ 6, -11 ≤ k ≤ 11, -28 ≤ l ≤ 28
Reflections collected	33578
Independent reflections	2189 [R _{int} = 0.0396, R _{sigma} = 0.0174]
Data/restraints/parameters	2189/0/125
Goodness-of-fit on F ²	1.041
Final R indexes [I ≥ 2σ (I)]	R ₁ = 0.0361, wR ₂ = 0.0930
Final R indexes [all data]	R ₁ = 0.0439, wR ₂ = 0.0986
Largest diff. peak/hole / e Å ⁻³	0.38/-0.26